Spins and Phonons in Graphene Nanostructures

Dissertation zur Erlangung des akademischen Grades eines Doktors der Naturwissenschaften (Dr. rer. nat.)

---

vorgelegt von Matthias Droth
an der Universität Konstanz

Universität Konstanz

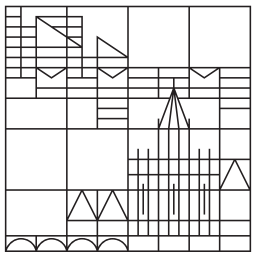

Mathematisch-Naturwissenschaftliche Sektion
Fachbereich Physik

Tag der mündlichen Prüfung:	12. Dezember 2014
Erster Referent:	Prof. Dr. Guido Burkard
Zweiter Referent:	Prof. Dr. Wolfgang Belzig

Acknowledgements

It is my great pleasure to thank Prof. Guido Burkard for supervision of my work and invaluable years in his research group at the University of Konstanz. I am grateful for the opportunity to work in an exciting and highly topical field of physics and to present our results at numerous international conferences. I thank him most sincerely for innumerable and invaluable discussions about physics and other topics. His instruction and guidance have taught me a lot.

I have also had great pleasure in the ongoing collaboration with Prof. Vitor Pereira and highly appreciate his effort explaining physics to me. The visit to the group of Prof. Lieven Vandersypen has been very instructive and I prize his enthusiasm in introducing me to the experimental side of spintronics. Both the Quantum Transport group at the Delft University of Technology and the theory group of the Graphene Research Centre at the National University of Singapore have been very welcoming and I owe them gratitude for their help and hospitality.

A lot of people have contributed to my studies. In particular, I also acknowledge discussions with Prof. Wolfgang Belzig, Prof. András Pályi, Prof. Jenni Adams, Prof. Lain-Jong Li, Prof. Cord Müller, Dr. Andor Kormányos, Dr. Philipp Struck, Dr. Martin Bruderer, Dr. Federica Haupt, Dr. Stijn Goossens, Dr. Victor Calado, Dr. Larysa Tryputen, Dr. Lung-Hao Hu, Dr. Marco Hachiya, Dr. Michael Pokojovy, Dr. Martin Trappe, Karina Guerrero, Fabio Hipolito, Alexandre Pachoud, Philipp Leicht, Felix Fehse, and Werner Schosser.

My former and current office colleagues Dr. Julia Hildmann, Dr. Erik Welander, Franziska Maier, Niklas Rohling, Marko Rančić, and Miguel Rodriguez deserve very special thanks for instructive discussions and good times. Proper respect goes to all other former and current group members that have contributed to an interactive and productive environment. In particular, I thank everybody who has proofread parts of this thesis.

Finally, I acknowledge general funding from the European Science Foundation (ESF) within the EuroGRAPHENE project CONGRAN and from the Deutsche Forschungsgemeinschaft. Special thanks to Dr. Ana Helman, Dr. Aigars Ekers, and to Catherine Lobstein from the ESF for their support with additional funding opportunities that enabled both very educational stays in Delft and in Singapore.

Abstract

Quantum information science relies on quantum systems with sufficiently long coherence times. A spintronics implementation in graphene would benefit from the low density of nuclear spins in carbon and small spin-orbit interactions. The coupling of the spin to lattice dynamics puts an upper bound on spin coherence times. In addition, phonons in graphene are interesting due to the monatomic thickness of the material, accompanied by the lowest surface mass density of all solid materials. The prospects for quantum information science, nanoelectromechanical systems, and for nanotechnology in general inspire us to study the theory of spins and phonons in graphene nanostructures.

We give an introduction to graphene and its properties and also comment on the development of research related to graphene and other two-dimensional materials like hexagonal boron nitride (hBN). We review the basic electronic properties of monolayer graphene and hBN in detail. Klein's paradox is most important for the confinement of charge carriers in graphene. Bilayer systems, in particular a graphene/hBN heterostructure, are also discussed. We use the continuum model to derive electron-phonon couplings, spin-phonon coupling, the change of the Fermi velocity under external loading, and the deformation of the Brillouin zone under uniform strain. Parts of our studies rely on the modern theory of polarization or on Peierls' phase. To this end, we also demonstrate the necessary concepts of the geometric phase.

We use the continuum model to derive the acoustic phonons in graphene nanoribbons for fixed as well as for free lateral boundaries. In-plane and out-of-plane deformations are treated separately. Fixed boundaries lead to gapped phonon dispersions and free boundaries to gapless ones. As expected, our results are in accordance with previous results for bulk graphene if the phonon wavenumber is much shorter than the ribbon width.

Building on these results, we calculate the electron spin relaxation in armchair graphene nanoribbon quantum dots. The combination of spin-orbit interaction and electron-phonon coupling to in-plane phonons yields an effective spin-phonon coupling. Out-of-plane phonons are also considered but give no lowest order contribution to the spin relaxation rate T_1^{-1}. We find Van Vleck cancellation and interference effects of the deformation potential and the bond-length change. As a result, spin relaxation times can exceed the range of seconds, which would be most suitable for graphene-based quantum computing. For magnetic fields below B=0.5 T, free mechanic boundaries lead to a relaxation rate that scales as $T_1^{-1} \propto B^5$. For fixed boundaries, the gapped phonon spectrum bears the potential to suppress spin relaxation in lowest order.

The bond-length change manifests itself in the low-energy description of hBN, as for graphene, via a strain-induced pseudomagnetic gauge field. We evolve the sublattice potential adiabatically from its value for graphene to that of boron nitride and use the modern theory of polarization to calculate the piezoelectric effect of hBN. We find that all symmetry constraints are met and we provide an estimate of 3 eV for the so far unknown coupling strength of the strain-induced gauge field in hBN. The resulting values

of 7.5×10^{-11} As/m (3×10^{-13} m/V) for the strength of the converse (direct) piezoelectric effect are a factor of 2 smaller than those obtained from first-principle calculations for a relaxed ion situation.

Graphene nanoflakes with vacancies can exhibit interesting magnetic behavior. We describe such a system with two vacancies with a full tight-binding model that respects an external magnetic field via Peierls' phase. This leads to a magnetic field dependence of the exchange coupling between the localized vacancy states. The magnetic ordering is antiferromagnetic ($J\geq0$) and, depending on the size of the flake and the position of the vacancies, can be tuned over several orders of magnitude or even switched on ($J>0$) and off ($J=0$). This *in situ* tunability of the magnetic behavior is most interesting for spintronics applications.

Zusammenfassung

Die Quanteninformatik hängt von quantenmechanischen Systemen mit genügend langen Kohärenzzeiten ab. Eine spintronischen Realisierung in Graphen würde von der geringen Kernspindichte in Kohlenstoff und einer schwachen Spin-Bahn-Kopplung profitieren. Die Kopplung des Spins an die Gitterdynamik bestimmt eine Obergrenze für die Spinkohärenzzeiten. Außerdem sind Gitterschwingungen in Graphen interessant, weil dieses Material lediglich ein Atom dick ist und die geringste Flächenmassendichte aller Festkörper besitzt. Die Perspektiven für das Quantenrechnen, für nanoelektromechanische Systeme und für die Nanotechnologie allgemein inspirieren uns, die Theorie über Spin und Phononen in Graphennanostrukturen zu studieren.

Wir geben eine Einleitung zu Graphen und seinen Eigenschaften und kommentieren auch die Entwicklung von Forschung mit Bezug zu Graphen bzw. anderen zweidimensionalen Materialien wie z.B. hexagonales Bornitrid (hBN). Die elektronischen Eigenschaften von einlagigem Graphen bzw. Bornitrid werden im Detail dargelegt. Das Klein-Paradox ist besonders relevant wenn es um den räumlichen Einschluss von Ladungsträgern in Graphen geht. Doppellagige Systeme, insbesondere eine Graphen/hBN Heterostruktur werden ebenfalls diskutiert. Wir benutzen das Kontinuumsmodell um Elektron-Phonon-Kopplungen, Spin-Phonon-Kopplung, die Änderung der Fermigeschwindigkeit bei äußerer Belastung und die Deformation der Brillouin Zone unter gleichförmiger Verformung herzuleiten. In Teilen unserer Studien machen wir uns die moderne Theorie der Polarisation oder die Peierls-Phase zunutze. Zu diesem Zweck demonstrieren wir die notwendigen Konzepte der geometrischen Phase.

Wir benutzen das Kontinuumsmodell um die akustischen Phononen in Graphennanobändern sowohl für fixierte als auch für freie laterale Ränder herzuleiten. Deformationen innerhalb und außerhalb der Ebene werden separat voneinander behandelt. Fixierte Ränder führen zu Phonondispersionen mit Lücke und freie Ränder führen zu Dispersionen ohne Lücke. Wenn die Phononwellenlänge sehr viel kürzer als die Breite des Nanobandes ist, stimmen unsere Resultate — wie erwartet — mit bisherigen Resultaten für ausgedehntes Graphen überein.

Aufbauend auf diesen Resultaten berechnen wir die Spinrelaxation von Elektronen in Quantenpunkten auf Graphennanobändern mit gestaffelten[1] Rändern. Die Kombination von Spin-Bahn-Wechselwirkung und Elektron-Phonon-Kopplung zu Phononen in der Graphenebene führt zu einer effektiven Spin-Phonon-Kopplung. Gitterschwingungen aus der Ebene heraus werden ebenfalls berücksichtigt, liefern in niedrigster Ordnung jedoch keinen Beitrag zur Spinrelaxationsrate T_1^{-1}. Wir finden Van Vleck-Auslöschung sowie Interferenz zwischen dem Deformationspotential und dem Mechanismus aufgrund der anisotropen Änderung der Bindungslänge. Daraus ergibt sich, dass die Spinrelaxationszeiten den Sekundenbereich übertreffen können, was sehr passend für graphenbasiertes Quantenrechnen wäre. Für Magnetfelder unterhalb B=0.5 T führen freie mechanische Ränder zu einer Relaxationsrate, die wie $T_1^{-1} \propto B^5$ skaliert. Bei fixierten Rändern birgt die Energielücke in der Phonondispersion die Möglichkeit, Spinrelaxation in niedrigster

[1] Diese Übersetzung von „armchair (edges)“ ist [Balasubramanian(2011)] entnommen.

Ordnung zu unterdrücken.

Die anisotrope Änderung der Bindungslänge manifestiert sich in der niederenergetischen Modellierung von hBN, wie für Graphen, in einem von der Verspannung induzierten pseudomagnetischen Eichfeld. Wir ändern das Untergitterpotential adiabatisch vom Wert für Graphen zu dem von Bornitrid und benutzen die moderne Theorie der Polarisation um den Piezoeffekt in hBN zu errechnen. Wir finden Übereinstimmung mit allen Symmetriebedingungen und geben einen Schätzwert von 3 eV für die bis dato unbekannte Kopplungsstärke des von der Verspannung bewirkten Eichfeldes in hBN an. Die resultierenden Werte von 7.5×10^{-11} As/m (3.0×10^{-13} m/V) für die Stärke des umgekehrten (direkten) Piezoeffekt sind um einen Faktor 2 kleiner als jene, die per *Ab-initio*-Rechnungen für eine Situation mit relaxierten Ionen ermittelt wurden.

Graphennanoflocken mit Leerstellen können ein interessantes magnetisches Verhalten zeigen. Wir beschreiben solch ein System mit zwei Fehlstellen per Linearkombination atomarer Orbitale in zweiter Quantisierung, wobei ein äußeres Magnetfeld über die Peierls-Phase berücksichtigt wird. Dies führt zu einer Magnetfeldabhängigkeit des Austauschwechselwirkung zwischen den an den Lehrstellen lokalisierten Zuständen. Die magnetische Ordnung ist antiferromagnetisch ($J\geq0$) und kann, je nach Größe der Flocke und Position der Leerstellen, über mehrere Größenordnungen eingestellt oder sogar ein- ($J>0$) und ausgeschaltet ($J=0$) werden. Die Einstellbarkeit des magnetischen Verhaltens — im laufenden Experiment — ist höchst interessant für Anwendungen der Spintronik.

Contents

1. Introduction

Quantum mechanics describes fundamental particles and systems at the nanoscale, that is, systems where at least one spatial dimension is confined to a length of $1 - 100\,\mathrm{nm}$. Larger systems may also be described by quantum mechanics but act like a bath into which the quantum features are dissipated. Unless the system is well isolated from its surrounding environment, quantum effects can be neglected and classical physics applies[1] [Zurek(2003)]. Quantum mechanics plays a role for many nanoscale technologies, summarized as *nanotechnology* [Feynman(1960)]. Areas for nanotechnology applications lie in medicine, electronics, bio-engineering, material science, energy storage, and many more. The invention of the scanning tunneling microscope in 1981 was a milestone for nanotechnology as it allowed for precise imaging of individual atoms and molecules as well as for their manipulation [Binnig1982Pat, Bai]. Around that time, the commercial semiconductor industry has reached the sub-micron standard [Soclof1983Pat, Veendrick] and nanotechnology has drawn great benefit from the industry's maturity and ongoing effort to downsize circuitry. According to Moore's law, the number of transistors on integrated circuits roughly doubles within every two years [Moore(1965)]. Due to additional improvements in transistor quality, computing performance doubles about every eighteen months. This rule of thumb has held for five decades — also because competing semiconductor manufacturers have soon started viewing it as an industry goal — and remains valid today. Moore's law is not a law by nature and will come to an end eventually, maybe in slightly more than a decade when the 1 nm benchmark should be reached and interfering quantum effects deem further miniaturization uneconomical [Lloyd(2000), Kish(2002), Thompson(2006)]. Yet computing performance can still increase dramatically[2], possibly with the advent of quantum computing.

Quantum computing relies on the quantum bit or *qubit* as the fundamental carrier of information rather than on the classical bit (binary digit) employed by classical computing [Nielsen&Chuang]. Qubits are a generalization of classical bits in that they contain classical bits as special cases. The concept of quantum computing was first proposed in 1980 and received a major boost when Peter Shor found an algorithm for efficient factorization of integers using a quantum computer [Manin(1980), Feynman(1982), Deutsch(1985), Shor(1994), Shor (1997)]. While quantum effects become a hindrance for classical computers with nanometer-sized transistors, quantum computing aims at exploiting exactly those effects. A quantum computer should conform a list of requirements known as the five DiVincenzo criteria [DiVincenzo(1998), DiVincenzo(1999)]. In particular, the ma-

[1] Bose-Einstein condensates are an example for macroscopic systems that are sufficiently isolated from their outside environment to exhibit quantum phenomena at the length scale of millimeters, visible with the naked eye [Anderson(1995)]. Here, we are not concerned with such exotic systems but focus on solid state physics at the nanoscale.

[2] Note that originally, Moore's law refers to the density of transistors and not to performance.

chine should

1. have a sufficient number of qubits,
2. allow for initialization of the memory before each computation,
3. have a sufficiently low error rate,
4. feature a universal set of logic gates for computing, and
5. provide reliable output of the final result.

Despite their intuitive nature, meeting these criteria poses great challenges. For example, the fourth criterion demands not only the use of but control over the quantum state which is most easily perturbed by decoherence, i.e., uncontrolled influences from the environment. The third criterion demands that coherence be maintained for a sufficiently long time, about 10^4 times the clock cycle[3].

One proposed implementation of quantum computing is the Loss-DiVincenzo quantum computer that uses electron spin states, confined in single electron quantum dots, as qubits. One- and two-qubit gates can be implemented by adjusting tunneling barriers and/or by external fields, thus allowing for universal quantum computing [Loss(1998), Hanson(2007)]. While classical computing encodes information in the charge this proposal of a quantum computing relies on the spin but keeps the electron as the particle that carries that degree of freedom. Such a spintronics ansatz benefits from the expertise in controlling electrons in semiconductor heterostructures [Hanson(2007)]. As stated above, reliable quantum computation requires qubits with coherence times that exceed the clock time[3] by about 10^4 [DiVincenzo(1999)]. For spin qubits, the most relevant sources of decoherence are (i) interactions with nuclear spins, (ii) interaction with lattice vibrations, mediated by spin-orbit coupling, and (iii) charge fluctuations [Petta(2005), Khaetskii(2001), Zhang(2009)]. Effects (i) and (ii) are typically strong in III-V semiconductors but weak in carbon-based materials like diamond, carbon nanotubes, and graphene [Hanson(2007), Trauzettel(2007)].

Among those, graphene has a particularly low spin-orbit interaction [Kuemmeth(2008), Kane(2005), Min(2006), Gmitra(2009)]. Its unmatched mechanical strength and the lowest surface mass density of all solid state materials are not only relevant for phonon-induced decoherence but also make graphene most suitable for nanoelectromechanical systems with unprecedented sensitivity [Steele(2009), Duerloo(2012), Qi(2012)]. These prospects motivate our studies of spins and phonons in graphene nanostructures. A detailed discussion of graphene and its prospects follows next.

1.1. Graphene and its potential in nanotechnology

Graphene is a monatomically thin layer of carbon atoms (Fig. 1.1 (a)) and the parent material for carbon allotropes of all spatial dimensionalities. Mono-, bi-, and few-layer graphene are (quasi)[4] two-dimensional [Geim(2007), CastroNeto(2009)]. Many layers of

[3]For specific codes, coherence times of 10^2 clock cycles may suffice [Barends(2014)].

[4]We consider monolayer graphene as truly two-dimensional but bi- and multilayers not, see Appendix B.

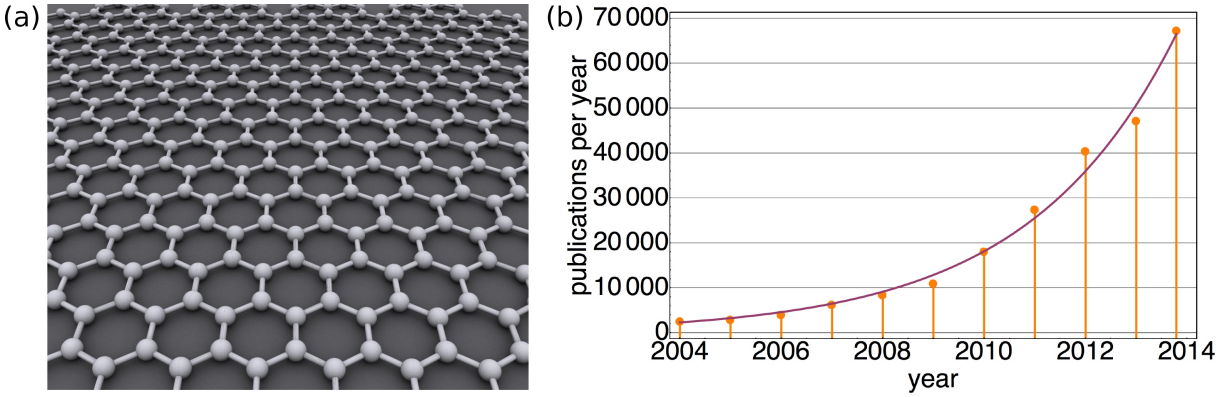

Figure 1.1.: (a) An artist's interpretation of the graphene lattice as a ball-and-stick model [CCBYSA3.0]. The atomic distance in graphene is 1.42×10^{-10} m [CastroNeto(2009)]. (b) At the time of this writing, the exponential growth of publications related to graphene continues. The data (orange bullets) are based on custom range searches for *graphene* on a freely accessible web search engine [Scholar]. The last data point represents the results in the year 2014 until October 15$^{\text{th}}$. The red fit is given by $p = 2324e^{0.3426(a-2004)}$, where p stands for the number of publications per year and a represents the end date of a year.

graphene stacked atop each other form three-dimensional graphite [Wallace(1947)]. Carbon nanotubes correspond to rolled up graphene [Iijima(1991), Suzuura(2002)] and narrow graphene nanoribbons can be produced by unzipping carbon nanotubes [Kosynkin(2009)]. Both these structures are quasi one-dimensional carbon allotropes. Forming a graphene sheet to a sphere leads to quasi zero-dimensional fullereni [Kroto(1985)]. Graphene nanoflakes, also known as nano-islands, are also quasi zero-dimensional. Although fullereni do not only contain hexagonal rings, all carbon atoms remain sp^2-hybridized, in similarity to graphene. In fact, the ending *-ene* in *graphene* has its origins in organic chemistry, where it is used to indicate sp^2-hybridization (e.g. in *butene* etc.). Diamond, a three-dimensional allotrope, consists of sp^3-hybridized carbon atoms and is thus chemically very different from graphene.

Three-dimensional graphite is a native element mineral that has been known and used for centuries, e.g. in pencils. The word *graphite*, derived from the Ancient Greek γράφω (*pen, to write*), literally means *writing stone*. Its layered crystal structure, which has been anticipated since 1859, was confirmed around the beginning of the previous century with the emergence of diffraction techniques [Brodie(1859), Hassel(1924), Bernal(1924)]. When writing with a pencil, pieces of graphite separate along these layers and stick to the paper. Though invisible to the naked eye, multi- or even monolayer graphene are produced in this everyday process [Geim(2008)]. For a better understanding of bulk graphite, Wallace calculated the electronic structure of a single graphite layer, i.e., of graphene [Wallace(1947)]. The paramount *Dirac equation* for massless electrons in graphene was pointed out later on [DiVincenzo(1984), Semenoff(1984)]. According to the Mermin-Wagner theorem, there can be no crystalline order in two dimensions [Mermin(1966), Mermin(1968)], implying that graphene would crumple at finite temperatures. However,

this crumpling can be avoided by fixing graphene to some stabilizing structure, e.g. a substrate [Novoselov(2004), Meyer(2007)]. Atomistic Monte Carlo simulations for free-floating graphene at room temperature show the formation of ripples with typical heights of half an atomic distance. These ripples give the material some three-dimensional texture and keep it from crumpling [Fasolino(2007)].

Multi- and monolayer graphene samples have been fabricated and studied long before 2004 [Ruess(1948), Boehm(1962), Oshima(1997)], yet it was not until then that Konstantin Novoselov and Andre Geim isolated monolayer graphene via micromechanical exfoliation — also publicized as *Scotch tape technique*, in reference to the manufacturer of the adhesive tape used in the process — and transferred it onto a thin layer of SiO_2 atop a silicon wafer. The SiO_2 couples only weakly to the graphene and preserves the Dirac-like, massless behavior of its electrons. At the same time, the underlying silicon electrode can be used to tune the chemical potential. This setup enabled the first observation of the anomalous quantum Hall effect in graphene [Novoselov(2004)], followed by a boom in graphene research with, as of this writing, an exponential growth of graphene-related publications and patents, see Fig. 1.1 (b) and [Savage(2012)].

- In graphene, three out of the four valence electrons of carbon form a planar sp^2 hybrid perpendicular to the remaining p_z orbital. The trigonal sp^2 hybrids are responsible for the hexagonal lattice structure and the in-plane mechanic properties. The resulting bonding and antibonding σ bands are split far apart and can usually be neglected when studying the electronic properties of graphene. Due to the hexagonal structure, the unit cell of graphene contains two carbon atoms, each of which can be attributed to a sublattice, A and B, respectively. The p_z orbitals form bonding and antibonding π bands that are degenerate at the corners of the Brillouin zone — usually labelled as K *points* or *Dirac points* — and determine the electronic behavior of graphene [CastroNeto(2009)]. In bi- or multilayer graphene and in graphite, the p_z electrons form interlayer van der Waals bonds and are thus responsible for the stability of said structures. In monolayer graphene, they also contribute to the bending rigidity of out-of-plane deformations. Due to the lack of a direct restoring force, out-of-plane deformations are still very soft. This is in stark contrast to in-plane deformations where graphene has a tensile strength of 130 GPa, higher than any other material [Lee(2008)].

- The natural abundance of carbon isotopes is 99% for ^{12}C and 1% for ^{13}C. The radioactive isotope ^{14}C, important for radiocarbon dating of biological samples, has an abundance of 10^{-12} and needs no further consideration for typical nanoscale applications. The resulting atomic weight of, on average, 12.01 u and the atomic distance of 1.42 Å in the monatomically thin, hexagonal lattice lead to a surface mass density of $\rho = 7.61 \times 10^{-7} \frac{\mathrm{kg}}{\mathrm{m}^2}$, the lowest value of all solid state materials. With $\rho = 7.65 \times 10^{-7} \frac{\mathrm{kg}}{\mathrm{m}^2}$, the surface mass density of two-dimensional hexagonal boron nitride (hBN) — a non-dimeric insulator with a hexagonal lattice similar to graphene — is only slightly higher [CastroNeto(2009), Paszkowicz(2002)].

- Due to the linear electronic dispersion, described by a Dirac-like Hamiltonian, the electrons in graphene behave quasi-relativistically. Instead of the speed of light c, the electrons in the π bands move with the Fermi velocity $v_F \approx \frac{c}{300}$. The

strongly reduced velocity and the absence of a bandgap allow for realization of Klein's paradox, the tunneling of electrons through barriers with transmission probabilities close or equal to unity [Klein(1929), Katsnelson(2006)]. Though fascinating, this feature is a hindrance for typical semiconductor applications that rely on electrostatic confinement of charge carriers. There are (at least) three setups that lead to a bandgap [Recher(2010)]. (i) Armchair graphene nanoribbons can be both metallic (i.e. gapless) or semiconducting (i.e. gapped), depending on the number of atoms across the lateral ribbon direction [Fujita(1996), Brey(2006), Trauzettel(2007), Ruffieux(2012)]. (ii) Flat monolayer graphene with different potentials for the sublattices A and B. This can be realized by placing graphene on top of hBN such that the two graphene sublattices feel different potentials from the atoms in the hBN layer [Sławińska(2010), Struck(2010)]. Due to the lattice mismatch between graphene and hBN and also due to misalignment of the respective crystal axes, the sublattice potential might average out on a large scale. Yet experiments show that this is not necessarily the case [Hunt(2013)]. (iii) Bi- or multilayer graphene with a perpendicular electric field that may be generated with a back gate [Min(2007), Goossens(2012)].

- It is also found that graphene has an extremely high electron mobility. At room temperature and a technologically relevant carrier density of $10^{12}\,\mathrm{cm}^{-2}$, the mean free path for intrinsic electron-acoustic phonon scattering is greater than $2\,\mu$m. This corresponds to purely ballistic transport and an electron mobility of $2\times10^{5}\,\mathrm{cm}^{2}\mathrm{V}^{-1}\mathrm{s}^{-1}$, exceeding that of InSb (highest known inorganic semiconductor mobility) and that of carbon nanotubes (previously highest known organic semiconductor mobility). These intrinsic values may be reduced by extrinsic effects. For example, SiO_2 substrate phonons would limit the room temperature mobility to $4\times10^{4}\,\mathrm{cm}^{2}\mathrm{V}^{-1}\mathrm{s}^{-1}$ [Chen(2008)]. The electron mobility is limiting factor for high transistor frequencies. Graphene transistors on a SiC substrate have been operated at 100 GHz, twice as fast as equivalent silicon-based transistors [Lin(2010)]. The according mobilities lie between 900 and $1520\,\mathrm{cm}^{2}\mathrm{V}^{-1}\mathrm{s}^{-1}$.

- Due to the linear, gapless dispersion, the light absorption rate of graphene is independent of the photon frequency and given by $\pi\alpha = 2.3\%$ per layer, where $\alpha = 1/137$ is the fine structure constant. The formulation in terms of α allows to measure the fine structure constant via light absorption [Nair(2008)].

- The heat conductivity in graphene is dominated by acoustic phonons and exceeds the values of copper and carbon nanotubes, both superb heat conductors. This makes graphene most suitable for thermal management and power-consuming electronics applications [Balandin(2008)].

- The low nuclear charge of carbon leads to a small spin-orbit coupling at the atomic level. Accordingly, both the intrinsic and the extrinsic spin-orbit couplings for band electrons in graphene are weak when compared to typical semiconductors [Kane(2005), Min(2006), Gmitra(2009)]. For carbon nanotubes, the orbital motion around the circumferential direction gives rise to a strong spin-orbit effect [Kuemmeth(2008)]. This does not occur in graphene, yet the spin-orbit coupling can be enhanced by out-of-plane deformations that lead to an overlap of π and σ band

electrons [Konschuh(2010), Balakrishnan(2013), Gmitra(2013)]. A low spin-orbit coupling is beneficial for electron spin coherence as it mediates an effective spin-phonon coupling [Khaetskii(2001), Tombros(2007), Rudner(2010), Struck(2010)]. Another source of decoherence is the coupling to nuclear spins. Yet the only carbon isotope carrying a nuclear spin is ^{13}C, with an abundance of 1%. Moreover, the different magnetic momenta of electrons and nuclei suppress the coupling at magnetic fields above $\approx$10 mT [Trauzettel(2007)]. Weak sources of decoherence should make graphene a prime material for spintronics. Some experiments show that spin lifetimes in graphene are still shorter than expected [Tombros(2007), Balakrishnan(2013)] and there is an ongoing debate on what effects might be the cause and how to avoid them [Tombros(2008), Pesin(2012), Gmitra(2013)].

- In addition to the real electron spin that may be used for spintronics, the electron system has two more binary degrees of freedom. Charge carriers may occupy sublattices A and/or B. This *sublattice spin* is usually referred to as *pseudospin*. The hexagonal structure of the honeycomb lattice is reflected in the reciprocal lattice, which has also a hexagonal configuration (Fig. 2.1). The Brillouin zone contains exactly two high symmetry points, K and K', at which the π bands of graphene are degenerate. Consequently, the K- and K'-points are valleys in the conduction band dispersion. The *valley spin* or *isospin* describes, which valley a certain state — conduction or valence — occupies and bears the promise of *valleytronics* [Rycerz(2007), CastroNeto(2009), Rohling(2012)].

- Magnetic materials are essential for modern technology, yet ideal graphene is non-magnetic. However, magnetism in graphene can still be realized in several scenarios [Yazyev(2010)]. (i) According to Lieb's theorem, the ground state of graphene structures features a finite magnetization if the number of atoms in sublattice A is different from the number of atoms in sublattice B [Lieb(1989)]. This is relevant for quasi zero-dimensional systems like graphene nanoflakes where a small sublattice imbalance does not average out [Ezawa(2007), Grujić(2013), Leicht(2014)]. (ii) Chiral graphene nanoribbons feature magnetic edge state, as has been shown theoretically and experimentally [Yazyev(2008), Yazyev(2011), Tao(2011)]. (iii) Bulk graphene can become magnetic due to lattice vacancies or due to functionalization, e.g., via magnetic adatoms or molecules [Yazyev(2007), Palacios(2008), Hong(2013)].

- External magnetic fields induce an anomalous half-integer quantum Hall effect in graphene [Novoselov(2005), Zhang(2005)]. But also strain can give rise to Landau level quantization. In the low-energy description of Dirac electrons, the effect of anisotropic strain on the electron dispersion can be formulated in terms of a valley-dependent pseudomagnetic gauge field that can far exceed feasible external magnetic fields [Suzuura(2002), Guinea(2009), Levy(2010)].

Thanks to its particular properties, graphene has many potential applications. Electronic devices benefit from the high charge carrier mobility and unrivaled heat conduction [Lin(2010), Balandin(2008)]. Possibly, graphene will supplant silicon in transistor technology [Thompson(2006), Lin(2011), Savage(2012)]. For spintronics applications, graphene bears the promise of long coherence times due to the rarity of nuclear spins in carbon and a low spin-orbit interaction [Trauzettel(2007), Yazyev(2008), Recher(2010), Tao(2011),

Goossens(2012)]. Its transparency and flexibility make it suitable for next-generation displays and devices that can be folded like a sheet of paper [Nair(2008), Bae(2010)]. The constant light absorption rate over a wide spectral range make it interesting for solar cells [Wang(2008), Bol2012Pat]. Other energy-related applications include supercapacitors, that benefit from its conductivity and unmatched surface to volume ratio, as well as batteries, where it is a promising electrode material [ElKady(2012), Hu(2013)]. The mechanical properties and the low surface mass density make graphene most suitable for nanoelectromechanical devices that can be used as mass- or pressure sensors with unprecedented susceptibility [Steele(2009), Duerloo(2012), Qi(2012)]. Biomedical applications like drug delivery benefit form the biocompatibility of carbon and graphene nanopores allow for rapid DNA sequencing [Sun(2008), Min(2011)]. The fact that not even helium can pass through graphene makes it suitable for functional coatings and barriers [Bunch(2008)]. Other materials applications include aerogels and advanced composites that make use of its mechanic strength and low weight [Worsley(2010), Kim(2012)], lubricants, or functional fluids like liquid ink [Novoselov(2012), Savage(2012)].

In the wake of graphene, other two-dimensional graphene like flat hBN and transition metal dichalcogenides have gained attention by the scientific community [Novoselov(2005), Dean(2010), Wang(2012)]. All these materials feature different properties. By stacking different two-dimensional materials on top of each other — held together by van der Waals forces — it is envisioned to tailor physical properties in such van der Waals heterostructures [Novoselov(2012), Geim(2013)]. The concept is similar but not limited to the bandgap engineering in semiconductor alloys by controlling their composition and might open up a plethora of new possibilities in nanotechnology.

Carbon is environmentally friendly, ubiquitous, and cheap — key assets for commercialization. In 2013, the European Commission appointed the Graphene Flagship with a budget of one billion EUR over the next ten years to support the transition from academic research to industry applications [Saini(2014)]. But not only Europe, also the USA, China, South Korea, and other countries as well as individual companies invest heavily in graphene and erect multimillion dollar facilities dedicated to two-dimensional materials. In fact, Europe has recently fallen behind China and the USA in terms of publications and patents [Savage(2012), Shapira]. South Korea's Samsung, a key player in graphene, spends more than twelve billion USD a year on research and development[5] and contributed to major breakthroughs towards mass production of high-quality graphene at reduced cost [Kim(2009), Bae(2010), Lee(2014)]. In spite of the intense research interest, commercial graphene electronics is still waiting in the wings and it is not clear if it will fly above silicon anytime soon. The silicon industry has taken more than half a century to reach its current status. For graphene technology, the journey has only just begun [Savage(2012), Shapira].

[5]This number relates to general, not to graphene-specific research and development [Samsung2014SR].

1.2. Outline

After motivating our studies and an introductory part to graphene, we continue with an overview of established basics and techniques that we rely on throughout this work. In Chapter 2, we use a tight-binding description to review the fundamental electronic properties of graphene and hBN as well as their bilayers and a graphene/hBN heterostructure. The effect of strain on the electron structure is the topic of Chapter 3. In particular, we discuss electron-phonon couplings and the deformation of the Brillouin zone in the case of homogeneous strain. Chapter 4 contains an introductory part about geometric phases. For later use, we discuss electric polarization in the context of adiabatic transport as well as the connection between Peierls' phase and a modified tight-binding model.

After reviewing the established groundwork, we turn to the main results of our studies. In Chapter 5, we use the continuum model to derive the acoustic phonons in graphene nanoribbons. Due to the monatomic thickness of graphene, this classical model requires some modifications with implications for the inferred acoustic phonons. Building on these results, we turn to the electron spin relaxation in armchair graphene nanoribbon quantum dots in Chapter 6. We calculate the relaxation time T_1 for different quantum dot aspect ratios, confinement potentials, and boundary conditions of the acoustic phonons. In Chapter 7, we use an analytic model to derive the piezoelectric effect in planar hBN. Our model involves an adiabatic evolution of the sublattice potential as well as the strain-induced pseudomagnetic vector potential, thus benefiting from the work in the previous chapters. Graphene nanoflakes are an interesting system for spintronics. In Chapter 8, we study the exchange coupling between two localized defect states in such systems. A magnetic field is included in the tight-binding description via Peierls' phase. We summarize our results and give an outlook on ongoing and possible future projects in Chapter 9.

In the appendices, we discuss some additional details. Appendix A contains basics on qubit coherence, spin qubits in general, and electron spin qubits in carbon in particular. A detailed derivation of the continuum model for two-dimensional materials like graphene and hBN is presented in Appendix B. Symmetry constraints on the components of the piezoelectric tensor of hBN are explained in Appendix C. Finally, we review relevant groundwork for our ongoing work on the spin relaxation in bilayer graphene quantum dots in Appendix D.

2. Electronic structures of graphene and hexagonal boron nitride

In this section, we derive the electronic structures of graphene and hexagonal boron nitride (hBN). While pristine graphene has no bandgap and has gained a lot of attention due to its fascinating electronic features [Wallace(1947), Semenoff(1984), DiVincenzo(1984), Novoselov(2004), CastroNeto(2009), Katsnelson], hBN is an insulator that can help preserve graphene's praised electronic properties [Giovannetti(2007), Sławińska(2010)].

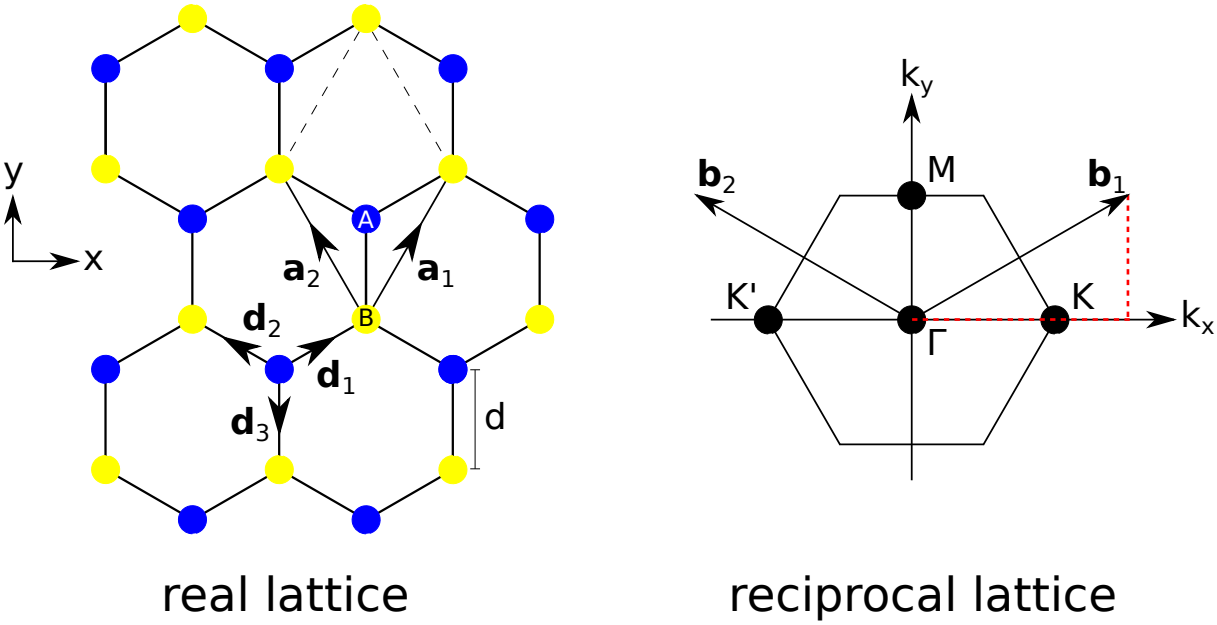

Figure 2.1.: Graphene and hBN are two-dimensional monolayers with a hexagonal lattice due to sp^2-hybridization of the constituent atoms. Together with the dashed lines, the vectors $\boldsymbol{a}_1$ and $\boldsymbol{a}_2$ indicate a unit cell in the real lattice. The unit cell contains two atoms that occupy the inequivalent sublattices A and B, respectively. The atomic distance d equals 1.42 Å for graphene and 1.44 Å for hBN. Both for graphene and for hBN, the low-energy physics is determined by the dispersion around the high symmetry points K and K' at the corners of the Brillouin zone. The red dashed line shows the path $\Gamma KM\Gamma$, along which we plot the dispersion for a variety of situations.

The honeycomb lattice common to both monolayer graphene and hBN is shown in Fig. 2.1. For graphene, both inequivalent sublattices are occupied by carbon atoms and for hBN, one sublattice (we choose sublattice A throughout this work) is occupied by a boron atom

and the other (sublattice B) is occupied by a nitrogen atom. The lattice constant is given by $a = \sqrt{3}d$, where the atomic distance d equals 1.42 Å for graphene and 1.44 Å for hBN [CastroNeto(2009), Paszkowicz(2002)]. The lattice vectors of the hexagonal lattice are given by

$$\boldsymbol{a}_1 = \frac{a}{2}(1, \sqrt{3})\,, \quad \boldsymbol{a}_2 = \frac{a}{2}(-1, \sqrt{3})\,. \tag{2.1}$$

The reciprocal lattice vectors $\boldsymbol{b}_i$ have to be orthonormal to the real space lattice vectors. The choice

$$\boldsymbol{b}_1 = \frac{2\pi}{\sqrt{3}a}(\sqrt{3}, 1)\,, \quad \boldsymbol{b}_2 = \frac{2\pi}{\sqrt{3}a}(-\sqrt{3}, 1) \tag{2.2}$$

conforms the requirement $\boldsymbol{a}_i \cdot \boldsymbol{b}_j = 2\pi\delta_{ij}$. The three nearest neighbor atoms are translated by

$$\boldsymbol{d}_1 = \frac{d}{2}(\sqrt{3}, 1)\,, \quad \boldsymbol{d}_2 = \frac{d}{2}(-\sqrt{3}, 1)\,, \quad \boldsymbol{d}_3 = (0, -d) \tag{2.3}$$

w.r.t. an A atom and by $-\boldsymbol{d}_i$ w.r.t. a B atom. The six second-nearest neighbor atoms are located at

$$\boldsymbol{a}_1\,, \quad \boldsymbol{a}_2\,, \quad \boldsymbol{a}_3 = \boldsymbol{a}_2 - \boldsymbol{a}_1\,, \quad \boldsymbol{a}_4 = -\boldsymbol{a}_1\,, \quad \boldsymbol{a}_5 = -\boldsymbol{a}_2\,, \quad \boldsymbol{a}_6 = -\boldsymbol{a}_3 \tag{2.4}$$

w.r.t to an atom of any sublattice. In analogy to these linear combinations of $\boldsymbol{a}_1$ and $\boldsymbol{a}_2$ that connect to the six neighboring unit cells in real space, the neighboring unit cells in reciprocal space can be found by linear combination of $\boldsymbol{b}_1$ and $\boldsymbol{b}_2$. The perpendicular bisectors to these connecting vectors define the hexagonal Brillouin zone. Due to the trigonal symmetry of the real lattice, there are only two inequivalent corners labeled K and K' (Fig. 2.1 (b)), for which we choose

$$\boldsymbol{K} = \frac{4\pi}{3a}(1, 0)\,, \quad \boldsymbol{K}' = \frac{4\pi}{3a}(-1, 0)\,. \tag{2.5}$$

2.1. Monolayer tight-binding model

A detailed derivation of the energy spectrum and the Dirac Hamiltonian of graphene has already been shown in [Droth(2010)]. Therefore, we focus only on the main steps, here. Boron, carbon, and nitrogen are consecutive elements in the second period with electron configurations [He] $2s^2\ 2p^1$ (B), [He] $2s^2\ 2p^2$ (C), and [He] $2s^2\ 2p^3$ (N). In graphene, the four outer shell electrons of carbon form an sp^2-hybrid that leads to the honeycomb structure and the remaining p_z-orbital is responsible for the electronics around the charge neutrality point [CastroNeto(2009)]. The same happens in hBN, where the nitrogen atom cedes its fifth outer shell electron to the boron atom, which makes hBN insulating [Sławińska(2010)]. In bulk, the collective sp^2-hybrids form the bonding and antibonding σ-bands and the p_z-orbitals form the bonding and antibonding π-bands. In a tight-binding description with nearest and second-nearest neighbor hoppings, the π-bands of graphene and hBN can be described by

$$H = \sum_{i=1}^{N} \left(\left(E_{p_z}^{(A)} a_i^\dagger a_i + E_{p_z}^{(B)} b_i^\dagger b_i \right) + t \sum_{j=1}^{3} \left(a_i^\dagger b_{ij} + b_i^\dagger a_{ij} \right) + t' \sum_{l=1}^{6} \left(a_i^\dagger a_{il} + b_i^\dagger b_{il} \right) \right)\,, \tag{2.6}$$

where i runs over all N unit cells, the on-site energy for an electron on sublattice A (B) is $E_{p_z}^{(A)}$ ($E_{p_z}^{(B)}$), and a_i (b_i) annihilates an electron in sublattice A (B) of the i-th unit cell. Nearest neighbors to an A (B) atom in unit cell i are labeled b_{ij} (a_{ij}) and t is the hopping between nearest neighbors. Likewise, we use a_{il}, b_{il} and t' for second nearest neighbors. It should be noted that the second-nearest neighbor hopping between boron atoms will be different to the hopping between nitrogen atoms, $t'_{\mathrm{BB}} \neq t'_{\mathrm{NN}}$. However, using a single value simplifies the calculation and still allows for a better fit to results from experiment or density functional theory (DFT) calculations. Hermitian conjugate terms occur implicitly by the summation over i. With the Fourier representations of the fields a_i and b_i,

$$a_i = \frac{1}{\sqrt{N}} \sum_{\boldsymbol{k}} e^{-i\boldsymbol{k}\cdot\boldsymbol{R}_i} a(\boldsymbol{k})\,, \quad b_i = \frac{1}{\sqrt{N}} \sum_{\boldsymbol{k}} e^{-i\boldsymbol{k}\cdot\boldsymbol{R}_i} b(\boldsymbol{k})\,, \tag{2.7}$$

where $\boldsymbol{k}$ is the momentum, Eq. (2.6) can be rewritten as

$$H = \sum_{\boldsymbol{k}} \left(a^\dagger(\boldsymbol{k}), b^\dagger(\boldsymbol{k})\right) \underbrace{\begin{pmatrix} E_{p_z}^{(A)} + t'g(\boldsymbol{k}) & tf(\boldsymbol{k}) \\ tf^*(\boldsymbol{k}) & E_{p_z}^{(B)} + t'g(\boldsymbol{k}) \end{pmatrix}}_{=\tilde{\mathcal{H}}(\boldsymbol{k})} \begin{pmatrix} a(\boldsymbol{k}) \\ b(\boldsymbol{k}) \end{pmatrix} \tag{2.8}$$

where $f(\boldsymbol{k}) = \sum_{j=1}^{3} e^{-i\boldsymbol{k}\cdot\boldsymbol{d}_j}$ and $g(\boldsymbol{k}) = \sum_{l=1}^{6} e^{-i\boldsymbol{k}\cdot\boldsymbol{a}_l}$. With $E_0 = (E_{p_z}^{(A)} + E_{p_z}^{(B)})/2$ and $\Delta = (E_{p_z}^{(A)} - E_{p_z}^{(B)})/2$, we find $\tilde{\mathcal{H}}(\boldsymbol{k}) = E_0 + \mathcal{H}(\boldsymbol{k})$, where

$$\mathcal{H}(\boldsymbol{k}) = \begin{pmatrix} \Delta + t'g(\boldsymbol{k}) & tf(\boldsymbol{k}) \\ tf^*(\boldsymbol{k}) & -\Delta + t'g(\boldsymbol{k}) \end{pmatrix}. \tag{2.9}$$

For convenience, we neglect to write the creation and annihilation operators explicitly from now on. Moreover, we disregard the energy shift E_0 and find that the eigenvalues of $\mathcal{H}(\boldsymbol{k})$ are given by

$$E_\pm(\boldsymbol{k}) = \pm\sqrt{\Delta^2 + t^2(3 + h(\boldsymbol{k}))} + t'h(\boldsymbol{k})\,, \tag{2.10}$$

with $h(\boldsymbol{k}) = 2\cos(\sqrt{3}dk_x) + 4\cos(\sqrt{3}dk_x/2)\cos(3dky/2)$. The upper (lower) sign denotes the conduction (valence) band. Fig. 2.2 shows the dispersion relation of (a) graphene and (b) hBN with parameters specified in the caption.

The term $t^2(3 + h(\boldsymbol{k}))$ vanishes at the corners of the Brillouin zone (K and K'). That leads to a splitting of 2Δ between the valence and the conduction band. An expansion around $\tau\boldsymbol{K} + \boldsymbol{q}$, where the valley index $\tau = +1$ (-1) stands for the K (K') valley and $|\boldsymbol{q}| \ll |\boldsymbol{K}$ yields

$$h(\tau\boldsymbol{K} + \boldsymbol{q}) \approx -3 + \frac{9d^2|\boldsymbol{q}|^2}{4} - \tau\frac{9d^3(q_x^3 - 3q_xq_y^2)}{8} - \frac{27d^4|\boldsymbol{q}|^4}{64}\,. \tag{2.11}$$

The third order term is proportional to $\tau(q_x^3 - 3q_xq_y^2)/|\boldsymbol{q}|^3 = \tau\sin(3\phi) = \sin(3\tau\phi)$ with $\phi = \arctan\frac{q_y}{q_x}$ and reflects the trigonal lattice symmetry that gives rise to a trigonal warping around the K-points [CastroNeto(2009)]. For graphene, the bandgap is zero

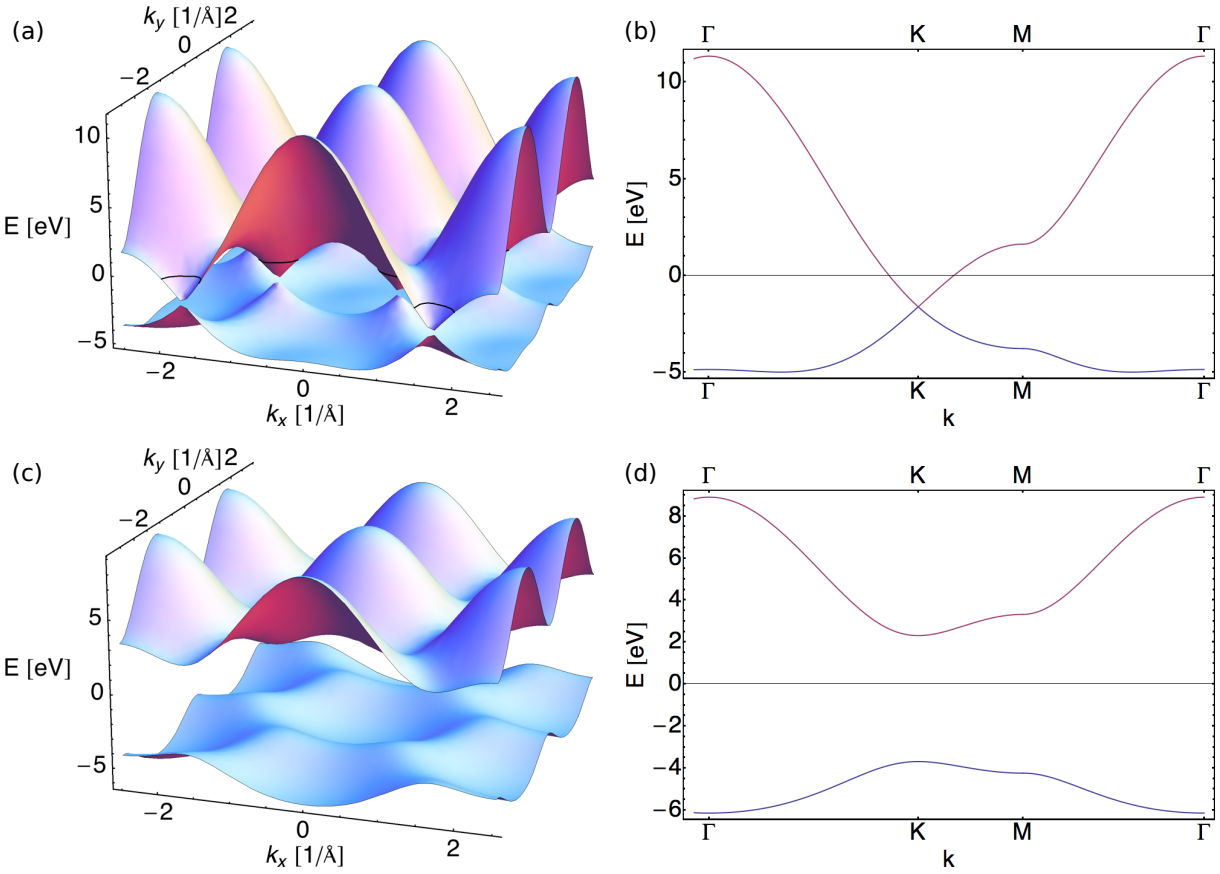

Figure 2.2.: Dispersions $E(\boldsymbol{k})$ for (a,b) graphene and (c,d) hBN. We plot Eq. (2.10) with $d = 1.42$ Å, $\Delta = 0$, $t_1 = 2.7$ eV and, $t_2 = 0.2t_1$ for graphene and with $d = 1.44$ Å, $\Delta = 3$ eV, $t_1 = 2.3$ eV and, $t_2 = 0.1t_1$ for hBN. The black horizontal in (a) and (b) indicates the energy of the p_z orbital of carbon, which we set to zero. In (c) and (d), the energy is measured w.r.t. the mean of the distinct p_z orbitals of boron and nitride. In (a) and (c), the symmetry of the reciprocal lattice shown in Fig. 2.1 is apparent. The path $\Gamma K M \Gamma$ through the Brillouin zone in (b) and (d) corresponds to the red, dashed line in Fig. 2.1.

$(\Delta = 0)$ and up to second order in q, the energy bands are given by

$$\begin{aligned} E(\tau\boldsymbol{K}+\boldsymbol{q}) &\approx \pm t \underbrace{\sqrt{\frac{9d^2|\boldsymbol{q}|^2}{4} - \frac{9|\boldsymbol{q}|^3}{8}\sin(3\tau\phi) - \frac{27d^4|\boldsymbol{q}|^4}{64}}}_{\approx \frac{3d|\boldsymbol{q}|}{2} + \frac{1}{2\frac{3d|\boldsymbol{q}|}{2}}\left(-\frac{9|\boldsymbol{q}|^3}{8}\sin(3\tau\phi) - \frac{27d^4|\boldsymbol{q}|^4}{64}\right)} + t'\left(-3 + \frac{9d^2|\boldsymbol{q}|^2}{4}\right) \\ &\approx -3t' \pm \underbrace{\frac{3td}{2}}_{=\hbar v_F}|\boldsymbol{q}| + \left(\mp\frac{3td^2}{8}\sin(3\tau\phi) + \frac{9t'd^2}{4}\right)|\boldsymbol{q}|^2 + \mathcal{O}(|\boldsymbol{q}|^3)\,. \end{aligned} \tag{2.12}$$

The gapless, linear dispersion around the K-points explains the notion of *Dirac points*. The Fermi velocity v_F is the analog to the speed of light in the linear dispersion of photons. However, $v_F = \frac{3td}{2\hbar} \approx 10^6 \frac{\mathrm{m}}{\mathrm{s}}$ is about a factor 300 smaller than the speed of light. For hBN,

the low-energy expansion around the K-points is

$$\begin{aligned} E_{\pm}(\tau\boldsymbol{K}+\boldsymbol{q}) &\approx \sqrt{\Delta^2}+\frac{1}{2\sqrt{\Delta^2}}t^2(3+h(\tau\boldsymbol{K}+\boldsymbol{q}))+t'h(\tau\boldsymbol{K}+\boldsymbol{q}) \\ &\approx \Delta-3t'+\left(\frac{9t^2d^2}{8\Delta}+\frac{9t'd^2}{4}\right)|\boldsymbol{q}|^2+\mathcal{O}(|\boldsymbol{q}|^3)\,. \end{aligned} \tag{2.13}$$

The trigonal warping appears only in higher order. Despite the gapless, non-linear dispersion, the K-points of hBN are sometimes also referred to as Dirac points because of the similarities with graphene. In contrast to the linear spectrum of graphene around $\tau\boldsymbol{K}$, the parabolic dispersion of hBN allows for the definition of an effective mass,

$$m^* = \hbar^2\left(\frac{\partial E(\tau\boldsymbol{K}+\boldsymbol{q})}{\partial|\boldsymbol{q}|^2}\right)^{-1} \approx \hbar^2\left(\frac{9}{2}d^2\left(\frac{t^2}{\Delta}+t'\right)\right)^{-1}. \tag{2.14}$$

With the same parameters as in Fig. 2.2, we resolve $m^* = 376\,\frac{\mathrm{keV}}{c^2} = 0.74\;m_\mathrm{e}$, where c is the speed of light in vacuum and $m_\mathrm{e} = 511\,\frac{\mathrm{keV}}{c^2}$ is the bare electron mass.

2.1.1. Low-energy Hamiltonian

Many questions in solid state electronics can be answered by just looking at the top edge of the valence band and the bottom edge of the conduction band for these are the states that require the least energy to change occupation. Therefore, we shall delve a little deeper into the low-energy description of the Hamiltonian Eq. (2.9). At the corners of the Brillouin zone, the function $f(\boldsymbol{k})$ vanishes,

$$f(\tau\boldsymbol{K}) = \sum_j e^{-i\tau\boldsymbol{K}\cdot\boldsymbol{d}_j} = \underbrace{e^{\overbrace{-i\tau\frac{4\pi}{3\sqrt{3}d}\frac{\sqrt{3}d}{2}}^{=-i\tau 2\pi/3}}}_{=-\frac{1}{2}-\tau\frac{\sqrt{3}}{2}i} + \left(-\frac{1}{2}+\tau\frac{\sqrt{3}}{2}i\right)+1=0\,, \tag{2.15}$$

and around the K-points, $f(\boldsymbol{k}) = \sum_{j=1}^{3} e^{-i\boldsymbol{k}\cdot\boldsymbol{d}_j}$ is given by

$$\begin{aligned} f(\tau\boldsymbol{K}+\boldsymbol{q}) &\approx \sum_j e^{-i\tau\boldsymbol{K}\cdot\boldsymbol{d}_j}(1-i\boldsymbol{d}_j\cdot\boldsymbol{q}) = \left(-\frac{1}{2}-\tau\frac{\sqrt{3}}{2}i\right)\left(1-id\frac{\sqrt{3}q_x+q_y}{2}\right) \\ &\quad+\left(-\frac{1}{2}+\tau\frac{\sqrt{3}}{2}i\right)\left(1-id\frac{-\sqrt{3}q_x+q_y}{2}\right)+1(1+idq_y) \\ &= -\tau\frac{3}{2}dq_x+i\frac{1}{2}dq_y+idq_y = -\frac{3}{2}d(\tau q_x-iq_y)\,. \end{aligned} \tag{2.16}$$

Disregarding the hopping between second-nearest neighbors, the low-energy approximation of Eq. (2.9) is

$$\mathcal{H}_D = \begin{pmatrix} \Delta & \hbar v_F(\tau q_x - iq_y) \\ \hbar v_F(\tau q_x+iq_y) & -\Delta \end{pmatrix} = \hbar v_F(\tau\sigma_x q_x+\sigma_y q_y)+\Delta\sigma_z\,, \tag{2.17}$$

where we use the Pauli matrices $(\sigma_x, \sigma_y, \sigma_z)$ in their standard representation to denote matrices in the (A, B) sublattice basis. For $\Delta = 0$, i.e. graphene, Eq. (2.17) is well known as the *Dirac Hamiltonian*. The eigenenergies $E_\pm$ of $\mathcal{H}$ can be calculated as follows

$$\begin{aligned} &\begin{vmatrix} \Delta - E_\pm & \hbar v_F(\tau q_x - i q_y) \\ \hbar v_F(\tau q_x + i q_y) & -\Delta - E_\pm \end{vmatrix} = E_\pm^2 - \Delta^2 - (\hbar v_F)^2(q_x^2 + q_y^2) = 0\,, \\ \Rightarrow \quad & E_\pm = \pm \underbrace{\sqrt{(\hbar v_F)^2(q_x^2 + q_y^2) + \Delta^2}}_{=\lambda}\,. \end{aligned} \tag{2.18}$$

Due to the alternative representation $\mathcal{H}_D = (\hbar v_F \tau q_x, \hbar v_F q_y, \Delta) \cdot (\sigma_x, \sigma_y, \sigma_z)$ of the Hamiltonian, it is intuitive to represent the first vector in spherical coordinates. Then, the eigensystem $|\psi_\pm^\tau\rangle$ takes the form

$$\begin{aligned} &\begin{pmatrix} \Delta \mp \lambda & \hbar v_F(\tau q_x - i q_y) \\ \hbar v_F(\tau q_x + i q_y) & -\Delta \mp \lambda \end{pmatrix} \cdot \begin{pmatrix} \psi_{1,\pm}^\tau \\ \psi_{2,\pm}^\tau \end{pmatrix} = 0 \\ &\{\hbar v_F \tau q_x = \lambda \sin\theta\cos\phi\,, \quad \hbar v_F \tau q_y = \lambda \sin\theta \sin\phi\,, \quad \Delta = \lambda\cos\theta\} \\ \Rightarrow \quad &\begin{pmatrix} \cos\theta \mp 1 & \tau e^{-i\tau\phi} \\ \sin\theta \tau e^{i\tau\phi} & -\cos\theta \mp 1 \end{pmatrix} \cdot \begin{pmatrix} \psi_{1,\pm}^\tau \\ \psi_{2,\pm}^\tau \end{pmatrix} = 0\,, \end{aligned} \tag{2.19}$$

where the upper (lower) sign stands for the conduction (valence) band. With the ansatz $\psi_{1,\pm}^\tau = \cos\theta \pm 1$, the first row becomes $-\sin^2\theta + \sin\theta\tau e^{-i\tau\phi}\psi_{2,\pm}^\tau = 0$ and we resolve $\psi_{2,\pm}^\tau = \sin\theta\tau e^{i\tau\phi}$. Then the second row is $\sin\theta\tau e^{i\tau\phi}(\cos\theta \pm 1 - \cos\theta \mp 1) = 0$. With $|\psi_{1,\pm}^\tau|^2 = \cos^2\theta \pm 2\cos\theta + 1$ and $|\psi_{2,\pm}^\tau|^2 = \sin^2\theta$, we find $|\psi_\pm^\tau|^2 = 2(1 \pm \cos\theta)$ and the normalized eigenstates

$$|\psi_\pm^\tau\rangle = \begin{pmatrix} \pm\frac{\sqrt{1\pm\cos\theta}}{\sqrt{2}} \\ \frac{\tau \sin\theta e^{i\tau\phi}}{\sqrt{2(1\pm\cos\theta)}} \end{pmatrix} \quad \Rightarrow \quad \mathcal{H}_D|\psi_\pm^\tau\rangle = E_\pm|\psi_\pm^\tau\rangle\,, \tag{2.20}$$

where the eigenenergies are given by Eq. (2.18).

Assuming periodic boundaries in both x- and y-direction, the density of states in reciprocal space is $D_{\boldsymbol{q}} = \frac{4}{(2\pi)^2/(L_x L_y)} = \frac{A}{\pi^2}$, where L_x and L_y are the extensions of the sample in x- and y-direction, respectively, and $A = L_x L_y$ is the surface area of the sample. The factor of 4 comes about from spin- and valley- degeneracy. The density of states in energy space, $D(E)$, is related to $D_{\boldsymbol{q}}$ via

$$\begin{aligned} &D(E)|\mathrm{d}E| = \mathrm{d}N = D_{\boldsymbol{q}}\mathrm{d}q^2 = \frac{A}{\pi^2} S_{\boldsymbol{q}}(E)\mathrm{d}q_\perp \\ \Rightarrow \quad &D(E) = \frac{A}{\pi^2}\frac{S_{\boldsymbol{q}}(E)}{|\mathrm{d}E/\mathrm{d}q_\perp|}\,, \end{aligned} \tag{2.21}$$

where $\mathrm{d}N$ is the change of the number of states, $S_{\boldsymbol{q}}(E)$ is the length of the energy contour in one valley[1] and the differential $\mathrm{d}q$ is the length of an outward-pointing, differential $\boldsymbol{q}$-vector that is oriented perpendicularly on the contour line with length $S_{\boldsymbol{q}}(E)$. The energy

[1] We consider only one valley, since the other valley is already included with the two-fold valley-degeneracy. Special care has to be taken around the Γ-point, where there is only one contour. Only half the contour length may be considered in this case.

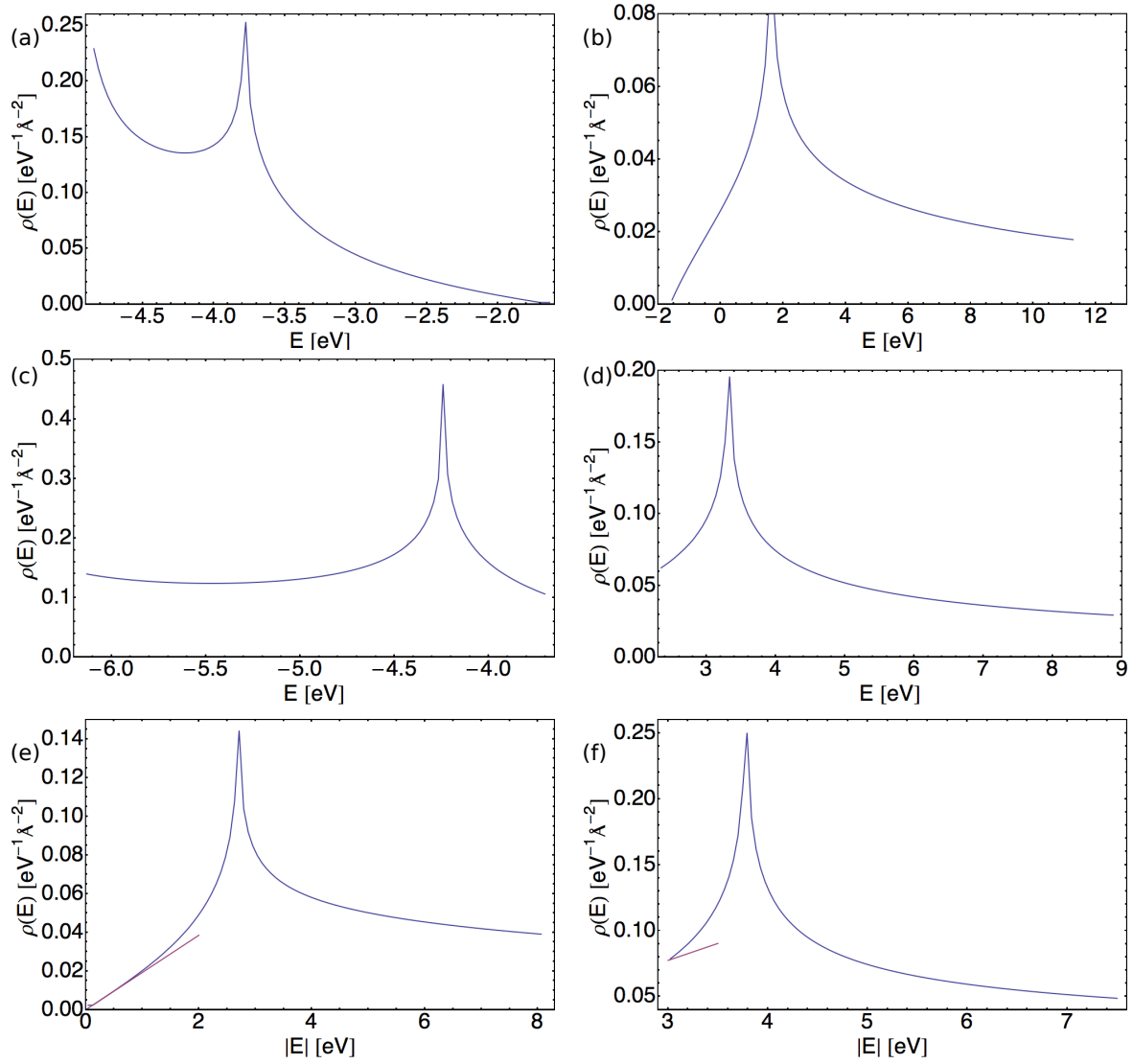

Figure 2.3.: Density of states per surface area (DSA) for the valence band (a) and for the conduction band (b) of graphene with first and second nearest neighbors in Eq. (2.10). In (c) and (d), we show the fg results for hBN. The blue line in (e) shows the DSA in the conduction band of graphene without second nearest neighbor hopping, i.e., it corresponds to (b) with $t' = 0$. Note that $|E_-(\boldsymbol{k})| = E_+(\boldsymbol{k})$ for $t' = 0$. The red line shows an approximation as given by Eq. (2.22). For hBN (f), this approximation is only useful in the immediate vicinity of the K point.

shift $\mathrm{d}E$ associated with $\mathrm{d}q_\perp$ may well be negative, which is why its norm must be taken. The energy contour may have a complicated form, e.g., due to trigonal warping, such that it is not straightforward to determine $S_{\boldsymbol{q}}(E)$. This can be done numerically. In the low-energy model with nearest neighbors only, the energy contours are circles around K and K' since $E_\pm(\boldsymbol{q}) = E_\pm(|\boldsymbol{q}|)$ in Eq. (2.18). From that equation, we find

(i) $|\boldsymbol{q}|(E) = \frac{\sqrt{E^2-\Delta^2}}{\hbar v_F}$, $\quad (|E| \geq \Delta)$ and

(ii) $\left|\frac{\mathrm{d}E}{\mathrm{d}q_\perp}\right| = \frac{1}{2|E|}(\hbar v_F)^2 2|\boldsymbol{q}| \overset{\text{(i)}}{=} \frac{\sqrt{E^2-\Delta^2}}{|E|}\hbar v_F\,, \quad (|E| \geq \Delta).$

With $S_{\boldsymbol{q}}(E) = 2\pi|\boldsymbol{q}|$, the density of states per surface area, $\rho(E) = \frac{D(E)}{A}$, is thus given by

$$\rho(E) = \theta(|E|-\Delta)\frac{A}{A\pi^2}\frac{2\pi|\boldsymbol{q}(E)|}{|\mathrm{d}E/\mathrm{d}q_\perp|} = \theta(|E|-\Delta)\frac{2|E|}{\pi(\hbar v_F)^2}\,. \tag{2.22}$$

Fig. 2.3 shows the density of states per surface area in graphene and hBN for the bands given by Eq. (2.10) with neighbors up to second order, up to first order, and only in the vicinity of K, for the bands given by Eq. (2.18).

In analogy to the real electron spin, the sublattice degree of freedom is interpreted as *pseudospin*. The according helicity operator is defined as

$$h = \frac{\boldsymbol{\sigma}^{(*)}\cdot\boldsymbol{q}}{2|\boldsymbol{q}|}\,, \tag{2.23}$$

with $\boldsymbol{\sigma} = (\sigma_x, \sigma_y)$ for the K-valley and $\boldsymbol{\sigma}^* = (-\sigma_x, \sigma_y)$ for the K'-valley. For graphene, h commutes with $\mathcal{H}_D$ as both operators have the same structure,

$$\begin{aligned} & h = \mathcal{H}_D\frac{1}{\hbar v_F 2|\boldsymbol{q}|} && (\Delta = 0) \\ \Rightarrow \quad & [h, \mathcal{H}_D] \propto [\mathcal{H}_D, \mathcal{H}_D] = 0\,. \end{aligned} \tag{2.24}$$

Since the proportionality constant is positive, $\frac{1}{\hbar v_F 2|\boldsymbol{q}|} > 0$, the eigenvalues of $\mathcal{H}_D$ and h to a common eigenstate must have equal sign. Conduction band states ($E > 0$) will have positive helicity and valence band states ($E < 0$) will have negative helicity, that is, electrons in graphene exhibit *chirality*. For $\Delta \neq 0$, $\mathcal{H}_D$ and h do not commute since $[\tau\sigma_x q_x + \sigma_y q_y, \sigma_z] = \tau q_x(-2i\sigma_y) + q_y(2i\sigma_x) \neq 0$, unless $\boldsymbol{q} = 0$.

2.1.2. Klein paradox in graphene

For graphene ($\Delta = 0$), the angle θ in Eq. (2.20) has the value $\frac{\pi}{2}$ and the eigenstates simplify to

$$|\psi_\pm^\tau\rangle = \frac{1}{\sqrt{2}}\begin{pmatrix}\pm 1\\ \tau e^{i\tau\phi}\end{pmatrix}\,. \tag{2.25}$$

In Fig. 2.4 (a), we sketch a situation where an incident electron or hole of energy E hits a potential barrier of height V and length D at an angle α and is transmitted through the barrier with probability $T(\alpha)$. In the different regions shown in the sketch, the wave function is given by the following expressions

$$\begin{aligned} \psi_{I,\pm}^\tau(\boldsymbol{r}) &= \frac{1}{\sqrt{2}}\begin{pmatrix}s\\ \tau e^{i\tau\phi}\end{pmatrix}e^{i(q_x x + q_y y)} + \frac{r}{\sqrt{2}}\begin{pmatrix}s\\ \tau e^{-i\tau\phi}\end{pmatrix}e^{i(q_x x - q_y y)}\,, \\ \psi_{II,\pm}^\tau(\boldsymbol{r}) &= \frac{a}{\sqrt{2}}\begin{pmatrix}s'\\ \tau e^{i\tau\phi'}\end{pmatrix}e^{i(q'_x x + q'_y y)} + \frac{b}{\sqrt{2}}\begin{pmatrix}s'\\ \tau e^{-i\tau\phi'}\end{pmatrix}e^{i(q'_x x - q'_y y)}\,, \\ \psi_{III,\pm}^\tau(\boldsymbol{r}) &= \frac{t}{\sqrt{2}}\begin{pmatrix}s\\ \tau e^{i\tau\phi}\end{pmatrix}e^{i(q_x x + q_y y)}\,, \end{aligned} \tag{2.26}$$

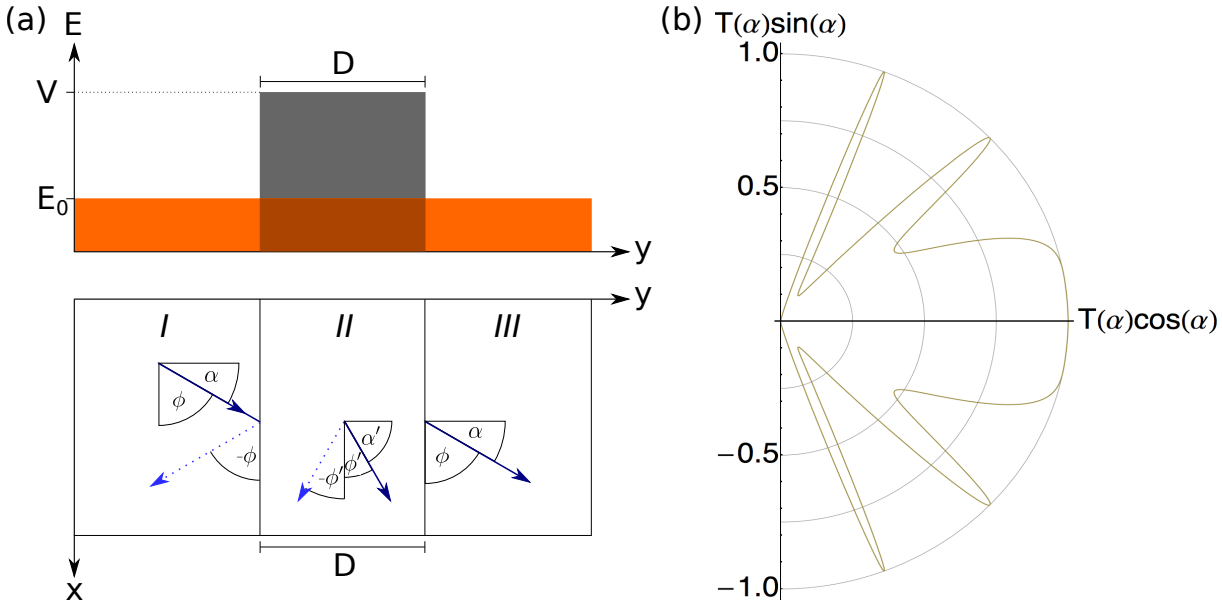

Figure 2.4.: (a) Side view (upper sketch) and top view (lower sketch) of a potential barrier. A particle hits the barrier at the angle $\alpha = \phi - \frac{\pi}{2}$, where $\phi = \arctan \frac{q_y}{q_x}$. The transmitted part of the wave function propagates with the same angles. But in the barrier region, the angles change to the primed ones. (b) According to the Klein paradox, the transmission probability can be unexpectedly large [Klein(1929), Katsnelson(2006), Beenakker(2008), Katsnelson]. We plot $T(\alpha)$ as given by Eq. (2.30) with the parameters $E_0 = 75$ meV, $V = 200$ meV, and $D = 200$ nm.

where $s = \operatorname{sgn} E$, $s' = \operatorname{sgn}(E - V)$, $q_x' = q_x$, and

$$q_y' = \sqrt{\left(\frac{E-V}{\hbar v_F}\right)^2 - q_x^2}\,. \tag{2.27}$$

Since the Hamiltonian (2.17) is of first order, only the wave function must be continuous but not necessarily its gradient. The two matching conditions

$$\begin{aligned} \psi^\tau_{I,\pm}(x,0) &= \psi^\tau_{II,\pm}(x,0)\,, \\ \psi^\tau_{II,\pm}(x,D) &= \psi^\tau_{III,\pm}(x,D) \end{aligned} \tag{2.28}$$

on the two-component wave functions fix the four parameters r, a, b, and t, which we resolve with MATHEMATICA. The complicated expression for $T = tt^*$ can be simplified to

$$T(\phi) = \frac{\sin^2\phi \sin^2\phi'}{\cos(Dq_y')\sin^2\phi\sin^2\phi' + (1 - ss'\cos\phi\cos\phi')^2\sin(Dq_y')}\,. \tag{2.29}$$

With $\cos\phi = -\sin\left(\phi - \frac{\pi}{2}\right)$ and $\sin\phi = \cos\left(\phi - \frac{\pi}{2}\right)$, this expression can be written in terms of the incident angle $\alpha = \phi - \frac{\pi}{2}$,

$$T(\alpha) = \frac{\cos^2\alpha\cos^2\alpha'}{\cos^2(Dq_y')\cos^2\alpha\cos^2\alpha' + (1 - ss'\sin\alpha\sin\alpha')^2\sin^2(Dq_y')}\,. \tag{2.30}$$

Notably, $T(\alpha) = T(-\alpha)$ has the same form for electrons and holes, and in both valleys. For $Dq'_y = n\pi$ with an integer n, the barrier becomes completely transparent, $T(\alpha) = 1$, independent of α. This is the Klein paradox [Klein(1929), Katsnelson(2006), Beenakker(2008), Katsnelson]. In Fig. 2.4 (b), we plot $T(\alpha)$ as given by Eq. (2.30). For $|V| \gg |E|$, Eq. (2.27) implies that $q'_y \gg q'_x$ and thus $\phi' \approx 0$ and $T(\alpha)$ can be simplified to

$$\begin{aligned} T(\alpha) &\approx \frac{\cos^2\alpha}{\cos^2(Dq'_y)\cos^2\alpha + \sin^2(Dq'_y) + \underbrace{(\cos^2(Dq'_y)\sin^2\alpha - \cos^2(Dq'_y)\sin^2\alpha)}_{=0}} \\ &= \frac{\cos^2\alpha}{\underbrace{\cos^2(Dq'_y)\underbrace{(\cos^2\alpha + \sin^2\alpha)}_{=1} + \sin^2(Dq'_y)}_{=1} - \cos^2(Dq'_y)\sin^2\alpha} \\ &= \frac{\cos^2\alpha}{1 - \cos^2(Dq'_y)\sin^2\alpha}\,. \end{aligned} \tag{2.31}$$

2.2. Bilayer systems

In this section, we discuss several bilayer system, where each layer is either a graphene or an hBN sheet. Bilayer graphene is can be obtained via mechanical cleavage of graphite and occurs naturally as a side product when monolayer graphene is produced with the exfoliation technique. Bilayer graphene is an interesting material on its own because it resembles graphene is many aspects, e.g. pseudo- and valleyspin, but also allows for easy generation of a bandgap with an external electric field [McCann(2006), McCann(2006-2)]. As for graphene, mono- and bilayer hBN can be produced by mechanical cleavage of three-dimensional hexagonal boron nitride. Recently, graphene/hBN bilayers have gained a lot of interest because experiments indicate that hBN can protect graphene from contamination without compromising its electronic properties [Dean(2010)].

Fig. 2.5 shows two hexagonal monolayers with sublattices A and B in the top layer and sublattices A' and B' in the bottom layer. The atomic distances are identical in both layers[2]. While the A atoms are directly on top of the B' atoms, sublattice B is on top of the hexagon centers of the lower sheet. In a minimal tight-binding model, we consider only nearest neighbor hoppings, that is, two independent copies of the Hamiltonian (2.9) without t' but with an interlayer hopping t_{12} between sublattices A and B',

$$\mathcal{H}_{bl}(\boldsymbol{k}) = \begin{pmatrix} E_{p_z}^{(A)} & t_1 f(\boldsymbol{k}) & 0 & t_{12} \\ t_1 f^*(\boldsymbol{k}) & E_{p_z}^{(B)} & 0 & 0 \\ 0 & 0 & E_{p_z}^{(A')} & t_2 f(\boldsymbol{k}) \\ t_{12} & 0 & t_2 f^*(\boldsymbol{k}) & E_{p_z}^{(B')} \end{pmatrix}. \tag{2.32}$$

One parameter on the diagonal can be eliminated by an energy shift but here, we keep all parameters for clarity. Depending on the actual system, substitutions can still be useful

[2] This is not exactly true for the graphene/hBN bilayer and will be discussed in Subsec. 2.2.2.

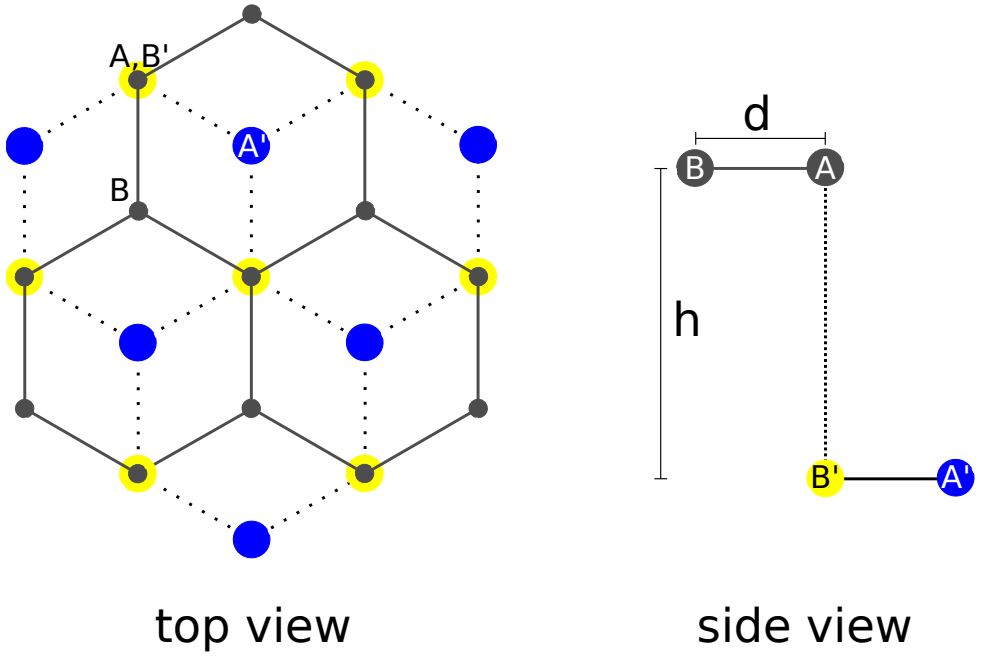

Figure 2.5.: Hexagonal bilayers are comprised of two vertically stacked hexagonal monolayers. In the most stable AB stacking configuration, an A atom of the top layer is directly on top of a B atom of the lower layer (which we label B'), while the B atom of the top layer is on top of the middle of a benzene ring in the lower layer. Accordingly, the A atom of the lower layer (which we label A') is directly underneath the center of a hexagon in the top layer. The side view shows the interlayer distance h and the intralayer atomic distance d approximately to scale. In bilayer graphene, $h/d = \frac{3.35\ \text{Å}}{1.42\ \text{Å}} \approx 2.4$, and in bilayer hBN $h/d = \frac{3.57\ \text{Å}}{1.44\ \text{Å}} \approx 2.5$ [Rakhmanov(2012), Ribeiro(2011), CastroNeto(2009), McCann(2006), Ohta(2006)].

later on. In this parametric form it is not possible to diagonalize Eq. (2.32), but at the corners of the Brillouin zone, Eq. (2.15) holds and the eigenvalues are easily found to be

$$E_1 = E_{p_z}^{(B)}\,, \quad E_2 = E_{p_z}^{(A')}\,, \quad E_{3,4} = \frac{1}{2}\left(E_{p_z}^{(A)} + E_{p_z}^{(B')} \pm \sqrt{(E_{p_z}^{(A)} - E_{p_z}^{(B')})^2 + 4t_{12}^2}\right)\,. \tag{2.33}$$

2.2.1. Bilayer graphene and bilayer hBN

Bilayer graphene can occur in two different stackings, namely AB stacking and AA stacking. The lattice of AB stacked bilayer graphene corresponds to Fig. 2.5 and has sublattice A on sublattice B'. In principle, it is also possible that both atoms in the top layer are directly on top of the two atoms in the bottom layer: A on A' and B on B'. Yet this AA stacking is unstable [Rakhmanov(2012)] and hence we will not further discuss it, here.

For unbiased AB stacked bilayer graphene, all p_z orbitals have the same energy, which we set to zero, and the intralayer hoppings are identical, $t_1 = t_2$. The resulting eigenenergies

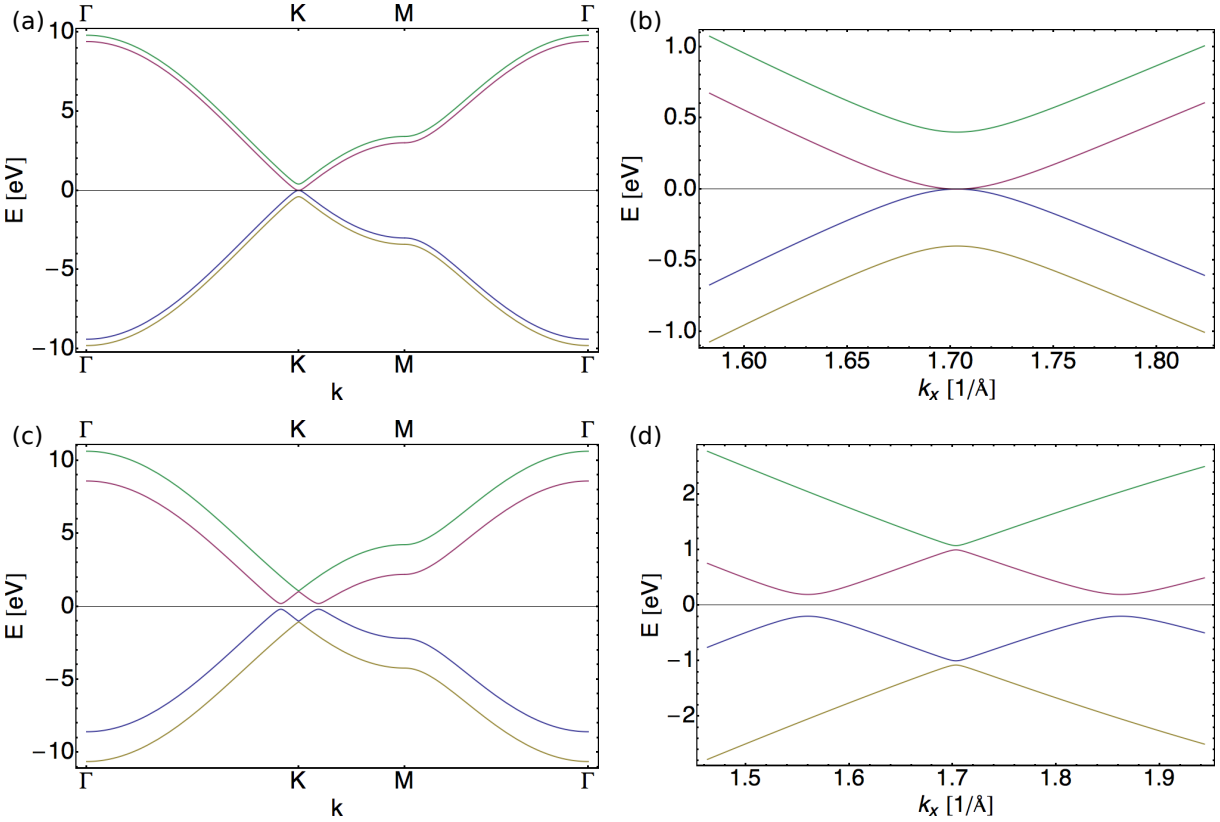

Figure 2.6.: (a) and (b) show the dispersion of bilayer graphene without an external electric field along the path $\Gamma KM\Gamma$ in the Brillouin zone (a) and in the vicinity of K (b). We plot Eq. (2.34) with $d = 1.42$ Å, $t_1 = 3.2$ eV, and $t_{12} = 0.4$ eV [Ohta(2006), Sławińska(2010)]. (c) and (d) correspond to (a) and (b), yet we plot Eq. (2.35) for an electric field $E_F \approx 6\frac{\mathrm{V}}{\mathrm{nm}}$ such that $U = 1$ eV.

are

$$E_{1-4}(\boldsymbol{k}) = \pm\sqrt{|f(\boldsymbol{k})|^2 t_1^2 + \frac{1}{2}\left(t_{12}^2 \pm \sqrt{4|f(\boldsymbol{k})|^2 t_1^2 t_{12}^2 + t_{12}^4}\right)}, \tag{2.34}$$

$$|f(\boldsymbol{k})|^2 = 3 + 2\cos(\sqrt{3}dk_x) + 2\cos\left(\frac{d}{2}(\sqrt{3}k_x - 3k_y)\right) + 2\cos\left(\frac{d}{2}(\sqrt{3}k_x + 3k_y)\right).$$

In Fig. 2.6 (a) and (b), we plot the dispersion along the $\Gamma KM\Gamma$ path through the Brillouin zone with the parameters specified in the caption. The interlayer spacing of bilayer graphene, $h = 3.35$ Å, does not enter the model (2.32). The lattice constant is the same as for monolayer graphene, $a = \sqrt{3}d = 2.46$ Å [Ohta(2006), McCann(2006), CastroNeto(2009)].

If an external electric field is applied perpendicularly to the graphene bilayer, the electrons in the top layer will be exposed to a different potential than the electrons in the bottom layer, which we model with $E_{p_z}^{(A)} = E_{p_z}^{(B)} = +U$ and $E_{p_z}^{(A')} = E_{p_z}^{(B')} = -U$. Otherwise, the

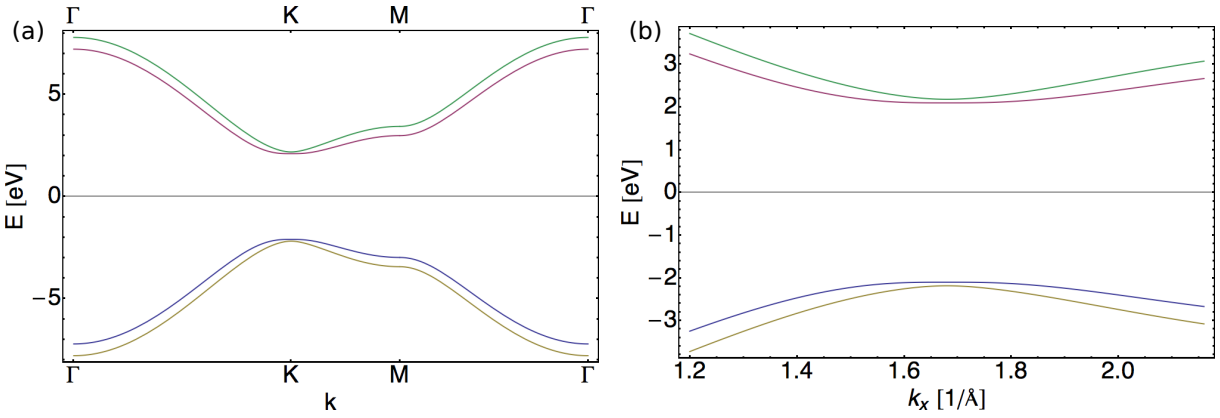

Figure 2.7.: Dispersion of bilayer hBN along the path $\Gamma K M \Gamma$ through the Brillouin zone (a) and in the vicinity of K (b). We plot Eq. (2.36) with $d = 1.44$ Å, $\Delta = 2.1$ eV, $t_1 = 2.4$ eV, $t_{12} = 0.6$ eV [Ribeiro(2011), Rakhmanov(2012)]. Note that both the upper and the lower bands have a finite splitting at K, as is easily seen from Eq. (2.33) with $t_{12} \neq 0$.

system is identical to the unbiased case discussed before. The eigenenergies are now

$$E_{1-4}(\boldsymbol{k}) = \pm\sqrt{U^2 + |f(\boldsymbol{k})|^2 t_1^2 + \frac{1}{2}\left(t_{12}^2 \pm \sqrt{4|f(\boldsymbol{k})|^2 t_1^2 (t_{12}^2 + 4U^2) + t_{12}^4}\right)}, \tag{2.35}$$

and we plot them in Fig. 2.6 (c) and (d) for $U = 1$ eV, i.e., for an electric field of $E_F \approx 6\frac{\mathrm{V}}{\mathrm{nm}}$.

In monolayer hBN, the two sublattices are occupied by two different atoms. This leads to a rich structure for bilayer hBN [Ribeiro(2011)]. The AA stacking of bilayer graphene has two analogies in bilayer hBN: boron on boron and nitrogen on nitrogen (AA) and boron on nitrogen and vice versa (AA'). The AB stacking of bilayer graphene has even three analogies: boron on boron (AB'), nitrogen on nitrogen ($A'B$), and boron on nitrogen (AB). Ribeiro and Peres have found that the AB stacked bilayer hBN is the most stable configuration and hence, we will only consider this stacking. The interlayer distance of bilayer hBN is $h = 3.57$ Å and the lattice constant is $a = 2.51$ Å. [Ribeiro(2011)]. The system is similar to unbiased bilayer graphene yet with different energies for boron and nitrogen atoms, $E_{p_z}^{(A)} = E_{p_z}^{(A')} = +\Delta$ and $E_{p_z}^{(B)} = E_{p_z}^{(B')} = -\Delta$. The eigenenergies for bilayer hBN without an external electric field are

$$E_{1-4}(\boldsymbol{k}) = \pm\sqrt{\Delta^2 + |f(\boldsymbol{k})|^2 t_1^2 + \frac{1}{2}\left(t_{12}^2 \pm \sqrt{4|f(\boldsymbol{k})|^2 t_1^2 t_{12}^2 + t_{12}^4}\right)}, \tag{2.36}$$

and we plot them in Fig. 2.7. In addition, an external electric field as for biased graphene can be imposed. The according eigenenergies are

$$E_{1-4}(\boldsymbol{k}) = \pm\sqrt{\Delta^2 + U^2 + |f(\boldsymbol{k})|^2 t_1^2 + \frac{1}{2}\left(t_{12}^2 \pm \sqrt{4|f(\boldsymbol{k})|^2 t_1^2 (t_{12}^2 + 4U^2) + (t_{12}^2 + 4U\Delta)^2}\right)}. \tag{2.37}$$

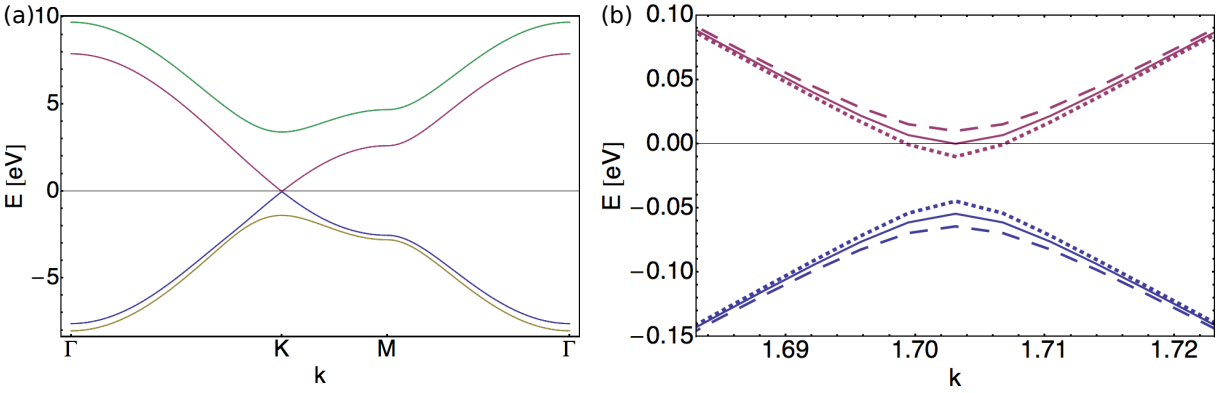

Figure 2.8.: Dispersion relation of a graphene/hBN bilayer along the $\Gamma KM\Gamma$ path through the Brillouin zone (a) and in the vicinity of K (b). We apply Eq. (2.32), i.e., we assume AB stacking. For this model, it has been shown that the interlayer coupling to a boron atom is preferred over the coupling to nitrogen. We use $E_{p_z}^{(A)} = -E_{p_z}^{(B)} = \Delta$, $E_{p_z}^{(A')} = -1.40$ eV, $E_{p_z}^{(B')} = 3.34$ eV, $d = 1.42$ Å, $t_1 = 2.79$ eV, $t_2 = 2.64$ eV, and $t_{12} = 0.43$ eV [Sławińska(2010)]. The solid line corresponds to $\Delta = 0$, and the dashed (dotted) line to $(-)0.01$ eV.

Note that Eqs. (2.34), (2.35) and (2.36) are special cases of Eq. (2.37). Unbiased bilayer hBN is an insulator with a gap of more than 5 eV [Han(2008)] and an external electric field which substantially changes this bandgap would also have a strong impact on other bands not considered in this model. Therefore, we will not further discuss bilayer hBN with $U \neq 0$.

2.2.2. Graphene/hBN bilayer

Sławińska *et al.* have modeled this system with Eq. (2.32). Assuming that (i) the p_z orbitals of the two carbon atoms have the same energy, (ii) that the atomic distances in the two sheets are identical, and (iii) that the interlayer coupling occurs between a carbon and a boron atom, they can fit the remaining parameters to DFT results [Giovannetti(2007), Sławińska(2010)]. However, there is in fact a lattice mismatch of about 2% between the two sheets. For perfect alignment of the two sheets, this leads to a Moiré potential with a periodicity of 14 nm [Woods(2014)] and it has been shown both experimentally and theoretically that the Moiré potential leads to a sublattice potential for the graphene plane [Hunt(2013), Kindermann(2012)]. That is, in principle, one can respect the lattice mismatch by using the model of Sławińska *et al.* with an additional sublattice potential Δ for the graphene plane.

However, there is no consensus on the strength of the sublattice potential. Moreover, the graphene/hBN bilayer cannot be obtained via mechanical cleavage since there is no parent material but it must be constructed bottom-up. As a consequence, the two sheets are usually not perfectly aligned but with a nonzero twist angle between their crystal axes. This is different from bilayer graphene and bilayer hBN, which can both be obtained top-down from their parent crystals. As a consequence, the Moiré periodicity as well as

the sublattice splitting differ from sample to sample [Hunt(2013), Woods(2014)]. In the model (2.32), sublattice A couples to a boron atom [Giovannetti(2007)] while sublattice B does not. In a naïve picture, the nitrogen atom should couple equally to A after half a Moiré period. Yet experiments and DFT calculations show that these influences do not cancel out and Δ remains finite [Woods(2014), Hunt(2013), Giovannetti(2007)]. As a consequence, the sign of the sublattice potential Δ does also matter.

In Fig. 2.8 we show the dispersion of a graphene/hBN bilayer with $E_{p_z}^{(A)} = -E_{p_z}^{(B)} = \Delta$, $E_{p_z}^{(A')} = -1.40$ eV, and $E_{p_z}^{(B')} = 3.34$ eV for three cases, $\Delta = 0$ and $\Delta = \pm 0.01$ eV. Here, $E_{p_z}^{(A')}$ and $E_{p_z}^{(B')}$ are the energies of the nitrogen and the boron sites, respectively, shifted by the energy of the carbon p_z orbital. In the cases of finite sublattice splitting, we use $\Delta = \pm 0.01$ eV, as found in a recent measurement with small twist angle [Hunt(2013)]. Even for $\Delta = 0$, it is not straightforward to diagonalize Eq. (2.32) because $t_1 \neq t_2$, i.e., Fig. 2.8 shows numerical results. We find that the sublattice potential Δ can increase or decrease the gap present for $\Delta = 0$, depending on its sign. The interlayer distance is $h = 3.22$ Å [Giovannetti(2007)].

3. The effects of lattice deformations on electrons in graphene and boron nitride

In this chapter, we discuss the effects of strain on the electronic structure of graphene and two-dimensional hexagonal boron nitride (hBN) in terms of the continuum model (Appendix B). The underlying effect is that the hopping amplitude between two atoms in Eq. (2.6) depends on their spatial separation and hence changes upon strain. Furthermore, homogeneous strain changes the shape of the unit cell (real space) and hence also modifies the Brillouin zone (reciprocal space). For in-plane acoustic phonons, we consider two different electron-phonon couplings, namely the deformation potential and the bond-length change. For out-of-plane acoustic phonons, we discuss the deflection coupling between phonons and spin, which is mediated by intrinsic spin-orbit coupling.

3.1. Effects on the low-energy Hamiltonian

We focus on low-energy electronic states that are described by Eq. (2.17). For these states, we derive the effects of bond-length change between nearest neighbors, the change of the Fermi velocity, and the deformation potential [Suzuura(2002), CastroNeto(2009)].

3.1.1. Bond-length change

We have obtained the Hamiltonian in Eq. (2.17) from Eq. (2.9) by exploiting Eq. (2.15). However, in the presence of strain, the nearest neighbor hopping t_{ij} between atoms i and j usually depends on the hopping direction and hence cannot be factored out of the sum $\sum_j t_{ij} e^{-i\tau \boldsymbol{K}\cdot\boldsymbol{d}_j}$, as we did for Eq. (2.15). The bond-length change between atoms i and j is given by the projection

$$\delta u^{(ij)} = \frac{\boldsymbol{d}_j}{d} \cdot \underbrace{(\boldsymbol{u}(\boldsymbol{R}_i) - \boldsymbol{u}(\boldsymbol{R}_i + \boldsymbol{d}_j))}_{\approx \kappa(\boldsymbol{d}_j\cdot\boldsymbol{\nabla})\boldsymbol{u}(\boldsymbol{R}_i)} \approx d\kappa\, \hat{\boldsymbol{d}}_j \cdot \Big((\hat{\boldsymbol{d}}_j \cdot \boldsymbol{\nabla})\boldsymbol{u}(\boldsymbol{R}_i) \Big) \,, \tag{3.1}$$

where $\hat{\boldsymbol{d}}_j$ is the unit vector pointing from atom i to atom j and the scalar quantity $\kappa = \frac{\mu}{\sqrt{2}B}$ follows from microscopic details and depends on the bulk (B) and shear (μ) moduli [Suzuura(2002), Harrison-2]. The hopping between the two atoms is $t_{ij} = t_{ij,0} + \delta t_{ij}$,

where $t_{ij,0}$ corresponds to t in the unstrained case of Eq. (2.9) and

$$\delta t_{ij}(\boldsymbol{R}_i) = \frac{\partial t_{ij}}{\partial d}\delta u^{(ij)} \approx \underbrace{d\frac{\partial t_{ij}}{\partial d}}_{=:\beta}\kappa\,\hat{\boldsymbol{d}}_j\cdot\Big((\hat{\boldsymbol{d}}_j\cdot\boldsymbol{\nabla})\boldsymbol{u}(\boldsymbol{R}_i)\Big) = \beta\kappa\,\hat{\boldsymbol{d}}_j\cdot\Big((\hat{\boldsymbol{d}}_j\cdot\boldsymbol{\nabla})\boldsymbol{u}(\boldsymbol{R}_i)\Big)\,. \quad (3.2)$$

The sum $\sum_j t_{ij}e^{-i\tau\boldsymbol{K}\cdot\boldsymbol{d}_j}$ can now be written as $\sum_j(t_{ij,0}+\delta t_{ij})e^{-i\tau\boldsymbol{K}\cdot\boldsymbol{d}_j}$, where the first term vanishes because of Eq. (2.15) and the second term gives

$$\begin{aligned}
A(\boldsymbol{R}_i) &= -\beta\kappa\sum_j\hat{\boldsymbol{d}}_j\cdot(\hat{\boldsymbol{d}}_j\cdot\boldsymbol{\nabla})\boldsymbol{u}(\boldsymbol{R}_i)e^{-i\tau\boldsymbol{K}\cdot\boldsymbol{d}_j} = -\beta\kappa\left(\begin{pmatrix}\sqrt{3}\\1\end{pmatrix}\frac{\sqrt{3}\partial_x+\partial_y}{4}\begin{pmatrix}u_x\\u_y\end{pmatrix}e^{-i\tau\frac{2\pi}{3}}\right.\\
&\quad\left.+\begin{pmatrix}-\sqrt{3}\\1\end{pmatrix}\frac{-\sqrt{3}\partial_x+\partial_y}{4}\begin{pmatrix}u_x\\u_y\end{pmatrix}e^{+i\tau\frac{2\pi}{3}}+\begin{pmatrix}0\\-1\end{pmatrix}(-\partial_y)\begin{pmatrix}u_x\\u_y\end{pmatrix}e^{0}\right)\\
&= -\beta\kappa\left(\frac{3\partial_x u_x+\sqrt{3}\partial_y u_x+\sqrt{3}\partial_x u_y+\partial_y u_y}{4}\frac{-1-i\tau\sqrt{3}}{2}\right.\\
&\quad\left.+\frac{3\partial_x u_x-\sqrt{3}\partial_y u_x-\sqrt{3}\partial_x u_y+\partial_y u_y}{4}\frac{-1+i\tau\sqrt{3}}{2}+\partial_y u_y\right)\\
&= -\beta\kappa\left(u_{xx}\left(-\frac{3}{4}\right)+u_{xy}\left(-i\tau\frac{3}{2}\right)+u_{yy}\frac{3}{4}\right) = \beta\kappa\left(\frac{3}{4}(u_{xx}-u_{yy})+i\tau\frac{3}{2}u_{xy}\right)\\
&= A_x - i\tau A_y\,, \qquad \Rightarrow \quad A_x = \frac{3}{4}\beta\kappa(u_{xx}-u_{yy})\,,\quad A_y = -\frac{3}{2}\beta\kappa u_{xy}\,. \qquad (3.3)
\end{aligned}$$

The continuity of the deformation field $\boldsymbol{u}(\boldsymbol{r})$ lies at the heart of the continuum model, so we can extend $A(\boldsymbol{R}_i)$ continuously to $A(\boldsymbol{r})$. Our result corresponds to the term $tf(\boldsymbol{k})$ in Eq. (2.9), i.e., hopping from sublattice B to sublattice A. For hopping from sublattice A to sublattice B, we get $A^*(\boldsymbol{r})$, as one would expect from correspondence with Eq. (2.9). We thus find that the effect of bond-length change between nearest neighbors can be written as

$$\mathcal{H}_{\mathrm{BLC}} = \begin{pmatrix}0 & A_x-i\tau A_y\\ A_x+i\tau A_y & 0\end{pmatrix} = \sigma_x A_x+\sigma_y\tau A_y = \tau\sigma_x(\tau A_x)+\sigma_y(\tau A_y)\,, \quad (3.4)$$

where we have adopted the form of the low-energy Hamiltonian Eq. (2.17) in the last step. After absorbing the prefactor $\frac{1}{\hbar v_F}$ in $\boldsymbol{A} := (A_x, A_y)$ and with $\tilde{\boldsymbol{q}} = \boldsymbol{q}+\tau\boldsymbol{A}$, we can rewrite Eq. (2.17) as

$$\tilde{\mathcal{H}}_D = \mathcal{H}_D+\mathcal{H}_{\mathrm{BLC}} = \hbar v_F\left(\tau\sigma_x\tilde{q}_x+\sigma_y\tilde{q}_y\right)+\Delta\sigma_z\,, \quad (3.5)$$

and interpret $\tau\boldsymbol{A}$ as a pseudomagnetic gauge field that does not break time reversal symmetry (TRS) because it has different signs in K and K'. The conservation of TRS is necessary since (i) $\mathcal{H}_{\mathrm{BLC}}$ is caused entirely by strain, which conserves TRS and (ii) $\mathcal{H}_D$ conserves TRS. In graphene, the coupling constant of $\mathcal{H}_{\mathrm{BLC}}$ is typically assumed to be $g_2 = \frac{3}{4}\beta\kappa \approx 1.5$ eV [Suzuura(2002), Struck(2010)]. For hBN, we use $g_2 = 3$ eV, as will be discussed in Chapter 7.

3.1.2. Change of Fermi velocity

In the above Subsection, we have found that strain can give rise to pseudomagnetic gauge fields due to bond-length change between nearest neighbors. However, this picture seems to be incomplete because isotropic strain $u_{xx} = u_{yy} \neq 0 = u_{xy}$ yields $\boldsymbol{A} = 0$ in Eq. (3.3), even though the bond lengths between nearest neighbors do change.

Isotropic strain implies that all bond lengths change identically, that is, $\delta u^{(ij)}$ does not depend on $\hat{\boldsymbol{d}}_j$ in Eq. (3.1). Consequently, neither δt_{ij} nor $t_{ij} = t_{ij,0} + \delta t_{ij}$ depend on $\hat{\boldsymbol{d}}_j$ and we can factor t_{ij} out of the sum $t_{ij} \sum_j e^{-i\tau \boldsymbol{K}\cdot\boldsymbol{d}_j}$. This situation is identical to the unstrained case of Eq. (2.15) but with t_{ij} instead of $t_{ij,0}$. With a finite momentum $\boldsymbol{q}$ w.r.t. $\tau\boldsymbol{K}$, we obtain the low-energy Hamiltonian of Eq. (2.17), where the Fermi velocity is determined by

$$\begin{aligned} \delta t_{ij} &\overset{(*)}{=} \beta\kappa \begin{pmatrix} 0 \\ -1 \end{pmatrix} \cdot (-\partial_y \boldsymbol{u}) = \beta\kappa u_{yy} = \beta\kappa |u| \,, \\ \hbar\tilde{v}_F &= \frac{3(t_{ij,0} + \delta t_{ij})d}{2} = \hbar v_F + \frac{3\beta\kappa|u|d}{2} \,. \end{aligned} \tag{3.6}$$

In the step $(*)$, we have evaluated Eq. (3.2) for $\hat{\boldsymbol{d}}_j = (0, -1)$. Due to the isotropic strain, every choice of $\hat{\boldsymbol{d}}_j$ yields the same result. The change of the Fermi velocity is usually neglected since (i) it is linear in strain *and* (ii) a finite momentum $\boldsymbol{q}$ is required to observe the effect. Theory and experiment indicate that electron-electron interactions also change the Fermi velocity. This effect might dominate over the one caused by strain [Kotov(2012), Elias(2011)].

3.1.3. Deformation potential

The calculation of the bond-length change can also be applied to the hopping between second-nearest neighbors, i.e., the terms $t' g(\boldsymbol{k})$ in Eq. (2.9). With

$$\delta t'_{ij}(\boldsymbol{R}_i) = \frac{\partial t'_{ij}}{\partial a} \delta u^{(ij)} \approx \underbrace{a \frac{\partial t'_{ij}}{\partial a}}_{=:\beta'} \kappa' \, \hat{\boldsymbol{a}}_j \cdot ((\hat{\boldsymbol{a}}_j \cdot \boldsymbol{\nabla}) \boldsymbol{u}(\boldsymbol{R}_i)) = \beta' \kappa' \, \hat{\boldsymbol{a}}_j \cdot ((\hat{\boldsymbol{a}}_j \cdot \boldsymbol{\nabla}) \boldsymbol{u}(\boldsymbol{R}_i)) \,, \tag{3.7}$$

where κ' is scalar quantity similar to κ, we find

$$\phi(\boldsymbol{r}) = -\beta' \kappa' \sum_j \hat{\boldsymbol{a}}_j \cdot (\hat{\boldsymbol{a}}_j \cdot \boldsymbol{\nabla}) \boldsymbol{u}(\boldsymbol{r}) e^{-i\tau \boldsymbol{K}\cdot\boldsymbol{a}_j} = \frac{3\beta'\kappa'}{2} (u_{xx} + u_{yy}) \,. \tag{3.8}$$

Because of Eq. (2.4), the result depends neither on the valley (τ) nor on the sublattice. The resulting Hamiltonian can be written as a scalar and is hence referred to as the *deformation potential*,

$$\mathcal{H}_{\mathrm{VEP}} = g_1 (u_{xx} + u_{yy}) \,, \tag{3.9}$$

where a value of $g_1 \approx 30$ eV is usually assumed for the coupling constant in graphene [Suzuura(2002), Mariani(2009), Struck(2010)]. We are not aware of published values for g_1 in hBN.

3.2. Distortion of the Brillouin zone

In the case of homogeneous strain u, the periodicity of the lattice is still preserved but the shape of the unit cell depends on u. The same holds for the Brillouin zone [Pereira(2009)]. An arbitrary but homogeneous strain u_{ij} deforms a real space vector $\boldsymbol{v}$ to

$$\bar{\boldsymbol{v}} = \underbrace{\begin{pmatrix} 1+u_{xx} & u_{xy} \\ u_{xy} & 1+u_{yy} \end{pmatrix}}_{=1+u} \begin{pmatrix} v_x \\ v_y \end{pmatrix} = \begin{pmatrix} (1+u_{xx})v_x + u_{xy}v_y \\ u_{xy}v_x + (1+u_{yy})v_y \end{pmatrix} , \tag{3.10}$$

and the length of the deformed vector is approximated by

$$\begin{aligned} |\bar{\boldsymbol{v}}|^2 &= \left((1+u_{xx})^2 v_x^2 + 2(1+u_{xx})u_{xy}v_x v_y + u_{xy}^2 v_y^2\right) \\ &\quad + \left(u_{xy}^2 v_x^2 + 2u_{xy}(1+u_{yy})v_x v_y + (1+u_{yy})^2 v_y^2\right) \\ &\approx (1+2u_{xx})v_x^2 + 2u_{xy}v_x v_y + 2u_{xy}v_x v_y + (1+2u_{yy})v_y^2 \\ &= (1+2u_{xx})v_x^2 + (1+2u_{yy})v_y^2 + 4u_{xy}v_x v_y \,, \\ \Rightarrow |\bar{\boldsymbol{v}}| &\approx \sqrt{v_x^2 + v_y^2 + 2(u_{xx}v_x^2 + u_{yy}v_y^2 + 2u_{xy}v_x v_y)} \\ &\approx |\boldsymbol{v}| + \frac{1}{2|\boldsymbol{v}|}\, 2(u_{xx}v_x^2 + u_{yy}v_y^2 + 2u_{xy}v_x v_y) \\ &= |\boldsymbol{v}| + \frac{u_{xx}v_x^2 + 2u_{xy}v_x v_y + u_{yy}v_y^2}{|\boldsymbol{v}|} \,. \end{aligned} \tag{3.11}$$

Throughout our derivation, we neglect terms of order $\mathcal{O}(u^2)$ and higher. With Eq. (3.10), the lattice vectors given by Eq. (2.1) become

$$\bar{\boldsymbol{a}}_1 = \frac{a}{2}\begin{pmatrix} 1+u_{xx}+\sqrt{3}u_{xy} \\ u_{xy}+\sqrt{3}+\sqrt{3}u_{yy} \end{pmatrix} , \quad \bar{\boldsymbol{a}}_2 = \frac{a}{2}\begin{pmatrix} -1-u_{xx}+\sqrt{3}u_{xy} \\ -u_{xy}+\sqrt{3}+\sqrt{3}u_{yy} \end{pmatrix} . \tag{3.12}$$

The condition $\bar{\boldsymbol{a}}_i \cdot \bar{\boldsymbol{b}}_j = 2\pi\delta_{ij}$ determines the lattice vectors of the reciprocal lattice,

$$2\pi\delta_{ij} = \langle \boldsymbol{b}_i, \boldsymbol{a}_j \rangle = \langle \boldsymbol{b}_i, u^{-1}u\boldsymbol{a}_j \rangle = \langle (u^{-1})^\dagger \boldsymbol{b}_i, \bar{\boldsymbol{a}}_j \rangle = \langle \bar{\boldsymbol{b}}_i, \bar{\boldsymbol{a}}_j \rangle \,, \tag{3.13}$$

i.e., we can identify $\bar{\boldsymbol{b}}_i$ with $(u^{-1})^\dagger \boldsymbol{b}_i$. From Eq. (3.10), it is clear that the strain tensor u acts on vectors like a matrix. In general, this matrix is not unitary, but since u is a symmetric and real two-by-two matrix, it is straightforward to resolve

$$\begin{aligned} (u^{-1})^\dagger = u^{-1} &= \begin{pmatrix} 1+u_{yy} & -u_{xy} \\ -u_{xy} & 1+u_{xx} \end{pmatrix} \underbrace{\frac{1}{1+u_{xx}+u_{yy}+u_{xx}u_{yy}-u_{xy}^2}}_{\approx \frac{1}{1} - \frac{1}{1^2}(u_{xx}+u_{yy}+u_{xx}u_{yy}-u_{xy}^2) \approx 1-u_{xx}-u_{yy}} \\ &\approx \begin{pmatrix} (1+u_{yy})(1-u_{xx}-u_{yy}) & -u_{xy}(1-u_{xx}-u_{yy}) \\ -u_{xy}(1-u_{xx}-u_{yy}) & (1+u_{xx})(1-u_{xx}-u_{yy}) \end{pmatrix} \\ &\approx \begin{pmatrix} 1-u_{xx} & -u_{xy} \\ -u_{xy} & 1-u_{yy} \end{pmatrix} =: u_{\mathrm{rec}} \,. \end{aligned} \tag{3.14}$$

By acting u_{rec} on the lattice vectors of reciprocal space, we find

$$\bar{\boldsymbol{b}}_1 = \frac{2\pi}{a}\begin{pmatrix} 1-u_{xx}-\frac{u_{xy}}{\sqrt{3}} \\ -u_{xy}+\frac{1}{\sqrt{3}}-\frac{u_{yy}}{\sqrt{3}} \end{pmatrix} , \quad \bar{\boldsymbol{b}}_2 = \frac{2\pi}{a}\begin{pmatrix} -1+u_{xx}-\frac{u_{xy}}{\sqrt{3}} \\ u_{xy}+\frac{1}{\sqrt{3}}-\frac{u_{yy}}{\sqrt{3}} \end{pmatrix} . \tag{3.15}$$

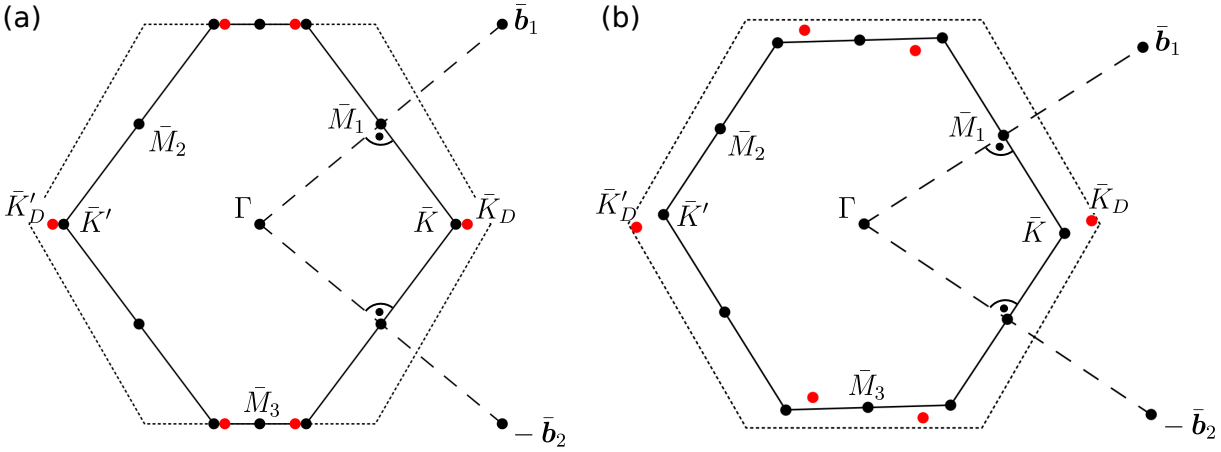

Figure 3.1.: To scale deformed Brillouin zone for a homogeneous strain of (a) $u_{xx} = 0.3$, $u_{xy} = u_{yy} = 0$ and (b) $u_{xx} = 0.2$, $u_{yy} = 0.1$, $u_{xy} = 0.02$. The dotted line represents the Brillouin zone for $u = 0$. The Γ-point lies at the origin of our coordinate system and hence does not change position. The $\bar{K}$-points lie at the intersections of the perpendicular bisectors of lattice vectors $\bar{\boldsymbol{b}}_i$ and the $\bar{M}$-points are given by $\bar{\boldsymbol{M}}_i = \bar{\boldsymbol{b}}_i/2$, where $\bar{\boldsymbol{b}}_3 = -(\bar{\boldsymbol{b}}_1 + \bar{\boldsymbol{b}}_2)$. The Dirac points lie at $\tau\bar{\boldsymbol{K}}_D = \tau(\boldsymbol{K} - \boldsymbol{A})$, where $\boldsymbol{A} = \frac{3\beta\kappa}{4\hbar v_F}(u_{xx} - u_{yy}, -2u_{xy})$. Here, we use a value of $\frac{3\beta\kappa}{4\hbar v_F} = 0.6/\text{Å}$, typical for hBN [Pereira(2009), Ribeiro(2009), Ribeiro(2011)].

We leave it to the reader to verify that $\bar{\boldsymbol{a}}_i \cdot \bar{\boldsymbol{b}}_j = 2\pi\delta_{ij}$ indeed holds up to $\mathcal{O}(u)$. Next, we would like to know how the high-symmetry points K and K' transform under strain. Applying u_{rec} on $\tau\boldsymbol{K}$ yields the wrong result since we have obtained u_{rec} in an approximation, which only suffices to find $\bar{\boldsymbol{b}}_j$ such that the condition $\bar{\boldsymbol{a}}_i \cdot \bar{\boldsymbol{b}}_j = 2\pi\delta_{ij}$ holds. However, we can proceed by remembering that the points $\tau\boldsymbol{K}$ lie at the corners of the Brillouin zone, i.e., at the intersections of the perpendicular bisectors of lattice vectors $\bar{\boldsymbol{b}}_i$, as shown in Fig. 3.1. The perpendicular bisector to $\bar{\boldsymbol{b}}_1$ is given by

$$\bar{\boldsymbol{M}}_1 + k_x^{(1)}\begin{pmatrix} 1 \\ \frac{-1}{\bar{b}_{1,y}/\bar{b}_{1,x}} \end{pmatrix} \approx \frac{\pi}{a}\begin{pmatrix} 1 - u_{xx} - \frac{u_{xy}}{\sqrt{3}} \\ -u_{xy} + \frac{1}{\sqrt{3}} - \frac{u_{yy}}{\sqrt{3}} \end{pmatrix} + k_x^{(1)}\begin{pmatrix} 1 \\ \sqrt{3}(u_{xx} - u_{yy} - 1) - 2u_{xy} \end{pmatrix}, \quad (3.16)$$

where we have used $\bar{\boldsymbol{M}}_1 = \bar{\boldsymbol{b}}_1/2$. Likewise, the perpendicular bisector to $-\bar{\boldsymbol{b}}_2$ can be parametrized as

$$-\bar{\boldsymbol{M}}_2 + k_x^{(2)}\begin{pmatrix} 1 \\ \frac{-1}{\bar{b}_{2,y}/\bar{b}_{2,x}} \end{pmatrix} \approx \frac{\pi}{a}\begin{pmatrix} 1 - u_{xx} + \frac{u_{xy}}{\sqrt{3}} \\ -u_{xy} - \frac{1}{\sqrt{3}} + \frac{u_{yy}}{\sqrt{3}} \end{pmatrix} + k_x^{(2)}\begin{pmatrix} 1 \\ \sqrt{3}(1 - u_{xx} + u_{yy}) - 2u_{xy} \end{pmatrix}, \quad (3.17)$$

and $\bar{\boldsymbol{K}}$ is the point where both bisectors meet. From the upper components, we resolve $k_x^{(2)} = k_x^{(1)} - \frac{2\pi}{\sqrt{3}a}u_{xy}$ such that the matching condition on the lower components yields

$$\begin{aligned} & k_x^{(1)} \approx \frac{\pi}{3a}(1 + u_{xx} + \sqrt{3}u_{xy} - 2u_{yy}), \\ \Rightarrow \quad & \bar{\boldsymbol{K}} = \bar{\boldsymbol{M}}_1 + k_x^{(1)}\begin{pmatrix} 1 \\ \frac{-1}{\bar{b}_{1,y}/\bar{b}_{1,x}} \end{pmatrix} \overset{(3.16)}{\approx} \frac{4\pi}{3a}\begin{pmatrix} 1 - \frac{u_{xx}}{2} - \frac{u_{yy}}{2} \\ -2u_{xy} \end{pmatrix}. \end{aligned} \quad (3.18)$$

A similar construction can be used to find $\bar{\boldsymbol{K}}' = -\bar{\boldsymbol{K}}$. This is expected, since $\boldsymbol{K}' = -\boldsymbol{K}$ and strain is centrosymmetric.

We emphasize that for finite strain, the high symmetry points $\tau\bar{\boldsymbol{K}}$ at the corners of the Brillouin zone do not coincide with the Dirac points, where the valence and conduction bands of graphene become degenerate. In Eq. (3.5), the degeneracy ($\Delta = 0$) occurs for $\tilde{\boldsymbol{q}} = 0$, i.e., for $\boldsymbol{q} = -\tau\boldsymbol{A}$, where $\boldsymbol{q}$ is measured w.r.t. the corner of the unstrained Brillouin zone $\tau\boldsymbol{K}$. Consequently, the Dirac points in a uniformly strained lattice, which we label $\bar{K}_D$ and $\bar{K}'_D$ to avoid confusion, are located[1] at $\tau\bar{\boldsymbol{K}}_D = \tau(\boldsymbol{K} - \boldsymbol{A})$. In the derivation of Eq. (3.5), we have assumed that strain changes the hopping amplitude t_{ij} but we did not consider the effect of strain on the exponent of $e^{-i\tau\boldsymbol{K}\cdot\boldsymbol{d}_j}$. For discussion of this effect, we refer to [Hasegawa(2006), Wunsch(2008), Pereira(2009)].

3.3. Spin-phonon coupling

Phonons, i.e. quantized lattice deformations $\boldsymbol{u}$ do not have spin and hence cannot couple to spin directly but only in combination with spin-orbit coupling. The spin-orbit interaction in graphene is given by

$$\mathcal{H}_{\mathrm{SOI}} = \underbrace{\lambda_I \sigma_z \tau_z s_z}_{=\mathcal{H}_I} - \underbrace{\lambda_R(\sigma_x \tau_z s_y - \sigma_y s_x)}_{=-\mathcal{H}_R}, \tag{3.19}$$

where $\mathcal{H}_I$ is the intrinsic or Dresselhaus-type coupling with $\lambda_I = 12\ \mu$eV and $\mathcal{H}_R$ is the extrinsic or Rashba-type coupling with an electric-field dependent coupling strength $\lambda_R = 5\ \mu\mathrm{eV} \times E[\mathrm{V/nm}]$ [Kane(2005), Min(2006), Gmitra(2009)]. For a derivation of $\mathcal{H}_{\mathrm{SOI}}$, we refer to [Droth(2010)].

3.3.1. Coupling to in-plane phonons

The deformation potential Eq. (3.9) and the bond-length change Eq. (3.4) constitute the coupling of electrons to acoustic in-plane phonons, $\mathcal{H}_{\mathrm{EPC}} = \mathcal{H}_{\mathrm{VEP}} + \mathcal{H}_{\mathrm{BLC}}$. In combination with Rashba-type spin-orbit coupling, $\mathcal{H}_{\mathrm{EPC}}$ can give rise to spin-phonon coupling via the following *admixture mechanism* [Khaetskii(2001), Hanson(2007)]. In first-order perturbation theory, $\mathcal{H}_R$ changes momentum-spin product states $|\boldsymbol{k}, s\rangle^{(0)} := |\boldsymbol{k}\rangle|s\rangle$ to

$$\begin{aligned} |\boldsymbol{k}\uparrow\rangle &= |\boldsymbol{k}\uparrow\rangle^{(0)} + \sum_{\boldsymbol{k}'\neq\boldsymbol{k}} |\boldsymbol{k}'\downarrow\rangle^{(0)} \frac{{}^{(0)}\langle\boldsymbol{k}'\downarrow|\mathcal{H}_R|\boldsymbol{k}\uparrow\rangle^{(0)}}{E_k - E_{k'} + g\mu_B B}, \\ |\boldsymbol{k}\downarrow\rangle &= |\boldsymbol{k}\downarrow\rangle^{(0)} + \sum_{\boldsymbol{k}'\neq\boldsymbol{k}} |\boldsymbol{k}'\uparrow\rangle^{(0)} \frac{{}^{(0)}\langle\boldsymbol{k}'\uparrow|\mathcal{H}_R|\boldsymbol{k}\downarrow\rangle^{(0)}}{E_k - E_{k'} - g\mu_B B}, \end{aligned} \tag{3.20}$$

where the energy difference in the nominator includes the Zeeman splitting with the g-factor of graphene, $g = 2$, and the Bohr magneton μ_B. The perturbed states include

[1] We remind the reader that the prefactor $\frac{1}{\hbar v_F}$ needs to be absorbed in $\boldsymbol{A}$ as given by Eq. (3.3).

contributions from both spin orientations. Consequently, the matrix element

$$\langle \boldsymbol{k}\downarrow|\mathcal{H}_{\mathrm{EPC}}|\boldsymbol{k}\uparrow\rangle = \sum_{\boldsymbol{k}'\neq\boldsymbol{k}} \left(\frac{(\mathcal{H}_{\mathrm{EPC}})_{\boldsymbol{k}\boldsymbol{k}'}(\mathcal{H}_R)^{\downarrow\uparrow}_{\boldsymbol{k}'\boldsymbol{k}}}{E_k - E_{k'} + g\mu_B B} + \frac{(\mathcal{H}_{\mathrm{EPC}})_{\boldsymbol{k}'\boldsymbol{k}}(\mathcal{H}_R)^{\downarrow\uparrow}_{\boldsymbol{k}\boldsymbol{k}'}}{E_k - E_{k'} - g\mu_B B} \right) , \tag{3.21}$$

where $(\mathcal{H}_R)^{\downarrow\uparrow}_{\boldsymbol{k}'\boldsymbol{k}}$ labels the spin-flipping term in the numerator of Eq. (3.20) and $(\mathcal{H}_{\mathrm{EPC}})_{\boldsymbol{k}\boldsymbol{k}'}$ labels the according (spin-conserving) matrix element of the electron-phonon coupling, will usually be finite. To ensure conservation of the Zeeman energy, a phonon must be created or annihilated during the spin-flipping process described by Eq. (3.21).

3.3.2. Coupling to out-of-plane phonons

The intrinsic spin-orbit coupling of graphene, $\mathcal{H}_I = \lambda_I \sigma_z \tau_z s_z$, involves the Pauli matrices σ_z (pseudospin), τ_z (valley spin), and s_z (real spin). Usually, σ_z, τ_z, and s_z all refer to the cartesian coordinates of a flat lattice with $\boldsymbol{n}(\boldsymbol{r}) = \boldsymbol{e}_z$, where $\boldsymbol{n}(\boldsymbol{r})$ is a vector normal to the graphene sheet. However, out-of-plane phonons locally tilt the sheet such that in general $\boldsymbol{n}(\boldsymbol{r}) \nparallel \boldsymbol{e}_z$, where $\boldsymbol{n}(\boldsymbol{r}) \approx (-\partial_x u_z, -\partial_y u_z, 1)$ for small tilts [CastroNeto(2009)]. Curvature can also contribute significantly to spin-orbit coupling [Kuemmeth(2008)] but this effect becomes negligible for long-wavelength phonons. Here, we consider such long-wavelength phonons at the center of the Brillouin zone and hence focus only on a small tilt of the graphene sheet.

While pseudospin σ_z and valley spin τ_z are directly linked to the lattice and hence to the *locally tilted frame* Σ', real spin s_z can be linked to an external magnetic field $\boldsymbol{B}$ and hence to the *laboratory frame* Σ, see Fig. 3.2 (a) and (b). Due to $\mathcal{H}_I$, the electrons feel an effective magnetic field while they propagate through the lattice. With $\lambda_I = 12\,\mu$eV [Gmitra(2009), Struck(2010)] and in terms of the Zeeman energy $s_z g\mu_B B/2$, this effective magnetic field has a strength of $B_I = \frac{\lambda_I}{g\mu_B B/2} \approx 0.2$ T. For $B_I \gg B$, the real electron spin will be linked to the lattice while for $B \gg B_I$, it will be linked to $\boldsymbol{B}$. Here, we consider the latter case where s_z is linked to $\boldsymbol{B}$ and hence to the laboratory frame. Thus, in the locally tilted frame with $\boldsymbol{e}'_z \parallel \boldsymbol{n}(\boldsymbol{r})$, the intrinsic spin-orbit coupling can be written as $\mathcal{H}_I = \lambda_i \sigma'_z \tau'_z s'_z$, where $\sigma'_z = \sigma_z$, $\tau'_z = \tau_z$, and $s'_z = \boldsymbol{n}(\boldsymbol{r}) \cdot \boldsymbol{s}$. Pseudospin and valley spin are linked to the the locally tilted lattice and hence their description in the locally tilted frame is identical to their description for a non-tilted lattice in the laboratory frame. Here, real spin is linked to the laboratory frame and hence its description in the locally tilted frame involves $\boldsymbol{n}(\boldsymbol{r})$, see Fig. 3.2 (c) and (d). The intrinsic spin-orbit coupling is thus given by

$$\mathcal{H}_I = \lambda_I \sigma_z \tau_z (s_z - \partial_x u_z s_x - \partial_y u_z s_y) , \tag{3.22}$$

and directly couples acoustic out-of-plane phonons to spin. Now, $\mathcal{H}_I$ includes s_x and s_y, which can flip the spin. This effect is also referred to as *deflection coupling* [Struck(2010), Rudner(2010)].

Similar considerations can be made for the extrinsic spin-orbit coupling, which then takes the form

$$\mathcal{H}_R = -\lambda_R \left(\tau_z \sigma_x (s_y + \partial_y u_z s_z) - \sigma_y (s_x + \partial_x u_z s_z) \right) , \tag{3.23}$$

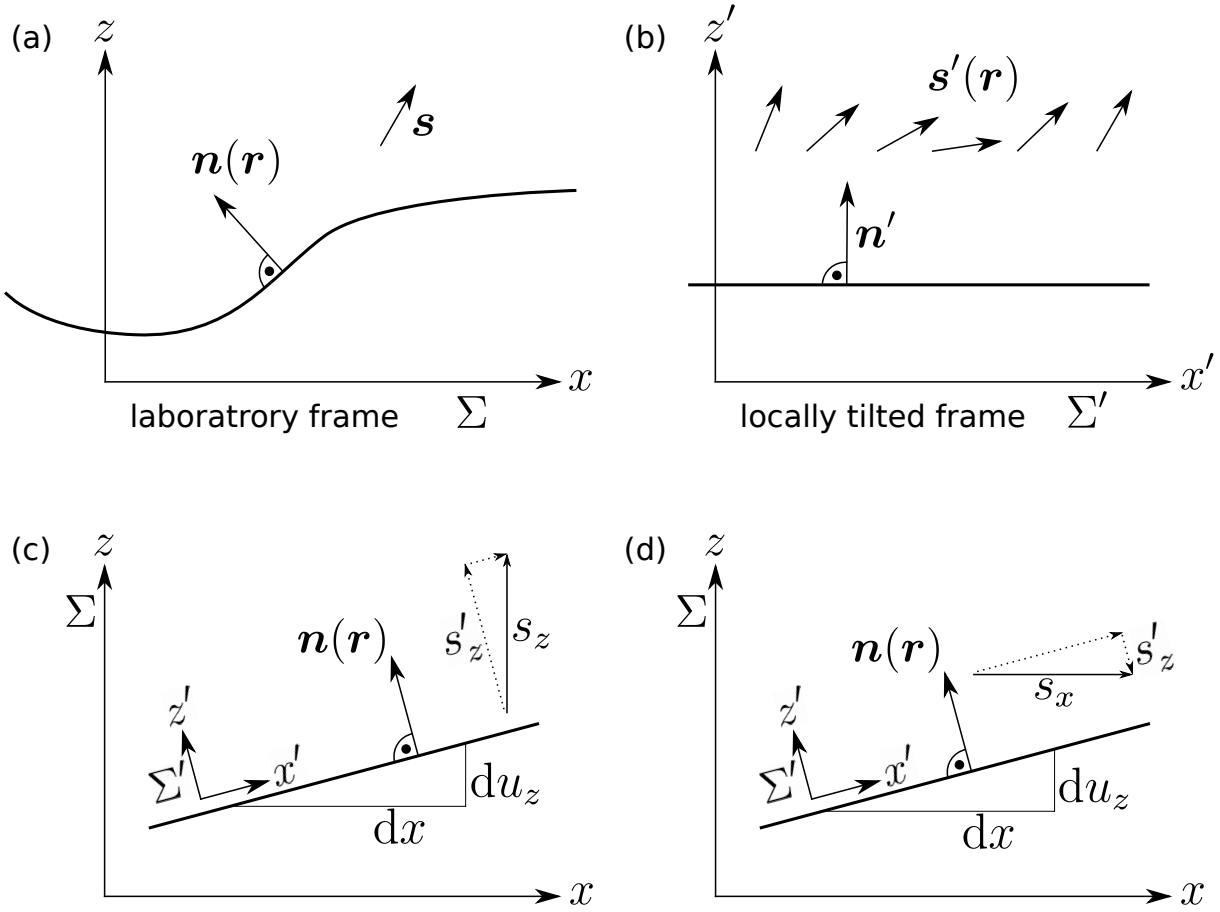

Figure 3.2.: (a) Due to out-of-plane deformations, the normal vector $\boldsymbol{n}(\boldsymbol{r})$ is usually not parallel to $\boldsymbol{e}_z$. For an external magnetic field $B \gg B_I$, the spin $\boldsymbol{s}$ is easily expressed in the laboratory frame Σ rather than in the sheet- or locally tilted frame Σ'. (b) In the locally tilted frame of the graphene sheet, the spin $\boldsymbol{s}'(\boldsymbol{r})$ depends on the local tilt, i.e., on $\boldsymbol{n}(\boldsymbol{r})$. In (c) and (d), we assume a small tilt with $\partial_x u_z(\boldsymbol{r}) \ll 1$ and $\partial_y u_z(\boldsymbol{r}) = 0$. (c) For $s_x = s_y = 0$, we get $s'_z \approx s_z$ and (d) for $s_y = s_z = 0$, we get $s'_z \approx -\partial_x u_z s_x$. Similar considerations can be made for the y-coordinate. In total, we find $s'_z = -\partial_x u_z s_x - \partial_y u_z s_y + s_z = \boldsymbol{n}(\boldsymbol{r}) \cdot \boldsymbol{s}$.

yet the additional terms do not contain s_x or s_y and thus do not contribute to spin relaxation.

4. Two applications of the geometric phase

In 1956, Shivaramakrishnan Pancharatnam first introduced the notion of the geometric phase in the context of polarized light [Pancharatnam(1956)]. Today, the geometric phase is also commonly known as *Berry phase*, named after Sir Michael Berry who has rediscovered the concept and applied it to the Aharonov-Bohm effect [Berry(1984), Ehrenberg(1949), Aharonov(1959)]. Since then, the theory has been generalized and applied to many different situations.

Here, we give a short introduction to the concept so the calculation of the piezoelectric effect via a geometric phase as well as Peierls' phase can be applied in Chapter 7 and Chapter 8, respectively. For an in-depth introduction to geometric phases, we refer to [Xiao(2010)] and to [Bohm].

4.1. The polarization via a geometric phase

First, we introduce the evolution of a state w.r.t. an adiabatic control parameter and then, we discuss adiabatic transport [Xiao(2010)]. The polarization density is linked to the current density via a Maxwell equation and the continuity equation. If the electronic Hamiltonian depends on some parameter, the dispersion will usually be affected by a change of this parameter. In short, the integral of this response over the entire Brillouin zone can be expressed in terms of a current density that changes the polarization density.

4.1.1. Adiabatic evolution

Let us assume, the Hamiltonian $\mathcal{H}(\boldsymbol{R}(t))$ depends on parameters[1] $\boldsymbol{R}(t)$ that change adiabatically during some process [Xiao(2010)]. At every instant, the wave function $|\psi(t)\rangle$ obeys the Schrödinger equation,

$$i\hbar\partial_t|\psi(t)\rangle = \mathcal{H}(t)|\psi(t)\rangle\,, \tag{4.1}$$

[1]The effect of an external magnetic field can be described by a parameter vector in real space. Then, the Berry connection, Eq. (4.7), equals the magnetic vector potential, and the Berry curvature, Eq. (4.22), equals the magnetic field $\boldsymbol{B} = \boldsymbol{\nabla} \times \boldsymbol{A}$. However, we emphasize that usually, the parameter vector is *not* a vector in real space.

and also at every instant, there is a basis of *instantaneous eigenstates* $\{|n(t)\rangle\}$ that suffice $\mathcal{H}(t)|n(t)\rangle = E_n(t)|n(t)\rangle$. Within that basis, the wave function can be expressed as

$$|\psi(t)\rangle = \sum_n e^{-\frac{i}{\hbar}\int_0^t E_n(t')\mathrm{d}t'} a_n(t)|n(t)\rangle\,. \tag{4.2}$$

The exponent with the eigenenergy $E_n(t)$ would suffice to describe the time evolution of the eigenstate $|n(t)\rangle$ if $\mathcal{H}(t)$ was time-independent. Since $\mathcal{H}(t)$ changes with time, the probability density $|\langle \boldsymbol{r}|n(t)\rangle|^2$ will usually also change in time, yet said phase does not describe this evolution. Obviously, the weight $a_n(t)$ of a certain component $|n(t)\rangle$ of $|\psi(t)\rangle$ can also depend on time. Now, we calculate[2]

$$\begin{aligned}
\langle n|i\hbar\partial_t|\psi\rangle &= \sum_l \langle n|i\hbar\frac{-i}{\hbar}E_l(t)e^{-\frac{i}{\hbar}\int_0^t E_l(t')\mathrm{d}t'}a_l(t)|l\rangle \\
&\quad +\langle n|i\hbar e^{-\frac{i}{\hbar}\int_0^t E_l(t')\mathrm{d}t'}\dot{a}_l(t)|l\rangle + \langle n|i\hbar e^{-\frac{i}{\hbar}\int_0^t E_l(t')\mathrm{d}t'}a_l(t)|\partial_t l\rangle \\
&= E_n(t)e^{-\frac{i}{\hbar}\int_0^t E_n(t')\mathrm{d}t'}a_n(t) \\
&\quad +i\hbar e^{-\frac{i}{\hbar}\int_0^t E_n(t')\mathrm{d}t'}\dot{a}_n(t) + \sum_l i\hbar e^{-\frac{i}{\hbar}\int_0^t E_l(t')\mathrm{d}t'}a_l(t)\langle n|\partial_t l\rangle\,,
\end{aligned} \tag{4.3}$$

which — because of Eq. (4.1) — must coincide with

$$\langle n|\mathcal{H}(t)|\psi\rangle = \sum_l \langle n|e^{-\frac{i}{\hbar}\int_0^t E_l(t')\mathrm{d}t'}a_l(t)E_l(t)|l\rangle = e^{-\frac{i}{\hbar}\int_0^t E_n(t')\mathrm{d}t'}a_n(t)E_n(t)\,. \tag{4.4}$$

That is, the two last terms in Eq. (4.3) must cancel each other, which we express as

$$\dot{a}_n(t) = -\sum_l a_l(t)\langle n|\partial_t l\rangle e^{-\frac{i}{\hbar}\int_0^t [E_l(t')-E_n(t')]\mathrm{d}t'}\,. \tag{4.5}$$

It is always possible to write $\langle n|\partial_t l\rangle = \dot{\boldsymbol{R}}(t)\cdot\langle n|\frac{\partial}{\partial \boldsymbol{R}(t)}|l\rangle$. In the adiabatic limit, the parameters $\boldsymbol{R}$ change slowly in time, i.e. $\dot{\boldsymbol{R}}\approx 0$. This[3] implies $\langle n|\partial_t l\rangle \approx 0$, such that in zeroth order, Eq. (4.5) becomes

$$\dot{a}_n(t) \overset{(4.5)}{=} 0\,. \tag{4.6}$$

This equation leads to the *quantum adiabatic theorem*: if the system is initially in the n-th eigenstate, it will stay in that state afterwards [Xiao(2010)]. To proceed, we introduce the *Berry connection*

$$\boldsymbol{A}^{(n)}(\boldsymbol{R}) = i\langle n|\frac{\partial}{\partial \boldsymbol{R}}|n\rangle\,, \tag{4.7}$$

[2]To ensure readability, we drop the time dependence from all states. All states still do depend on time.

[3]We stick to the notation used in [Xiao(2010)] but remark that both $\dot{\boldsymbol{R}}$ and $\langle n|\partial_t l\rangle$ are generally dimensionful quantities and hence require some reference w.r.t. which they can be considered *small* or *large*. Here, $\dot{\boldsymbol{R}}$ and $\langle n|\partial_t l\rangle$ (and also $\ddot{\boldsymbol{R}}$ in Eq. (4.13)) are sufficiently small if $\dot{\phi}\ll\omega$, where $\dot{\phi}=\max_i\dot{\phi}_i$ is the maximum of the angular velocities $\dot{\phi}_i$ that describe the rotation rate of the eigenaxes in the Hilbert space as $\mathcal{H}(t)$ evolves [Messiah]. The frequency ω corresponds to the minimal energy splitting in the spectrum, $\hbar\omega=\min_{i,j\neq i}(E_i-E_j)$.

which is a gauge-dependent quantity. Under the gauge change $|n\rangle \mapsto e^{i\zeta(\boldsymbol{R})}|n\rangle$, the Berry connection is mapped as follows:

$$\begin{aligned}\boldsymbol{A}^{(n)}(\boldsymbol{R}) \mapsto ie^{-i\zeta(\boldsymbol{R})}\langle n|\frac{\partial}{\partial \boldsymbol{R}}|e^{i\zeta(\boldsymbol{R})}n\rangle &= ie^{-i\zeta(\boldsymbol{R})}\left(\langle n|i\frac{\partial\zeta(\boldsymbol{R})}{\partial\boldsymbol{R}}e^{i\zeta(\boldsymbol{R})}|n\rangle + e^{i\zeta(\boldsymbol{R})}\langle n|\frac{\partial}{\partial\boldsymbol{R}}|n\rangle\right)\\ &= -\frac{\partial\zeta(\boldsymbol{R})}{\partial\boldsymbol{R}} + \boldsymbol{A}^{(n)}(\boldsymbol{R})\,. \end{aligned} \tag{4.8}$$

With the right choice of $\zeta_n(\boldsymbol{R})$, the condition of *parallel transport*[4],

$$\langle n|\frac{\partial n}{\partial t}\rangle = \dot{\boldsymbol{R}}\cdot\langle n|\frac{\partial}{\partial\boldsymbol{R}}|n\rangle \overset{(4.7)}{=} \dot{\boldsymbol{R}}\cdot\frac{\boldsymbol{A}^{(n)}(\boldsymbol{R})}{i} = 0\,, \tag{4.9}$$

i.e., $\boldsymbol{A}^{(n)}(\boldsymbol{R}) \perp \dot{\boldsymbol{R}}$ can be satisfied. In particular, Eq. (4.9) does not over-determine the system. Those states with the right gauge — i.e. those states that obey the parallel transport condition — shall be denoted $\{|\tilde{n}\rangle\}$.

Let $|\tilde{n}\rangle$ be the initial state, i.e., $a_{\tilde{n}}(0) = 1$ and $a_{\tilde{n}'\neq\tilde{n}} = 0$ in Eq. (4.2). In first order, Eq. (4.5) becomes

$$\dot{a}_{\tilde{n}}(t) = -\sum_{\tilde{l}} \underbrace{a_l(0)}_{\uparrow\,=\delta_{\tilde{n}l}}\langle\tilde{n}|\partial_t\tilde{l}\rangle e^{-\frac{i}{\hbar}\int_0^t[E_{\tilde{l}}(t')-E_{\tilde{n}}(t')]\mathrm{d}t'} \propto \langle\tilde{n}|\partial_t\tilde{n}\rangle \overset{(*)}{=} 0\,, \tag{4.10}$$

$$\dot{a}_{\tilde{n}'\neq\tilde{n}}(t) = \underbrace{-\langle\tilde{n}'|\partial_t\tilde{n}\rangle}_{=:u(t)}\underbrace{e^{-\frac{i}{\hbar}\int_0^t[E_{\tilde{n}}(t')-E_{\tilde{n}'}(t')]\mathrm{d}t'}}_{=:\dot{v}(t)} \tag{4.11}$$

$$\begin{aligned}\Rightarrow\ a_{\tilde{n}'\neq\tilde{n}}(t) &= a_{\tilde{n}'\neq\tilde{n}}(0) + \int_0^t \dot{a}_{\tilde{n}'\neq\tilde{n}}(t')\mathrm{d}t' = 0 + \int_0^t(\dot{u}v)\mathrm{d}t' - \underbrace{\int_0^t \dot{u}v\mathrm{d}t'}_{=0} = u(t)v(t)\\ &= -\frac{\langle\tilde{n}'|\partial_t\tilde{n}\rangle}{E_{\tilde{n}}(t)-E_{\tilde{n}'}(t)}i\hbar e^{-\frac{i}{\hbar}\int_0^t[E_{\tilde{n}}(t')-E_{\tilde{n}'}(t')]\mathrm{d}t'}\,. \end{aligned} \tag{4.12}$$

In the step $(*)$, we have exploited the condition of parallel transport, Eq. (4.9). Moreover, we have used

$$\begin{aligned} v(t) &= \frac{i\hbar}{E_{\tilde{n}}(t)-E_{\tilde{n}'}(t)}e^{-\frac{i}{\hbar}\int_0^t[E_{\tilde{n}}(t')-E_{\tilde{n}'}(t')]\mathrm{d}t'}\,,\\ \dot{u}(t) &= -\partial_t\left(\dot{\boldsymbol{R}}\langle\tilde{n}'|\frac{\partial}{\partial\boldsymbol{R}}|\tilde{n}\rangle\right)\\ &= -\underbrace{\ddot{\boldsymbol{R}}}_{\uparrow\,\approx 0}\cdot\langle\tilde{n}'|\frac{\partial\tilde{n}}{\partial\boldsymbol{R}}\rangle - \underbrace{\dot{\boldsymbol{R}}\cdot\left(\langle\dot{\boldsymbol{R}}\cdot\frac{\partial\tilde{n}'}{\partial\boldsymbol{R}}|\frac{\partial\tilde{n}}{\partial\boldsymbol{R}}\rangle + \langle\tilde{n}'|\frac{\partial}{\partial\boldsymbol{R}}|\dot{\boldsymbol{R}}\cdot\frac{\partial\tilde{n}}{\partial\boldsymbol{R}}\rangle\right)}_{\mathcal{O}(\dot{\boldsymbol{R}}^2)\approx 0} \approx 0\,. \end{aligned} \tag{4.13}$$

When calculating $\dot{v}(t)$, the term from acting ∂_t on the exponent is of order $\mathcal{O}(\dot{\boldsymbol{R}}^0)$ and hence dominates over the term from acting ∂_t on the nominator since the time dependence of the energies stems from the Hamiltonian $\mathcal{H}(\boldsymbol{R}(t))$, which implies $\partial_t E_{\tilde{n}}(t) = \dot{\boldsymbol{R}}\cdot\frac{\partial E_n(\boldsymbol{R})}{\partial\boldsymbol{R}} =$

[4]The term *parallel transport* is intuitive in that under this condition, the state $|n\rangle$ is perpendicular to its gradient $|\partial_t n\rangle$.

$\mathcal{O}(\dot{\boldsymbol{R}})$. This justifies the assignment of $v(t)$ in view of $\dot{v}(t)$ in Eq. (4.11). As for integration constants, we need only be concerned with the expression given by Eq. (4.12), where the constants are correct in an approximation since $a_{\tilde{n}'\neq\tilde{n}}(0) = 0$ and $\langle\tilde{n}'|\partial_t|\tilde{n}\rangle \approx 0$ due to the adiabatic limit[3] mentioned below Eq. (4.5). With Eqs. (4.10) and (4.12), the state given by Eq. (4.2) takes — in first order of ∂_t — the form

$$\begin{aligned} |\psi_{\tilde{n}}\rangle &= e^{-\frac{i}{\hbar}\int_0^t E_{\tilde{n}}(t')\mathrm{d}t'} \underbrace{a_{\tilde{n}}(t)}_{=1}|\tilde{n}\rangle + \sum_{\tilde{n}'\neq\tilde{n}} \frac{-\langle\tilde{n}|\partial_t\tilde{n}\rangle}{E_{\tilde{n}}(t) - E_{\tilde{n}'}(t)} i\hbar e^{-\frac{i}{\hbar}\int_0^t [E_{\tilde{n}}(t') - E_{\tilde{n}'}(t') + E_{\tilde{n}'}(t')]\mathrm{d}t'}|\tilde{n}'\rangle \\ &= e^{-\frac{i}{\hbar}\int_0^t E_{\tilde{n}}(t')\mathrm{d}t'} \left(|\tilde{n}\rangle - i\hbar \sum_{\tilde{n}'\neq\tilde{n}} |\tilde{n}'\rangle \frac{\langle\tilde{n}'|\partial_t\tilde{n}\rangle}{E_{\tilde{n}}(t) - E_{\tilde{n}'}(t)} \right) . \end{aligned} \tag{4.14}$$

When using this equation in a calculation, the states $\{|\tilde{n}\rangle\}$ can be replaced by states with some other phase/gauge choice, provided the terms containing these states are gauge invariant [Xiao(2010)].

4.1.2. Adiabatic transport and electric polarization

The relevant parameters for adiabatic transport are $\boldsymbol{R} = (\boldsymbol{q}, t)$, where $\boldsymbol{q}$ is a wavevector within the first Brillouin zone and t labels time. For simplicity, we consider a one-dimensional system and choose the q-space representation. The velocity operator in q-space is given by

$$v(q,t) = \frac{\partial\mathcal{H}(q,t)}{\hbar\partial q} . \tag{4.15}$$

At time t and up to first order, the velocity of a state initially ($t = 0$) in band n and with wavenumber q is given by

$$\begin{aligned} v_n(q,t) &= \langle\psi_n|\frac{\partial\mathcal{H}(q,t)}{\hbar\partial q}|\psi_n\rangle \\ &= \left(\langle n| + i\hbar \sum_{n'\neq n} \frac{\langle\partial_t n|n'\rangle\langle n'|}{E_n - E_{n'}} \right) \frac{\partial\mathcal{H}}{\hbar\partial q} \left(|n\rangle - i\hbar \sum_{n'\neq n} \frac{|n'\rangle\langle n'|\partial_t n\rangle}{E_n - E_{n'}} \right) \\ &= \langle n|\frac{\partial\mathcal{H}(q,t)}{\hbar\partial q}|n\rangle - i \sum_{n'\neq n} \left(\frac{\langle n|\frac{\partial\mathcal{H}}{\partial q}|n'\rangle\langle n'|\partial_t n\rangle}{E_n - E_{n'}} - \frac{\langle\partial_t n|n'\rangle\langle n'|\frac{\partial\mathcal{H}}{\partial q}|n\rangle}{E_n - E_{n'}} \right) , \end{aligned} \tag{4.16}$$

where we have used Eq. (4.14) and dropped the tilde from the states in the second step. For any set of orthonormal eigenstates $\{|n\rangle\}$ of some Hamiltonian $\mathcal{H}$, the following expressions hold:

$$\begin{aligned} \langle n|\frac{\partial\mathcal{H}}{\partial\boldsymbol{R}}|n'\rangle &= \langle n| \left(\frac{\partial}{\partial\boldsymbol{R}} \sum_m E_m|m\rangle\langle m| \right) |n'\rangle \\ &= \sum_m \left(\frac{\partial E_m}{\partial\boldsymbol{R}}\langle n|m\rangle\langle m|n'\rangle + E_m\langle n|\frac{\partial m}{\partial\boldsymbol{R}}\rangle\langle m|n'\rangle + E_m\langle n|m\rangle\langle\frac{\partial m}{\partial\boldsymbol{R}}|n'\rangle \right) \\ &= \frac{\partial E_n}{\partial\boldsymbol{R}}\langle n|n'\rangle + \langle\frac{\partial n}{\partial\boldsymbol{R}}|n'\rangle(E_n - E_{n'}) . \end{aligned} \tag{4.17}$$

For the second term in the second line, we have used $0 = \frac{\partial}{\partial \boldsymbol{R}}\delta_{nm} = \frac{\partial\langle n|m\rangle}{\partial \boldsymbol{R}} = \langle\frac{\partial n}{\partial \boldsymbol{R}}|m\rangle + \langle n|\frac{\partial m}{\partial \boldsymbol{R}}\rangle \Rightarrow \langle n|\frac{\partial m}{\partial \boldsymbol{R}}\rangle = -\langle\frac{\partial n}{\partial \boldsymbol{R}}|m\rangle$. Similarly, we find

$$\langle n'|\frac{\partial \mathcal{H}}{\partial \boldsymbol{R}}|n\rangle = \frac{\partial E_{n'}}{\partial \boldsymbol{R}}\langle n'|n\rangle + \langle\frac{\partial n'}{\partial \boldsymbol{R}}|n\rangle(E_{n'} - E_n) = \frac{\partial E_{n'}}{\partial \boldsymbol{R}}\langle n'|n\rangle + \langle n'|\frac{\partial n}{\partial \boldsymbol{R}}\rangle(E_n - E_{n'})\,, \quad (4.18)$$

and we can rewrite Eq. (4.16) as

$$v_n(q,t) = \langle n|\frac{\partial \mathcal{H}(q,t)}{\hbar\partial q}|n\rangle - i\sum_{n'\neq n}\left(\langle\partial_q n|n'\rangle\langle n'|\partial_t n\rangle - \langle\partial_t n|n'\rangle\langle n'|\partial_q n\rangle\right)\,. \quad (4.19)$$

The first term can be evaluated using the Hellmann-Feynman theorem [Güttinger(1932), Hellmann, Feynman(1939)],

$$\begin{aligned}\frac{\partial E_n(q,t)}{\partial q} &= \frac{\partial}{\partial q}\langle n|\mathcal{H}(q,t)|n\rangle = \langle\frac{\partial n}{\partial q}|\mathcal{H}(q,t)|n\rangle + \langle n|\frac{\partial \mathcal{H}(q,t)}{\partial q}|n\rangle + \langle n|\mathcal{H}(q,t)|\frac{\partial n}{\partial q}\rangle \\ &= \langle n|\frac{\partial \mathcal{H}(q,t)}{\partial q}|n\rangle + E_n\underbrace{\left(\langle\frac{\partial n}{\partial q}|n\rangle + \langle n|\frac{\partial n}{\partial q}\rangle\right)}_{=\frac{\partial}{\partial q}\langle n|n\rangle=\frac{\partial 1}{\partial q}=0} = \langle n|\frac{\partial \mathcal{H}(q,t)}{\partial q}|n\rangle\,. \end{aligned} \quad (4.20)$$

Our ansatz includes the parallel transport condition given by Eq. (4.9), $\langle n|\frac{\partial n}{\partial t}\rangle = 0$. We can thus include the terms with $n' = n$ in the second term of Eq. (4.19) and trace out the projectors $\sum_{n'}|u_{n'}\rangle\langle u_{n'}| = 1$,

$$v_n(q,t) = \frac{\partial E_n(q,t)}{\hbar\partial q} - \underbrace{i\left(\langle\partial_q n|\partial_t n\rangle - \langle\partial_t n|\partial_q n\rangle\right)}_{=\Omega_{qt}^{(n)}}\,. \quad (4.21)$$

The second term is known as the *Berry curvature*,

$$\begin{aligned}\Omega_{ab}^{(n)} &= \frac{\partial}{\partial R_a}A_b^{(n)}(\boldsymbol{R}) - \frac{\partial}{\partial R_b}A_a^{(n)}(\boldsymbol{R}) \\ &= i\left(\langle\frac{\partial n(\boldsymbol{R})}{\partial R_a}|\frac{\partial n(\boldsymbol{R})}{\partial R_b}\rangle - \langle\frac{\partial n(\boldsymbol{R})}{\partial R_b}|\frac{\partial n(\boldsymbol{R})}{\partial R_a}\rangle\right)\,, \end{aligned} \quad (4.22)$$

where $\boldsymbol{A}^{(n)}(\boldsymbol{R})$ is the Berry connection from Eq. (4.7). In contrast to the Berry connection, the Berry curvature is gauge-independent since the gauge-dependent term in Eq. (4.8) is canceled in Eq. (4.22), $\frac{\partial\zeta^n}{\partial R_a\partial R_b} - \frac{\partial\zeta^n}{\partial R_b\partial R_a} = 0$. We can thus write the average velocity of a state initially in band n, with momentum q, and at time t as

$$v_n(q,t) = \frac{\partial E_n(q,t)}{\hbar\partial q} - \Omega_{qt}^{(n)}\,. \quad (4.23)$$

The resulting charge current density j is obtained by summing up the contributions from all wavenumbers q inside the Brillouin zone (BZ) for all filled bands n,

$$j = -e\sum_{n,q}v_n(q,t) = -e\sum_n\int_{\mathrm{BZ}}\frac{\mathrm{d}q}{2\pi}\left(\frac{\partial E_n(q,t)}{\hbar\partial q} - \Omega_{qt}^{(n)}\right) = e\sum_n\int_{\mathrm{BZ}}\frac{\mathrm{d}q}{2\pi}\Omega_{qt}^{(n)}\,, \quad (4.24)$$

where $-e$ is the electron charge. Due to the periodicity of the Brillouin zone, $E_n(q,t)$ has the same value at both integration boundaries and the first integral vanishes.

The polarization density $\boldsymbol{P}(\boldsymbol{r})$ is connected to the current density $\boldsymbol{j}(\boldsymbol{r})$ via the equation $\boldsymbol{\nabla}\cdot\boldsymbol{P}(\boldsymbol{r}) = -\rho(\boldsymbol{r})$ and the continuity equation [Ashcroft&Mermin, Marder, Xiao(2010)],

$$\begin{aligned} & \partial_t(\boldsymbol{\nabla}\cdot\boldsymbol{P}(\boldsymbol{r})) = -\partial_t\rho(\boldsymbol{r}) \overset{(*)}{=} \boldsymbol{\nabla}\cdot\boldsymbol{j}(\boldsymbol{r}) \\ \Rightarrow \quad & \boldsymbol{\nabla}\cdot(\partial_t\boldsymbol{P}(\boldsymbol{r}) - \boldsymbol{j}(\boldsymbol{r})) = 0 \\ \Rightarrow \quad & \int_V \boldsymbol{\nabla}\cdot(\partial_t\boldsymbol{P}(\boldsymbol{r}) - \boldsymbol{j}(\boldsymbol{r})) = 0\,. \end{aligned} \tag{4.25}$$

In the last step, we integrate over an arbitrary volume V. Up to a divergence-free part[5], we find $\partial_t\boldsymbol{P}(\boldsymbol{r}) = \boldsymbol{j}(\boldsymbol{r})$. That is, the change of polarization $\Delta\boldsymbol{P}$ is given by

$$\begin{aligned} \Delta\boldsymbol{P}(\boldsymbol{r}) &= \int_0^T \partial_t\boldsymbol{P}(\boldsymbol{r})\mathrm{d}t = \int_0^T \boldsymbol{j}(\boldsymbol{r})\mathrm{d}t\,, \\ &= \int_{\lambda_i}^{\lambda_f} \frac{\partial\boldsymbol{P}(\boldsymbol{r})}{\partial t}\frac{\partial t}{\partial\lambda}\mathrm{d}\lambda = \int_{\lambda_i}^{\lambda_f} \partial_\lambda\boldsymbol{P}(\boldsymbol{r})\mathrm{d}\lambda\,, \end{aligned} \tag{4.26}$$

where we have substituted time t by some arbitrary but adiabatically varying parameter λ with $\lambda(0) = \lambda_i$ and $\lambda(T) = \lambda_f$. By inserting Eq. (4.24) into Eq. (4.26), we obtain the change of the polarization density [Mele(2002), Xiao(2010)],

$$\Delta P_i = e\sum_n \int_{\lambda_i}^{\lambda_f} \mathrm{d}\lambda \int_{\mathrm{BZ}} \frac{\mathrm{d}^D q}{(2\pi)^D}\Omega^{(n)}_{q_i\lambda}\,. \tag{4.27}$$

We have generalized to a system of dimension D, such that the i-th component of $\Delta\boldsymbol{P}$ is related to the i-th component of the wavevector $\boldsymbol{q}$ via $\Omega^{(n)}_{q_i\lambda}$. The factor $\partial_\lambda t$ that occurs in Eq. (4.26) cancels with $\partial_t\lambda$, which occurs in the Berry curvature upon substitution of t with λ in Eq. (4.22).

4.2. Derivation of Peierls' phase

A magnetic field $\boldsymbol{B}$ can be expressed in terms of a spatially varying vector potential $\boldsymbol{A}(\boldsymbol{r})$ that is typically respected by virtue of Peierls' substitution, i.e., redefinition of the momentum operator (see below). For tight-binding calculations which do not contain the momentum operator, the question arises how the magnetic field can be included in the model. Here, we explain how $\boldsymbol{A}(\boldsymbol{r})$ can be gauged away locally, with the result of a modified hopping amplitude $t_{ij}e^{i\phi}$ where ϕ is Peierls' phase [Peierls(1933), Bohm].

[5] According to [Xiao(2010)] and [Hirst(1997)], the divergence-free part is usually given by the magnetization current, which vanishes identically in the bulk.

4.2.1. Tight-binding model with modified Wannier states

Typical tight-binding models rely on Wannier states,

$$\begin{aligned} w_n(\boldsymbol{r}-\boldsymbol{R}_i) &= \langle \boldsymbol{r}|w_n(\boldsymbol{R}_i)\rangle \\ &= \frac{1}{\sqrt{N_s}}\sum_{\boldsymbol{q}} e^{-i\boldsymbol{q}\cdot\boldsymbol{R}_i}\psi_{\boldsymbol{q}}(\boldsymbol{r})\,, \end{aligned} \tag{4.28}$$

i.e., on superpositions of Bloch states $|\psi_{\boldsymbol{q}}(\boldsymbol{r})\rangle$. The number of sites is denoted by N_s. Due to the different phases $e^{i\boldsymbol{q}\cdot\boldsymbol{r}}$, the Bloch functions more and more cancel for larger and larger distances from $\boldsymbol{R}_i$. That is, the Wannier states are localized at lattice sites $\boldsymbol{R}_i$, which makes them suitable for tight-binding calculations [Nolting7, Bohm]. In the following, we shall use modified Wannier states

$$|\tilde{w}_n(\boldsymbol{R}_i)\rangle = e^{-ie\boldsymbol{A}(\boldsymbol{R}_i)\cdot\frac{\boldsymbol{r}-\boldsymbol{R}_i}{\hbar}}|w_n(\boldsymbol{R}_i)\rangle\,. \tag{4.29}$$

Because $|w_n(\boldsymbol{R}_i)\rangle$ is localized but still no eigenstate of the position operator $\boldsymbol{r}$, these modified states only form a non-orthogonal basis. However, the scalar product

$$\begin{aligned} \langle\tilde{w}_n(\boldsymbol{R}_i)|\tilde{w}_n(\boldsymbol{R}_j)\rangle &= \langle w_n(\boldsymbol{R}_i)|e^{ie\left(\boldsymbol{A}(\boldsymbol{R}_i)\cdot\frac{\boldsymbol{r}-\boldsymbol{R}_i}{\hbar}-\boldsymbol{A}(\boldsymbol{R}_j)\cdot\frac{\boldsymbol{r}-\boldsymbol{R}_j}{\hbar}\right)}|w_n(\boldsymbol{R}_j)\rangle \\ &= e^{ie\frac{\boldsymbol{A}(\boldsymbol{R}_j)\cdot\boldsymbol{R}_j-\boldsymbol{A}(\boldsymbol{R}_i)\cdot\boldsymbol{R}_i}{\hbar}}\underbrace{\langle w_n(\boldsymbol{R}_i)|e^{ie\frac{\boldsymbol{A}(\boldsymbol{R}_i)-\boldsymbol{A}(\boldsymbol{R}_j)}{\hbar}\cdot\boldsymbol{r}}|w_n(\boldsymbol{R}_j)\rangle}_{(*)} \end{aligned} \tag{4.30}$$

is still negligibly small for $\boldsymbol{R}_i \neq \boldsymbol{R}_j$

(i) if $|\boldsymbol{R}_i-\boldsymbol{R}_j| \gg \Delta_r$, where Δ_r is the width of the Wannier states $|w_n(\boldsymbol{R}_i)\rangle$;

(ii) or if $|\boldsymbol{R}_i-\boldsymbol{R}_j| \lesssim \Delta_r$ and $\frac{eB\Delta_r^2}{\hbar} \ll 1$.

In the latter case, the exponent in the expression $(*)$ is basically constant where the overlap is large and thus can be put in front of the expression. Since the last condition of (ii) becomes $B \ll \frac{\hbar}{e\Delta_r^2} \approx 10^4$ T for $\Delta_r = 2.5$ Å, the basis $\{|\tilde{w}_n(\boldsymbol{R}_i)\rangle\}_i$ can be treated as orthogonal for typical tight-binding calculations. In the following, we assume that always either condition (i) or condition (ii) holds. We can thus treat $\{|\tilde{w}_n(\boldsymbol{R}_i)\rangle\}_i$ as an orthonormal basis of spatially localized states. Let $\tilde{a}^\dagger_{n,i}$ ($\tilde{a}_{n,i}$) be the creation (annihilation) operator of the modified Wannier state given by Eq. (4.29). Suppose some Hamiltonian $\tilde{\mathcal{H}}$ — whose specific form does not matter at this stage — acts on a modified Wannier states. The resulting state can be expressed as follows,

$$\tilde{\mathcal{H}}|\tilde{w}_n(\boldsymbol{R}_i)\rangle = \sum_j \tilde{h}_n(\boldsymbol{R}_j-\boldsymbol{R}_i)|\tilde{w}_n(\boldsymbol{R}_j)\rangle\,. \tag{4.31}$$

The coefficients $\tilde{h}_n(\boldsymbol{R}_j - \boldsymbol{R}_i)$ can be interpreted as the hopping amplitudes $\tilde{t}_{ij}^{(n)}$ between sites i and j within the tight-binding model of modified Wannier states,

$$\begin{aligned}
\tilde{\mathcal{H}}\tilde{a}_{n,i}^\dagger|0\rangle &= \sum_j \tilde{h}_n(\boldsymbol{R}_j - \boldsymbol{R}_i)\tilde{a}_{n,j}^\dagger|0\rangle\,, \\
\Rightarrow\ \tilde{\mathcal{H}} &= \tilde{\mathcal{H}}\sum_i |\tilde{w}_n(\boldsymbol{R}_i)\rangle\langle\tilde{w}_n(\boldsymbol{R}_i)| = \sum_{i,j} \underbrace{\tilde{h}_n(\boldsymbol{R}_j - \boldsymbol{R}_i)}_{=:\tilde{t}_{ij}^{(n)}} |\tilde{w}_n(\boldsymbol{R}_j)\rangle\langle\tilde{w}_n(\boldsymbol{R}_i)| \\
&= \sum_{i,j} \tilde{t}_{ij}^{(n)}\tilde{a}_{n,j}^\dagger|0\rangle\langle 0|\tilde{a}_{n,i} = \sum_{i,j}\tilde{t}_{ij}^{(n)}\tilde{a}_{n,j}^\dagger\tilde{a}_{n,i}\,. \qquad (4.32)
\end{aligned}$$

For simplicity, we have only specified the initial and final states of the electron involved in the hopping, $|\tilde{w}_n(\boldsymbol{R}_i)\rangle$ and $|\tilde{w}_n(\boldsymbol{R}_j)\rangle$. Instead of $\boldsymbol{R}_i$ and $\boldsymbol{R}_j$, we may write $\boldsymbol{R}_{i,1}$ and $\boldsymbol{R}_{j,1}$ to specify the initial and final sites of the hopping electron. The sites of the $N-1$ electrons that do not hop, here, may be denoted as $\boldsymbol{R}_{i,2}$ through $\boldsymbol{R}_{i,N}$. Implicitly, the notation $|\tilde{w}_n(\boldsymbol{R}_i)\rangle$ refers to the complete state of N electrons, $|\tilde{w}_n(\boldsymbol{R}_{i,1}), \tilde{w}_n(\boldsymbol{R}_{i,2}), \ldots, \tilde{w}_n(\boldsymbol{R}_{i,N})\rangle$. By expressing these states with the according creation and annihilation operators, one finds the $N-1$-dimensional identity of the subspace not containing the hopping electron in the last line and the last equality becomes clear. An explicit demonstration can be found in [Nolting7].

For $\boldsymbol{A} = 0$, we can drop the tilde from the (un-)modified Wannier states and all other quantities, and Eq. (4.32) becomes the well-known tight-binding Hamiltonian for zero magnetic field, $\mathcal{H} = \sum_{i,j} t_{i,j}^{(n)} a_{n,j}^\dagger a_{n,i}$.

4.2.2. Peierls' substitution and phase

As mentioned before, within *Peierls' substitution*, the momentum $\boldsymbol{p} = \frac{\hbar}{i}\boldsymbol{\nabla}$ is replaced by an expression which includes the magnetic vector potential $\boldsymbol{A}(\boldsymbol{r})$,

$$\frac{\hbar}{i}\boldsymbol{\nabla} \mapsto \frac{\hbar}{i}\boldsymbol{\nabla} + e\boldsymbol{A}(\boldsymbol{r})\,. \qquad (4.33)$$

Acting this operator on a modified Wannier state, one finds

$$\begin{aligned}
\left(\frac{\hbar}{i}\boldsymbol{\nabla} + e\boldsymbol{A}(\boldsymbol{r})\right)|\tilde{w}_n(\boldsymbol{R}_i)\rangle &= e^{-ie\boldsymbol{A}(\boldsymbol{R}_i)\cdot\frac{\boldsymbol{r}-\boldsymbol{R}_i}{\hbar}}\left(\frac{\hbar}{i}\,\frac{-ie\boldsymbol{A}(\boldsymbol{R}_i)}{\hbar} + \frac{\hbar}{i}\boldsymbol{\nabla} + e\boldsymbol{A}(\boldsymbol{r})\right)|w_n(\boldsymbol{R}_i)\rangle \\
&\approx e^{ie\boldsymbol{A}(\boldsymbol{R}_i)\cdot\frac{\boldsymbol{r}-\boldsymbol{R}_i}{\hbar}}\,\frac{\hbar}{i}\boldsymbol{\nabla}|w_n(\boldsymbol{R}_i)\rangle\,, \qquad (4.34)
\end{aligned}$$

where the third term on the r.h.s. of the first equality approximately cancels with the first term if condition (ii) is valid, i.e. $\boldsymbol{A}(\boldsymbol{r}) \approx \boldsymbol{A}(\boldsymbol{R}_i)$ in the vicinity of $\boldsymbol{R}_i$, where $|w_n(\boldsymbol{R}_i)\rangle$ has its dominant contribution. To demonstrate the concept, we consider the Hamiltonian

$\tilde{\mathcal{H}} = \frac{p^2}{2m}$ such that for $\boldsymbol{A} = 0$, we get $\tilde{\mathcal{H}} = \mathcal{H} = \frac{-\hbar^2\Delta}{2m}$. With

$$\begin{aligned}
\tilde{\mathcal{H}}|\tilde{w}_n(\boldsymbol{R}_i)\rangle &= \frac{1}{2m}\left(\frac{\hbar}{i}\boldsymbol{\nabla} + e\boldsymbol{A}(\boldsymbol{r})\right)^2 |\tilde{w}_n(\boldsymbol{R}_i)\rangle \\
&\overset{(4.34)}{\approx} \frac{\frac{\hbar}{i}\boldsymbol{\nabla} + e\boldsymbol{A}(\boldsymbol{r})}{2m} e^{-ie\boldsymbol{A}(\boldsymbol{R}_i)\cdot\frac{\boldsymbol{r}-\boldsymbol{R}_i}{\hbar}} \frac{\hbar}{i}\boldsymbol{\nabla}|w_n(\boldsymbol{R}_i)\rangle \\
&= \frac{e^{-ie\boldsymbol{A}(\boldsymbol{R}_i)\cdot\frac{\boldsymbol{r}-\boldsymbol{R}_i}{\hbar}}}{2m}\left(\frac{\hbar}{i}\,\frac{-ie\boldsymbol{A}(\boldsymbol{R}_i)}{\hbar} + \frac{\hbar}{i}\boldsymbol{\nabla} + e\boldsymbol{A}(\boldsymbol{r})\right)\frac{\hbar}{i}\boldsymbol{\nabla}|w_n(\boldsymbol{R}_i)\rangle \\
&\approx e^{-ie\boldsymbol{A}(\boldsymbol{R}_i)\cdot\frac{\boldsymbol{r}-\boldsymbol{R}_i}{\hbar}}\,\frac{-\hbar^2\Delta}{2m}|w_n(\boldsymbol{R}_i)\rangle = e^{-ie\boldsymbol{A}(\boldsymbol{R}_i)\cdot\frac{\boldsymbol{r}-\boldsymbol{R}_i}{\hbar}}\mathcal{H}|w_n(\boldsymbol{R}_i)\rangle\,, \quad (4.35)
\end{aligned}$$

the action of the Hamiltonian with finite $\boldsymbol{A}$ on a state with finite $\boldsymbol{A}$ (l.h.s.) can be expressed in terms of these quantities with $\boldsymbol{A} = 0$ and an additional phase (r.h.s.). The second approximation is the same as the one used in Eq. (4.34). Using Eq. (4.31) for $\boldsymbol{A} = 0$ leads to

$$\begin{aligned}
\tilde{\mathcal{H}}|\tilde{w}_n(\boldsymbol{R}_i)\rangle &\overset{(4.35)}{\approx} e^{-ie\boldsymbol{A}(\boldsymbol{R}_i)\cdot\frac{\boldsymbol{r}-\boldsymbol{R}_i}{\hbar}} \sum_j \underbrace{\overbrace{h_n(\boldsymbol{R}_j - \boldsymbol{R}_i)}^{=t_{ij}^{(n)}}\overbrace{|w_n(\boldsymbol{R}_j)\rangle}^{\overset{(4.31)}{=}\mathcal{H}|w_n(\boldsymbol{R}_i)\rangle}}_{} \\
&= e^{-ie\boldsymbol{A}(\boldsymbol{R}_i)\cdot\frac{\boldsymbol{r}-\boldsymbol{R}_i}{\hbar}} \sum_j t_{ij}^{(n)} e^{ie\boldsymbol{A}(\boldsymbol{R}_j)\cdot\frac{\boldsymbol{r}-\boldsymbol{R}_j}{\hbar}}|\tilde{w}_n(\boldsymbol{R}_j)\rangle \\
&= \sum_j t_{ij}^{(n)} e^{i\frac{e}{\hbar}[(\boldsymbol{A}(\boldsymbol{R}_j)-\boldsymbol{A}(\boldsymbol{R}_i))\cdot\boldsymbol{r}+\boldsymbol{A}(\boldsymbol{R}_i)\cdot\boldsymbol{R}_i-\boldsymbol{A}(\boldsymbol{R}_j)\cdot\boldsymbol{R}_j]}|\tilde{w}_n(\boldsymbol{R}_j)\rangle\,. \quad (4.36)
\end{aligned}$$

For $|\boldsymbol{R}_i - \boldsymbol{R}_j| \gg \Delta_r$, the coefficients / hopping amplitudes $h_n(\boldsymbol{R}_j - \boldsymbol{R}_i) = t_{ij}^{(n)}$ can be neglected since the overlap of the involved Wannier states is basically zero[6]. Consequently, we focus on $|\boldsymbol{R}_i - \boldsymbol{R}_j| \cong \Delta_r$, and — if condition (ii) is valid — approximate the position operator with the mean of both lattice sites, $\boldsymbol{r} \approx \frac{\boldsymbol{R}_i+\boldsymbol{R}_j}{2}$. The square bracket in the

[6]Their rapid decay with increasing distance is why hopping amplitudes $t_{ij}^{(n)}$ between distant atoms are usually neglected in tight-binding calculations. In fact, many models rely on nearest neighbor hoppings only. The decay of the $t_{ij}^{(n)}$ is closely connected to the conditions (i) and (ii) at the beginning of this derivation. If condition (ii) applies, the effect of the magnetic field is small enough to capture it with the discussed approximations — at least for spatially close sites $\boldsymbol{R}_i$ and $\boldsymbol{R}_j$. If condition (i) applies, the approximations do actually not suffice, but this does not matter as the overlap and hence the hopping amplitude between the two sites can be neglected in this case.

exponent now becomes

$$\begin{aligned}
(\boldsymbol{A}(\boldsymbol{R}_j)-\boldsymbol{A}(\boldsymbol{R}_i))\cdot\overbrace{\frac{\boldsymbol{R}_i+\boldsymbol{R}_j}{2}}^{\approx\boldsymbol{r}}+\boldsymbol{A}(\boldsymbol{R}_i)\cdot\boldsymbol{R}_i-\boldsymbol{A}(\boldsymbol{R}_j)\cdot\boldsymbol{R}_j & \\
= \quad \boldsymbol{A}(\boldsymbol{R}_j)\cdot\frac{\boldsymbol{R}_j+\boldsymbol{R}_i-2\boldsymbol{R}_j}{2}+\boldsymbol{A}(\boldsymbol{R}_i)\cdot\frac{2\boldsymbol{R}_i-\boldsymbol{R}_i-\boldsymbol{R}_j}{2} & \\
= \quad (\boldsymbol{A}(\boldsymbol{R}_j)+\boldsymbol{A}(\boldsymbol{R}_i))\cdot\frac{\boldsymbol{R}_i-\boldsymbol{R}_j}{2}\,; & \\
\Rightarrow\ \tilde{\mathcal{H}}|\tilde{w}_n(\boldsymbol{R})\rangle \overset{(4.36)}{\approx} \sum_j t_{ij}^{(n)} e^{i\frac{e}{2\hbar}(\boldsymbol{A}(\boldsymbol{R}_i)+\boldsymbol{A}(\boldsymbol{R}_j))\cdot(\boldsymbol{R}_i-\boldsymbol{R}_j)}|\tilde{w}_n(\boldsymbol{R}_j)\rangle & \\
\approx \quad \sum_j t_{ij}^{(n)} e^{-i\frac{e}{\hbar}\int_{\boldsymbol{R}_i}^{\boldsymbol{R}_j}\boldsymbol{A}(\boldsymbol{r})\cdot\mathrm{d}\boldsymbol{r}}|\tilde{w}_n(\boldsymbol{R}_j)\rangle\,. & \qquad (4.37)
\end{aligned}$$

The last approximation relies on

$$\frac{\boldsymbol{A}(\boldsymbol{R}_i)+\boldsymbol{A}(\boldsymbol{R}_j)}{2}\cdot(\boldsymbol{R}_i-\boldsymbol{R}_j) \;=\; \int_{\boldsymbol{R}_j}^{\boldsymbol{R}_i}\frac{\boldsymbol{A}(\boldsymbol{R}_i)+\boldsymbol{A}(\boldsymbol{R}_j)}{2}\cdot\mathrm{d}\boldsymbol{r}\approx-\int_{\boldsymbol{R}_i}^{\boldsymbol{R}_j}\boldsymbol{A}(\boldsymbol{r})\cdot\mathrm{d}\boldsymbol{r}\,, \quad (4.38)$$

where $\mathrm{d}\boldsymbol{r}\parallel\boldsymbol{R}_j-\boldsymbol{R}_i$. The Hamiltonian

$$\begin{aligned}
\tilde{\mathcal{H}} \quad &= \quad \sum_i \tilde{\mathcal{H}}|\tilde{w}_n(\boldsymbol{R}_i)\rangle\langle\tilde{w}_n(\boldsymbol{R}_i)| \\
&\overset{(4.37)}{=} \quad \sum_{i,j} t_{ij}^{(n)} e^{-i\frac{e}{\hbar}\int_{\boldsymbol{R}_i}^{\boldsymbol{R}_j}\boldsymbol{A}(\boldsymbol{r})\cdot\mathrm{d}\boldsymbol{r}}\underbrace{|\tilde{w}_n(\boldsymbol{R}_j)\rangle\langle\tilde{w}_n(\boldsymbol{R}_i)|}_{=\tilde{a}_{n,j}^\dagger\tilde{a}_{n,i}} \\
&= \quad \sum_{i,j} t_{ij}^{(n)} e^{-i\frac{e}{\hbar}\int_{\boldsymbol{R}_i}^{\boldsymbol{R}_j}\boldsymbol{A}(\boldsymbol{r})\cdot\mathrm{d}\boldsymbol{r}}\tilde{a}_{n,j}^\dagger\tilde{a}_{n,i}\,, \qquad (4.39)
\end{aligned}$$

has exactly the form of Eq. (4.32) with

$$\tilde{t}_{ij}^{(n)}(\boldsymbol{A}) = t_{ij}^{(n)} e^{-i\frac{e}{\hbar}\int_{\boldsymbol{R}_i}^{\boldsymbol{R}_j}\boldsymbol{A}(\boldsymbol{r})\cdot\mathrm{d}\boldsymbol{r}}\,, \quad (4.40)$$

where the integral together with the prefactor $\frac{e}{\hbar}$ is known as *Peierls' phase* [Peierls(1933)]. Care must be taken for the direction of the hopping: the hopping amplitude from i to j is $\tilde{t}_{ij}^{(n)}$, but from j to i it is $\tilde{t}_{ji}^{(n)}=(\tilde{t}_{ij}^{(n)})^*$. If y can be parametrized in x and the Landau gauge $\boldsymbol{A}(\boldsymbol{r})=-By\boldsymbol{e}_x$ is used, Peierls' phase can be written as

$$\begin{aligned}
\frac{e}{\hbar}\int_{\boldsymbol{R}_i}^{\boldsymbol{R}_j}\boldsymbol{A}(\boldsymbol{r})\cdot\mathrm{d}\boldsymbol{r} \;&=\; -\frac{e}{\hbar}\int_{x_i}^{x_j}By(x)\mathrm{d}x=-\frac{eB}{\hbar}\int_{x_i}^{x_j}(\frac{\partial y}{\partial x}x+y_i)\mathrm{d}x \\
&=\; -\frac{eB}{\hbar}\left(\frac{\partial y}{\partial x}\frac{x_j^2-x_i^2}{2}+y_i(x_j-x_i)\right)=-\frac{eB}{\hbar}(x_j-x_i)\left(\frac{\partial y}{\partial x}\frac{x_j+x_i}{2}+y_i\right) \\
&=\; -\frac{eB}{2\hbar}(x_j-x_i)(y_j+y_i)\,. \qquad (4.41)
\end{aligned}$$

5. Acoustic phonons and spin relaxation in graphene nanoribbons

In this chapter, we present an adapted version of our manuscript that has been published in Physical Review B **84**, 155404 (2011).

Abstract

Phonons are responsible for limiting both the electron mobility and the spin relaxation time in solids and provide a mechanism for thermal transport. In view of a possible transistor function as well as spintronics applications in graphene nanoribbons, we present a theoretical study of acoustic phonons in these nanostructures. Using a two-dimensional continuum model which takes into account the monatomic thickness of graphene, we derive Hermitian wave equations and infer phonon creation and annihilation operators. We elaborate on two types of boundary configuration, which we believe can be realized in experiment: (i) fixed and (ii) free boundaries. The former leads to a gapped phonon dispersion relation, which is beneficial for high electron mobilities and long spin lifetimes. The latter exhibits an ungapped dispersion and a finite sound velocity of out-of-plane modes at the center of the Brillouin zone. In the limit of negligible boundary effects, bulk-like behavior is restored. We also discuss the deformation potential, which in some cases gives the dominant contribution to the spin relaxation rate T_1^{-1}.

5.1. Introduction

Its interesting electronic, mechanical, and thermal properties have made graphene a promising candidate for a wide range of applications, including ballistic transistors as well as [Novoselov(2004), Lin(2010), Lemme(2007)] spintronics and nanoelectromechanical devices and heat management [Trauzettel(2007), GarciaSanchez(2008), Balandin(2008), Nika(2009)]. There are, however, a number of challenges: (i) for epitaxial graphene, which is desirable for a controlled, large-scale production, the strong coupling to a substrate compromises these properties, (ii) graphene has no bandgap, a handicap for typical semiconductor applications, and (iii) acoustic phonons limit the carrier mobility relevant for transistor functions [Ouyang(2008), Finkenstadt(2007), Farmer(2009), Betti(2011), Yoon(2011)].

The first issue can be overcome by removing substrate material from underneath the carbon layer [Meyer(2007), Nair(2008), Bolotin(2008), Shivaraman(2009), Lima(2010)] such that a trench is formed and the electronic properties of free-standing graphene are restored. The second challenge is met by graphene nanoribbons (GNRs), graphene strips with a width at the nanometer scale (e.g., $L \sim 1\,\mu$m, $W \sim 30\,$nm) which can exhibit a bandgap [Wang(2011), Han(2007)]. Combining these advantages, the free-standing GNR obtained from epitaxial graphene on a trenched substrate is a very interesting design that deserves a detailed discussion of its phonons. In this paper, we use a continuum model to study the acoustic phonon properties and displacement fields $\boldsymbol{u}(\boldsymbol{r}) = (u_x, u_y, u_z)$ (out-of-plane modes shown in Fig. 5.1) of two different types of GNR that we think can be realized in experiment: (i) extended graphene that covers a thin trench, resulting in a GNR parallel to the trench and with fixed lateral boundaries, Fig. 5.2 (a); (ii) a strip of graphene that stretches over a wide trench, leading to a GNR perpendicular to the trench and with free lateral boundaries, Fig. 5.2 (b). For both setups, we derive the low-energy acoustic phonon spectra from a continuum model that respects the monatomic structure of graphene and write down the quantum mechanical form of these phonons.

Our results can be probed experimentally via established techniques like electron energy loss spectroscopy or Brillouin light scattering [Oshima(1988), Mohr(2007)]. In addition to the electron mobility, the phononic behavior is essential for carbon-based nanoelectromechanical systems [GarciaSanchez(2008), Steele(2009)]. A recent example where the electron-phonon coupling has been observed experimentally is the Franck-Condon blockade in suspended carbon nanotube quantum dots [Leturcq(2009)]. Phonons also give rise to spin relaxation within a time T_1, which is important for spintronics devices [Trauzettel(2007), Khaetskii(2001), Kuemmeth(2008), Struck(2010)]. The spin-orbit interaction admixes different spin states $(\uparrow, \downarrow)$ and electron orbits k [see Eq. (5.16) below]. As a consequence, the electron-phonon coupling $\mathcal{H}_{\mathrm{EPC}}$ can mediate the Zeeman energy $g\mu_B B = \hbar\omega$, where g is the electron g-factor in graphene and μ_B denotes Bohr's magneton, to the phonon bath with phonon numbers n_ω. The rate for spin relaxation via emission of a phonon with energy $\hbar\omega$ is given by

$$\frac{1}{T_1} = \frac{2\pi}{\hbar} |\langle k\downarrow, n_\omega + 1 | \mathcal{H}_{\mathrm{EPC}} | k\uparrow, n_\omega \rangle|^2 \rho_{\mathrm{states}}(\hbar\omega)\,, \tag{5.1}$$

with an explicit dependence on the phonon density of states ρ_{states}. Several mecha-

 Matthias Droth and Guido Burkard, Physical Review B **84**, 155404 (2011).

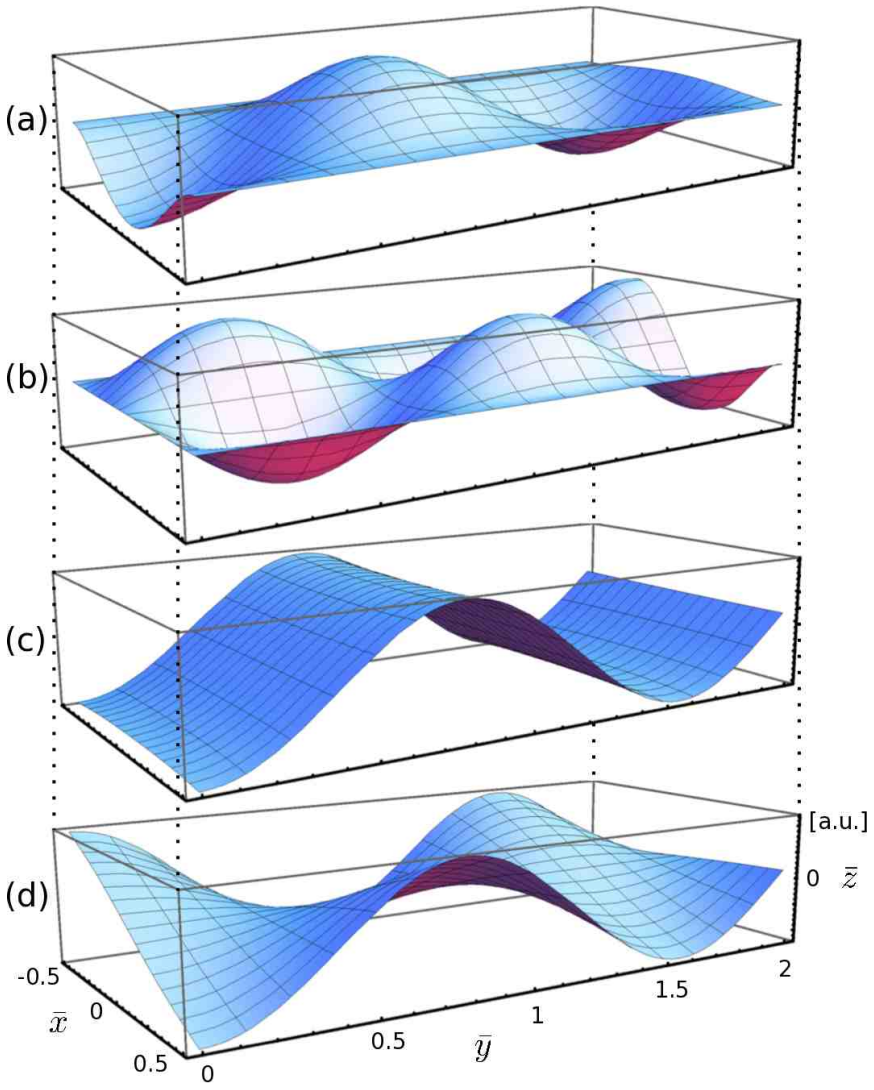

Figure 5.1.: Displacement field u_z of out-of-plane modes. The dimensionless coordinates are $\bar{x} = x/W$, $\bar{y} = y/W$, and $\bar{z} = z/W$. (a),(b) Fixed boundaries. (c),(d) Free boundaries. (a),(c) Fundamental mode. (b),(d) First overtone.

nisms contribute to T_1^{-1} and in some cases the deformation potential [Struck(2010), Mariani(2009)] gives the dominant contribution. If the Zeeman energy lies within the energy gap of GNR phonons with fixed boundaries and if the temperature is sufficiently low, the spin lifetime obtained from Eq. (5.1) diverges due to a vanishing density of states.

5.2. Continuum model in 2D

Low-energy acoustic phonons at the center of the Brillouin zone have a wavelength much larger than atomic distances and thus can be derived from continuum mechanics. The carbon atoms in graphene lie within a two-dimensional surface and this property is conserved upon deformations, making graphene a quasi two-dimensional material in three-

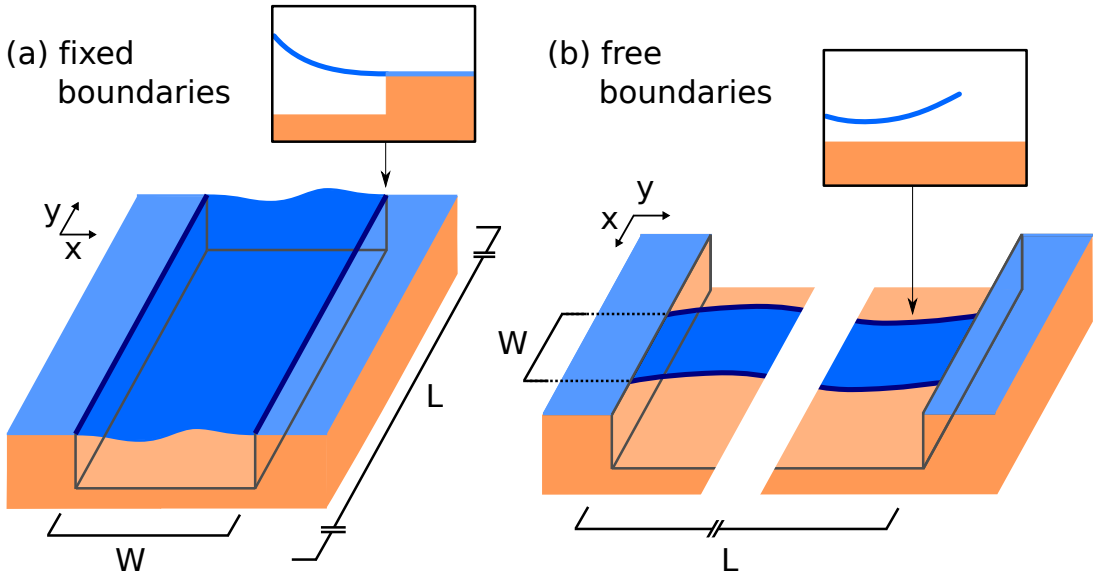

Figure 5.2.: Two nanoribbon configurations where graphene (blue) is spanned over a trenched substrate (orange): (a) fixed and (b) free boundaries. The coordinate system is chosen in such a way that the undeformed ribbon lies in the xy plane and that the y and ribbon axes coincide. We assume the ribbon length to be much larger than the ribbon width ($L \gg W$) and parallel lateral boundaries (dark blue) at $x = \pm W/2$.

dimensional (3D) real space. Consequently, all components of the displacement field $\boldsymbol{u}(\boldsymbol{r})$ can be nonzero but the components u_{iz} of the strain tensor $u_{ik} = (\partial_i u_k + \partial_k u_i)/2$ vanish identically. While u_{xz} and u_{yz} are known to vanish for thin plates in the xy plane in general, the monatomic thickness of graphene implies that u_{zz} must vanish as well. With $u_{iz} \equiv 0$, the elastic Lagrangian density of monolayer graphene is given by

$$\mathcal{L} = \mathcal{T} - \mathcal{V} = \frac{\rho}{2}\dot{\mathbf{u}}^2 - \frac{\kappa}{2}\left(\Delta u_z\right)^2 - \frac{\lambda}{2}u_{ii}^2 - \mu u_{ik}^2 \,, \tag{5.2}$$

where $\Delta = \partial_x^2 + \partial_y^2$, the sum convention with $u_{ii} = u_{xx} + u_{yy} + u_{zz}$ and $u_{ik}^2 = u_{xx}^2 + u_{xy}^2 + \cdots$ has been used, ρ is the surface mass density, and κ is the bending rigidity [Landau&Lifschitz, Suzuura(2002), Mariani(2008), Mariani(2009)]. Note that the 3D bulk elastic constants have been replaced by their 2D analogs $\lambda = 2h\mu_{3D}\lambda_{3D}/(2\mu_{3D} + \lambda_{3D})$ and $\mu = h\mu_{3D}$ where h is the plate thickness. The bulk and shear moduli are then given as $B = \lambda + \mu$ and μ, respectively.

Application of the Euler-Lagrange formalism to the functional (5.2) leads to the coupled set of differential equations for in-plane modes

$$\begin{aligned} \rho\,\ddot{u}_x &= (B+\mu)\partial_x^2 u_x + \mu\,\partial_y^2 u_x + B\,\partial_x\partial_y u_y \,, \\ \rho\,\ddot{u}_y &= (B+\mu)\partial_y^2 u_y + \mu\,\partial_x^2 u_y + B\,\partial_x\partial_y u_x \,, \end{aligned} \tag{5.3}$$

which are decoupled from the differential equation for the out-of-plane modes,

$$\rho\,\ddot{u}_z = -\kappa\left(\partial_x^2 + \partial_y^2\right)^2 u_z \,. \tag{5.4}$$

Matthias Droth and Guido Burkard, Physical Review B **84**, 155404 (2011).

Assuming nanoribbon alignment with the y-axis, fixed boundaries are described by

$$\begin{aligned} u_x = u_y &= 0 \qquad \text{(in plane)}, \\ u_z = \partial_x u_z &= 0 \qquad \text{(out of plane)} \end{aligned} \tag{5.5}$$

at $x = \pm W/2$; see Fig. 5.2 (a). While these boundary conditions hold for both 2D and 3D lattices, we emphasize that lattice dimensionality does affect free boundaries. For free edges in 2D it is required that, at $x = \pm W/2$,

$$\left.\begin{aligned} \partial_x u_x + \sigma \partial_y u_y &= 0 \\ \partial_x u_y + \partial_y u_x &= 0 \end{aligned}\right\} \quad \text{(in plane)},$$

$$\left.\begin{aligned} \partial_x^3 u_z + (2-\sigma)\partial_x \partial_y^2 u_z &= 0 \\ \partial_x^2 u_z + \sigma \partial_y^2 u_z &= 0 \end{aligned}\right\} \quad \text{(out of plane)}, \tag{5.6}$$

where the quantity σ denotes Poisson's ratio, Fig. 5.2 (b). Together with Young's modulus $\mathcal{E} = h\mathcal{E}_{3\mathrm{D}}$, σ relates to the bulk and shear moduli as

$$B = \frac{\mathcal{E}}{2(1-\sigma)}, \quad \mu = \frac{\mathcal{E}}{2(1+\sigma)}. \tag{5.7}$$

5.3. Classical solution

Typically, the length of a graphene nanoribbon exceeds its width many times, $L \gg W$ [Jiao(2009), Kosynkin(2009), Shivaraman(2009), Li(2008)], thus allowing for a plane wave ansatz along the y direction with periodic boundaries. Due to their decoupling, in-plane modes $u_{x/y}(x,y,t) = f_{x/y}(x)\exp[i(qy-\omega t)]$ and out-of-plane modes $u_z(x,y,t) = f_z(x)\exp[i(qy-\omega t)]$ can be treated separately[1].

Exploiting the plane wave ansatz and denoting the i-th derivative of f as $f^{(i)}$, Eq. (5.3) can be written as $\mathcal{M}_{xy}(f_x, f_y) = -\rho\omega^2(f_x, f_y)$, where

$$\mathcal{M}_{xy}\colon \begin{pmatrix} f_x \\ f_y \end{pmatrix} \mapsto \begin{pmatrix} (B+\mu) f_x^{(2)} - \mu q^2 f_x + iBq f_y^{(1)} \\ -(B+\mu) q^2 f_y + \mu f_y^{(2)} + iBq f_x^{(1)} \end{pmatrix}. \tag{5.8}$$

The general solution of this eigenvalue problem is given by $(f_x, f_y) = \sum_{i=1}^{4} c_i \boldsymbol{a}_i \exp[\lambda_i x]$, with $\boldsymbol{a}_1 = (1, iq/\lambda_1)$, $\boldsymbol{a}_2 = (1, iq/\lambda_2)$, $\boldsymbol{a}_3 = (1, i\lambda_3/q)$, $\boldsymbol{a}_4 = (1, i\lambda_4/q)$, and $\lambda_{1,2} = \pm\sqrt{q^2 - \rho\omega^2/(B+\mu)}$, $\lambda_{3,4} = \pm\sqrt{q^2 - \rho\omega^2/\mu}$.

Fixed boundaries are characterized by $f_x(\pm W/2) = f_y(\pm W/2) = 0$ and by virtue of the λ_i, the set of linear equations deriving from these boundary conditions depends on the parameters q and ω. A numerical treatment of this linear system yields the dispersion relation [Figs. 5.3 (a) and 5.3 (e)] as well as the coefficients c_i for the explicit form of the in-plane mode with fixed boundaries [Figs. 5.4 (a) and 5.4 (b)]. Other boundary conditions and the out-of-plane modes can be treated likewise.

[1] The physical displacement (see Figs. 5.1 and 5.4) is obtained by taking the real part.

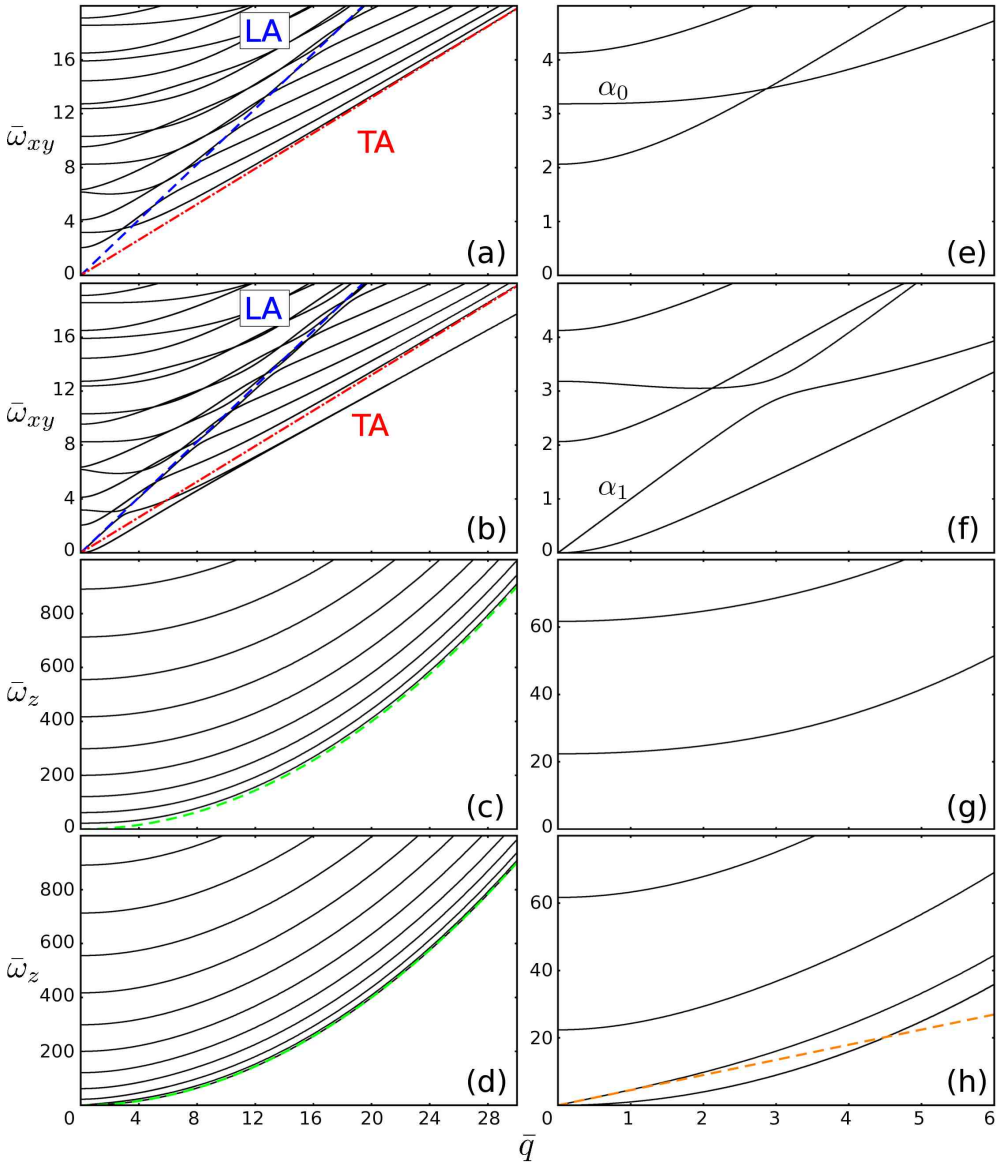

Figure 5.3.: Dispersion relations obtained from the procedure described in Sec. 5.3. The wavenumber q is given by $\bar{q} = qW$ and the frequency ω of in-plane (out-of-plane) phonons by $\bar{\omega}_{xy} = \omega\sqrt{\rho/\mathcal{E}}\,W$ ($\bar{\omega}_z = \omega\sqrt{\rho/\kappa}\,W^2$). (a) In-plane modes with fixed boundaries. (b) In-plane modes with free boundaries. (c) Out-of-plane modes with fixed boundaries. (d) Out-of-plane modes with free boundaries. (e)-(h) Dispersion relations (a)-(d) at the center of the Brillouin zone. (a),(c),(e),(g) Modes with fixed boundaries exhibit a gap. (b),(d),(f),(h) Modes with free boundaries are gapless. (a),(b) Despite the coupling of transverse and longitudinal modes, we find predominantly longitudinal and transverse modes on lines which we label LA (dashed blue line) and TA (dash-dotted red line), respectively. (c),(d) Independent of the boundaries, out-of-plane modes disperse quadratically for large wave numbers (dashed green line). (h) Free out-of-plane modes feature a branch with linear dispersion at the zone center (dashed orange line).

 Matthias Droth and Guido Burkard, Physical Review B **84**, 155404 (2011).

The eigenvalue problem obtained from Eq. (5.4) is $\mathcal{M}_z f_z = (\rho\omega^2/\kappa - q^4) f_z$, where the map $\mathcal{M}_z$ and its eigenfunctions and eigenvalues are given by

$$\mathcal{M}_z : \; f_z \mapsto f_z^{(4)} - 2q^2 f_z^{(2)} \tag{5.9}$$

and $f_z = \sum_{i=1}^{4} d_i e^{\lambda_i x}$ with $\lambda_i = \pm\sqrt{q^2 \pm \omega\sqrt{\rho/\kappa}}$.

5.4. Mode orthonormality and quantization

In order to quantize the vibrational spectrum of the graphene nanoribbon in terms of phonon creation and annihilation operators, the eigenfunctions of the original differential operators [Eqs. (5.3) and (5.4)] must be orthogonal. While orthogonality of eigenmodes with different wavenumbers q follows from the plane wave ansatz, eigenmodes with same q require orthogonal functions $(f_{(\alpha,q),x},\, f_{(\alpha,q),y})$ and $f_{(\alpha,q),z}$. The index (α, q) labels the phonon branch α and the wavenumber q of a specific eigenmode.

The map (5.8) is Hermitian and hence has orthogonal eigenfunctions if and only if the scalar product $\int_{-W/2}^{+W/2} \mathrm{d}x \left(f_x^*, f_y^*\right) \mathcal{M}_{xy} (f_x, f_y)^{\mathrm{T}}$ is real for all vector functions (f_x, f_y) in the domain of $\mathcal{M}_{xy}$. One easily shows via partial integration that $\mathcal{M}_{xy}$ is Hermitian if and only if the boundary terms satisfy

$$(B+\mu) f_x^* f_x^{(1)} + \mu f_y^* f_y^{(1)} + iBq f_x^* f_y \big|_{-\frac{W}{2}}^{+\frac{W}{2}} \in \mathbb{R} \tag{5.10}$$

and that both fixed and free boundaries do indeed satisfy this condition. The general in-plane displacement field is

$$\boldsymbol{u}_{\parallel} = \sum_{\alpha,q} r_{(\alpha,q)} \left(f_{(\alpha,q),x} \boldsymbol{e}_x + f_{(\alpha,q),y} \boldsymbol{e}_y \right) e^{iqy} \,, \tag{5.11}$$

where the harmonic time dependence has been absorbed in the normal coordinate. Using the orthogonality relations mentioned above, one can resolve the normal coordinate and derive the Lagrangian and the canonical momentum. The identification

$$r_{(\alpha,q)} = \sqrt{\hbar/2\rho LW\omega_{(\alpha,q)}} (b_{(\alpha,q)} + b_{(\alpha,-q)}^{\dagger}) \,, \tag{5.12}$$

where $b_{(\alpha,q)}^{\dagger}$ ($b_{(\alpha,q)}$) creates (annihilates) an (α, q)-phonon, complies with coordinate-momentum commutation relations, and allows for a quantum mechanical formulation of Eq. (5.11). Quantization of the out-of-plane modes is achieved in the very same way. The Hermiticity of $\mathcal{M}_z$ follows from

$$f_z^* f_z^{(3)} - f_z^{*(1)} f_z^{(2)} - 2q^2 f_z^* f_z^{(1)} \big|_{-\frac{W}{2}}^{+\frac{W}{2}} \in \mathbb{R} \tag{5.13}$$

and, as above, fixed as well as free boundaries do satisfy this condition. The general out-of-plane displacement is given by

$$\boldsymbol{u}_{\perp} = \sum_{\alpha,q} r_{(\alpha,q)} f_{(\alpha,q),z} \boldsymbol{e}_z e^{iqy} \,. \tag{5.14}$$

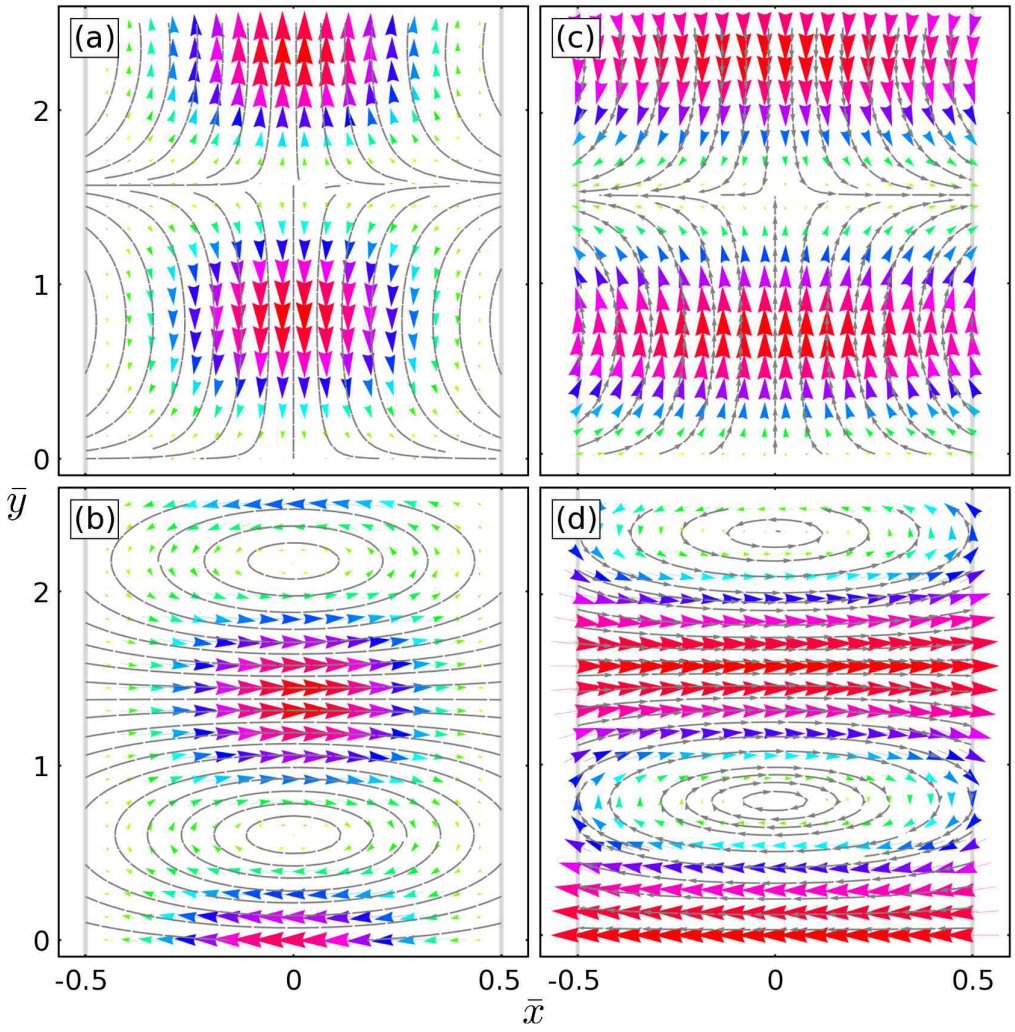

Figure 5.4.: Displacement vector field (u_x, u_y) of in-plane modes. Size and color of the arrows indicate the magnitude of the local deformation. We use the dimensionless coordinates $\bar{x} = x/W$ and $\bar{y} = y/W$. (a),(b) Fixed boundaries. (c),(d) Free boundaries. (a),(c) Predominantly longitudinal modes. (b),(d) Predominantly transverse modes.

5.5. Discussion of phonon spectra

As specific values for sound velocities, etc., depend on the elastic constants, we shall first discuss these constants before turning to the properties of acoustic phonons. Due to their decoupling, in-plane and out-of-plane phonons can be treated separately. For each case we will consider fixed and free boundaries.

5.5.1. Elastic constants

For graphene, most elastic constants remain to be settled by experiment and some seem to exhibit a temperature dependence, which we do not take into account here. Moreover,

Matthias Droth and Guido Burkard, Physical Review B **84**, 155404 (2011).

a consistent set of constants must respect Eq. (5.7). The Zeeman energy for typical laboratory magnetic fields ($\sim 1\,\mathrm{T}$) marks $\sim 1\,\mathrm{K}$ as the temperature range where the phonon properties can be probed via electron spin relaxation.

Cited values for Poisson's ratio σ of graphene range from 0.145 to 0.416 [Reddy(2006)] but accumulate around $\sigma = 0.16$, which we use in our calculations [Lee(2008), Faccio(2009), Kudin(2001)]. Young's modulus of a quasi two-dimensional material, $\mathcal{E} = \mathcal{E}_{3\mathrm{D}} h$, follows from its corresponding 3D bulk value and its associated thickness h. While the most common literature value of $\mathcal{E}_{3\mathrm{D}}$ for graphene is 1 TPa [Lee(2008), Faccio(2009), Kudin(2001)], a much smaller value, 0.5 TPa, has been found in at least one experiment [Frank(2007)]. We use $\mathcal{E} = 3.4\,\mathrm{TPa\AA}$, the product of 1 TPa and the interlayer spacing of graphite, 3.4 Å. Substituting our choices for σ and $\mathcal{E}$ into Eq. (5.7), we find $B = 12.6\,\mathrm{eV/\AA^2}$ and $\mu = 9.1\,\mathrm{eV/\AA^2}$ for the bulk and shear moduli, respectively, in agreement with literature values [Gazit(2009), Kudin(2001)]. All these values are in agreement with results of simulations for zero temperature [Zakharchenko(2011)].

The bending rigidity of graphene, κ, is mainly determined by the out-of-plane p_z orbitals such that it cannot be inferred from other elastic constants. It has been shown that κ decreases with increasing temperature [Liu(2009)]. Literature values for zero temperature range from 0.85 to 1.22 eV and we choose $\kappa = 1.1\,\mathrm{eV}$ [Fasolino(2007), Gazit(2009), Liu(2009), Kudin(2001)].

The mass density of graphene, $\rho = 7.61 \times 10^{-7}\,\mathrm{kg/m^2}$, follows directly from the atomic weight of natural carbon, 12.01 u, and the interatomic distance in graphene, 1.42 Å.

5.5.2. In-plane phonons

The dispersion relation of in-plane modes with fixed boundaries is gapped and features infinitely many branches with different energies originating from the zone center, Figs. 5.3 (a) and 5.3 (e). The gap relates to the energy necessary for fixing the boundaries and is given by $2.1\,\hbar\sqrt{\mathcal{E}/\rho}\,/W$. For $W = 30\,\mathrm{nm}$, this gap will be 1.0 meV, corresponding to a magnetic field of 8.4 T. For large wave numbers, all branches converge to a common line, which we label TA. A second line, labeled LA, is supported by different branches throughout the dispersion relation. Due to coupling at the ribbon boundaries there are no purely transverse or longitudinal modes. However, we do find that the modes on the TA (LA) line have predominantly transverse (longitudinal) character, Figs. 5.4 (a) and 5.4 (b). The corresponding sound velocities are $v_{\mathrm{LA}} = 22\,\mathrm{km/s}$ and $v_{\mathrm{TA}} = 14\,\mathrm{km/s}$, independent of the ribbon width. These values and the ratio $v_{\mathrm{LA}}/v_{\mathrm{TA}} = 1.6$ are in good agreement with previous calculations for bulk graphene (19.5 km/s, 12.2 km/s) [Falkovsky(2008)] and carbon nanotubes (19.9 km/s, 12.3 km/s) [Suzuura(2002)]. Nevertheless, we point out that our sound velocities are proportional to $\sqrt{\mathcal{E}/\rho}$, a value that is still under discussion for graphene. The approach to linear, bulk-like behavior is expected for large wave numbers, where the finite ribbon width appears like bulk for short-wavelength phonons.

For free boundaries, the dispersion relation of in-plane modes is ungapped and the two branches that start at zero energy converge slightly below the TA line, Figs. 5.3 (b) and 5.3 (f). The sound velocities and linear behavior for large wave number do not

depend on boundary conditions, as one would expect from the same argument as above. Predominantly transverse and predominantly longitudinal modes are shown in Figs. 5.4 (c) and 5.4 (d). The typical zero-point motion amplitude of in-plane modes is 40 fm.

5.5.3. Out-of-plane phonons

The dispersion relation of out-of-plane modes with fixed boundaries is shown in Figs. 5.3 (c) and 5.3 (g). The gap due to the fixed boundary conditions is given by $22.4\,\hbar\sqrt{\kappa/\rho}\,/W^2$, which yields $7.9\,\mu$eV for $W = 30\,$nm. The corresponding magnetic field is 68 mT. There are infinitely many branches that correspond to different transverse excitations, Figs. 5.1 (a) and 5.1 (b). Again, away from the zone center, all branches approach bulk behavior, that is, a quadratic dispersion for out-of-plane modes [Falkovsky(2008)].

Similarly, the out-of-plane modes with free boundaries disperse quadratically as in the bulk, for large wave numbers, Figs. 5.3 (d) and 5.3 (h). The dispersion relation is gapless and one branch exhibits a finite sound velocity at the zone center. This sound velocity amounts to about 70 m/s for $W = 30\,$nm, is proportional to $\sqrt{\kappa/\rho}\,/W$, and hence goes to zero for large W, again in agreement with bulk graphene. The typical zero-point motion amplitude of out-of-plane modes is 0.4 pm.

5.6. Deformation potential and spin relaxation

Several mechanisms contribute to spin relaxation: out-of-plane modes via direct spin-phonon coupling and in-plane phonons via the deformation potential and bond-length change [Struck(2010)]. Due to inversion symmetry, piezoelectric coupling does not occur in graphene. Here, we discuss the deformation potential, which gives the dominant contribution to T_1^{-1} under certain conditions.

We find that any given in-plane phonon branch α couples either via bond-length change or via the deformation potential, depending on whether its displacement field is even or odd in the x coordinate[2]. The branch that originates from $\bar{\omega}_{xy} = 3.2$ in Fig. 5.3 (e), labeled α_0, has a flat dispersion at the zone center and couples to the spin only via the deformation potential[2]. As a consequence of the density of states in Eq. (5.1), this mechanism will give the dominant contribution if the magnetic field is tuned to a value where the Zeeman energy is close to the Van Hove singularity of α_0 and coupling to out-of-plane modes is weak. Van Hove singularities also occur for out-of-plane modes at different values of $\bar{\omega}_z$, Figs. 5.3 (c) and 5.3 (g). However, $\bar{\omega}_{xy}$ and $\bar{\omega}_z$ scale differently with W, which allows us to choose a ribbon width where there is a singularity for in-plane modes (α_0) but not for out-of-plane modes. This situation will be discussed below.

[2] After publication of this work, we have found that, in fact, both the deformation potential and the bond-length change couple only to branches with a displacement field odd in x. In lowest order, even branches do not give rise to electron-phonon coupling. Up to certain special cases that do not matter, here, the deformation potential is the dominant coupling on the odd branches α_0 and α_1 [Droth(2013)].

Matthias Droth and Guido Burkard, Physical Review B **84**, 155404 (2011).

For the branch labeled α_1 in Fig. 5.3 (f), which is linear near the zone center, the spin couples to phonons only via the deformation potential, as well[2]. Even though its density of states is finite, we discuss its contribution to Eq. (5.1) as it is in accordance with previous results for semiconductor quantum dots [Khaetskii(2001)].

In leading order, the deformation potential depends only on in-plane phonons,

$$\mathcal{H}_{\mathrm{EPC}} = g_{\mathrm{D}} \boldsymbol{\nabla} \cdot \boldsymbol{u}_{\parallel}(x,y)\,, \tag{5.15}$$

where $g_D \approx 30\,\mathrm{eV}$ is the coupling strength [Struck(2010), Suzuura(2002)] and $\boldsymbol{\nabla} = (\partial_x, \partial_y)$. The deformation potential is independent of the electron spin $(\uparrow,\downarrow)$ but it does couple different electron orbits (k). As a consequence, $\mathcal{H}_{\mathrm{EPC}}$ couples to spin indirectly when Rashba-type spin-orbit interaction, $\mathcal{H}_R$, is taken into account. In lowest order, the spin-orbit-perturbed electronic states are given by

$$|k\uparrow\rangle = |k\uparrow\rangle^{(0)} + \sum_{k'\neq k} |k'\downarrow\rangle^{(0)} \frac{{}^{(0)}\langle k'\downarrow|\mathcal{H}_R|k\uparrow\rangle^{(0)}}{E_k - E_{k'} + g\mu_B B}\,, \tag{5.16}$$

where the superscript (0) indicates unperturbed product states. Using these spin-orbit admixed states, we find

$$\begin{aligned} &\langle k\downarrow|\mathcal{H}_{\mathrm{EPC}}|k\uparrow\rangle \\ &= \sum_{k'\neq k} \left[\frac{(\mathcal{H}_{\mathrm{EPC}})_{kk'}(\mathcal{H}_R)^{\downarrow\uparrow}_{k'k}}{E_k - E_{k'} + g\mu_B B} + \frac{(\mathcal{H}_{\mathrm{EPC}})_{k'k}(\mathcal{H}_R)^{\downarrow\uparrow}_{kk'}}{E_k - E_{k'} - g\mu_B B} \right], \end{aligned} \tag{5.17}$$

where we denote the numerator in Eq. (5.16) as $(\mathcal{H}_R)^{\downarrow\uparrow}_{k'k}$ and the spin-conserving transitions of $\mathcal{H}_{\mathrm{EPC}}$ accordingly. This is the matrix element required to calculate the relaxation rate in Eq. (5.1).

We find that for a given k', the two terms in Eq. (5.17) exactly cancel each other at $B = 0$. This effect is known as Van Vleck cancellation and is expected for time-reversal-symmetric systems. Moreover, $(\mathcal{H}_R)^{\downarrow\uparrow}_{k'k}$ vanishes if both k and k' are even or odd at the same time.

For fixed GNR edges, the phonon spectrum is gapped. In the range $3.2 \leq \bar{\omega}_{xy} \leq 3.3$, the branch α_0 shows an almost flat dispersion[3]. Its sound velocity increases as $v_{\alpha_0} \propto q^2$ such that the corresponding density of states behaves as $(\rho_{\mathrm{states}})_{\alpha_0} \propto q^{-2}$. The matrix element (5.17) varies as $q\,B^{0.5}$: the dipole approximation gives rise to one order in q and Van Vleck cancellation to one order in B [VanVleck(1940), Trauzettel(2007), Struck(2010), Droth(2010)], reduced by $\omega^{-0.5} \propto B^{-0.5}$ due to the prefactor in Eq. (5.12). In total, the contribution to the spin relaxation rate given by Eq. (5.1) is proportional to the magnetic field. Due to the Van Hove singularity of α_0 at $\bar{\omega}_{xy} = 3.2$, we expect that $T_1^{-1} \propto B$ is the dominant behavior in the range $3.8 \leq B \leq 4.0\,\mathrm{T}$ ($12.8 \leq B \leq 13.2\,\mathrm{T}$) for $W = 100\,\mathrm{nm}$ ($W = 30\,\mathrm{nm}$), where the density of states of out-of-plane modes is relatively small. These are accessible laboratory magnetic fields and hence allow for experimental examination of our results.

[3]After publication of this work, we have found that instead of α_0, only the branch originating at $\bar{\omega}_{xy} \approx 2$ yields a finite coupling. The subsequent discussion on $T_1^{-1} \propto B$ does not apply for α_0, see section VII B in [Droth(2013)].

If the magnetic field is tuned to a value where the Zeeman energy lies within the gap of both in-plane and out-of-plane phonons [Figs. 5.3 (e) and 5.3 (g)], the electron spin cannot flip due to phonon emission. Then, multiple-phonon processes, where the Zeeman energy corresponds to the difference between an absorbed and an emitted phonon, become important. Again due to the gap, these processes can be frozen out if the temperature T is low enough. As discussed in Sec. 5.5, the very soft out-of-plane modes have a much smaller gap, which therefore imposes a tighter condition and which scales as W^{-2}. Assuming $W = 30\,\mathrm{nm}$, the spin lifetime inferred from Eq. (5.1) diverges for $B < 68\,\mathrm{mT}$ and $T \ll 90\,\mathrm{mK}$. Very narrow GNRs with $W = 10\,\mathrm{nm}$ are studied experimentally, as well [Wang(2011)]. Accordingly, the requirements for such a ribbon would be $B < 0.61\,\mathrm{T}$ and $T \ll 0.8\,\mathrm{K}$.

GNRs with free edges have ungapped phonon spectra. Due to energy conservation, the Zeeman energy must match the phonon energy, such that only the two lowest branches in Fig. 5.3 (f) are accessible for low magnetic fields ($B \lesssim 100\,\mathrm{mT}$). The branch α_1 couples only via the deformation potential and the other branch is a pure shear mode. Due to its linear dispersion, we find $B \propto \omega \propto q$ and a constant density of states for α_1. The matrix element in Eq. (5.17) scales as $B^{2.5}$: one order in B arising each from the Van Vleck cancellation, dipole approximation, and the gradient[4] in Eq. (5.15), again reduced by the prefactor $\omega^{-0.5} \propto B^{-0.5}$ in Eq. (5.12). Consequently, for low magnetic fields, the contribution of deformation potential and spin-orbit coupling to the spin relaxation rate given by Eq. (5.1) scales with B^5. In semiconductors, $T_1^{-1} \propto B^5$ holds, as well [Khaetskii(2001)].

5.7. Conclusion

Acoustic phonons are relevant for many GNR applications and can be probed with established techniques [Oshima(1988), Mohr(2007)]. Using a continuum model that accounts for the monatomic thickness of graphene, we derive boundary conditions that lead to Hermitian wave equations. We focus on two types of boundary configurations: fixed and free boundaries. We explicitly give the corresponding classical solutions and, ensuring Hermiticity, infer a quantum theory with ribbon phonon creation and annihilation operators. Free boundaries lead to ungapped dispersion relations. In contrast, fixed boundaries lead to a gapped phonon dispersion of both in-plane and out-of-plane modes, which is most suitable for achieving high mobilities as well as long spin lifetimes. Regardless of the boundary configuration, all dispersion relations approach bulk behavior for wavelengths small compared to the ribbon width. Sound velocities that relate to transverse and longitudinal acoustical in-plane ribbon modes are in good accordance with values for bulk graphene. We also study phonon-induced spin relaxation in GNRs. We find that, if the Zeeman energy is tuned close to a Van Hove singularity of the density of states of in-plane phonons, the deformation potential can be the dominant effect for spin relaxation. In this case, it should be possible to probe our predicted behavior for T_1 experimentally. If the Zeeman energy lies within the gap of both in-plane and out-of-plane phonons with fixed boundaries and for low enough temperatures, coupling to the lattice is inhibited such that the spin lifetime obtained from Eq. (5.1) diverges.

[4] In the case of α_0, the gradient only gives a constant as $\lambda_i \propto \omega \approx$ const., there.

Matthias Droth and Guido Burkard, Physical Review B **84**, 155404 (2011).

6. Electron spin relaxation in graphene nanoribbon quantum dots

In this chapter, we present an adapted version of our manuscript that has been published in Physical Review B **87**, 205432 (2013).

Abstract
Graphene is promising as a host material for electron spin qubits because of its predicted potential for long coherence times. In armchair graphene nanoribbons (aGNRs) a small bandgap is opened, allowing for electrically gated quantum dots, and furthermore the valley degeneracy is lifted. The spin lifetime T_1 is limited by spin relaxation, where the Zeeman energy is absorbed by lattice vibrations, mediated by spin-orbit and electron-phonon coupling. We have calculated T_1 by treating all couplings analytically and find that T_1 can be in the range of seconds for several reasons: (i) low phonon density of states away from Van Hove singularities; (ii) destructive interference between two relaxation mechanisms; (iii) Van Vleck cancelation at low magnetic fields; (iv) vanishing coupling to out-of-plane modes in lowest order due to the electronic structure of aGNRs. Owing to the vanishing nuclear spin of ^{12}C, T_1 may be a good measure for overall coherence. These results and recent advances in the controlled production of graphene nanoribbons make this system interesting for spintronics applications.

6.1. Introduction

Graphene has attracted intense scientific interest for its mechanical, electronic, and other properties [Wallace(1947), Novoselov(2005), Nair(2008), Meyer(2007)]. Within the plane of its two-dimensional lattice it is extremely rigid while out-of-plane deformations are relatively soft due to the lack of a linear restoring force [Fasolino(2007), Gazit(2009)]. The absence of a bandgap leads to a quasi-relativistic behavior of the electrons that can be described by a Dirac-like Hamiltonian [Katsnelson(2006), CastroNeto(2009)]. However, for typical semiconductor applications like transistors or spintronics devices, it is favorable to work with a bandgap [Novoselov(2004), Farmer(2009), Hanson(2007), Trauzettel(2007)]. Due to Klein's paradox, a bandgap is necessary to confine charge carriers electrostatically in graphene [Klein(1929), Katsnelson(2006)]. There are different situations that lead to a bandgap in graphene and some of them have already been studied in view of spintronics applications [Trauzettel(2007), Recher(2010)].

Armchair graphene nanoribbons (aGNRs) can exhibit a bandgap and in addition allow for coupling of qubits in non-adjacent quantum dots (QDs) [Brey(2006), Han(2007), Braun(2011)]. Such a non-local coupling of qubits is ideal for fault-tolerant quantum computing and thus for scalability [Trauzettel(2007), Svore(2005)]. Over the past years, there has been substantial progress towards the goal of controlling the GNR edge termination within the production process and the controlled production of aGNRs might become feasible in the near future [Jiao(2009), Wang(2011), Zhang(2013)].

Spintronics applications like the Loss-DiVincenzo quantum computer require spin coherence times much longer than typical operation times [Loss(1998), DiVincenzo(1998)]. When the qubit is represented by the real electron spin, carbon materials are considered promising due to the small atomic spin-orbit coupling and weak interaction with nuclear spins in carbon [Trauzettel(2007), Bulaev(2008), Struck(2010)]. While the curvature significantly enhances intrinsic spin-orbit coupling and hence spin relaxation in carbon nanotubes, this effect should not occur in flat graphene [Kane(2005), Min(2006), Bulaev(2008), Kuemmeth(2008), Gmitra(2009)]. The natural abundance of ^{13}C, the only stable carbon isotope with a finite nuclear spin $I = 1/2$ is only 1%. The concentration of nuclear spins can be further decreased by depleting this isotope. For magnetic fields above the 10 mT-regime, flip-flop processes between nuclear spins and electronic spins become suppressed due to the different magnetic moments, $\mu_\mathrm{B} \gg \mu_\mathrm{nuc}$. We expect that T_2 is dominated by T_1 and that the spin relaxation time is a good measure for overall coherence, $T_1 \approx T_2/2$.

In this paper, we calculate the spin relaxation time T_1 for electrons that are confined in an aGNR QD. The finite width of the quasi one-dimensional aGNR leads to confinement in the transverse (x-) direction. As we will discuss in Sec. 6.3, aGNRs of appropriate width have a bandgap. This allows to avoid Klein's paradox and confine electrons in the longitudinal (y-) direction by means of an electrostatic potential $V(y)$. In a perpendicular magnetic field $B\boldsymbol{e}_z$, the two possible spin states of an electron inside the QD are split by the Zeeman energy $g\mu_\mathrm{B}B = \hbar\omega$, where $g = 2$ is the electron g-factor. Fig. 6.1 shows a sketch of the system.

Due to energy conservation, the Zeeman energy must be transferred to the lattice upon

 Matthias Droth and Guido Burkard, Physical Review B **87**, 205432 (2013).

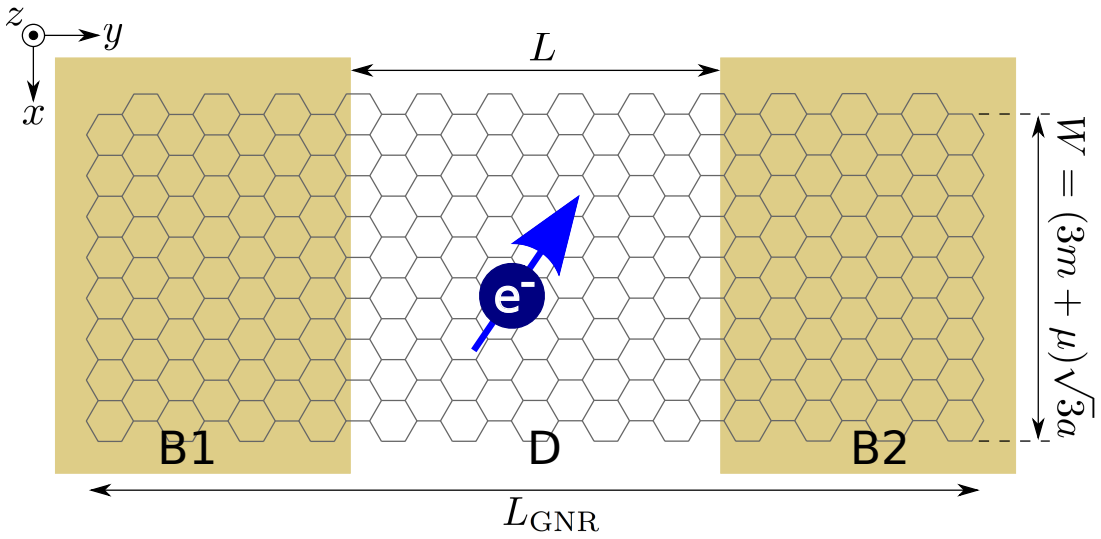

Figure 6.1.: Sketch of the system and definition of the coordinate frame. The GNR has armchair terminations in the x-direction. The width of the sketched aGNR is characterized by $m = 3$ and $\mu = -1$ which leads to a bandgap that allows for electrostatic confinement in the y-direction. The potential $V(y)$ defines the two barrier regions B1, B2 (shaded) and the dot region D, that lies symmetrically between the barrier regions. The interatomic distance in graphene is $a = 1.42\,\text{Å}$.

spin relaxation. For typical lab magnetic fields $B \lesssim 20\,\text{T}$, the Zeeman energy corresponds to low-energy acoustic phonons at the center of the Brillouin zone [Droth(2011)]. We consider two cases separately: (i) free and (ii) fixed boundaries. The electron-phonon coupling $\mathcal{H}_{\text{EPC}}$ comprises the deformation potential as well as the bond-length change and couples in-plane vibrational modes to the electronic state. By including the spin-orbit interaction $\mathcal{H}_{\text{SOI}}$, the spin thus becomes connected to the vibrational state of the system. The coupling to the out-of-plane modes is considered, as well. Yet such a coupling either vanishes identically due to the electronic structure in aGNRs or appears only in higher order.

This paper is organized as follows: In Sec. 6.2, we present our model and in Sec. 6.3, we recapitulate the bound states of aGNR QDs and explain the extended, quasi continuous states. Acoustic GNR phonons are shortly reviewed in Sec. 6.4. The effective spin-phonon coupling mechanisms that lead to T_1^{-1} via Fermi's golden rule are clarified in Sec. 6.5. In Sec. 6.6, we comment on the actual evaluation of T_1. The results are presented in Sec. 6.7 and discussed in Sec. 6.8.

6.2. Model

The Hamiltonian of the system is

$$\mathcal{H} = \mathcal{H}_{\text{elec}} + \mathcal{H}_{\text{phon}} + \mathcal{H}_{\text{SOI}} + \mathcal{H}_{\text{EPC}}\,, \tag{6.1}$$

where $\mathcal{H}_{\text{elec}}$ and $\mathcal{H}_{\text{phon}}$ describe the unperturbed electronic system and the unperturbed vibrational system, respectively. The spin-orbit interaction $\mathcal{H}_{\text{SOI}}$ leads to an admixture of opposite spin states such that the electron phonon coupling $\mathcal{H}_{\text{EPC}}$ can induce a spin flip. Denoting the Fermi velocity by v_{F} and the pseudospin by $\boldsymbol{\sigma}$, the unperturbed electronic part of the system obeys the Hamiltonian

$$\mathcal{H}_{\text{elec}} = -i\hbar v_{\text{F}} \begin{pmatrix} \sigma_x\partial_x + \sigma_y\partial_y & 0 \\ 0 & -\sigma_x\partial_x + \sigma_y\partial_y \end{pmatrix} + V(y) \tag{6.2}$$

with eigenstates $|k\rangle$. The pure vibrational modes are described by

$$\mathcal{H}_{\text{phon}} = \sum_{\alpha,q} \hbar\omega_{\alpha,q} \left(n_{\alpha,q} + \frac{1}{2} \right) , \tag{6.3}$$

where the summation runs over all phonon branches α and wavenumbers q. The angular frequency $\omega_{\alpha,q}$ of a vibrational mode is implicitly determined by α and q and $n_{\alpha,q}$ is the occupation number operator. The eigenstates are the occupation number states $|n_{\alpha,q}\rangle$.

Since $\mathcal{H}_{\text{EPC}}$ does not couple to the spin, the spin-orbit interaction $\mathcal{H}_{\text{SOI}}$ needs to be included in order to obtain a spin relaxing mechanism via admixture of electronic states [Khaetskii(2001)]. For this admixture, we consider both bound states confined inside the dot and extended, quasi continuous states energetically above the confinement potential.

As will be discussed in more detail, $\mathcal{H}_{\text{SOI}}$ perturbs the electron-spin product states $|k\rangle|s\rangle = |k\,s\rangle^{(0)}$, where $s = \uparrow, \downarrow$. We denote the first order perturbed states by $|k\,s\rangle$. Finally, the electron-phonon coupling leads to finite matrix elements $\langle k\downarrow|\mathcal{H}_{\text{EPC}}|k\uparrow\rangle$. This allows us to use Fermi's golden rule in order to calculate the spin relaxation rate

$$T_1^{-1} = \frac{2\pi}{\hbar} \sum_{\alpha,q} |\langle k\downarrow, n_{\alpha,q}+1|\mathcal{H}_{\text{EPC}}|k\uparrow, n_{\alpha,q}\rangle|^2 \rho_{\text{states}}(\hbar\omega_{\alpha,q}) , \tag{6.4}$$

where $\rho_{\text{states}}(\hbar\omega_{\alpha,q})$ is the phonon density of states at the respective energy. The result is a function of three parameters: (i) length-to-width ratio (aspect ratio) L/W of the QD, (ii) potential depth ΔV of the QD, and (iii) perpendicular magnetic field B. We find that T_1 can be as large as several seconds if ρ_{states} is small and the two mechanisms in $\mathcal{H}_{\text{EPC}}$ interfere destructively.

6.3. Electronic states

Due to the aGNR edges where the wavefunction vanishes on both sublattices, electronic states in an aGNR have transverse wavenumbers

$$q_n = \pi(n - \mu/3)/W , \tag{6.5}$$

where $n = 0, \pm1, \pm2, ...$ and $W = (3m + \mu)\sqrt{3}a$ is the ribbon width [Brey(2006)]. The width depends on $m \in \mathbb{N}$ and $\mu \in \{-1, 0, +1\}$. The interatomic distance is $a = 1.42\,\text{Å}$.

 Matthias Droth and Guido Burkard, Physical Review B **87**, 205432 (2013).

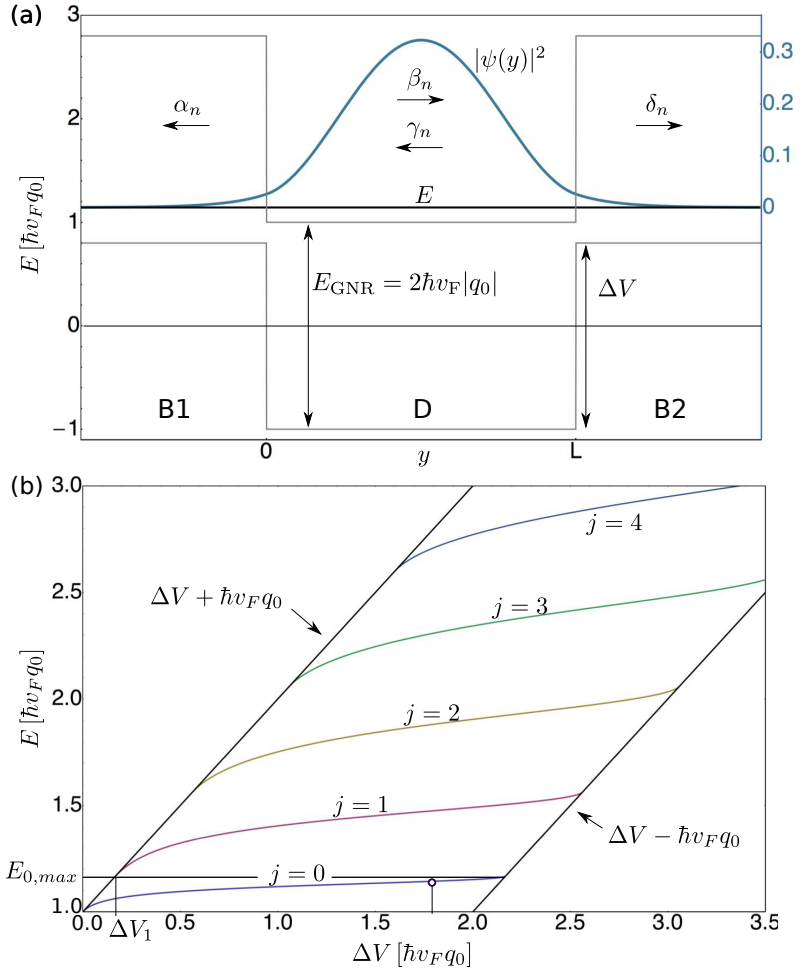

Figure 6.2.: Electron states in an aGNR QD. (a) Sketch of a bound state and (b) QD bound state energy spectrum given by roots of Eq. (6.12). (a) Due to armchair boundaries, the minimum transverse wavenumber is $q_0 = \pm\pi/3W$ for $\mu = \mp 1$. As a consequence, the conduction band is separated from the valence band by a gap of $E_{\mathrm{gap}} = 2\hbar v_{\mathrm{F}}|q_0|$. All energies shall be measured w.r.t. the middle of this bandgap inside the QD region. In the barrier regions, both bands are shifted by the barrier height ΔV. The resulting QD hosts at least one bound state. All bound states have the form given by Eq. (6.11) and decay exponentially for $y \to \pm\infty$. The arrows underneath the Greek letters indicate the directed character of the according part of the wavefunction. The plotted probability density $|\psi(y)|^2$ belongs to the lowest bound state for $L/W = 5$ and $\Delta V = 1.8\hbar v_{\mathrm{F}} q_0$. (b) Bound states exist for roots of Eq. (6.12) and can be plotted in a ΔV-E-plot. There is at least one bound state for all values of ΔV. As ΔV is increased, more bound states fit into the energy gap until the lowest state can leave the QD via valence states in the barrier regions. Notably, Eq. (6.12) has exactly one root for every value of $E \geq \hbar v_{\mathrm{F}} q_0$. We enumerate the bound states by $j = 0, 1, 2, \ldots$. The circled position on the $j = 0$ line marks the state plotted in panel (a). For the shown plot, the aspect ratio is $L/W = 5$.

Due to Eq. (6.5) and $E = \pm\hbar v_\mathrm{F}\sqrt{q_n^2 + k^2}$, where v_F is the Fermi velocity and k is the longitudinal electronic wavenumber, there is a bandgap $E_\mathrm{gap} = 2\hbar v_\mathrm{F}|q_0|$. Since $E_\mathrm{gap} = 0$ for $\mu = 0$, we assume $\mu = \pm 1$ from now on. Note that μ is determined by the number of atoms across the GNR, Fig. 6.1. Spinors with different transverse quantum number n are orthogonal such that we shall focus on the lowest transverse wavenumber with $|q_0| = \pi/3W$. The resulting gap $E_\mathrm{gap} = 2\hbar v_\mathrm{F}\pi/3W$ allows to avoid Klein's paradox and confine charge carriers electrostatically in a finite square potential [Trauzettel(2007)]

$$V(y) = \begin{cases} 0 & : y \in \mathrm{D} \quad \text{(dot region)}, \\ \Delta V & : y \in \mathrm{B1} \cup \mathrm{B2} \quad \text{(barrier regions)}. \end{cases} \tag{6.6}$$

The barrier region B1 extends from the left end of the aGNR to $y = 0$ and the barrier region B2 extends from $y = L$ to the right end. The dot region D lies symmetrically between the barrier regions. The resulting potential landscape is shown in Fig. 6.2 (a) together with a bound state, which will be discussed in the next subsection. The length of the QD is denoted by L and assumed to be much smaller than the overall ribbon length, $L \ll L_\mathrm{GNR}$. For concreteness, we assume an overall GNR length of $L_\mathrm{GNR} = 50W$ [Jiao(2009), Wang(2011)]. The finite square potential needs to be considered in the electronic dispersion relation, which becomes

$$E = V(y) \pm \hbar v_\mathrm{F}\sqrt{q_0^2 + k^2}\,. \tag{6.7}$$

Provided that the barrier height ΔV does not exceed a critical value $2\hbar v_\mathrm{F}|q_0| + \Delta V_1$, we can easily order bound states and extended states by their energies. The critical value and ΔV_1 will be explained in the next subsection - for now, we only assume that ΔV does not exceed it. Then, a state with energy $E \in [\hbar v_\mathrm{F}|q_0|, \hbar v_\mathrm{F}|q_0| + \Delta V]$ is *bound* since its longitudinal wavenumber k is real in the dot region and complex in the barrier regions, thus leading to an evanescent behavior. For $E > \hbar v_\mathrm{F}|q_0| + \Delta V$, the longitudinal wavenumber is real in all regions. This leads to *extended* waves. Both bound and extended states contribute to the admixture mechanism and thus shall be discussed in more detail.

6.3.1. Bound states

To describe bound states in aGNRs, one can assume an infinite ribbon [Trauzettel(2007)]. On one hand, L_GNR will always be finite in reality. On the other hand, bound states are mainly localized in the dot region $0 \le y \le L$ and decay exponentially in the barrier regions, as shown in Fig. 6.2 (a). As mentioned above, we assume $L \ll L_\mathrm{GNR}$, such that the overall ribbon still appears approximately infinite for bound states. This allows us to follow the description with $L_\mathrm{GNR} \to \infty$ for bound states [Trauzettel(2007)].

Accordingly, we denote the four component envelope wavefunction by

$$\psi = (\psi_A^{(K)}, \psi_B^{(K)}, -\psi_A^{(K')}, -\psi_B^{(K')}) \tag{6.8}$$

and assume plane waves along the ribbon, $\psi_{n,k}^{(\pm)}(x,y) = \chi_{n,k}^{(\pm)}(x)e^{\pm iky}$, where

$$\begin{aligned} \chi_{n,k}^{(+)} &= a_n^{(+)}(1, z_{n,k}, 0, 0)e^{iq_n x} + b_n^{(+)}(-z_{n,k}, 1, 0, 0)e^{-iq_n x} \\ &+ c_n^{(+)}(0, 0, -z_{n,k}, 1)e^{iq_n x} + d_n^{(+)}(0, 0, 1, z_{n,k})e^{-iq_n x} \end{aligned} \tag{6.9}$$

 Matthias Droth and Guido Burkard, Physical Review B **87**, 205432 (2013).

and

$$\chi_{n,k}^{(-)} = a_n^{(-)}(z_{n,k},1,0,0)e^{iq_n x} + b_n^{(-)}(1,-z_{n,k},0,0)e^{-iq_n x}$$
$$+c_n^{(-)}(0,0,1,-z_{n,k})e^{iq_n x} + d_n^{(-)}(0,0,z_{n,k},1)e^{-iq_n x}\,. \tag{6.10}$$

With $z_{n,k} = \pm(q_n + ik)/\sqrt{q_n^2+k^2}$, and longitudinal wavenumbers $k_\mathrm{D} = \sqrt{(E/\hbar v_F)^2 - q_n^2}$ (dot region), $\kappa_\mathrm{B} = k_\mathrm{B}/i = \sqrt{q_n^2 - ((E-e\Delta V)/\hbar v_F)^2}$ (barrier regions), bound states have the form

$$\psi = \begin{cases} \alpha_n \chi_{n,\kappa_\mathrm{B}}^{(-)} e^{\kappa_\mathrm{B} y} & : y \in \mathrm{B1}, \\ \beta_n \chi_{n,k_\mathrm{D}}^{(+)} e^{ik_\mathrm{D} y} + \gamma_n \chi_{n,k_\mathrm{D}}^{(-)} e^{-ik_\mathrm{D} y} & : y \in \mathrm{D}, \\ \delta_n \chi_{n,\kappa_\mathrm{B}}^{(+)} e^{-\kappa_\mathrm{B}(y-L)} & : y \in \mathrm{B2}. \end{cases} \tag{6.11}$$

The matching conditions at the interfaces B1/D and D/B2 (that is, at $y = 0, L$) are discussed in [Trauzettel(2007)] and can be met for roots of the transcendental equation

$$\tan(k_\mathrm{D} L) = \frac{k_\mathrm{D}\kappa_\mathrm{B}}{\pm\sqrt{q_n^2-\kappa_\mathrm{B}^2}\sqrt{q_n^2+k_\mathrm{D}^2}-q_n^2}\,. \tag{6.12}$$

For $|q_0| = \pi/3W$ and $L/W = 5$, Fig. 6.2 (b) shows these roots as a function of the barrier height ΔV. There is a finite number of longitudinal excitations for any given ΔV. The different bound states can be enumerated by $j = 0, 1, 2, ...$ and have distinct coloring in our figure. The j-th bound state has j nodes inside the dot region. For a given excitation, ΔV can be increased until the valence band reaches the energy of the lowest state which can now leave the QD via valence states in the barrier regions. Note that this occurs exactly when the argument on the l.h.s. of Eq. (6.12) equals a multiple of π. For the ground state, this means $k_\mathrm{D} \in [0, \pi/L]$ such that the maximum ground state energy is $E_{0,\max} = \hbar v_\mathrm{F}\sqrt{q_0^2 + (\pi/L)^2}$. States of higher energy belong to the j-th longitudinal excitation ($j > 0$) which begins at $\Delta V_j = \hbar v_\mathrm{F}(j\pi/L)$. For $\Delta V < \Delta V_1$, the ground state is the only bound state. This will be important for the evaluation of T_1, see Secs. 6.6 and 6.7.

The critical value for ΔV mentioned before is $\Delta V = 2\hbar v_\mathrm{F}|q_0| + \Delta V_1$. If the barrier height surpasses this value, the lowest state inside the QD can leave it via valence states in the barrier region. That is, the state becomes extended thus affecting the ordering of bound and extended states. Throughout this paper we assume that ΔV does not exceed this threshold such that the ground state belongs to $j = 0$.

6.3.2. Extended states

We assume $L_\mathrm{GNR} = 50W$ for the overall length of the GNR such that possible wavenumbers are $k_\mathrm{EB} = 0, \pm 2\pi/L_\mathrm{GNR}, ..., \pm\pi/a$ with lattice constant a. Since energy is conserved, the wavenumber becomes

$$k_\mathrm{ED} = \sqrt{\left(\sqrt{q_n^2+k_\mathrm{EB}^2} + \Delta V/\hbar v_F\right)^2 - q_n^2} \tag{6.13}$$

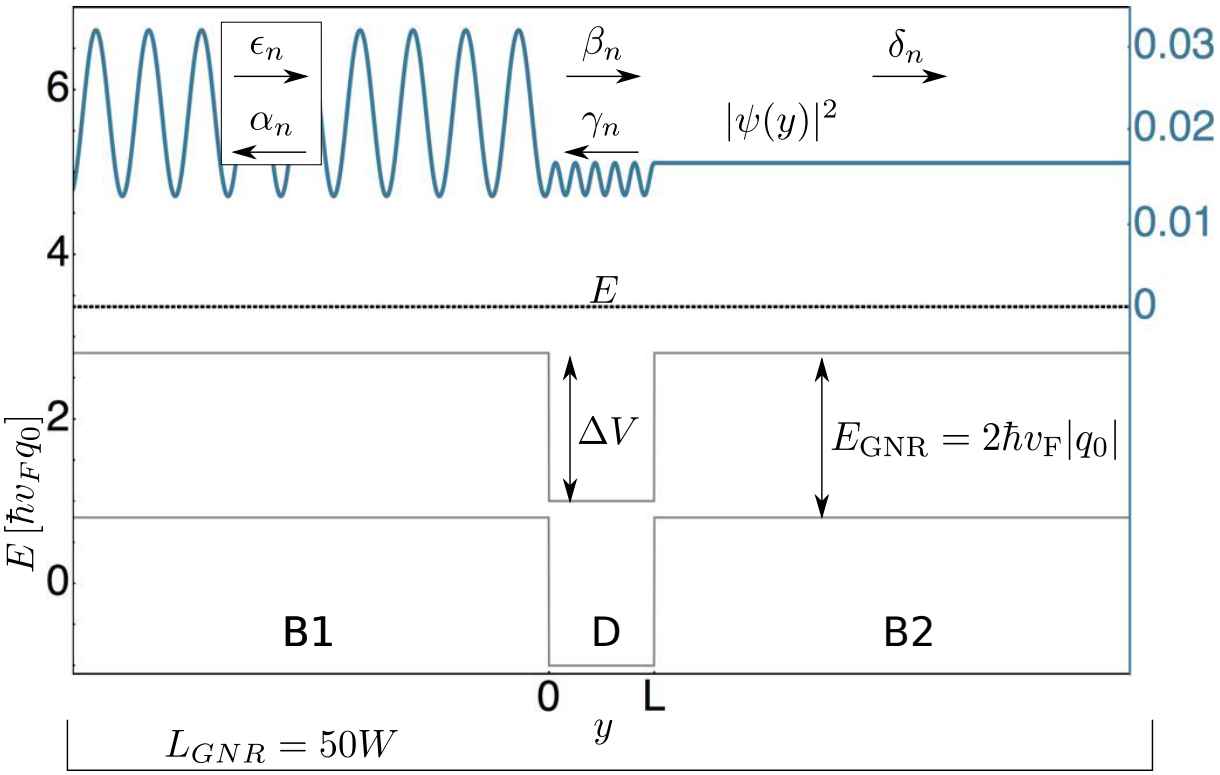

Figure 6.3.: Sketch of an extended state. The potential landscape, the aspect ratio L/W, and the barrier height ΔV are the same as in Fig. 6.2 (a) for bound states. The plotted probability density belongs to an extended state that is incident from the left as described by Eq. (6.14) and for which $k_{\mathrm{EB}} = 20\pi/L_{\mathrm{GNR}}$. The arrows underneath the Greek letters indicate the direction of propagation of the according part of the wavefunction.

in the dot region. Depending on the sign of k_{EB}, the state is incident from $y < 0$, leading to

$$\psi = \begin{cases} \epsilon_n \chi^{(+)}_{n,k_{\mathrm{EB}}} e^{ik_{\mathrm{EB}}y} + \alpha_n \chi^{(-)}_{n,k_{\mathrm{EB}}} e^{-ik_{\mathrm{EB}}y} & : y \in \mathrm{B1}, \\ \beta_n \chi^{(+)}_{n,k_{\mathrm{ED}}} e^{ik_{\mathrm{ED}}y} + \gamma_n \chi^{(-)}_{n,k_{\mathrm{ED}}} e^{-ik_{\mathrm{ED}}y} & : y \in \mathrm{D}, \\ \delta_n \chi^{(+)}_{n,k_{\mathrm{EB}}} e^{ik_{\mathrm{EB}}(y-L)} & : y \in \mathrm{B2}, \end{cases} \tag{6.14}$$

see Fig. 6.3, or it is incident from $y > L$, which is described by

$$\psi = \begin{cases} \alpha_n \chi^{(-)}_{n,k_{\mathrm{EB}}} e^{-ik_{\mathrm{EB}}y} & : y \in \mathrm{B1}, \\ \beta_n \chi^{(+)}_{n,k_{\mathrm{ED}}} e^{ik_{\mathrm{ED}}y} + \gamma_n \chi^{(-)}_{n,k_{\mathrm{ED}}} e^{-ik_{\mathrm{ED}}y} & : y \in \mathrm{D}, \\ \delta_n \chi^{(+)}_{n,k_{\mathrm{EB}}} e^{ik_{\mathrm{EB}}(y-L)} + \epsilon_n \chi^{(-)}_{n,k_{\mathrm{EB}}} e^{-ik_{\mathrm{EB}}(y-L)} & : y \in \mathrm{B2}. \end{cases} \tag{6.15}$$

The matching conditions at $y = 0, L$ can always be met. In contrast to bound states, extended states are propagating waves in the barrier regions.

 Matthias Droth and Guido Burkard, Physical Review B **87**, 205432 (2013).

6.4. Acoustic GNR phonons

The phonon energies we are interested in need to match the Zeeman splitting, $\hbar\omega = g\mu_\mathrm{B}B$, where ω is the phonon frequency, g the electron g-factor, and μ_B denotes Bohr's magneton. For typical lab magnetic fields $B \lesssim 20\,\mathrm{T}$, this implies low-energy acoustic phonons at the center of the Brillouin zone which can be modeled by continuum mechanics [Droth(2011), Landau&Lifschitz]. In this model, deformations are described by the displacement field $\boldsymbol{u}(\boldsymbol{r})$. While the components u_{xz} and u_{yz} of the strain tensor $u_{ik} = (\partial_i u_k + \partial_k u_i)/2$ are known to vanish for thin plates in general, the monatomic thickness of graphene implies that u_{zz} must vanish, as well. With $u_{iz} \equiv 0$, the elastic Lagrangian density of monolayer graphene is given by [Suzuura(2002), Mariani(2009), Droth(2011)]

$$\mathcal{L} = \mathcal{T} - \mathcal{V} = \frac{\rho}{2}\dot{\boldsymbol{u}}^2 - \frac{\kappa}{2}(\triangle u_z)^2 - \frac{B+\mu}{2}u_{ii}^2 + \mu u_{ik}^2\,, \tag{6.16}$$

where $\triangle = \partial_x^2 + \partial_y^2$, the sum convention with $u_{ii} = u_{xx} + u_{yy} + u_{zz}$ and $u_{ik}^2 = u_{xx}^2 + u_{xy}^2 + \cdots$ has been used, ρ is the mass density, and κ is the bending rigidity. The bulk (B) and shear (μ) moduli can be expressed by Poisson's ratio σ and Young's modulus $\mathcal{E}$. The numerical values of elastic and other constants we use are listed in Table 6.1. Eq. (6.16) shows that in-plane vibrations $\boldsymbol{u}_\parallel$ decouple from out-of-plane vibrations $\boldsymbol{u}_\perp$. By assuming $u_i(x,y) = f^i(x)\exp[i(qy - \omega t)]$ for a single mode and imposing free or fixed conditions as discussed in [Droth(2011)], we obtain the according phonon dispersions (Fig. 6.4) and the explicit displacement fields. The latter can be quantized and then take the form

$$\begin{aligned}\boldsymbol{u}_\parallel &= \sum_{\alpha,q} r_{\alpha,q}(f^x_{\alpha,q}\boldsymbol{e}_x + f^y_{\alpha,q}\boldsymbol{e}_y)e^{iqy}\,,\\ \boldsymbol{u}_\perp &= \sum_{\alpha,q} r_{\alpha,q} f^z_{\alpha,q}\boldsymbol{e}_z e^{iqy}\,,\end{aligned} \tag{6.17}$$

where q is the phonon wavenumber, α labels the phonon branch, and

$$r_{\alpha,q} = \sqrt{\hbar/(2\rho LW\omega_{\alpha,q})}(b_{\alpha,q} + b^\dagger_{\alpha,-q}) \tag{6.18}$$

is the normal coordinate. The operator $b_{\alpha,q}$ ($b^\dagger_{\alpha,q}$) annihilates (creates) a phonon on branch α with wavenumber q.

As discussed in the following section, we can neglect coupling to out-of-plane modes and focus on in-plane modes. The dimensionless frequency of in-plane modes $\bar{\omega}_{xy}$ is related to the physical frequency by $\bar{\omega}_{xy} = \omega\sqrt{\rho/\mathcal{E}}\,W$. In the continuum model, all branches extend to infinity but we are only interested in the range $\bar{\omega}_{xy} \in [0,5]$ since for a typical GNR width of $W = 30\,\mathrm{nm}$, $\bar{\omega}_{xy} = 5$ relates to a magnetic field of 20 T. The dimensionless wavenumber $\bar{q}$ is obtained from the physical wavenumber via $\bar{q} = qW$. For symmetry reasons explained in Sec. 6.6, not all branches contribute to spin relaxation but only those which are explicitly labeled in Fig. 6.4.

In the case of free boundaries, the branches α_2, α_4, and α_5 are relevant. While α_2 extends throughout the considered interval, α_5 only exists above $\bar{\omega}_{xy} = 4.16$, and α_4 needs further discussion. Its minimum is 3.05 and occurs at a finite value $\bar{q}_0$ where the density of states

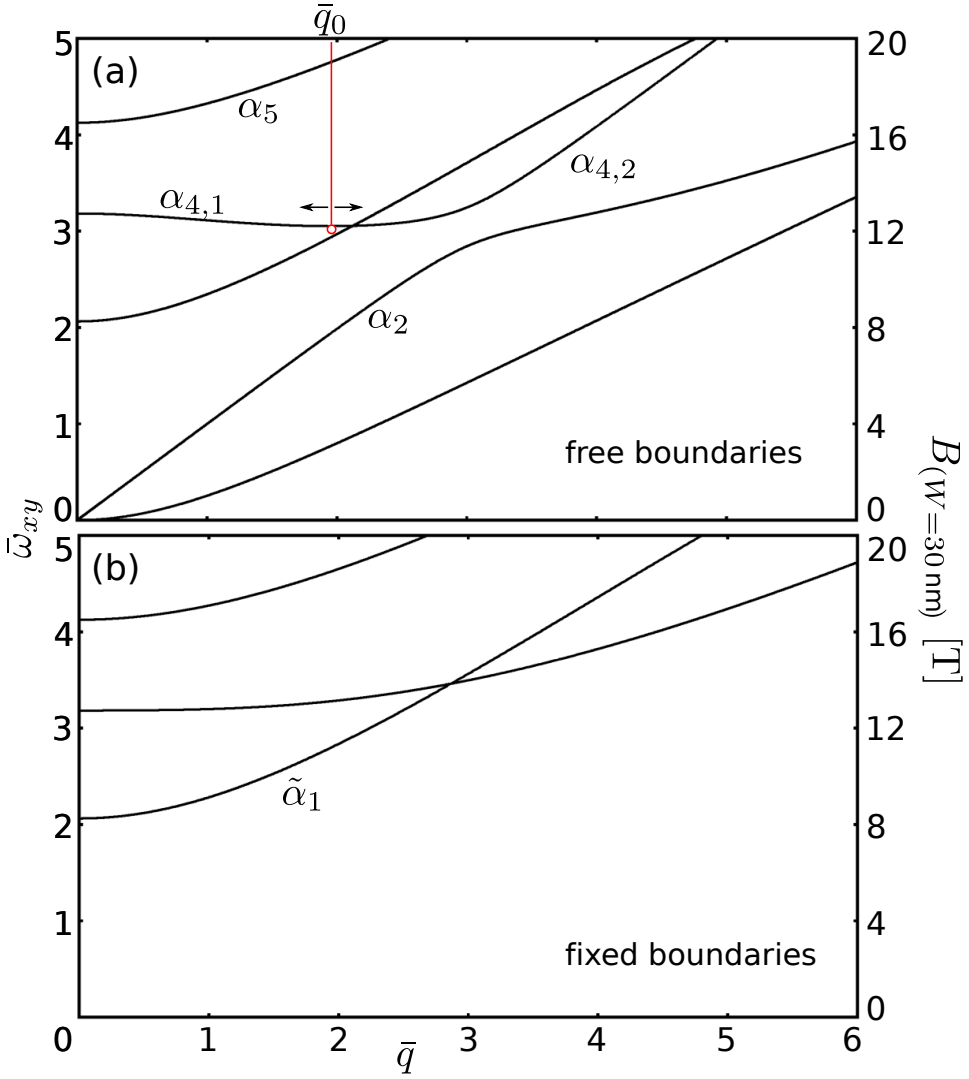

Figure 6.4.: Phonon dispersion for (a) free and (b) fixed boundaries. The dimensionless frequency $\bar{\omega}_{xy}$ is connected to the physical frequency by $\bar{\omega}_{xy} = \omega\sqrt{\rho/\mathcal{E}}\,W$, where the radicand contains elastic constants listed in Table 6.1. We restrict our interest to the frequency range $\bar{\omega}_{xy} \in [0, 5]$ since for $W = 30\,\mathrm{nm}$, the upper bound already relates to a magnetic field of 20 T. The scale on the r.h.s. shows the magnetic field for $W = 30\,\mathrm{nm}$. Due to parity w.r.t. x, only the labeled branches (α_i for free and $\tilde{\alpha}_1$ for fixed boundaries) assist in spin relaxation. (a) The phonon spectrum is gapless for free boundaries. The branch α_4 has a minimum and hence a diverging density of states for finite $\bar{q}$. Its constituent parts $\alpha_{4,1}$ and $\alpha_{4,2}$ shall be treated separately. (b) Fixed edges lead to gapped phonon spectrum. For $W = 30\,\mathrm{nm}$, this gap corresponds to 8.25 T. In our range of interest, the branch labeled $\tilde{\alpha}_1$ provides the only channel for spin relaxation.

has a Van Hove singularity. We consider two parts: for $\bar{q} < \bar{q}_0$, we label the branch $\alpha_{4,1}$ and its label for $\bar{q} > \bar{q}_0$ is $\alpha_{4,2}$. The range of $\alpha_{4,1}$ is $\bar{\omega}_{xy} \in [3.05, 3.18]$ and $\alpha_{4,2}$ extends from its minimum to infinity.

 Matthias Droth and Guido Burkard, Physical Review B **87**, 205432 (2013).

For fixed boundaries, we only need to consider the branch $\tilde{\alpha}_1$. It extends from $\bar{\omega}_{xy} = 2.06$ to infinity. We emphasize that for a typical GNR width of 30 nm, single phonon processes do not occur up to 8.25 T as there are no phonons below $\bar{\omega}_{xy} = 2.06$ for fixed boundaries.

6.5. Coupling mechanisms

Phonons do not couple to the electron spin directly. The relevant mechanism usually involves the spin-orbit interaction [Khaetskii(2001), Bulaev(2008), Struck(2010)]. In graphene, the spin-orbit interaction is given by

$$\mathcal{H}_{\mathrm{SOI}} = \mathcal{H}_I + \mathcal{H}_R = \lambda_I \tau_z \sigma_z s_z + \lambda_R(\tau_z \sigma_x s_y - \sigma_y s_x) \tag{6.19}$$

and we will consider it in order to obtain an indirect spin-phonon coupling [Kane(2005), Min(2006), Gmitra(2009)]. The intrinsic (Dresselhaus) term $\mathcal{H}_I$ has coupling strength λ_I and the Rashba (or extrinsic) term $\mathcal{H}_R$ couples with strength λ_R. The valley is denoted by τ_z, pseudospin by $\boldsymbol{\sigma}$, and real spin by $\boldsymbol{s}$. In the following, we show how the real electron spin can be connected to the vibrational state of the system by taking the spin-orbit interaction into account.

6.5.1. Coupling to in-plane modes

In first order perturbation theory, $\mathcal{H}_R$ corrects the electron-spin product states $|k\rangle|\uparrow\rangle = |k\uparrow\rangle^{(0)}$ to

$$|k\uparrow\rangle = |k\uparrow\rangle^{(0)} + \sum_{k' \neq k} |k'\downarrow\rangle^{(0)} \frac{{}^{(0)}\langle k'\downarrow|\mathcal{H}_R|k\uparrow\rangle^{(0)}}{E_k - E'_k + g\mu_{\mathrm{B}}B}\,, \tag{6.20}$$

and $|k\downarrow\rangle$ accordingly. We emphasize that the summation index k' runs over both bound and extended states. The potential depth and the aspect ratio determine how many bound states exist, Fig. 6.2 (b). For extended states, we consider all wavenumbers inside the first Brillouin zone, $k_{\mathrm{EB}} = 0, \pm 2\pi/L_{\mathrm{GNR}}, ..., \pm\pi/a$.

The second term in Eq. (6.20) admixes states with opposite spin such that the electron-phonon coupling $\mathcal{H}_{\mathrm{EPC}}$ can induce a spin flip [Khaetskii(2001)]

$$\langle k\downarrow|\mathcal{H}_{\mathrm{EPC}}|k\uparrow\rangle = \sum_{k' \neq k} \left[\frac{(\mathcal{H}_{\mathrm{EPC}})_{kk'}(\mathcal{H}_R)^{\downarrow\uparrow}_{k'k}}{E_k - E_{k'} + g\mu_{\mathrm{B}}B} + \frac{(\mathcal{H}_{\mathrm{EPC}})_{k'k}(\mathcal{H}_R)^{\downarrow\uparrow}_{kk'}}{E_k - E_{k'} - g\mu_{\mathrm{B}}B} \right], \tag{6.21}$$

where we denote the numerator in Eq. (6.20) as $(\mathcal{H}_R)^{\downarrow\uparrow}_{k'k}$ and the spin-conserving transitions of $\mathcal{H}_{\mathrm{EPC}}$ accordingly. We find that for a given k', the two terms in Eq. (6.21) exactly cancel each other at $B = 0$. This effect is known as Van Vleck cancelation and is expected for time-reversal-symmetric systems [VanVleck(1940)]. Moreover, $(\mathcal{H}_R)^{\downarrow\uparrow}_{kk'}$ vanishes if both k and k' represent bound states and the longitudinal excitation indices j_k,

$j_{k'}$ (see Fig. 6.2) are both even or both odd. In the electron phonon coupling Hamiltonian $\mathcal{H}_{\mathrm{EPC}}$, we consider the deformation potential $\mathcal{H}_{\mathrm{VEP}}$ as well as bond-length change $\mathcal{H}_{\mathrm{BLC}}$:

$$\begin{aligned}\mathcal{H}_{\mathrm{EPC}} &= \mathcal{H}_{\mathrm{VEP}} + \mathcal{H}_{\mathrm{BLC}}\,, \\ \mathcal{H}_{\mathrm{VEP}} &= g_1 \boldsymbol{\nabla}\cdot\boldsymbol{u}_{\parallel}\,, \\ \mathcal{H}_{\mathrm{BLC}} &= g_2 \begin{pmatrix} 0 & A_x - iA_y & 0 & 0 \\ A_x + iA_y & 0 & 0 & 0 \\ 0 & 0 & 0 & A_x + iA_y \\ 0 & 0 & A_x - iA_y & 0 \end{pmatrix},\end{aligned} \tag{6.22}$$

where $g_{1,2}$ are coupling constants, $(A_x, A_y) = (u_{xx} - u_{yy}, -2u_{xy})$, and the basis of Eq. (6.8) has been used [Suzuura(2002), Mariani(2009), CastroNeto(2009)].

6.5.2. Vanishing out-of-plane deflection coupling

Low-energy acoustic phonons at the center of the Brillouin zone have a wavelength much larger than the lattice constant and produce a local tilt of the GNR. In the local ribbon frame Σ' where $\boldsymbol{n} = \boldsymbol{e}'_z$ is the vector normal to the ribbon plane the local spin matrix is described by $s'_z = s_z - \partial_x u_z s_x - \partial_y u_z s_y$. As a consequence, the intrinsic spin-orbit interaction

$$\mathcal{H}_I = \lambda_I \tau_z \sigma_z (s_z - \partial_x u_z s_x - \partial_y u_z s_y) \tag{6.23}$$

becomes dependent on out-of-plane phonons such that these could flip the spin. This is known as deflection coupling [Rudner(2010), Struck(2010)]. However, there is a proportionality to τ_z in Eq. (6.23). Since the electronic states we use have the property that the wavefunction has equal weight on each valley[1], the contributions from K and K' add up to zero and the deflection coupling between spin and out-of-plane modes vanishes.

If the spin-orbit admixed states of Eq. (6.20) are used, there is a finite overlap only between both admixed parts such that the resulting mechanism is proportional to $\lambda_I \lambda_R^2$ and hence negligible.

Compared to in-plane phonons, both deformation potential and bond-length change appear only in higher order such that we neglect these mechanisms for out-of-plane phonons.

6.6. Evaluation of T_1

Using Eq. (6.4), we calculate the spin relaxation rate for the electron in the lowest bound state (ground state) of the QD. For concreteness, we assume $\mu = -1$ in Eq. (6.5). According to Eqs. (6.11), (6.14), and (6.15), both bound and extended states have a finite probability density in the barrier regions. However, bound states are localized in the dot region and decay exponentially in the barrier regions. In particular the ground state, plotted in Fig. 6.2 (a), has a very low probability density in the barrier regions. Its

[1] See Sec. 6.3 in this paper and Eqs. (34), (35) in the supplementary information of [Trauzettel(2007)].

overlap with another bound state in the barrier regions is negligible. Only high-energy extended states have a significant contribution outside the dot region. Yet the overlap of an extended state with the ground state outside the dot region will still be small and since they are energetically far apart, the contribution from the barrier regions can be neglected. As a consequence, we can restrict the integrals in Eq. (6.21) to the dot region.

As discussed in Sec. 6.4, we consider phonons with free boundaries as well as phonons with fixed boundaries. Not all branches contribute to spin relaxation: Because of mirror symmetry w.r.t. $x = 0$, $\mathcal{H}_{\mathrm{BLC}}$ and $\mathcal{H}_{\mathrm{VEP}}$ are even or odd in x, depending on what phonon branch they belong to. Due to their similar form[2], the mechanisms are either both even or both odd for a given branch. The x-dependencies of the electronic states in the matrix element $(\mathcal{H}_{\mathrm{EPC}})_{k'k}$ cancel out, $e^{i(q_0-q_0)x} = 1$, such that the x-integral vanishes if Eq. (6.22) is odd in x. The branches α_2, α_4, and α_5 in Fig. 6.4 (a) and $\tilde{\alpha}_1$ in Fig. 6.4 (b) have couplings $\mathcal{H}_{\mathrm{EPC}}$ that are even in x and hence can relax the spin.

For a given relaxation channel (α, q), both mechanisms $\mathcal{H}_{\mathrm{VEP}}$ and $\mathcal{H}_{\mathrm{BLC}}$ are combined in Eq. (6.4) coherently. Moreover, the couplings via bound states and extended states in Eq. (6.20) are added up in a coherent way. We are interested in the relaxation of the spin in the ground state, which corresponds to $j = 0$ in Fig. 6.2 (b) and hence restrict the barrier height to $\Delta V \in [0,\, 2\hbar v_{\mathrm{F}} q_0 + \Delta V_1]$. If ΔV exceeds this upper bound, valence states become available in the barrier regions and the lowest state inside the QD can leave the dot region. For $\Delta V < \Delta V_1$ on the other hand, the ground state is the only bound state such that the perturbation in Eq. (6.20) comes about only due to extended states, which fully determine the spin relaxation in this case.

For spin relaxation, Eq. (6.4) is proportional to $n_{\alpha,q} + 1$ and we assume $n_{\alpha,q} = 0$, i. e. sufficiently low temperature, $k_{\mathrm{B}}T \ll \hbar\omega = g\mu_{\mathrm{B}}B$. By k_{B} we denote Boltzmann's constant. Assuming a magnetic field of $B = 1\,\mathrm{T}$, this means $T \ll 1.3\,\mathrm{K}$. For $T \gtrsim 15\,\mathrm{K}$, spontaneous emission can be neglected since $n_{\alpha,q} \gg 1$ and one obtains the spin relaxation by multiplying our results with the expectation value of the Bose distribution

$$\langle n_{\alpha,q}(B,T)\rangle = \left(e^{\frac{g\mu_{\mathrm{B}}B}{k_{\mathrm{B}}T}} - 1\right)^{-1}. \tag{6.24}$$

The spin relaxation time T_1 is a good measure for overall coherence when pure dephasing, which comes from coupling to nuclear spins, is negligible. Due to the low density of nuclear spins in natural carbon and the very different magnetic moments $\mu_{\mathrm{B}} \gg \mu_{\mathrm{nuc}}$, we expect that flip-flop processes with nuclear spins can be neglected for magnetic fields above 10 mT. For a typical GNR width of $W = 30\,\mathrm{nm}$, 10 mT correspond to $\bar{\omega}_{xy} = 0.0025$. As a consequence, we restrict our calculations to the interval $\bar{\omega}_{xy} \in [0.0025, 5]$. The upper bound corresponds to a magnetic field of 20 T. All plots that show rates are cut off at these boundaries.

[2]Both mechanisms contain derivatives $\partial_{x,y}$. Due to the plate equation used in continuum mechanics (see Eq. (3) in [Droth(2011)]), $f^x(x)$ is odd when $f^y(x)$ is even and vice versa. While the derivative ∂_x applied to an even function returns an odd function and vice versa, the derivative ∂_y corresponds merely to a multiplication with iq.

6.7. Results

To calculate T_1, we need to use the specific values of the elastic constants that define the phonon spectrum. Young's modulus for the two-dimensional lattice of graphene is obtained by multiplying the bulk value with the thickness associated with graphene, $\mathcal{E} = \mathcal{E}_{3D}h$, where $h = 3.4\,\text{Å}$. For further discussion of the elastic constants, we refer to [Droth(2011)]. Table 6.1 gives an overview of the constants we use in our calculation. The Rashba type spin-orbit coupling is linear in the electric field and thus can be adjusted by an external electric field or by using a suitable substrate [Min(2006)]. The spin relaxation

$\sigma = 0.16$	[Lee(2008), Faccio(2009), Kudin(2001)]
$\mathcal{E} = 3.4\,\text{TPa}\,\text{Å}$	[Lee(2008), Faccio(2009), Kudin(2001)]
$B = 12.6\,\text{eV}/\text{Å}^2$	[Kudin(2001), Gazit(2009)]
$\mu = 9.1\,\text{eV}/\text{Å}^2$	[Kudin(2001), Gazit(2009)]
$\rho = 7.61 \times 10^{-7}\,\text{kg}/\text{m}^2$	$*$
$g_1 = 30\,\text{eV}$	[Suzuura(2002), Mariani(2009), Struck(2010)]
$g_2 = 1.5\,\text{eV}$	[Mariani(2009), Struck(2010)]
$\lambda_\text{R} = 40 \times 10^{-6}\,\text{eV}$	[Min(2006), Gmitra(2009), Struck(2010)]
$v_F = 8.8 \times 10^5\,\text{m/s}$	[CastroNeto(2009), Gmitra(2009), Struck(2010)]

Table 6.1.: Numerical values of the parameters we use in our calculation.
$*$ This value follows directly from the atomic weight of natural carbon, 12.01 u, and the interatomic distance in graphene, 1.42 Å.

time T_1 depends on three parameters: (i) the aspect ratio L/W of the QD, (ii) the potential depth ΔV of the QD, and (iii) the applied perpendicular magnetic field $B \propto \bar{\omega}_{xy}$. Moreover, the phonon spectrum and hence the spin relaxation depends on the mechanical boundary conditions. We discuss free boundary conditions separately from fixed boundaries.

6.7.1. Free boundary conditions

For symmetry reasons explained above, only the phonon branches with labels α_2, α_4 (consisting of parts $\alpha_{4,1}$ and $\alpha_{4,2}$), and α_5 in Fig. (6.4) (a) need to be considered. The respective rates of these relaxation channels are shown in Fig. 6.5 for an aspect ratio of $L/W = 5$ and a barrier height of $\Delta V = 1.8\hbar v_\text{F} q_0$. The allocation of panels to branches is as follows: panel (a) belongs to branch α_5, (b) to $\alpha_{4,1}$, (c) to $\alpha_{4,2}$, and (d) to α_2. Each panel shows four separate contributions to T_1^{-1} that come about from the two mechanisms in Eq. (6.22) and the admixture of bound states or of extended states in Eq. (6.20) for each mechanism. The coherent sum of all four contributions is displayed by the grey line. The deformation potential usually dominates over the bond-length change since its coupling constant is 20 times larger, Table 6.1. For $\Delta V = 1.8\hbar v_\text{F} q_0$, extended states are energetically far away from the ground state such that the contribution from the deformation potential with admixture of bound states dominates in Fig. 6.5. Oscillations in individual rates may be due to the phonon phase e^{iqy} that is integrated with the matrix

Matthias Droth and Guido Burkard, Physical Review B **87**, 205432 (2013).

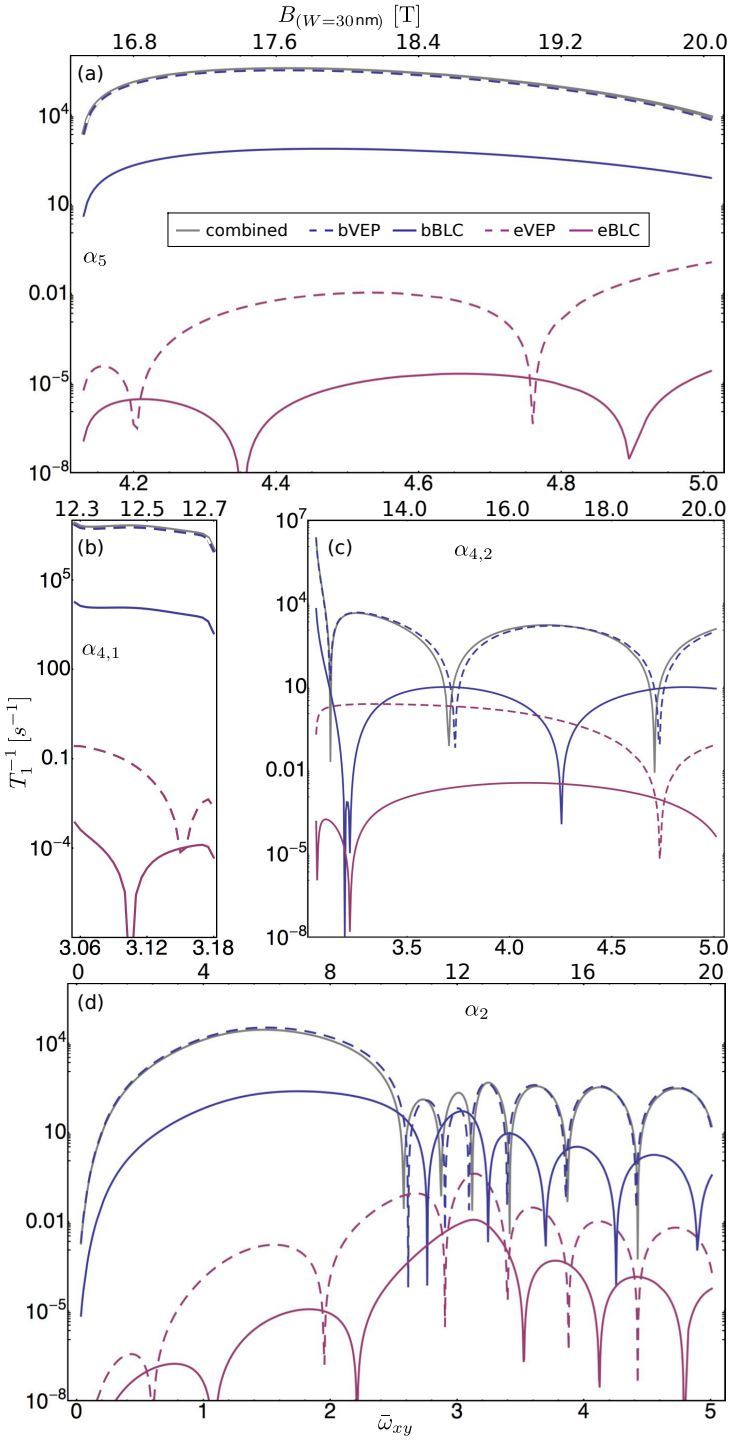

Figure 6.5.: Partial rates for various relaxation channels. For $L/W = 5$ and $\Delta V = 1.8\hbar v_\mathrm{F} q_0$, all contributions to the four relaxation channels α_5 (a), $\alpha_{4,1}$ (b), $\alpha_{4,2}$ (c), and α_2 (d) are shown. The contributions stem from $\mathcal{H}_\mathrm{VEP}$ with admixture of bound (labeled "bVEP") states or extended states ("eVEP") and from $\mathcal{H}_\mathrm{BLC}$ with the same admixtures ("bBLC" and "eBLC", respectively). These contributions are added up coherently to the "combined" relaxation of the respective channel.

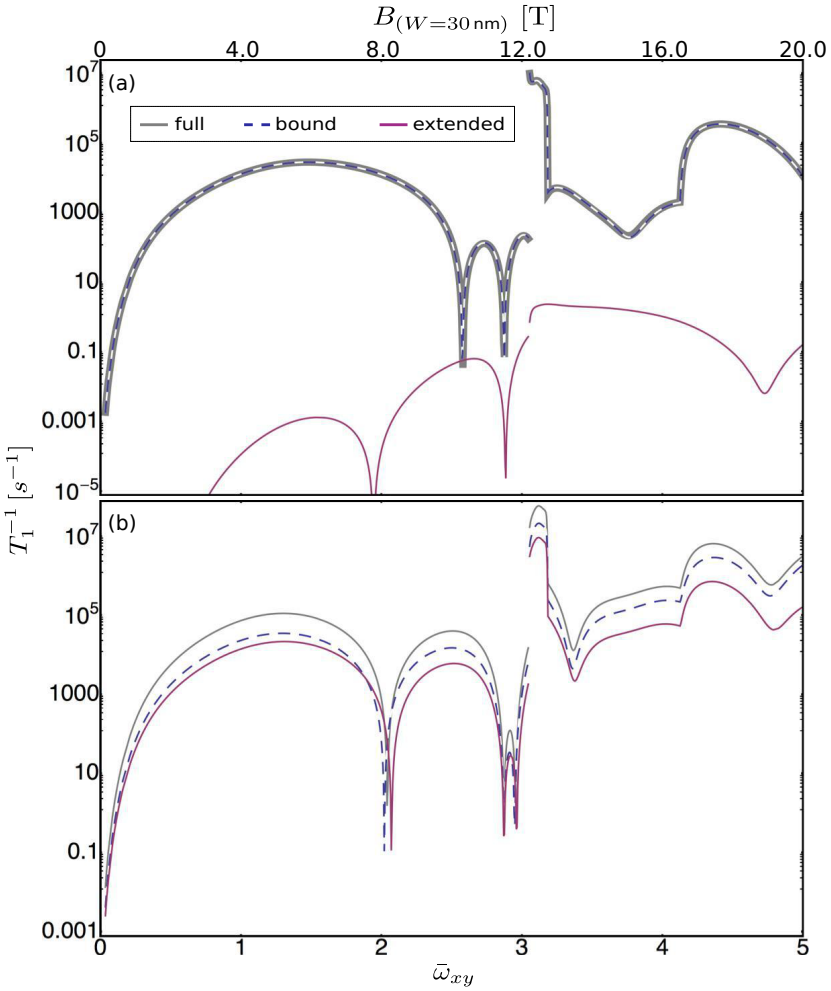

Figure 6.6.: The relaxation rates for different dot depths ΔV. By summing up the combined relaxation rates (see Fig. 6.5) of all channels available for a certain $\bar{\omega}_{xy}$, the full relaxation rate (grey line) is obtained. The lines labeled "bound" and "extended" are obtained in a similar way by considering only bound or extended states, respectively. At $\bar{\omega}_{xy} = 3.05$, T_1^{-1} is discontinuous due to the advent of the relaxation channel α_4 that has a diverging density of states at this point, Fig. 6.4 (a). Panel (a) accords to parameters $L/W = 5$ and $\Delta V = 1.8\hbar v_\mathrm{F} q_0$ as in Fig. 6.5. Clearly, the energetically far off extended states play a negligible role for such a deep dot. In panel (b), the barrier height is reduced to $0.2\hbar v_\mathrm{F} q_0$ such that extended states are about as important as bound states.

elements $(\mathcal{H}_\mathrm{EPC})_{k'k}$ and rotates according to the phonon dispersion when ω is changed. Panels (c) and (d) show that the matrix elements $(\mathcal{H}_\mathrm{VEP})_{k'k}$ and $(\mathcal{H}_\mathrm{BLC})_{k'k}$ may interfere destructively, thus decreasing T_1^{-1} by several orders of magnitude, yet typically not to zero.

In all these plots, the bottom scale shows $\bar{\omega}_{xy}$ and the top scale shows the magnetic field B that corresponds to $\bar{\omega}_{xy}$, assuming a width of $W = 30\,\mathrm{nm}$. Note, that T_1^{-1} does not depend on B and W separately, but only on the product $BW \propto \omega W \propto \bar{\omega}_{xy}$.

 Matthias Droth and Guido Burkard, Physical Review B **87**, 205432 (2013).

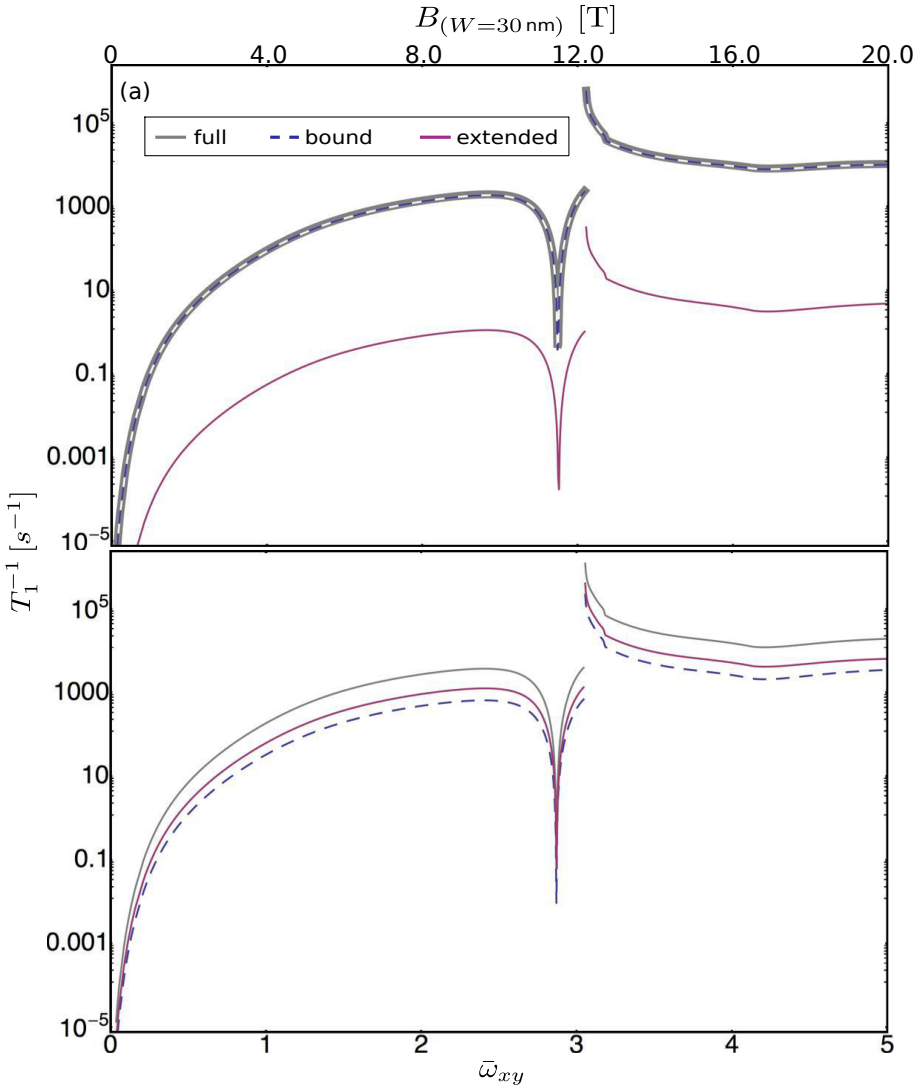

Figure 6.7.: This plot shows the same quantities as Fig. 6.6, yet for the aspect ratio $L/W = 2$. Again, the influence of extended states depends on the barrier height: $\Delta V = 2.0\hbar v_\mathrm{F} q_0$ in (a) and $\Delta V = 0.9\hbar v_\mathrm{F} q_0$ in (b). The extended states dominate in the latter case.

Fig. 6.6 (a) shows the full spin relaxation rate for the situation of Fig. 6.5, that is, the combined rates of all relaxation channels α_2, $\alpha_{4,1}$, $\alpha_{4,2}$, and α_5 (grey lines in Fig. 6.5) are summed up to the full relaxation rate T_1^{-1} (grey line in Fig. 6.6 (a)). The rate with the label "bound" ("extended") is obtained in a similar fashion, but only contributions with admixture of bound (extended) states are considered, here. For $\Delta V = 1.8\hbar v_\mathrm{F} q_0$, the admixture of bound states dominates the admixture of extended states by several orders of magnitude. Yet by lowering ΔV, the influence of extended states can be close to (Fig. 6.6 (b)) or even surpass the influence of the bound states. Fig. 6.7 shows two cases for an aspect ratio of $L/W = 2$. In panel (a), the barrier height is $\Delta V = 2.0\hbar v_\mathrm{F} q_0$ and extended states are basically irrelevant compared to the relaxation via bound states. However, panel (b) shows that for $\Delta V = 0.9\hbar v_\mathrm{F} q_0$, the major contribution comes from the extended states.

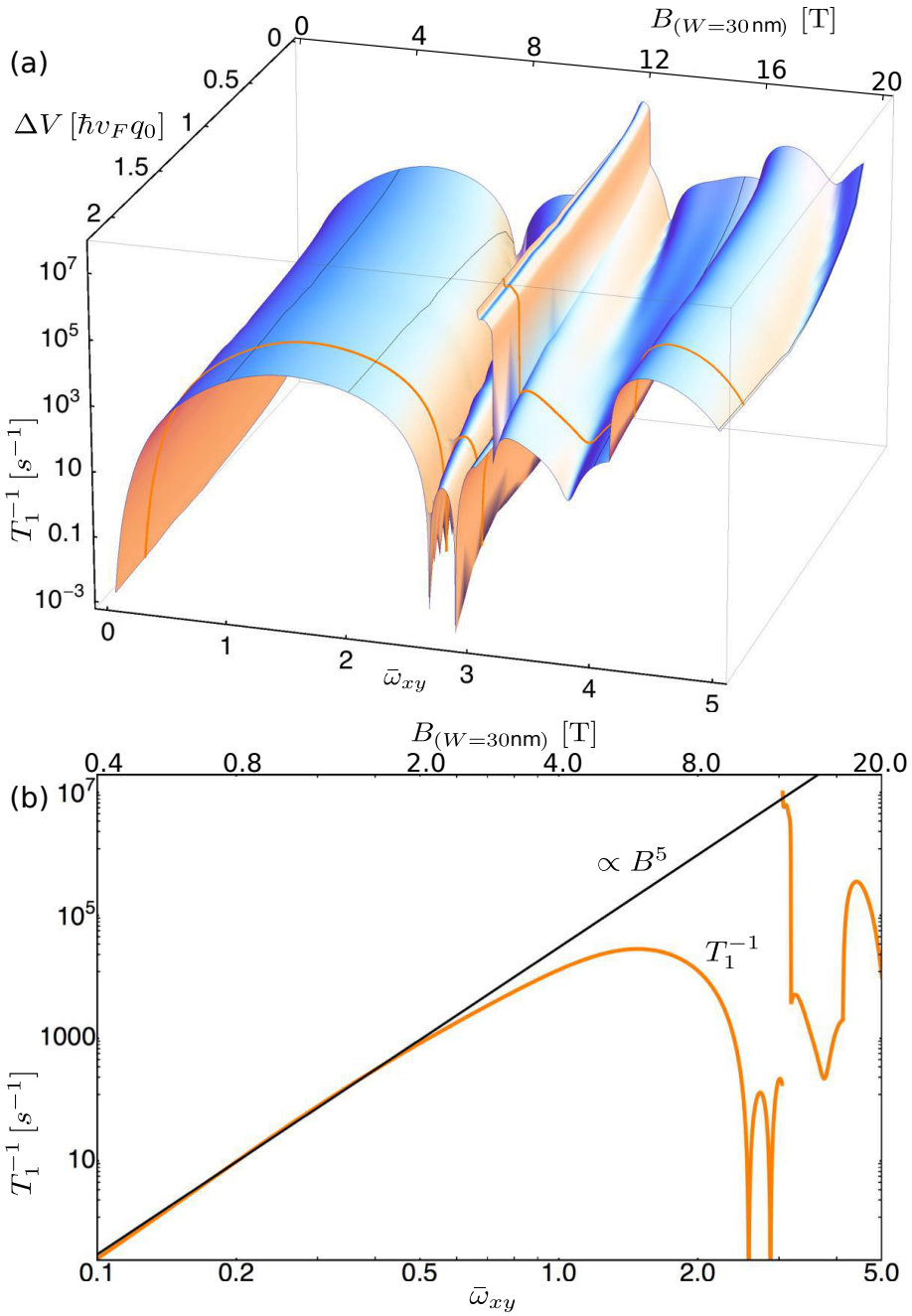

Figure 6.8.: Spin relaxation rate T_1^{-1} for an aGNR with aspect ratio $L/W = 5$ and free edges. (a) The rate is shown as a function of barrier height ΔV and phonon frequency $\bar{\omega}_{xy}$. The orange cut corresponds to the grey line in Fig. 6.6 (a) and is repeated in panel (b) with a doubly logarithmic scale that highlights the B^5 dependence in the interval $\bar{\omega}_{xy} \in [0.0025, 0.5]$.

Fig. 6.8 (a) shows T_1^{-1} as a function of parameters ΔV and $\bar{\omega}_{xy} \propto B$, and for a fixed aspect ratio of $L/W = 5$. In contrast to $\bar{\omega}_{xy}$, the barrier height hardly changes the qualitative picture. The orange cut at $\Delta V = 1.8\hbar v_\mathrm{F} q_0$ is repeated in panel (b) in a doubly logarithmic plot that highlights the B^5 dependence in the range $\bar{\omega}_{xy} \in [0.0025, 0.5]$. In this range, only the branch α_2 is available and has a linear dispersion $B \propto \omega \propto q$. The matrix elements

 Matthias Droth and Guido Burkard, Physical Review B **87**, 205432 (2013).

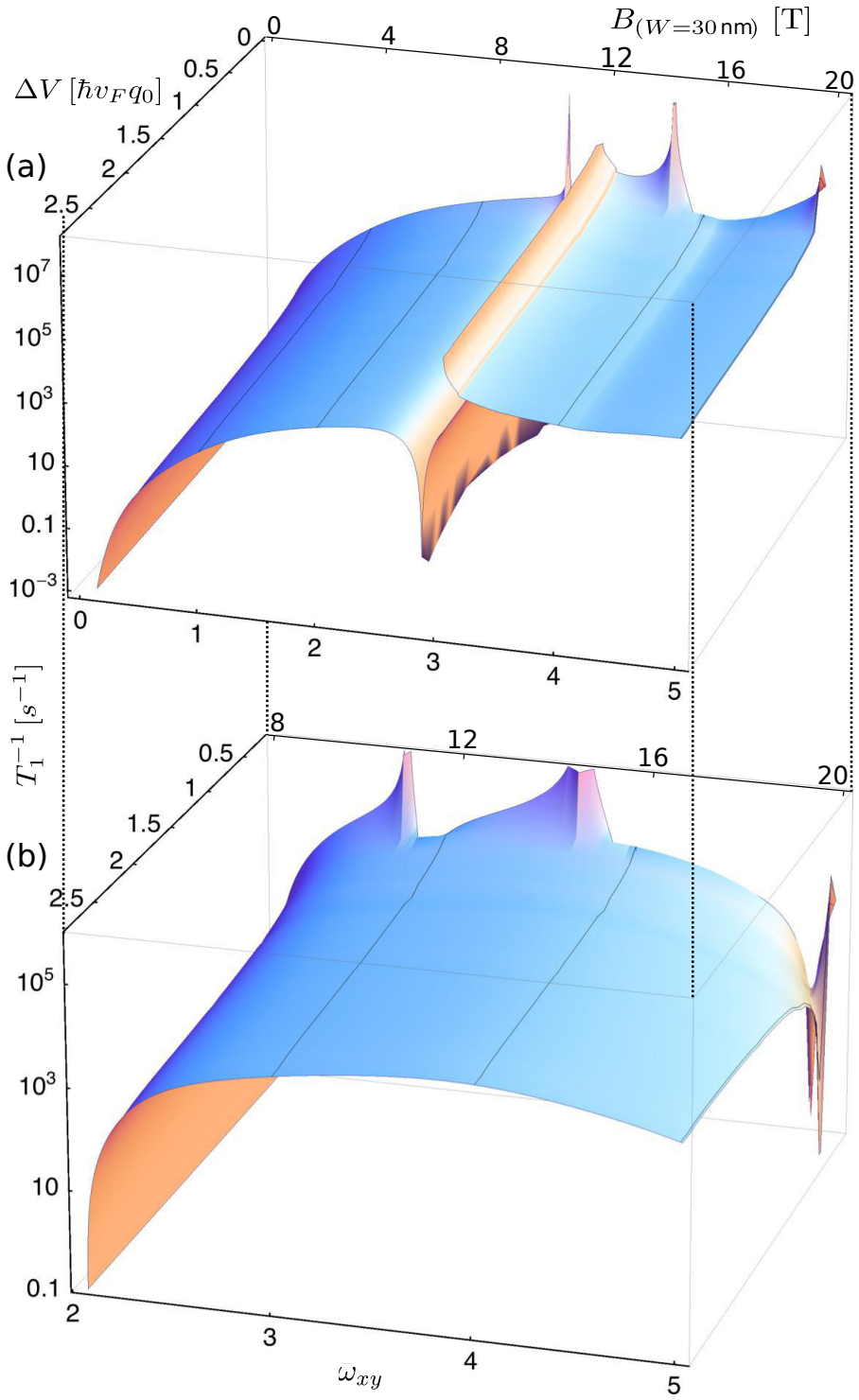

Figure 6.9.: The relaxation rate T_1^{-1} for (a) free and (b) fixed mechanic boundaries. (a) This case is similar to Fig. 6.8 (a) yet with aspect ratio $L/W = 2$. (b) Fixed boundary conditions and $L/W = 2$. Due to the gapped phonon spectrum, the rate T_1^{-1} vanishes below $\bar{\omega}_{xy} = 2.06$ for our model and with fixed boundaries. Moreover, T_1^{-1} is not discontinuous in $\bar{\omega}_{xy}$ as the branch $\tilde{\alpha}_1$ never becomes flat for finite $\bar{q}$, see Fig. 6.4 (b).

$(\mathcal{H}_{\mathrm{EPC}})_{k'k}$ have one power in B due to (i) the gradients $\propto q$ in Eq. (6.22), (ii) dipole approximation $\propto q$, and (iii) Van Vleck cancelation $\propto B$, each. Because of the prefactor $\propto \omega^{-0.5}$ in Eq. (6.18), we find $(\mathcal{H}_{\mathrm{EPC}})_{k'k} \propto B^{2.5}$. As α_2 is linear and hence $\rho_{\mathrm{states}} \propto B^0$ for this low-field regime, this explains $T_1^{-1} \propto B^5$. Destructive interference of matrix elements $(\mathcal{H}_{\mathrm{VEP}})_{k'k}$ and $(\mathcal{H}_{\mathrm{BLC}})_{k'k}$ can lead to a very small but nonzero relaxation rate.

Fig. 6.9 (a) shows a plot similar to Fig. 6.8 (a), yet for $L/W = 2$. The qualitative picture is much different from the aspect ratio $L/W = 5$. Figs. 6.6 - 6.9 (a) all show discontinuities at $\bar{\omega}_{xy} = 3.05$ that stem from the branch α_4, for which the density of states has a Van Hove singularity at $\bar{q}_0$ while the coupling $\mathcal{H}_{\mathrm{EPC}}$ remains finite, Fig. 6.4 (a).

6.7.2. Fixed boundary conditions

Most importantly, fixed boundaries result in a gapped phonon spectrum. This means that spin relaxation involving only one phonon cannot occur for magnetic fields that correspond to $\bar{\omega}_{xy} < 2.06$. Note, that for a typical width $W = 30\,\mathrm{nm}$, $\bar{\omega}_{xy} = 2.06$ corresponds to a magnetic field of 8.25 T. However, phonon scattering may still take place below this threshold. In contrast to our claim in [Droth(2011)], only the branch $\tilde{\alpha}_1$ contributes to the spin relaxation rate. Gradients, dipole approximation, and Van Vleck cancelation play the same role as for free boundaries, yet due to the gap the frequency ω is not proportional to some power of q such that there is no power law that connects T_1^{-1} and B as for free boundaries.

Fig. 6.9 (b) shows an analog to panel (a), yet for fixed boundaries. For aspect ratios larger than in Fig. 6.9 (b), oscillations occur which can again be explained with the phonon phase e^{iqy} that rotates according to the phonon dispersion when ω changes. These oscillations arise only if the dot length is large enough.

6.8. Discussion

The spin relaxation times we find in our work range from 10^{-7} seconds to beyond the second range. For cases where T_1 is very long, it can be expected that other mechanisms not considered here will dominate. Our results depend on the aspect ratio L/W, the barrier height ΔV, and the Zeeman splitting $g\mu_{\mathrm{B}}B \propto \bar{\omega}_{xy}$ but also on the mechanic boundary conditions that lead to different phonon dispersions. By choosing/adjusting these degrees of freedom properly, T_1 can be in the range of seconds. We attribute such long relaxation times to several effects:

(i) GNRs are quasi one-dimensional systems similar to carbon nanotubes. Both the phonon and the electron density of states are thus limited compared to bulk graphene [Bulaev(2008)].

(ii) Destructive interference between the deformation potential and the bond-length change as well as oscillations due to the phonon phase e^{iqy} that rotates according to the phonon dispersion when ω changes both reduce the relaxation rate T_1^{-1} by several orders of magnitude for specific magnetic fields.

Matthias Droth and Guido Burkard, Physical Review B **87**, 205432 (2013).

(iii) In contrast to other graphene QD systems, the electronic states in aGNRs are invariant under time reversal symmetry which leads to Van Vleck cancelation [VanVleck(1940), Trauzettel(2007), Struck(2010)]. As a result, Eq. (6.21) vanishes for $B = 0$.

(iv) Deflection coupling to out-of-plane modes vanishes as the evenly distributed weights on K and K' spinor components cancel out. As a result, only the very rigid in-plane modes need to be considered. This rigidity leads to a generally small density of phonon states ρ_{states} [Trauzettel(2007), Rudner(2010)].

(v) Phonons do not couple to spin directly so that spin-orbit coupling needs to be included. However, spin-orbit coupling in graphene is weak compared to other systems (e.g. carbon nanotubes) [Trauzettel(2007), Bulaev(2008), Gmitra(2009)].

(vi) The admixture of electronic states in Eq. (6.20) includes bound and extended states. However, only every second bound state contributes; for parity in y-direction, j_k and $j_{k'}$ may not be even or odd at the same time, Fig. 6.2 (b). States that are energetically far apart from the ground state play a small role in the sum which is usually the case for extended states, depending on ΔV. As a consequence, the admixture of these electronic states is suppressed [Khaetskii(2001), Trauzettel(2007)].

(vii) Due to parity in x-direction, not all phonon branches contribute to spin relaxation but only those with explicit labels in Fig. 6.4, for which Eq. (6.22) is even in x. This limits the number of relaxation channels [Droth(2011)]. It is an open question how strong the avoided relaxation channels contribute to T_1^{-1} if this symmetry is broken.

(viii) We assume phonon vacuum in Eq. (6.4). A finite temperature can be included by multiplying the rate T_1^{-1} with the expectation value of the Bose distribution $\langle n_{\alpha,q}(B,T)\rangle$ as explained in Sec. 6.6.

The carbon isotope ^{12}C has no nuclear spin and the natural abundance of ^{13}C, which has spin 1/2, is only 1%. Thus, pure dephasing which comes from coupling to nuclear spins is likely to play a minor role in graphene devices and $T_1 \approx T_2/2$ becomes a good measure for overall coherence. Our results show that electronic spin qubits in aGNRs are promising for spintronics applications like the Loss-DiVincenzo quantum computer. With view to recent advances in controlling the edge termination of GNRs it will be interesting to see whether aGNR spintronics can be realized in experiment.

7. Piezoelectricity in planar boron nitride via a geometric phase

The work presented in this chapter is based on a collaboration with Vitor Pereira from the Graphene Research Centre at the National University of Singapore. The manuscript is in preparation.

Abstract
Due to their low surface mass density, two-dimensional materials with a strong piezoelectric response are interesting for nanoelectromechanical systems with high susceptibility. In contrast to graphene, the two sublattices in two-dimensional hexagonal boron nitride (hBN) are occupied by different types of atoms, which allows for piezoelectricity. Recently, the piezoelectric tensor of extended hBN has been calculated via density functional theory (DFT). While an analytical description of piezoelectricity does exist for hBN nanotubes, this is, to our knowledge, not the case for two-dimensional hBN. We set up a Hamiltonian that involves the strain-induced pseudomagnetic field and derive the piezoelectric tensor using the modern theory of polarization. Our findings are in exact agreement with symmetry arguments and give an analytical explanation for the piezoelectric electron-phonon coupling in planar hBN. We also provide an estimation of the coupling strength and find a piezoelectric response similar to reported DFT results.

7.1. Introduction

Two-dimensional materials have become a subject of intense research efforts since the experimental discovery of graphene about one decade ago [Novoselov(2004), Eda(2008), CastroNeto(2009), Lin(2010)]. In addition to the monolayer of graphite, also transition metal dichalcogenides, hBN and other two-dimensional materials have gained a lot of attention due to outstanding electronic, magnetic, structural, and other properties [Novoselov(2005-2), Dean(2010), Radisavljevic(2011), Duerloo(2012)]. The prospect of stacking individual monolayer materials with different properties on top of each other holds the promise of a new paradigm on solid state physics as this modular concept of layered Van der Waals heterostructures might enable tailoring physical properties akin to the bandgap engineering of semiconductor heterostructures [Novoselov(2012), Geim(2013)].

A key role in such heterostructures would likely fall to hBN. While graphene is praised for its electronic properties, these are prone to interactions with a substrate and to contamination [Nomura(2006), Chen(2008), Chen(2008-2)]. With a large bandgap at the charge neutrality point of graphene and a lattice mismatch of less than 2%, hBN has the potential to preserve graphene's outstanding properties within such heterostructures [Robertson(1984), Dean(2010), Sławińska(2010), Britnell(2012), Paszkowicz(2002)]. Both graphene and hBN feature a honeycomb lattice with two atoms per unit cell. In contrast to graphene, the two sublattices of hBN are occupied with different atoms, boron (B) and nitrogen (N), see Fig. 7.1. This results in an ionic bond between the p_z orbitals and a bandgap [Robertson(1984), Watanabe(2004), Topsakal(2009), Bhowmick(2011)] of $\approx$6 eV. In addition, the inversion symmetry of the graphene lattice is lifted in hBN, thus allowing for piezoelectricity [Mele(2002), Duerloo(2012)].

Piezoelectricity is the response of the electronic state of a material when subjected to external stress. Depending on the material, the piezo effect can provide a strong coupling between the electronic and the mechanic state of matter. It has been shown that this coupling can be used to cool a nanoelectromechanical system (NEMS) into its mechanical quantum ground state [O'Connell(2010)]. Its strong piezoelectric response, high mechanical stability, and easy handling make hBN a prime material for novel technological applications. Due to its two-dimensional lattice, hBN has the lowest surface mass density of all piezoelectric crystals and might allow for NEMS with as yet unknown susceptibility [Bunch(2007)]. Moreover, hBN could provide the electromechanical coupling in a layered graphene/hBN heterostructure and thus mediate a mechanical interaction with the electronic properties of graphene.

In this article, we use the modern theory of polarization to calculate the piezoelectric tensor of hBN with the geometric phase approach [Vanderbilt(1990), Mele(2002), Xiao(2010)]. It has been shown for hBN nanotubes, that the dominant contribution ($\approx$80%) to the polarization comes from the π valence band and that the contribution from the σ valence bands has the same sign [Sai(2003)]. In a simple model, the π band of hBN is described by a linear Hamiltonian similar to the one of graphene, yet with a mass term that gives rise to a sublattice splitting [Hunt(2013)]. This ansatz has also been used to describe the chirality dependent piezoelectric response of hBN nanotubes [Mele(2002)].

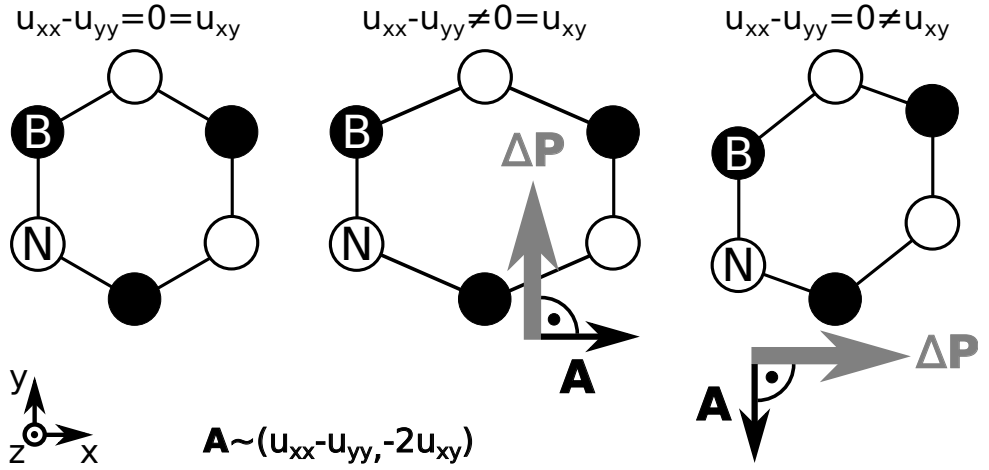

Figure 7.1.: The lattice of hBN does not posses an inversion center and hence allows for piezoelectricity. Strains u_{ij} that lift the trigonal symmetry generate a change in the polarization $\Delta \boldsymbol{P}$ that is perpendicular to the strain-induced pseudomagnetic vector potential $\boldsymbol{A}$.

Strain can be included in the Dirac-like Hamiltonian by virtue of Peierls' substitution with a valley-dependent pseudomagnetic vector potential [Suzuura(2002), CastroNeto(2009)]. The effect on the electron dispersion can be expressed in terms of a Berry curvature whose integral over the Brillouin zone yields the change of the electric polarization. We also provide an estimate for the so far unknown coupling constant of the pseudomagnetic vector potential in hBN. Using this ansatz, we calculate the components of the piezoelectric tensor. All symmetry constraints are satisfied and the numerical values are similar to those obtained via DFT calculations [Duerloo(2012), Nye]. Independently from our model, we find that the pseudomagnetic vector potential is perpendicular to the strain-induced polarization.

7.2. Model

In the vicinity of the high-symmetry points, the π bands of hBN are described by a Dirac-like Hamiltonian with a sublattice potential,

$$\mathcal{H} = \hbar v_F (q_x \sigma_x + \tau q_y \sigma_y) + \Delta \sigma_z \,, \tag{7.1}$$

where $\hbar v_F = \frac{3}{2}|t|d$, with the hopping amplitude t and the atomic distance d, $\boldsymbol{q}$ is the electron momentum w.r.t. the high-symmetry points K ($\tau = +1$) and K' ($\tau = -1$), and the sublattice pseudospin is denoted by Pauli matrices $\boldsymbol{\sigma}$. The sublattice potential Δ arises due to the different on-site energies of boron ($+\Delta > 0$) and nitrogen ($-\Delta$) atoms. For this Hamiltonian, the effect of strain on the electronic spectrum can be modeled with Peierls' substitution $\boldsymbol{q} \mapsto \tilde{\boldsymbol{q}} = \boldsymbol{q} + \tau \boldsymbol{A}$, where $\tau \boldsymbol{A}$ is the valley-dependent pseudomagnetic vector potential,

$$\begin{pmatrix} A_x \\ A_y \end{pmatrix} = \frac{3\beta\kappa}{4\hbar v_F} \begin{pmatrix} u_{xx} - u_{yy} \\ -2u_{xy} \end{pmatrix} . \tag{7.2}$$

Here, $\beta = d\frac{\partial t}{\partial d}$ describes the variation of the hopping amplitude w.r.t. bond-length change, κ depends on microscopic details, and u_{ij} is the strain tensor [Suzuura(2002), CastroNeto(2009)]. In Sec. 7.5, we will discuss the entire prefactor / coupling strength in more detail. Via $\boldsymbol{A}$, strain will affect the electron dispersion and thus give rise to a finite Berry curvature in the parameter space (q_x, q_y, λ), where λ parametrizes the the sublattice potential Δ. As is well known, graphene is described by Eq. (7.1) without the term $\Delta\sigma_z$ and, being centrosymmetric, does not exhibit piezoelectricity. In a gedanken-experiment, we can evolve λ adiabatically from 0 (graphene) to Δ (hBN). For nonzero $\boldsymbol{A}$, the polarization changes during this evolution. According to the theory of adiabatic transport, this change is given by [Mele(2002), Xiao(2010)]

$$\Delta P_i = 2e \sum_\tau \int_0^\Delta \mathrm{d}\lambda \int_{\mathrm{BZ}/2} \frac{\mathrm{d}^2 q}{4\pi^2} \Omega^{(\tau)}_{q_i,\lambda} \,, \tag{7.3}$$

where for a given valley τ, we only integrate half the Brillouin zone around that valley. Integration of the entire Brillouin zone is restored by the summation over τ. Moreover, we have included the prefactor 2 because of spin degeneracy of Eq. (7.1). The Berry curvature is given by

$$\Omega^{(\tau)}_{q_i\lambda} = i \left(\langle \frac{\partial u_\tau}{\partial q_i} | \frac{\partial u_\tau}{\partial \lambda} \rangle - \langle \frac{\partial u_\tau}{\partial \lambda} | \frac{\partial u_\tau}{\partial q_i} \rangle \right) , \tag{7.4}$$

where $|u_\tau\rangle$ is an eigenstate of Eq. (7.1) with $\boldsymbol{q} \mapsto \tilde{\boldsymbol{q}}$.

7.3. Integration of the Berry curvature

With the substitution $\boldsymbol{q} \mapsto \tilde{\boldsymbol{q}}$ and with units $\hbar v_F = 1$, Eq. (7.1) can be written as $\mathcal{H} = \boldsymbol{p}_\tau \cdot (\tau\sigma_x, \sigma_y, \sigma_z)$. In spherical coordinates, $\boldsymbol{p}_\tau = (\tilde{q}_x, \tilde{q}_y, \lambda)$ is represented by $\boldsymbol{p}_\tau = |E|(\sin\theta\cos\phi, \sin\theta\sin\phi, \cos\theta)$, where $E_\pm = \pm|E| = \pm(\tilde{q}_x^2 + \tilde{q}_y^2 + \lambda^2)^{1/2}$ are the eigenenergies of $\mathcal{H}$. Graphene corresponds to $\lambda = 0$ and hBN to $\lambda = \Delta$. Only filled states contribute to the polarization. The valence eigenstates $|u_\tau\rangle$ of $\mathcal{H}$ are given by

$$|u_\tau\rangle = \frac{1}{\sqrt{2}} \begin{pmatrix} -\sqrt{1-\cos\theta} \\ \frac{\tau e^{i\tau\phi}\sin\theta}{\sqrt{1-\cos\theta}} \end{pmatrix} . \tag{7.5}$$

Using the representation of $\boldsymbol{\nabla}_{\boldsymbol{p}_\tau}$ in spherical coordinates and $\partial_{q_i} = (\partial_{q_i}\tilde{q}_i)\partial_{\tilde{q}_i} = \partial_{\tilde{q}_i}$, one obtains the Berry curvature for the valence eigenstates,

$$\Omega^{(\tau)}_{q_x\lambda} = -\tau \frac{\sin\theta\sin\phi}{2|E|^2} = -\tau \frac{\tilde{q}_y}{2|E|^3} \,. \tag{7.6}$$

Without the prefactor $-e/4\pi^2$, the integral of $\Omega^{(\tau)}_{q_x\lambda}$ over λ in Eq. (7.3) yields

$$\int_0^\Delta \mathrm{d}\lambda \frac{\tau\tilde{q}_y}{|E|^3} = \frac{\tau\Delta\tilde{q}_y}{(\tilde{q}_x^2 + \tilde{q}_y^2)\sqrt{\Delta^2 + \tilde{q}_x^2 + \tilde{q}_y^2}} \,. \tag{7.7}$$

For each valley, we integrate Eq. (7.7) over a square [(-W,-W),(+W,+W)] centered around the high symmetry points K and K', respectively. The area of each square is exactly half the area of the Brillouin zone, i.e. $W = 3^{-3/4}\pi/d$. For the integral over q_x, we find

$$\begin{aligned}\int_0^{\Delta} \mathrm{d}\lambda \int_{-W}^{+W} \mathrm{d}q_x \frac{\tau\tilde{q}_y}{|E|^3} &= -\tau \arctan \frac{\Delta(-W+\tau A_x)}{\tilde{q}_y\sqrt{\Delta^2+(-W+\tau A_x)^2+\tilde{q}_y^2}} \\ &\quad +\tau \arctan \frac{\Delta(W+\tau A_x)}{\tilde{q}_y\sqrt{\Delta^2+(W+\tau A_x)^2+\tilde{q}_y^2}}\,. \end{aligned} \tag{7.8}$$

The integral of Eq. (7.8) over q_y results in a lengthy expression, that vanishes for $A_y = 0$ but is finite for $A_y \neq A_x = 0$, i.e., A_x can be neglected in lowest order. With $A_x = 0$, the integration over q_y simplifies and Eq. (7.3) becomes

$$\begin{aligned}\Delta P_x &= -\frac{e}{\pi^2}\sum_{s=\pm1}\left(\Delta \operatorname{arcoth}\frac{sW}{\sqrt{(A_y-sW)^2+W^2+\Delta^2}}\right. \\ &\quad +sW \operatorname{arcoth}\frac{\Delta}{\sqrt{(A_y-sW)^2+W^2+\Delta^2}} \\ &\quad \left.-(A_y-sW)\arctan\frac{sW\Delta}{(A_y-sW)\sqrt{(A_y-sW)^2+W^2+\Delta^2}}\right)\,, \end{aligned} \tag{7.9}$$

where we have already added up the contributions from both valleys. It follows that the derivative of ΔP_x w.r.t. A_y is given by

$$\begin{aligned}\frac{\partial P_x}{\partial A_y} &= \frac{e}{\pi^2}\left(\arctan\frac{W\Delta}{(A_y-W)\sqrt{(A_y-W)^2+W^2+\Delta^2}}\right. \\ &\quad \left.-\arctan\frac{W\Delta}{(A_y+W)\sqrt{(A_y+W)^2+W^2+\Delta^2}}\right)\,. \end{aligned} \tag{7.10}$$

The expression for $\frac{\partial P_y}{\partial A_x}$ — which is found with the same routine, starting from Eq. (7.6) — is identical but with A_y replaced by A_x and an overall minus sign.

7.4. Tensor components and symmetry

The components of the (converse) piezoelectric tensor d_{ijk} (e_{ijk}) are given by

$$d_{ijk} = \frac{\partial P_i}{\partial \sigma_{jk}}\,, \qquad e_{ijk} = \frac{\partial P_i}{\partial \epsilon_{jk}}\,, \tag{7.11}$$

where σ_{jk} is the stress tensor and $\epsilon_{jk} = \partial_k u_j$. The symmetric part of ϵ_{jk} is the strain tensor $u_{jk} = (\partial_k u_j + \partial_j u_k)/2$. The lattice of hBN belongs to the point group $\bar{6}m2$ (D_{3h}), which implies that

$$\begin{aligned} d_{211} &= -d_{222} = d_{112}\,, \\ d_{21} &= -d_{22} = d_{16}/2\,, \end{aligned} \tag{7.12}$$

while all other components vanish identically. In the second line, we use the matrix notation, i.e., $d_{21} = d_{211}$, $d_{22} = d_{222}$, and $d_{16} = 2d_{112}$. In contrast to the stress tensor, ϵ_{jk} is not symmetrized and hence $e_{16} = e_{112}$,

$$\begin{aligned} e_{211} &= -e_{222} = e_{112}\,, \\ e_{21} &= -e_{22} = e_{16}\,. \end{aligned} \tag{7.13}$$

We point out that for the point group $\bar{6}m2$, the orientation of the coordinates plays a role [Duerloo(2012), Nye]. Here, we use the standard orientation with a mirror plane perpendicular to the x-axis, see Fig. 7.1. The piezoelectric effect and the converse piezoelectric effect are connected by the fourth-rank elastic tensor, $e_{ij} = d_{ik}C_{jk}$, in matrix notation. From Eq. (7.2), it is clear that

$$e_{112} = \frac{\partial P_x}{\partial \epsilon_{xy}} = \frac{\partial A_y}{\partial \epsilon_{xy}} \frac{\partial P_x}{\partial A_y} = -\frac{3\beta\kappa}{4\hbar v_F} \frac{\partial P_x}{\partial A_y}\,. \tag{7.14}$$

Since the expression for $\partial P_y/\partial A_x$ is analog to Eq. (7.10) but has a different sign, the symmetry constraints given by Eq. (7.13) are indeed satisfied. All other components are zero. With this equation and $e_{ijk} = e_{ikj}$, the change of polarization upon strain is given by $\Delta P_x = e_{112}\epsilon_{xy} + e_{121}\epsilon_{yx} = 2e_{112}u_{xy}$ and $\Delta P_y = e_{211}\epsilon_{xx} + e_{222}\epsilon_{yy} = e_{112}(u_{xx} - u_{yy})$, i.e. $\Delta \boldsymbol{P} \sim (2u_{xy}, u_{xx} - u_{yy}) \perp \boldsymbol{A}$.

7.5. Estimation of the coupling strength — Result

The coupling strength $\frac{3}{4}\beta\kappa$ in Eq. (7.2) depends on the parameter κ and, via $\beta = d\frac{\partial t}{\partial d}$, on the variation of the hopping t upon bond-length change. As in graphene, the π band comes about due to electron hopping between the p_z-orbitals of the two sublattices. Because of the difference in electronegativity between boron and nitrogen atoms, there is an electron transfer from B to N. The bond thus gains an ionic character, in contrast to the purely covalent bond in graphene [Robertson(1984), Topsakal(2009)]. This leads to the term $\Delta\sigma_z$ in Eq. (7.1). In analogy to graphene, we assume an exponential decay of the hopping amplitude [Pereira(2009), Ribeiro(2009)],

$$t(d) = t_0 e^{-\alpha \frac{d-d_0}{d_0}}\,, \tag{7.15}$$

where $t_0 = t(d_0)$ denotes the hopping for the equilibrium bond length d_0. We fit the decay parameter α to the sparsely available data of t for different d. The work [Giraud(2012)] contains a tight-binding calculation of hBN with up to third-nearest neighbors and the results are consistent with typical results from DFT calculations, see e.g. [Topsakal(2009), Sławińska(2010), Duerloo(2012)]. Both the first- and the third-nearest neighbor hopping ($t^{(1)}$ and $t^{(3)}$, respectively) occur between B and N. With $t_0 = t^{(1)} = t(1.44\,\text{Å}) = -2.16\,\text{eV}$ and $t^{(3)} = t(2.88\,\text{Å}) = -0.08\,\text{eV}$ [Giraud(2012)], we find $\alpha = 3.3$, i.e., a value very similar to the one in graphene [Ribeiro(2009)]. Assuming $t_0 = -2.3\,\text{eV}$, we infer from Eq. (7.15) that $\beta = -\alpha t_0 = 7.6\,\text{eV}$ [Robertson(1984), Sławińska(2010), Ribeiro(2011)].

The parameter κ depends on microscopic details. Within a valence-force-field model, it is given by [Suzuura(2002), Harrison]

$$\kappa = \frac{\mu}{\sqrt{2}B} = \frac{1-\sigma}{\sqrt{2}(1+\sigma)}\,, \tag{7.16}$$

where we have expressed the bulk (B) and shear (μ) moduli in terms of Poisson's ratio σ and Young's modulus (which cancels out) in the second step [Droth(2011)]. Poisson's ratio is related to the components of the elastic tensor via $\sigma = C_{12}/C_{11}$ [Peng(2012)]. Typical values for hBN are $C_{11} = 300\,\mathrm{N/m}$ and $C_{12} = 53\,\mathrm{N/m}$, leading to $\kappa = 0.5$ [Duerloo(2012), Peng(2012)]. This results in a coupling strength of $\frac{3}{4}\beta\kappa = 3\,\mathrm{eV}$ in Eq. (7.2).

With the parameters listed in Table 7.1, evaluation of Eqs. (7.10) and (7.14) leads to $e_{112} = 7.5 \times 10^{-11}\,\mathrm{As/m}$. Since $e_{21} = d_{21}(C_{11} - C_{12})$ in matrix notation, this relates to $d_{211} = 3.0 \times 10^{-13}\,\mathrm{m/V}$.

$\beta = 7.6\,\mathrm{eV}$	$\kappa = 0.5$	$W = 2.39\,\mathrm{Å}^{-1}$
$\hbar v_F = 5.0\,\mathrm{eV\,Å}$	$\Delta = 3.2\,\mathrm{eV}$	$C_{11} - C_{12} = 247\,\mathrm{N\,m^{-1}}$

Table 7.1.: Numerical values of the parameters we use in our calculation. The parameters β and κ have been discussed in Sec. 7.5 and $W = 3^{-3/4}\pi/d$ follows from the atomic distance $d = 1.44\,\mathrm{Å}$ [Sławińska(2010), Paszkowicz(2002)]. The prefactor of the Hamiltonian, $\hbar v_F = 3|t|d/2$, is determined by said value for d and $|t| = 2.3\,\mathrm{eV}$ [Robertson(1984), Sławińska(2010), Ribeiro(2011)]. The given sublattice potential corresponds to a bandgap of 6.4 eV [Watanabe(2004), Sławińska(2010), Bhowmick(2011), Topsakal(2009)]. For the elastic constants, we have used $C_{11} = 300\,\mathrm{N/m}$ and $C_{12} = 53\,\mathrm{N/m}$ [Duerloo(2012)].

7.6. Discussion

We have calculated the piezoelectric tensor of flat hBN via the approach of a geometric phase taking into account only the π valence band by virtue of a low-energy, Dirac-like Hamiltonian. Strain is included in the model as a pseudomagnetic gauge field. We find $e_{112} = 7.5 \times 10^{-11}\,\mathrm{As/m}$ for the converse piezoelectric effect and $d_{211} = 3.0 \times 10^{-13}\,\mathrm{m/V}$ for the direct effect. All symmetry constraints on the tensor elements are satisfied. Due to symmetry, the strain-induced polarization is always perpendicular to the strain-induced gauge field, regardless of our model. We also provide an estimate for the so far unknown coupling strength of the gauge field in hBN and find $\frac{3}{4}\beta\kappa = 3\,\mathrm{eV}$.

To our knowledge, no experimental data for piezoelectricity in flat hBN has been published. However, we can compare our values to the DFT results in [Duerloo(2012)]. Our values are about a factor of 2 (5) smaller than the DFT results for relaxed (clamped) ions. There are several reasons why our calculation might possibly miss the physical values. First, our model involves only the π valence band but not the lower lying bands. For hBN nanotubes, the π states contribute about 80% to the effect [Sai(2003)]. Second, our

estimation for the coupling strength of the gauge field in hBN — which appears linearly in our model — while plausible, relies on sparse data, thus compromising reliability. Merely by doubling the coupling strength, we can fit our results to the relaxed ions DFT results of [Duerloo(2012)]. Third, the low-energy approximation with a Dirac-like Hamiltonian might fall short of a calculation that relies on the dispersion within the entire Brillouin zone.

8. Magnetic-field tunable antiferromagnetism in graphene nanoflakes

The work presented in this chapter has been submitted to Physical Review B for publication. A preprint version of our manuscript is available on arXiv.org under the identification number 1405.5451.

Abstract

Graphene nanoflakes are interesting because electrons are naturally confined in these quasi zero-dimensional structures, whereas confinement in bulk graphene would require a bandgap. Vacancies inside the graphene lattice lead to localized states and the spins of such localized states may be used for spintronics. We perform a tight-binding description of a nanoflake with two vacancies and include a perpendicular magnetic field via Peierls' phase. The tunnel coupling strength and from it the exchange coupling between the localized states can be obtained from the energy splitting between numerically calculated bonding and antibonding energy levels. This allows us to estimate the exchange coupling J, which governs the dynamics of coupled spins. We predict the possibility of switching in-situ from $J > 0$ to $J = 0$ by tuning the magnetic field. In the former case, the ground state will be antiferromagnetic with Néel temperatures accessible by experiment.

8.1. Introduction

Beyond the outstanding mechanical, optical, and electronic characteristics common to bulk graphene [Novoselov(2004), Lee(2008), Nair(2008), Kuzmenko(2008), Eda(2008), Lin(2010)], graphene nanoflakes are predicted to feature magnetic properties, as well [Fernández-Rossier(2007), Ezawa(2007), Yazyev(2010)]. These qualities make such nano-islands of graphene very interesting for spintronics and other applications [Trauzettel(2007), Petta(2005), Hong(2013)]. Lattice defects can be generated on purpose by means of ion or electron beam irradiation [Krasheninnikov(2007), Robertson(2013)] and are expected to give rise to magnetic moments of about one Bohr magneton. The associated magnetic ordering can in principle be ferromagnetic as well as antiferromagnetic [Lieb(1989), Yazyev(2007), Palacios(2008), Uchoa(2008), Grujić(2013)] and recent progress in spin sensitive measurements allows to probe these predictions [Wiesendanger(2009), Decker(2013), Nair(2012)]. In practice, however, modifying the magnetic properties of defect-induced magnetic graphene typically requires the preparation of new devices. Graphene nanoflakes can be grown using chemical vapor deposition, typically with zigzag boundaries and hexagonal symmetry of the entire flake [Luo(2011), Phark(2011), Subramaniam(2012)]. In addition, it has been reported that the interaction of the nano-island edges with the substrate smoothens the boundary and enhances the symmetry of the electronic wave functions [Hämäläinen(2011)]. In analogy to the hydrogen molecule, two localized states in a double quantum dot (DQD) can hybridize to form bonding and antibonding eigenstates of the combined system. In return, the localized states can be obtained by taking the even and odd superpositions of bonding and antibonding states. The exchange coupling J describes the coupling between the two localized spins [Burkard(2006), Schrieffer(1966)]. In this article, we calculate J as a function of the magnetic field and for different realistic flake configurations.

A typical graphene nanoflake with zigzag edges, hexagonal symmetry, and two lattice vacancies is sketched in Fig. 8.1. Each vacancy gives rise to localized states and thus serves as a quantum dot [Pereira(2006), Xiong(2007)]. The entire flake with two vacancies is therefore a realization of a DQD. If the vacancies are located at positions $\boldsymbol{r}_{\mathrm{vac}} = (0, \pm y)$, the flake retains some symmetry which, in our case, also applies to the probability densities of the electronic states. The complete eigensystem is found by numerical diagonalization of a tight-binding Hamiltonian where nearest neighbors up to third order are taken into account and a perpendicular magnetic field $\boldsymbol{B} \parallel \boldsymbol{e}_z$ is included via Peierls' phase. Interactions are effectively taken into account in a second step when calculating J. The retained symmetry allows us to superpose the eigenstates in a meaningful way. We calculate the exchange coupling J as a function of the magnetic field and for different flake configurations, which we specify by the number of benzene rings per edge, b, and the distance between the vacancies and the flake center, d, as shown in Fig. 8.1. We find that J can be tuned over several orders of magnitude within one device and can even vanish for certain flake configurations by changing the magnetic field. For finite J, the ground state of the system is antiferromagnetic and Néel temperatures up to $\approx 8\,\mathrm{K}$ put our results in reach of experimental analysis via spin-polarized scanning tunneling microscopy or SQUID magnetometry [Wiesendanger(2009), Decker(2013), Nair(2012)].

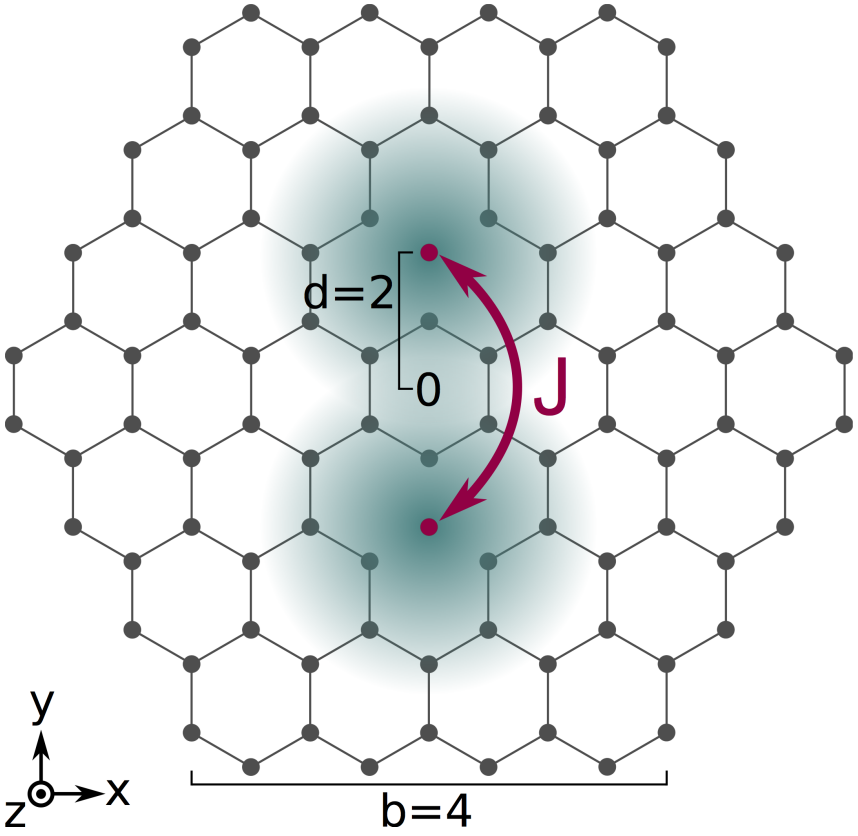

Figure 8.1.: Schematic of a hexagonal graphene nanoflake where grey dots indicate the locations of carbon atoms. The flake is specified by the number of benzene rings along each edge, b, and the distance d (in units of the atomic distance $a = 1.42\,\text{Å}$) of the vacancies, located at $\boldsymbol{r}_{\text{vac}} = (0, \pm y)$, from the cartesian origin in the flake center. The sketched island has a $(b = 4, d = 2)$ configuration. The vacancies (red dots) give rise to localized spin states (green shade) whose mutual dynamics is described by the exchange coupling J. A magnetic field $\boldsymbol{B} \parallel \boldsymbol{e}_z$ can be applied perpendicularly to the flake plane.

8.2. Tight-binding model

We consider a tight-binding Hamiltonian with hopping between neighbors up to third order,

$$\mathcal{H} = \sum_{\langle i,j \rangle} t_{ij}^{(1)} c_i^\dagger c_j + \sum_{\langle\langle i,j \rangle\rangle} t_{ij}^{(2)} c_i^\dagger c_j + \sum_{\langle\langle\langle i,j \rangle\rangle\rangle} t_{ij}^{(3)} c_i^\dagger c_j \,, \tag{8.1}$$

where the hopping from atom j to a neighbor of n-th order, i, depends on the magnetic field $\boldsymbol{B} \parallel \boldsymbol{e}_z$ via Peierls' phase,

$$\begin{aligned} t_{ij}^{(n)}(B) &= t_{ij}^{(n)}(0) \exp\left[i\frac{e}{\hbar} \int_{\boldsymbol{R}_i}^{\boldsymbol{R}_j} \boldsymbol{A}(\boldsymbol{r}) \cdot \mathrm{d}\boldsymbol{r} \right] \\ &= t_{ij}^{(n)}(0) \exp\left[i\frac{eB}{2\hbar}(y_i + y_j)(x_i - x_j) \right] . \end{aligned} \tag{8.2}$$

We use the Landau gauge $\boldsymbol{A}(\boldsymbol{r}) = -By\boldsymbol{e}_x$ and zero field hopping amplitudes $t_{ij}^{(1)}(0) = 2.8\,\mathrm{eV}$, $t_{ij}^{(2)}(0) = 0.7\,\mathrm{eV}$, and $t_{ij}^{(3)}(0) = 0.3\,\mathrm{eV}$. The operator $c_i^\dagger$ (c_i) creates (annihilates) an electron at site $\boldsymbol{R}_i$. At zero magnetic field, the symmetries of the Hamiltonian are the same as the lattice symmetries, as seen in Fig. 8.1: the mirror symmetries $\mathcal{M}_x : x \mapsto -x$ and $\mathcal{M}_y : y \mapsto -y$ as well as the rotation by π, $\mathcal{R}_2 : (x, y) \mapsto (-x, -y)$. At finite fields only the twofold rotation $\mathcal{R}_2$ remains.

The numerically obtained eigenstates have an arbitrary phase. However, we find that it is possible to multiply any eigenstate $|n\rangle$ with a phase such that $\langle \boldsymbol{r}|n\rangle = \langle n|\mathcal{M}_x\boldsymbol{r}\rangle$. While the probability density $|\langle \boldsymbol{r}|n\rangle|^2$ remains unaffected, these phase rotations do matter for the probability densities of even and odd superpositions of two eigenstates. In order to obtain states localized at $\boldsymbol{r}_{\mathrm{vac}}$ by forming these superpositions, it is necessary to perform these phase rotations on the (anti-)bonding eigenstates.

8.3. Localized states and exchange coupling

The graphene nanoflake with vacancies can be interpreted as a symmetric, unbiased DQD. Such a system can be described by the Hamiltonian

$$\mathcal{H}_{\mathrm{DQD}} = \begin{pmatrix} \bar{E} & t \\ t^* & \bar{E} \end{pmatrix} \tag{8.3}$$

where the localized states $\{|+y\rangle, |-y\rangle\}$ form the basis, t is the hopping amplitude from site to site and $\bar{E}$ is the degenerate eigenenergy for $t = 0$. An arbitrary gauge is taken into account via the phase ϕ, that is, $t = |t|e^{i\phi}$. The eigensystem of Eq. (8.3) is

$$E_\pm = \bar{E} \pm |t| \,, \tag{8.4}$$

$$|\psi_\pm\rangle = (|+y\rangle \pm e^{-i\phi}|-y\rangle)/\sqrt{2} \,. \tag{8.5}$$

Thus, the hybridized *bonding* ($|\psi_-\rangle$) and *antibonding* ($|\psi_+\rangle$) states are superpositions of the localized states and their energy splitting is given by $\Delta = 2|t|$.

The diagonalization of the tight-binding Hamiltonian Eq. (8.1) yields the bonding and antibonding eigenstates and the according energy spectrum. If two states $|\psi_\pm\rangle$, bonding and antibonding, are selected, then the according localized states $|\pm y\rangle$ are obtained by superposing these (anti-)bonding states. This corresponds to undoing the superposition in Eq. (8.5). The magnitude of the hopping between the localized states is easily obtained from the energy splitting between the (anti-)bonding states: $|t| = \Delta/2$. To do this, we

need to select a pair of bonding and antibonding states and superpose them after rotating them with phases as described at the end of Sec. 8.2.

We find that if hopping amplitudes beyond nearest neighbors are taken into account and B is finite[1], no degeneracies occur (except for spin, which will only be considered later). Since $\mathcal{R}_2$ commutes with the Hamiltonian Eq. (8.1), the energy eigenstates are also eigenstates of $\mathcal{R}_2$, with eigenvalues $+1$ (even) and -1 (odd). We consider any two states $|n\rangle$, $|m\rangle$ with (i) eigenenergies that lie next to each other in the discrete energy spectrum, $E_n = E_{m-1}$, and with (ii) opposite symmetry under the twofold rotation, $\langle n|\mathcal{R}_2|n\rangle\langle m|\mathcal{R}_2|m\rangle = -1$. We refer to the lower-energetic state as *bonding* and the higher energetic one as *antibonding*, see Eq. (8.5). In addition to $\mathcal{R}_2$, the lattice also possesses the symmetries $\mathcal{M}_x$ and $\mathcal{M}_y$. We find that the probability density of any eigenstate, $|\langle \boldsymbol{r}|n\rangle|^2$, also possesses these symmetries. Since the localized states are localized in the upper/lower half of the flake, their probability densities should only posses the symmetry $\mathcal{M}_x$. This symmetry fixes the relative phase in the superposition of the bonding and antibonding states.

The procedure described so far allows us to find the localized states $|\pm y\rangle$ for any selection of (anti-)bonding states. To describe the spin physics in the DQD, we include spin $\sigma = \uparrow, \downarrow$ and an on-site Coulomb repulsion U. It is well known that the system has six possible states: three spin triplets and three spin singlets [Burkard(2006)]. In the weak tunneling regime $|t| \ll U$, the triplet state $|T_0\rangle = \frac{1}{\sqrt{2}}(c^\dagger_{+y\uparrow}c^\dagger_{-y\downarrow} + c^\dagger_{+y\downarrow}c^\dagger_{-y\uparrow})|0\rangle$ and singlet state $|S\rangle = \frac{1}{\sqrt{2}}(c^\dagger_{+y\uparrow}c^\dagger_{-y\downarrow} - c^\dagger_{+y\downarrow}c^\dagger_{-y\uparrow})|0\rangle$ decouple from the other states and are effectively described by the Hamiltonian [Burkard(2006), Schrieffer(1966)]

$$\mathcal{H}_{\mathrm{TS}} \approx \begin{pmatrix} 0 & 0 \\ 0 & -J \end{pmatrix}, \quad J = \frac{4|t|^2}{U}, \tag{8.6}$$

where the basis is $\{|T_0\rangle, |S\rangle\}$ and the Coulomb repulsion is $U = e^2/4\pi\epsilon_0|r|$, with the elementary charge e and the vacuum permittivity ϵ_0. For $|r|$, we use the standard deviation of the probability density of the corresponding localized state. The Zeeman term $g\mu_B \boldsymbol{B}\cdot\boldsymbol{\Sigma}$, where g is the electron g-factor in graphene, μ_B is the Bohr magneton, and $\boldsymbol{\Sigma} = \boldsymbol{\sigma}_{+y} + \boldsymbol{\sigma}_{-y}$ is the total spin, commutes with $\mathcal{H}$ as well as $\mathcal{H}_{\mathrm{TS}}$ and hence does not affect the calculation of J.

8.4. Results

Since the nanoflake consists of a total number of N atoms, the tight-binding Hamiltonian Eq. (8.1) has dimension $N \times N$. Because of spin degeneracy, the N sorted eigenenergies E_n are only filled up to $E_{N/2}$ (counting from the bottom of the spectrum) by the p_z electrons. With doping, states in the range $E_{N/2} \pm \Delta V$, where we assume $\Delta V \approx 300\,\mathrm{meV}$, become accessible[2].

For a given flake, we calculate t for all pairs of numerically computed (anti-)bonding

[1] For $B = 0$, the Hamiltonian does not only possess the symmetry $\mathcal{R}_2$ but also $\mathcal{M}_x$ and $\mathcal{M}_y$, as described below Eq. (8.2). To avoid degeneracies, we use a vanishingly small magnetic field of $10^{-7}\,\mathrm{T}$ instead

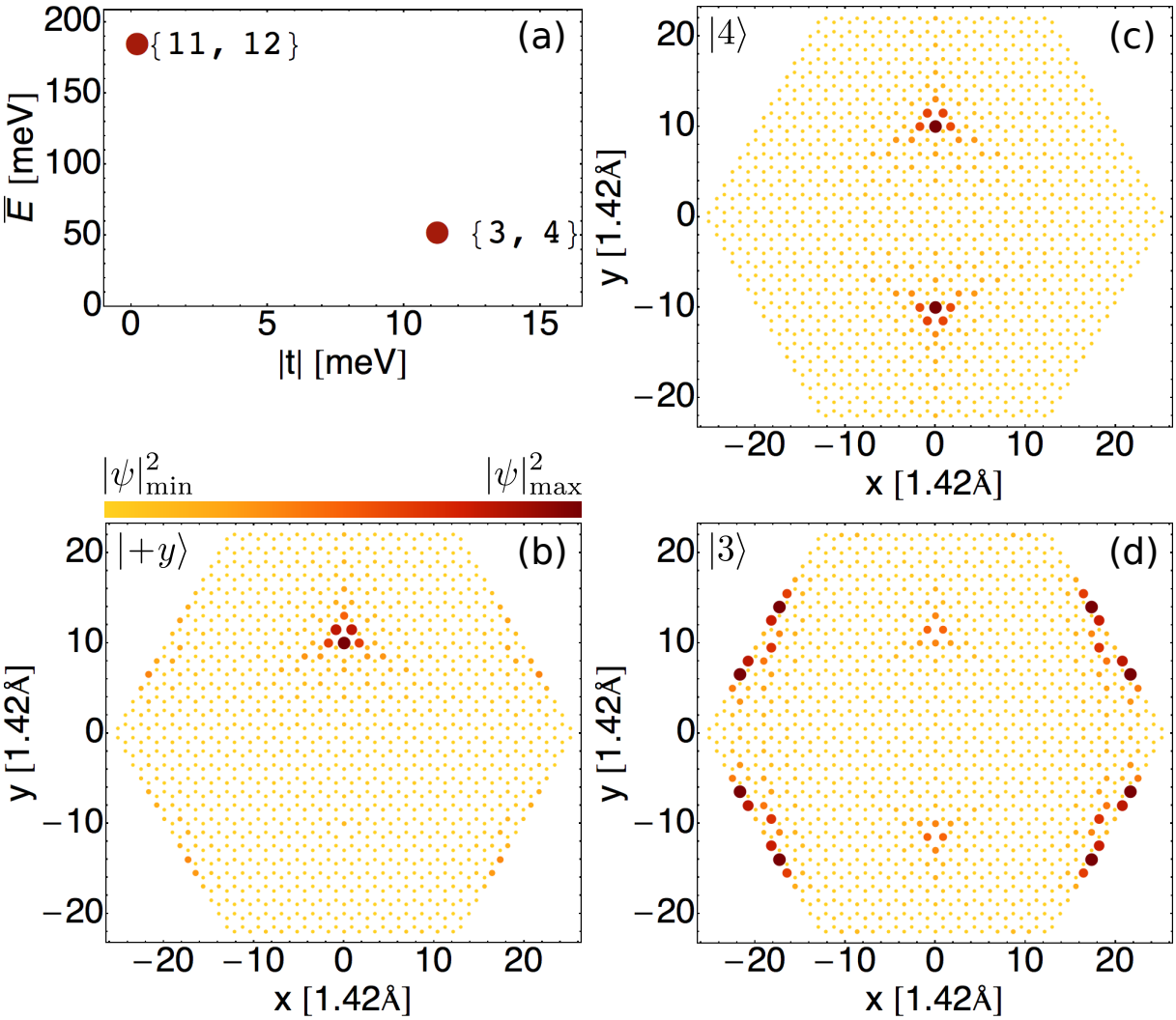

Figure 8.2.: Results for a $(b = 15, d = 11)$ flake. (a) Two pairs of (anti-)bonding states satisfy the criteria (i-v). For the corresponding localized states, we plot the energy $\bar{E}$ (w.r.t. $E_{N/2}$) vs. $|t|$. The hopping amplitude $|t|$ is maximal for the pair $\{|3\rangle, |4\rangle\}$. (b-d) Probability densities of (b) the localized state $|+y\rangle$, (c) of $|4\rangle$, and (d) of $|3\rangle$. The probability density of $|-y\rangle$ looks similar to the one of $|+y\rangle$, yet mirrored about the x-axis.

states, $\{|n\rangle, |m\rangle\}$, that satisfy three criteria, two of which have been introduced before: (i) the states need to lie next to each other in the spectrum, $m = n+1$ and (ii) they need to have opposite symmetry $\langle n|\mathcal{R}_2|n\rangle\langle m|\mathcal{R}_2|m\rangle = -1$. In addition, (iii) the states should become accessible via doping, $|E_{n,m} - E_{N/2}| \leq \Delta V$. To calculate the exchange coupling as described by Eq. (8.6), it is important that moreover (iv) no third state is involved in the superposition of localized states, $\min(\{E_n - E_{n-1}, E_{m+1} - E_m\}) > \Delta$ and that (v) terms higher than $\mathcal{O}(|t|/U)$ can be neglected, $|t| \ll U$.

of $B = 0$.

[2]The Fermi energy E_F is related to the carrier density n via $E_F = \hbar v_F \sqrt{\pi n}$, where $\hbar$ is the reduced Planck constant and $v_F \approx 10^6$ m/s is the Fermi velocity. High carrier densities have been reported e.g. in [Lin(2010)].

d \ b	10		15		20		30		40	
1	3.498 0.056	(1)	5.150 0.184	(1)	0.914 0.008	(1)	1.833 0.050	(3)	0.426 0.003	(2)
2	-	(0)	3.494 0.084	(3)	-	(0)	2.937 0.123	(1)	0.457 0.004	(4)
4	-	(0)	5.048 0.171	(1)	-	(0)	0.555 0.004	(1)	0.426 0.003	(3)
5	-	(0)	0.239 0.000‡	(1)	3.216 0.095	(2)	1.177 0.020	(3)	0.448 0.004	(5)
7	-	(0)	5.048 0.171	(1)	4.922 0.211	(2)	1.081 0.018	(6)	1.162 0.026	(2)
8	9.002 0.346	(1)	0.239 0.000‡	(1)	3.076 0.086	(2)	0.779 0.009	(2)	2.387 0.100	(5)
10	-	(0)	5.048 0.171	(2)	0.739 0.006	(1)	-	(0)	1.185 0.026	(6)
11	3.301 0.047	(1)	**11.125** **0.762**	**(2)**	3.298 0.102	(1)	0.526 0.004	(1)	0.460 0.004	(3)
13	7.839 0.297	(1)	-	(0)	1.555 0.026	(3)	0.783 0.007	(1)	1.162 0.026	(5)
14	-	(0)	2.428 0.037	(2)	2.002 0.038	(3)	0.302 0.001	(2)	0.562 0.006	(5)

Table 8.1.: Results for various flakes with parameters (b, d) (see Fig. 8.1). For vanishing magnetic field[1], we list the maximum hopping amplitude $|t|$ (upper number) and the maximal exchange coupling J (lower number) in meV. We underline (underdash) J if $J(B) = 0$ can be reached for $B < 15$ T ($B > 15$ T). The integer in parentheses behind $|t|$ and J indicates the number of (anti-)bonding pairs that satisfy the criteria (i-v). The numbers in boldface correspond to the case shown in Fig. 8.2 (a).
‡ The more accurate value is 0.00047 meV.

To simplify our notation, we now count eigenstates and eigenenergies w.r.t. the middle of the spectrum. That is, instead of $E_{N/2+n}$ we will just write E_n. Fig. 8.2 illustrates our results for a $(b = 15, d = 11)$ nanoflake. For this flake and at vanishing[1] magnetic field, two pairs of states fulfill the criteria (i-v), namely $\{|3\rangle, |4\rangle\}$ as well as $\{|11\rangle, |12\rangle\}$. In Fig. 8.2 (a), we plot the hopping amplitude that belongs to the corresponding localized states against the energy $\bar{E}$ of those localized states (Eq. (8.4)). Among the states satisfying the criteria (i-v), the states $|3\rangle$ and $|4\rangle$ lead to the highest hopping amplitude, namely $|t| = 11.1$ meV. Figs. 8.2 (b-d) show the probability densities of (b) the localized state $|+y\rangle$ and its parent states (c) $|4\rangle$ and (d) $|3\rangle$. The probability density of the localized state $|-y\rangle$ is not shown but can be obtained by applying the mirror symmetry $\mathcal{M}_y$ to the probability density of $|+y\rangle$.

For vanishing[1] magnetic field and any given combination of b and d, we now pick the pair of (anti-)bonding states that satisfies the criteria (i-v) and which has the highest hopping

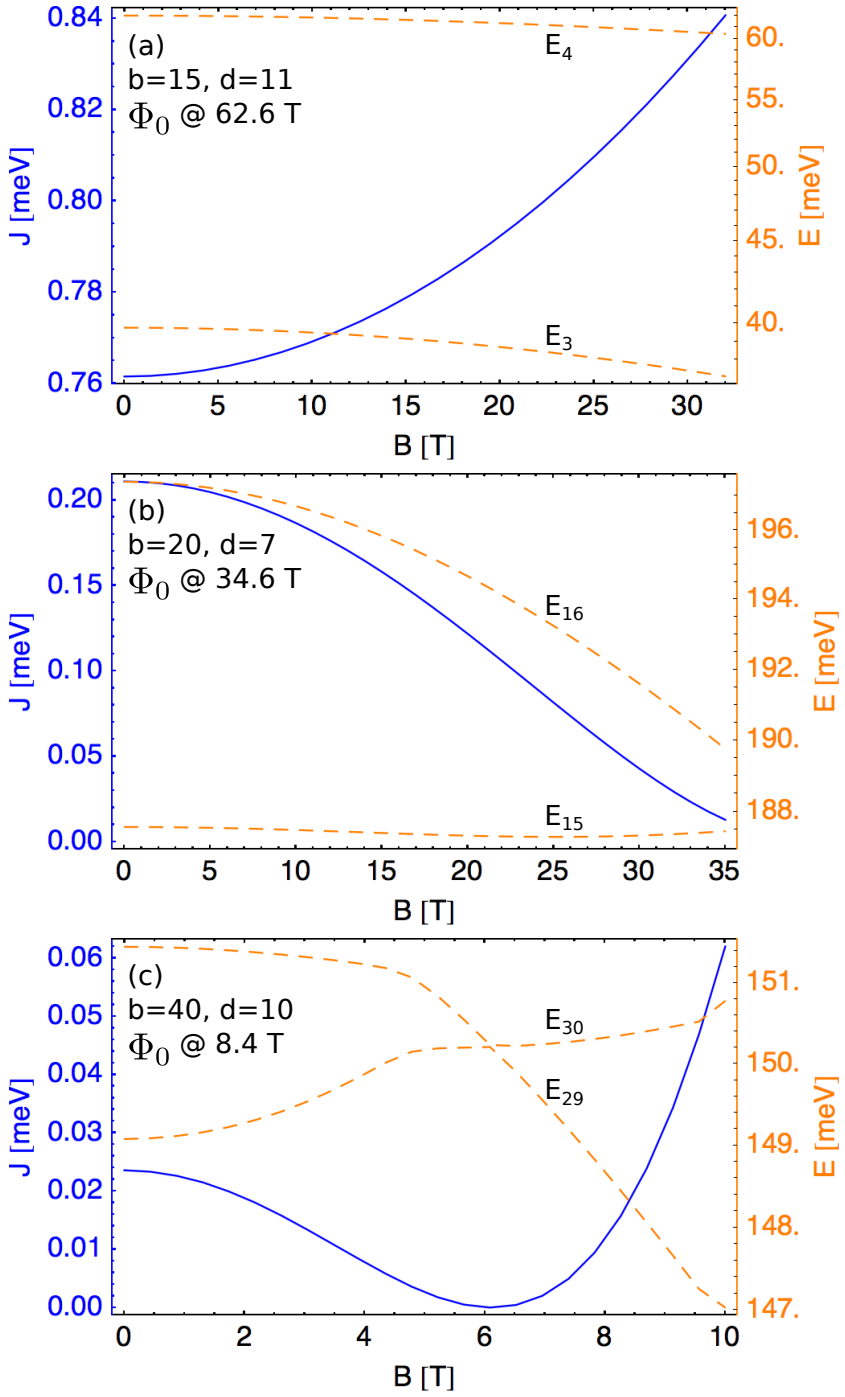

Figure 8.3.: The exchange coupling J (solid blue line and left axis) and the eigenenergies (dashed orange line and right axis) of the corresponding (anti-)bonding states are plotted against a magnetic field perpendicular to the plane of the flake. The flake parameters (b, d), the energy levels E_m and E_n, as well as the magnetic field at which one flux quantum passes through the flake are indicated in the plots. The behavior of $J(B)$ is very specific. Depending on the case, J can be tuned only weakly (a), over an order of magnitude (b), or can be switched off ($J = 0$) by tuning the spectrum into a degeneracy (c).

amplitude. This maximal hopping amplitude $|t|$ and the maximal exchange coupling J are listed in Table 8.1 for $b = 10, 15, 20, 30, 40$ and $d = 1, 2, 4, 5, 7, 8, 10, 11, 13, 14$. The upper numbers in the table indicate $|t|$ and the lower numbers indicate J, both in meV. The ensuing integer in parentheses shows the number of (anti-)bonding pairs that satisfy the criteria (i-v) for this combination of b and d. Since J is always positive, it is clear from Eq. (8.6) that the singlet state $|S\rangle$ is favored. The resulting antiferromagnetism should be stable up to the Néel temperature $T_\mathrm{N} \cong J/k_\mathrm{B}$, where k_B is Boltzmann's constant. The value of T_N for a given (b, d) configuration can be obtained by multiplying the according numerical value of J in Table 8.1 with 11.6 K.

Depending on d, the lattice site of the vacancy at $(0, +y)$ can have a nearest neighbor site either at $(0, y+a)$ or at $(0, y-a)$, see Fig. 8.1. The former case leads to a repetitive pattern of $|t|$ and J for e.g., $b = 15$ and $d = 4, 7, 10$ and the latter case applies for e.g., $b = 15$ and $d = 5, 8$. Such patterns occur for various parameters, yet some of them are concealed in Table 8.1 because the conditions (i-v) do not apply or the according hopping amplitude $|t|$ is not maximal for a given (b, d) configuration. Throughout a pattern, we find resembling probability densities of the localized states and numerically close but different values for $|t|$ and J. In all cases listed in Table 8.1, the flake edges play a non-negligible role, see e.g. Fig. 8.2 (d). As a consequence, $|t|$ and J vary strongly in b and d. For large enough b and d, we expect that the influence of b vanishes, and a smooth decay of $|t|$ and J w.r.t. d, yet we do not reach this regime.

The Hamiltonian Eq. (8.1) and hence its spectrum $\{E_n\}$ and the exchange coupling J depend on the magnetic field B. In Fig. 8.3, we plot J and the eigenenergies of the corresponding (anti-)bonding states $\{|E_n\rangle, |E_m\rangle\}$ against B. Typically, the properties of an electronic state change for magnetic fields of the order of $B = \Phi_0/A$, where $\Phi_0 = h/2e$ is the magnetic flux quantum with Planck's constant h and A is the surface area occupied by the state, which we approximate by the surface area of the flake.

We find that the Coulomb repulsion U depends only weakly on the magnetic field while the splitting $\Delta = E_m - E_n$ and hence $|t|$ depend strongly on B. That is, $J(B)$ is mainly determined by the behavior of $E_m(B) - E_n(B)$. Depending on the (b, d) configuration, the exchange coupling J can be tuned over a certain range (Figs. 8.3 (a,b)) and if a degeneracy $E_m(B) = E_n(B)$ occurs, it is even possible to switch the coupling on ($J > 0$) and off ($J = 0$) by tuning the system towards or away from the degeneracy (Fig. 8.3 (c)). In Table 8.1, we underline (underdash) J of those flake configurations, for which a degeneracy, i.e. $J(B) = 0$, can be reached with a magnetic field smaller (greater) than 15 T.

8.5. Conclusion and outlook

We have set up a tight-binding model for hexagonal graphene nanoflakes with zigzag edges and two vacancies at positions $\boldsymbol{r}_\mathrm{vac}=(0, \pm y)$. Symmetry allows us to infer the explicit form of the localized vacancy states from the bonding and antibonding eigenstates. This system is a realization of a DQD. In the weak tunneling regime, the triplet $|T_0\rangle$ and the singlet $|S\rangle$ are split by the exchange coupling J and their dynamics decouples

from other spin states. We have calculated J for states that can be reached via doping leading to a shift of the chemical potential by less than $\pm 300\,\mathrm{meV}$ and that satisfy the remaining criteria (i-v) described above. A perpendicular magnetic field is included in the tight-binding model via Peierls' phase and can be used to tune J by orders of magnitude, depending on the flake configuration (b, d). In particular, it thus is possible to tune the system into a degeneracy where $J{=}0$. This in-situ tunability of the exchange coupling can be very useful for spintronics and quantum information related applications as it allows for the modification of the magnetic properties without preparing a new device. The ground state spin configuration is antiferromagnetic. Depending on the lattice configuration, we have found Néel temperatures up to 8.8 K, which allows for experimental testing of our results. Ferromagnetic ordering, $J{<}0$, is conceivable by including non-local Coulomb interaction [Burkard(1999)]. Our calculation can be extended to include spin-orbit coupling or additional potentials that model a Moiré pattern or boundary effects. Assigning both vacancies to the same sublattice results in reduced symmetry. These cases might be treatable with a modified, less symmetry-dependent calculation.

9. Final remarks

Now, we sum up the results of our theoretical studies and point out the main results. We also discuss our ongoing work and promising areas of research for future projects.

9.1. Conclusion

Graphene is a novel, monatomically thin material with many interesting properties. A historical sketch of its discovery, properties, and its potential for nanotechnology have been outlined in Chapter 1. In particular, the low density of nuclear spins and an intrinsically weak spin-orbit interaction make it a promising material for spintronics applications like the Loss-DiVincenzo quantum computer. The lowest surface mass density of all crystals combined with its outstanding mechanic properties might enable nanoelectromechanical systems with yet unknown sensitivity. These prospects have motivated (and still do) our studies of spins and phonons in graphene nanostructures. In the wake of graphene, other two-dimensional materials like hBN have gained attention. The outstanding electronic properties of graphene are prone to surface contamination but might be protected in layered graphene/hBN heterostructures.

In Chapter 2, we have reviewed the electronic properties of graphene and hBN via tight-binding models. In the first part about monolayers, we have calculated the dispersion relations within the entire Brillouin zone and we have derived approximate Hamiltonians for momenta close to the high symmetry points K and K'. For graphene, this yields the well-known Dirac-Hamiltonian. We have also calculated the density of states and the effective mass. The Klein paradox makes it challenging to confine charge carriers in electrostatically defined graphene QDs. We have used a minimal tight-binding model to describe bilayer graphene without and with a perpendicular electric field. The latter case is interesting for applications as it leads to a field-tunable bandgap that can be used to avoid Klein tunneling. Moreover, we discuss bilayer hBN and a graphene/hBN heterostructure.

The effect of strain on the electronic structure of hexagonal lattices has been the topic of Chapter 3. Two types of electron-phonon coupling, namely the bond-length change and the deformation potential, have been inferred from the low-energy tight-binding description. In addition, strain also affects the Fermi velocity and the spin-orbit interaction mediates a coupling between the electron spin and out-of-plane deformations. Homogeneous strain preserves the lattice periodicity but changes the shape of the unit cell, which translates to a deformed Brillouin zone.

In Chapter 4, we have introduced basics of the geometric phase, also known as Berry's

phase. We have reviewed the adiabatic evolution of a system and the derivation of electric polarization via adiabatic transport. Moreover, we have reviewed the derivation of Peierls' phase via a tight-binding model with modified Wannier states and Peierls' well-known substitution.

We have used the continuum model to derive the acoustic phonons in graphene nanoribbons in Chapter 5. Due to the monatomic thickness of graphene, this model requires some modifications. In contrast to bulk graphene, nanoribbons have only one quasi continuous direction and the boundary conditions at the edges parallel to this direction play a significant role. We have found the classical solutions and have formulated them in terms of orthonormal eigenmodes. Via the Lagrangian and the canonical momentum, this leads to the quantized form. The dispersion relations of both in-plane and out-of-plane phonons are gapped for fixed boundary conditions and gapless for free boundary conditions. We have also inferred sound velocities that are in agreement with reported values. In the limit of infinite ribbon width (compared to the phonon wavelength), all our findings are in agreement with bulk graphene. We have also commented on preliminary results for the spin relaxation time.

A detailed study of electron spin relaxation in armchair graphene nanoribbon quantum dots has followed in Chapter 6. Coupling of the spin to in-plane phonons has been considered via Rashba-type spin-orbit interaction and an electron-phonon coupling comprising the deformation potential and the bond-length change. In lowest order, out-of-plane phonons play no role since the effective spin-phonon coupling differs only in the sign for K and K', and the electronic states have equal weight on both valleys. We have evaluated the spin relaxation rate for different QD aspect ratios, confinement potentials, and for fixed as well as for free boundary conditions of the lattice vibrations. We have found Van Vleck cancellation and destructive/constructive interference of the two in-plane electron-phonon couplings. As a result, the spin relaxation times range from $T_1{=}10^{-7}\,\mathrm{s}$ to beyond seconds. For free boundaries and magnetic fields up to $B{=}0.5\,\mathrm{T}$, we have found that the spin relaxation time T_1 scales as $T_1^{-1}{\propto}B^5$. In agreement with our previous work, fixed boundaries (gapped phonon spectrum) bear the opportunity to suppress spin relaxation in lowest order.

In Chapter 7, we have used an analytic model to derive the piezoelectric effect in planar hBN. Our model involves an adiabatic evolution of the sublattice potential as well as the strain-induced pseudomagnetic vector potential, which is based on the bond-length change and thus benefits from our previous work. The Berry curvature has been integrated analytically and we have found that the resulting components of the piezoelectric tensor conform all symmetry constraints. Their numerical values depend on the previously unknown coupling strength of said vector potential (in hBN), for which we have provided a first estimate. Our estimated coupling strength of 3 eV, relates to $e_{112}{=}7.5{\times}10^{-11}\,\mathrm{As/m}$ for the converse piezoelectric effect and to $d_{211}{=}3.0{\times}10^{-13}\,\mathrm{m/V}$ for the direct piezoelectric effect. Reported DFT results for relaxed (clamped) ions are about a factor 2 (5) greater than our values. Experimental data is not available, yet we have indicated why the true values might possibly be greater than ours.

Graphene nanoflakes are an interesting system for spintronics. In Chapter 8, we have studied the exchange coupling between two localized defect states in such systems. We

have made a full tight-binding ansatz that includes a perpendicular magnetic field via Peierls' phase. Each vacancy gives rise to a localized state such that the entire system with two vacancies can be interpreted as a double quantum dot. We have relied on symmetry and further criteria to identify localized vacancy states. The on-site Coulomb repulsion has been respected by means of a Schrieffer-Wolff transformation that leads to an effective Hamiltonian in the subspace of singlet $|S\rangle$ and triplet $|T_0\rangle$. These states are split by the exchange coupling J, which depends on the magnetic field. Since $J \geq 0$, the spin ordering is always antiferromagnetic. The according Néel temperatures can be as high as 8.8 K. Moreover, we have found that — depending on the exact shape of the flake — $J(B)$ can be tuned *in situ* over several orders of magnitude by adjusting the magnetic B-field. In some cases, we have even found that the antiferromagnetism can be switched on ($J>0$) and off ($J=0$) by tuning B.

9.2. Outlook

The field of graphene-related research still grows exponentially and both the public and the private sectors make massive investments in graphene and other two-dimensional materials. The production of high-quality graphene at an industrial scale and low cost will remain crucial for commercial applications but steady advances of production techniques in the past and the ongoing research effort indicate that further progress can be expected.

Relating to our studies, the production of atomically precise armchair graphene nanoribbons (aGNRs) has been a rather recent accomplishment [Ruffieux(2012)]. Yet the construction of electrostatically defined quantum dots in such atomically precise aGNRs still poses a huge challenge and it is unclear until when our results from Chapter 6 can be tested in experiment. Electrostatically defined quantum dots in bilayer graphene have already been realized [Goossens(2012)]. We thus envisage the calculation of spin coherence in bilayer graphene quantum dots. Basics of this project are presented in Appendix D.

Other two-dimensional materials like hBN have gained attention only recently so the absence of experimental data on the piezoelectricity of planar hBN is not surprising. To our knowledge, the only available data come from DFT calculations [Duerloo(2012)] and our theoretical study in Chapter 7, where we have used a low-energy approximation. The full description of π bands in hBN would likely lead to a more accurate result. Since the Hamiltonian remains two-by-two, the Berry curvature can still be integrated efficiently numerically.

Graphene nanoflakes with perfect hexagonal symmetry can already be realized and vacancies can be induced on purpose via electron or ion bombardment [Hämäläinen(2011), Krasheninnikov(2007)]. One possible extension of our work on the B-field tunable exchange coupling in such flakes (Chapter 8) would include non-local Coulomb interaction. We expect that the magnetic ordering can also be ferromagnetic in this case. It would be of great interest for spintronics to tune from ferromagnetic to antiferromagnetic ordering *in situ* with an external magnetic field.

A. Spin qubits and coherence

Quantum information relies on the use of quantum bits or *qubits* as the basic unit of quantum mechanical information. Qubits are more general than classical bits in that a qubit is an arbitrary (yet normalized) superposition of the quantum states $|0\rangle$ and $|1\rangle$,

$$|\psi\rangle = \alpha|0\rangle + \beta|1\rangle\,. \tag{A.1}$$

The coefficients α and β should obey $|\alpha|^2 + |\beta|^2 = 1$ to ensure a normalized state. Consequently, a qubit can contain much more information than a classical bit and quantum computing aims at exploiting this feature [Shor(1994), Shor (1997), Loss(1998), Gisin(2002), Nielsen&Chuang]. In the following, we first introduce qubit coherence and then, we turn to a special realization of qubits in the form of spin qubits. We also make a short comment on electron spin qubits in graphene [Droth(2010)].

Qubit coherence

Coherence refers to the stability of a relative phase that determines the interference of waves. A well-known example is the coherent light of a laser, where phase stability leads to constructive interference over long distances. Decoherence is the loss of coherence. Due to the wave functions used in quantum mechanics, coherence is intrinsically linked to qubits.

The third DiVincenzo criterion requires that the decoherence time of qubits be about 10^4 times longer than the clock cycle [DiVincenzo(1999)]. While coherence is no condition for classical computing, it is absolutely crucial to quantum computing. The advantages of a quantum computer come at the necessity for coherent qubits (and many other requirements). The qubit state in (A.1) can be rewritten as[1]

$$|\psi\rangle = \cos\frac{\theta}{2}|0\rangle + e^{i\phi}\sin\frac{\theta}{2}|1\rangle\,, \tag{A.2}$$

where θ determines the ratio $|\alpha/\beta|$ and ϕ is the relative phase. Both angles are real numbers and together, they parametrize the Bloch sphere as shown in Fig. A.1 (a). The poles correspond to the only two states available for a classical bit. Qubits, in contrast, can take a state anywhere on the entire sphere [Nielsen&Chuang].

The qubit state is prone to unwanted interactions with the environment. As part of a larger system, the qubit interferes with other quantum states. Unless the system is very well isolated from its outer environment — which is usually not the case[2] — there will be

[1] A common phase of both summands has no physical meaning and is set to zero.

[2] A counterexample are Bose-Einstein condensates.

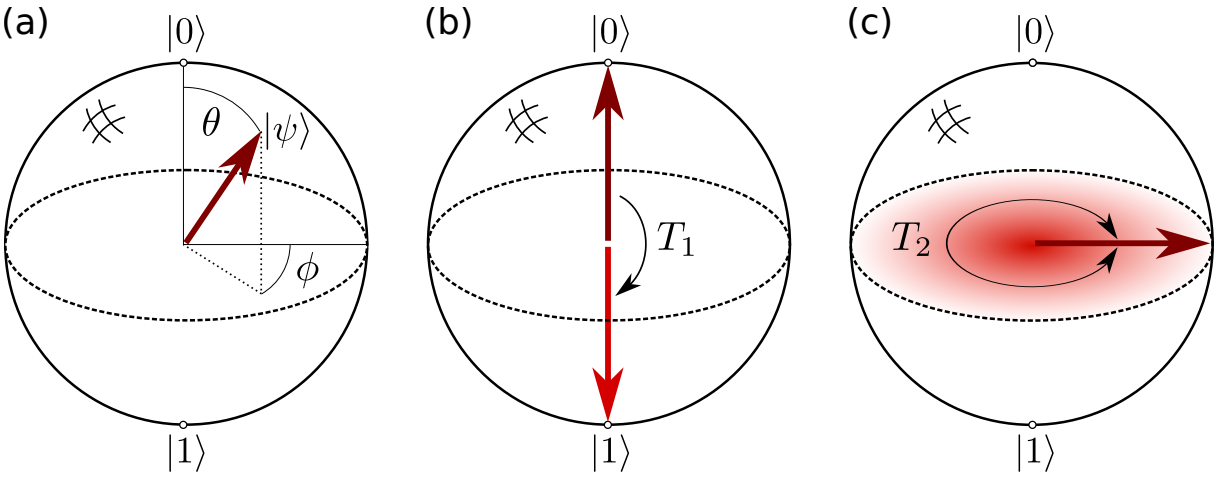

Figure A.1.: (a): Each point on the Bloch sphere corresponds to a qubit state. The angle θ determines the contributions from $|0\rangle$ and $|1\rangle$ while ϕ denotes their relative phase. (b): For $E_0 > E_1$ the higher energy state $|0\rangle$ decays to $|1\rangle$ on the relaxation timescale T_1. This means that an initial superposition will eventually lose its $|0\rangle$ component and hence the relative phase ϕ. (c): The phase may also fade without energy exchange, thus leading to a mixture of qubit states. Such effects further increase the decay rate of the off-diagonal elements in (A.3), which is characterized by the dephasing timescale T_2. If relaxation induced dephasing is the only contribution it follows that $T_2 = 2\,T_1$.

an uncontrollable interference with unknown quantum states which affects the qubit and cannot be undone completely. However, a partial recovery of the initial qubit state can be achieved [Petta(2005)].

The meaning of the timescales T_1 and T_2, which characterize the coherence of an initially well-defined qubit, can be illustrated on the Bloch sphere. If there is an energy difference[3], say $E_0 > E_1$, the transition $|0\rangle \to |1\rangle$ involves the exchange of energy and is described by the relaxation time T_1, Fig. A.1 (b). The dephasing time T_2 relates to the fading out of the relative phase ϕ, thus leading to a mixed state, see Fig. A.1 (c). No energy exchange is necessary but the process is still irreversible if it leads to an increase of entropy.

For concreteness, consider a qubit state that is initially represented by the density matrix

$$\rho(t{=}0) = |\psi\rangle\langle\psi| = \begin{pmatrix} \cos^2\frac{\theta}{2} & \cos\frac{\theta}{2}\sin\frac{\theta}{2}e^{-i\phi} \\ \cos\frac{\theta}{2}\sin\frac{\theta}{2}e^{i\phi} & \sin^2\frac{\theta}{2} \end{pmatrix} = \begin{pmatrix} |\alpha|^2 & \alpha\beta^* \\ \beta\alpha^* & |\beta|^2 \end{pmatrix} \tag{A.3}$$

and corresponds to a pure state. Due to interference with other, possibly mixed quantum states, the phase ϕ smears out uniformly and the density matrix becomes a mixture of states of all phases,

$$\rho(t \to \infty) = \int_{\phi=0}^{2\pi} \frac{\mathrm{d}\phi}{2\pi} |\psi\rangle\langle\psi| = \int_{\phi=0}^{2\pi} \frac{\mathrm{d}\phi}{2\pi} \begin{pmatrix} \cos^2\frac{\theta}{2} & \cos\frac{\theta}{2}\sin\frac{\theta}{2}e^{-i\phi} \\ \cos\frac{\theta}{2}\sin\frac{\theta}{2}e^{i\phi} & \sin^2\frac{\theta}{2} \end{pmatrix} = \begin{pmatrix} |\alpha|^2 & 0 \\ 0 & |\beta|^2 \end{pmatrix}. \tag{A.4}$$

[3]This is the case for e.g. Zeeman-split spin qubits.

The off-diagonal elements vanish since $e^{i\phi} + e^{i(\phi+\pi)} = 0$. This is called dephasing. Unaffected by this consideration, the relaxation $|0\rangle \to |1\rangle$ demands

$$\rho(t \to \infty) = \begin{pmatrix} 0 & 0 \\ 0 & 1 \end{pmatrix} . \tag{A.5}$$

Here, the off-diagonal terms vanish, as well, and this means that relaxation is always accompanied by dephasing[4]. On the other hand, dephasing can occur independently of relaxation. It can be shown that $T_2 \leq 2\,T_1$, making T_2 the more restrictive time for qubit coherence. The equality holds if relaxation induced dephasing is the only contribution to T_2^{-1}, [Chirolli(2008), Levitt].

Spin qubits

For real applications, qubits need to be represented by physical systems with a binary degree of freedom to which the values 0 and 1 can be assigned. A great many proposals for physical implementations have been made from pretty much all disciplines of physics [DiVincenzo(1998), DiVincenzo(1999)]. These proposals include internal states of ions in a trap [Cirac(1995)], atoms in optical lattices [Brennen(1999), Jaksch(1999)], nuclear magnetic resonance [Chuang(1998), Vandersypen(2001)] and superconducting electrons in a Josephson Junction [Wallraff(2004)], to name just a few.

Loss and DiVincenzo have proposed a solid state implementation using the electron spin states in coupled quantum dots (QDs) [Loss(1998)]. This can be called a *spintronics* implementation in that it is envisioned to exploit as many techniques of standard electronics as possible but with the electron spin replacing the electron charge as the relevant physical quantity. We remark that nuclear spins can also be used as qubits and also belong to the field of spintronics [Kane(1998), Childress(2006)]. Nuclear and electronic spins qubits share many similarities, yet here, we focus on electron spin qubits. With a view to the DiVincenzo criteria, we shortly comment on the perspective of the proposal by Loss and DiVincenzo[5]. Due to the applications in classical computing there is an unmatched experience in the fabrication of solid state devices [Hanson(2007)]. Extrapolating to quantum systems, it is natural to assume that a solid state implementation could be scaled up to a full-scale quantum computer (criterion 1). At sufficiently low temperatures, the spin memory can easily be initialized by applying a strong magnetic field (criterion 2). Another expected advantage are long coherence times and control over them via design parameters (criterion 3). Logic gates can be realized by controlling external electric magnetic fields and the overlap of distinct QD electrons (criterion 4). The result of a spin-based computation could be read out by converting the spin to a charge degree of freedom, which can be measured conveniently (criterion 5).

The electron (or nuclear) spin is a two level system with states $|\uparrow\rangle$ and $|\downarrow\rangle$, which are Zeeman-split in the presence of a magnetic field, $E_\uparrow - E_\downarrow = g\mu_B B$. It is natural to assign these states the values $|0\rangle$ and $|1\rangle$, respectively (or the other way round), such that one

[4] A finite relaxation time $T_1 < \infty$ would also affect a classical bit, where the phase plays no role. But for qubits, T_1 also implies a fading/loss of the phase, i.e. decoherence.

[5] For a more elaborate disquisition, we refer the reader to the original articles, [Loss(1998), DiVincenzo(1998), DiVincenzo(1999)].

spin represents one qubit. On the other hand, two spins can form a singlet state ($|S\rangle$) or one out of three triplet states ($|T_-\rangle$, $|T_0\rangle$, $|T_+\rangle$). Assuming quantization along the z-axis, only $|S\rangle$ and $|T_0\rangle$ share the s_z=0 subspace, and can thus be interpreted as $|0\rangle$ and $|1\rangle$. Thereby, two spins represent one qubit,

$$\begin{aligned} &\text{single spin qubit:} && |0\rangle = |\uparrow\rangle\,, && |1\rangle = |\downarrow\rangle\,, \\ &\text{double spin qubit:} && |0\rangle = |S\rangle = \frac{|\uparrow\downarrow\rangle - |\downarrow\uparrow\rangle}{\sqrt{2}}\,, && |1\rangle = |T_0\rangle = \frac{|\uparrow\downarrow\rangle + |\downarrow\uparrow\rangle}{\sqrt{2}}\,. \end{aligned} \tag{A.6}$$

The parametrization of the Bloch sphere as given by Eq. (A.2) applies for both cases. In particular, the states $|\uparrow\downarrow\rangle$ and $|\downarrow\uparrow\rangle$ occur on the equator of the double spin Bloch sphere.

Electron spin qubits in carbon

To maintain control over the electron in a QD, it is highly desirable, although not compelling, that the dot be made of semiconducting material. Indeed, GaAs QDs are probably the most successful and most studied system [Hanson(2007), Awschalom(2013), Takakura(2014)].

The low nuclear charge of carbon leads to a small spin-orbit coupling and therefore long electron spin coherence times. Natural carbon consists of 99% ^{12}C and 1% ^{13}C, with nuclear spins 0 and 1/2, respectively[6]. The low density of nuclear spins relates to a weak dephasing from these nuclear spins that can be even further suppressed by removing the ^{13}C atoms by, e.g., purification techniques or preselection of samples. This makes carbon based materials interesting for a solid state implementation of electron spin qubits. Accordingly, a lot of research focuses on QDs and spin coherence in carbon nanotubes, diamond vacancies, and graphene [Gaebel(2006), Tombros(2007), Trauzettel(2007), Steele(2009), Struck(2010), Pályi(2012), Goossens(2012)].

[6]The radioactive isotope ^{14}C has a negligible abundance of 10^{-12} and nuclear spin 0.

B. Continuum model for 2D materials

While electronic bonds determine the spring constants between adjacent volume or surface elements, the body of the system is determined by the positions of the atoms because they make up basically the entire mass. As a consequence, special care must be taken when the continuum model is applied to materials with two-dimensional lattices like mono- and bilayer graphene. Of course, these materials still have a three-dimensional body because they consist of particles with wave functions that extend into all three spatial dimensions. However, the notion of continuity in the out-of-plane direction is not justified for materials with a thickness of only a few atoms or even only one single atom.

In monolayer graphene and monolayer hBN, all atoms lie strictly within the same — possibly distorted — plane. That is, it is not possible to compress or dilate these materials in the direction locally perpendicular to said plane. A description with the continuum model is still possible by putting according quantities to zero. We stress that this approach does not necessarily hold for quasi two-dimensional systems where not all atoms lie within the same plane, e.g., bilayer materials or buckled monolayer materials like silicene. Therefore, we restrict the following modification of the continuum model [Chaikin&Lubensky, Landau&Lifschitz] to two-dimensional materials like monolayer graphene and hBN, that are truly two-dimensional in the sense of the continuum model [Droth(2010)].

Strain tensor

External forces deform solid bodies to a certain extent, thus changing their shape as well as their volume. A point inside the undeformed body, described by the position vector $\boldsymbol{r}$, shall be displaced to $\boldsymbol{r'}$ after the deformation. Then

$$\boldsymbol{u} = \boldsymbol{r'} - \boldsymbol{r} \tag{B.1}$$

is called the *displacement vector* with components u_i, which usually depend on the position. The deformation of the entire object is known if $\boldsymbol{u}(\boldsymbol{r})$ can be determined for the whole body.

With $\mathrm{d}x_i$ we denote the components of the vector connecting two infinitesimally close volume elements prior to the deformation. In first order they change to

$$\mathrm{d}x_i' = \mathrm{d}x_i + \mathrm{d}u_i \approx \mathrm{d}x_i + \frac{\partial u_i}{\partial x_j}\mathrm{d}x_j \tag{B.2}$$

after the deformation. Accordingly, the distance between the points changes from

$$\mathrm{d}l = \sqrt{\mathrm{d}x_1^2 + \mathrm{d}x_2^2 + \mathrm{d}x_3^2} \tag{B.3}$$

to

$$\mathrm{d}l' = \sqrt{\mathrm{d}x_1'^2 + \mathrm{d}x_2'^2 + \mathrm{d}x_3'^2}\,. \tag{B.4}$$

Taking the square of the last two equations results in $\mathrm{d}l^2 = \mathrm{d}x_i^2$and

$$\begin{aligned} \mathrm{d}l'^2 &= \mathrm{d}x_i'^2 = (\mathrm{d}x_i + \mathrm{d}u_i)^2 = \mathrm{d}x_i^2 + 2\mathrm{d}x_i\mathrm{d}u_i + \mathrm{d}u_i^2 \\ &\overset{(B.2)}{\approx} \mathrm{d}l^2 + 2\frac{\partial u_i}{\partial x_k}\mathrm{d}x_k\mathrm{d}x_i + \frac{\partial u_i}{\partial x_k}\frac{\partial u_i}{\partial x_l}\mathrm{d}x_k\mathrm{d}x_l\,. \end{aligned} \tag{B.5}$$

Using

$$\frac{\partial u_i}{\partial x_k}\mathrm{d}x_i\mathrm{d}x_k = \frac{\partial u_i}{\partial x_k}\mathrm{d}x_k\mathrm{d}x_i \overset{i\leftrightarrow k}{=} \frac{\partial u_k}{\partial x_i}\mathrm{d}x_i\mathrm{d}x_k \tag{B.6}$$

the second term can be written as

$$\left(\frac{\partial u_i}{\partial x_k} + \frac{\partial u_k}{\partial x_i}\right)\mathrm{d}x_i\mathrm{d}x_k\,, \tag{B.7}$$

and we find

$$\mathrm{d}l'^2 \approx \mathrm{d}l^2 + 2u_{ik}\mathrm{d}x_i\mathrm{d}x_k\,, \tag{B.8}$$

where

$$u_{ik} = \frac{1}{2}\left(\frac{\partial u_i}{\partial x_k} + \frac{\partial u_k}{\partial x_i} + \frac{\partial u_l}{\partial x_i}\frac{\partial u_l}{\partial x_k}\right) \tag{B.9}$$

is defined as the *strain tensor*. As a symmetric tensor, u_{ik} can be diagonalized with $u^{(1)} := u_{11}$, $u^{(2)} := u_{22}$ and $u^{(3)} := u_{33}$ being the eigenvalues of u_{ik}. Then Eq. (B.8) takes the form

$$\begin{aligned} \mathrm{d}l'^2 &\approx (\delta_{ik} + 2u_{ik})\mathrm{d}x_i\mathrm{d}x_k \\ &= (1 + 2u^{(1)})\mathrm{d}x_1^2 + (1 + 2u^{(2)})\mathrm{d}x_2^2 + (1 + 2u^{(3)})\mathrm{d}x_3^2\,. \end{aligned} \tag{B.10}$$

Each summand corresponds to the length shift along one of the three orthogonal principal axes. For example the length element $\mathrm{d}x_1$is elongated or compressed to $\mathrm{d}x_1' = \sqrt{1 + 2u^{(1)}}\mathrm{d}x_1$. Consequently the relative length shifts $(\mathrm{d}x_i' - \mathrm{d}x_i)/\mathrm{d}x_i$along the principal axes are $\sqrt{1 + 2u^{(i)}} - 1$.

Usually, deformations throughout the body are small, that is relative length shifts resulting from such a deformation are small compared to unity. In this case second order terms can be neglected such that the relative length shifts become

$$\frac{\mathrm{d}x_i' - \mathrm{d}x_i}{\mathrm{d}x_i} = \sqrt{1 + 2u^{(i)}} - 1 \approx u^{(i)}\,, \tag{B.11}$$

and the strain tensor can be written as

$$u_{ik} \approx \frac{1}{2}\left(\frac{\partial u_i}{\partial x_k} + \frac{\partial u_k}{\partial x_i}\right)\,. \tag{B.12}$$

The volume element is given by $\mathrm{d}V = \mathrm{d}x_1\mathrm{d}x_2\mathrm{d}x_3$ and with (B.11) the deformed volume element is

$$\begin{aligned} \mathrm{d}V' &= \mathrm{d}x_1'\mathrm{d}x_2'\mathrm{d}x_3' = (1+u^{(1)})\mathrm{d}x_1(1+u^{(2)})\mathrm{d}x_2(1+u^{(3)})\mathrm{d}x_3 \\ &= (1+u^{(1)})(1+u^{(2)})(1+u^{(3)})\mathrm{d}V\,. \end{aligned} \tag{B.13}$$

Respecting only first order terms again,

$$\mathrm{d}V' \approx (1+u^{(1)}+u^{(2)}+u^{(3)})\mathrm{d}V\,, \tag{B.14}$$

such that the relative volume change becomes

$$\frac{\mathrm{d}V'-\mathrm{d}V}{\mathrm{d}V} \approx u^{(1)}+u^{(2)}+u^{(3)} = u_{ii}\,. \tag{B.15}$$

Stress tensor

In a non-deformed body all molecules are arranged in their mechanical equilibrium positions, that is, all internal forces acting on a volume element sum up to zero. External forces will change the arrangement of molecules in the body and thus cause a deformation. The internal tensions resulting from this deformation seek to restore the non-deformed arrangement and counteract the external forces. The effective internal force acting on a certain volume can be denoted as

$$\int \boldsymbol{F}\mathrm{d}V\,, \tag{B.16}$$

where said volume is integrated and $\boldsymbol{F}$ is the force per volume such that the force acting on $\mathrm{d}V$ is $\boldsymbol{F}\mathrm{d}V$. By introducing the *stress tensor* σ_{ik} via

$$F_i = \frac{\partial \sigma_{ik}}{\partial x_k} \tag{B.17}$$

and using Gauss' Law[1] it is possible to rewrite Eq. (B.16) as

$$\int F_i\mathrm{d}V = \int \frac{\partial\sigma_{ik}}{\partial x_k}\mathrm{d}V = \oint \sigma_{ik}\mathrm{d}f_k\,. \tag{B.18}$$

We notice that $\sigma_{ik}\mathrm{d}f_k$ is the i-th component of the force acting on the surface element $\mathrm{d}f$. Consider a surface normal to the x-axis. Then σ_{xx} is the force per surface unit that acts normal to this surface and σ_{yx} and σ_{zx} are the forces acting tangential to it, see Fig. B.1.

In mechanical equilibrium, all internal tensions on a volume element must cancel each other, that is

$$\frac{\partial\sigma_{ik}}{\partial x_k} = F_i = 0\,. \tag{B.19}$$

[1]The integral of a gradient over a volume can be replaced by an integral over the surface enclosing said volume: $\int \frac{\partial h_i}{\partial x_i}\mathrm{d}V = \oint h_i \mathrm{d}f_i$, where $\mathrm{d}\boldsymbol{f}$ is a vector normal to the enclosing surface.

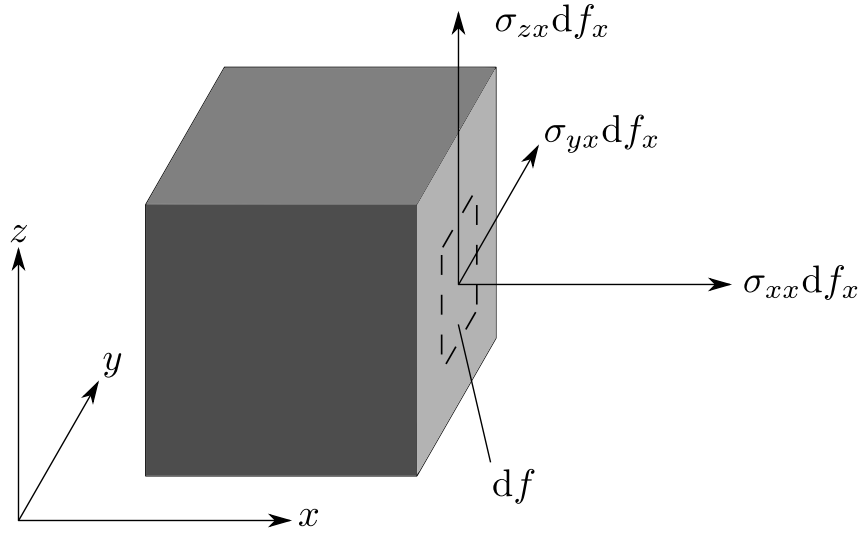

Figure B.1.: By virtue of Gauss' law, the force acting on a volume element $\mathrm{d}V$ can be expressed in terms of the strain tensor σ_{ik}. The i-th component of the force acting on the surface element $\mathrm{d}f$ is given by $\sigma_{ik}\mathrm{d}f_k$.

We denote the external force per surface element of the body with $\boldsymbol{P}$ such that the surface element $\mathrm{d}f$ experiences the force $\boldsymbol{P}\mathrm{d}f$. This force deforms the body until it is counteracted by internal strain $\sigma_{ik}\mathrm{d}f_k$. With such boundary conditions, equilibrium is achieved when $P_i\mathrm{d}f = \sigma_{ik}\mathrm{d}f_k$. Using $\mathrm{d}f_k = \eta_k\mathrm{d}f$, where η_k is the unit vector normal to the surface, this condition becomes

$$\sigma_{ik}\eta_k = P_i\,. \tag{B.20}$$

Consider a small deformation δu_i. The required mechanical energy per volume is $\delta R = F_i\delta u_i = \frac{\partial\sigma_{ik}}{\partial x_k}\delta u_i$. Integrating the entire volume yields

$$\int \delta R\mathrm{d}V = \int \frac{\partial\sigma_{ik}}{\partial x_k}\delta u_i\mathrm{d}V\,, \tag{B.21}$$

the total work required for the deformation of the body. Using partial integration and Gauss' Law, we find

$$\int \delta R\mathrm{d}V = \oint \sigma_{ik}\delta u_i\mathrm{d}f_k - \int \sigma_{ik}\frac{\partial\delta u_i}{\partial x_k}\mathrm{d}V\,. \tag{B.22}$$

The first term vanishes for $\sigma_{ik} = 0$ or if an infinite body with $\delta u_i = 0$ at infinity is assumed. Also making use of the symmetry[2] of σ_{ik} the above can be written as

$$\begin{aligned}\int \delta R\mathrm{d}V &= -\frac{1}{2}\int \sigma_{ik}\left(\frac{\partial\delta u_i}{\partial x_k} + \frac{\partial\delta u_k}{\partial x_i}\right)\mathrm{d}V = -\frac{1}{2}\int \sigma_{ik}\delta\left(\frac{\partial u_i}{\partial x_k} + \frac{\partial u_k}{\partial x_i}\right)\mathrm{d}V \\ &= -\int \sigma_{ik}\delta u_{ik}\mathrm{d}V\,,\end{aligned} \tag{B.23}$$

[2]The stress tensor σ_{ik} is not unambiguously fixed by Eq. (B.17) but allows for the addition of a gradient $\frac{\partial\chi_{ikl}}{\partial x_l}$ (where $\chi_{ikl} = -\chi_{ilk}$). By virtue of this gradient the stress tensor can be symmetrized. For more details we refer the reader to [Landau&Lifschitz].

such that $\delta R = -\sigma_{ik}\delta u_{ik}$. The differential internal energy per volume, $\mathrm{d}E$ equals the difference between the thermal energy absorbed by the volume element and the mechanical work performed by its internal tensions,

$$\mathrm{d}E = T\mathrm{d}S - \mathrm{d}R = T\mathrm{d}S + \sigma_{ik}\mathrm{d}u_{ik}\,. \tag{B.24}$$

A Legendre transformation from variable T to S leads to the differential of the free energy,

$$\mathrm{d}F = \mathrm{d}(E - TS) = \mathrm{d}E - S\mathrm{d}T - T\mathrm{d}S = -S\mathrm{d}T + \sigma_{ik}\mathrm{d}u_{ik}\,. \tag{B.25}$$

From the thermodynamical potentials Eqs. (B.24) and (B.25), it is easy to derive the stress tensor:

$$\begin{aligned} \sigma_{ik} &= \left(\frac{\partial E}{\partial u_{ik}}\right)_S\,, \\ \sigma_{ik} &= \left(\frac{\partial F}{\partial u_{ik}}\right)_T\,. \end{aligned} \tag{B.26}$$

Below, we focus on the stress tensor in terms of the free energy.

The elastic energy functional for a monatomic plate

For the description of two-dimensional materials, we expand the free energy per surface area[3], $F(T, u_{ik})$, in powers of u_{ik}. Since the free energy is a scalar, each of its summands must be a scalar, too. The temperature is assumed to remain constant during the deformation, which is necessary to exclude thermal expansion. Then, starting from mechanical equilibrium, $u_{ik} = 0$ implies $\sigma_{ik} = 0$ and therefore

$$\frac{\partial F}{\partial u_{ik}} \overset{\text{(B.26)}}{=} 0\,, \tag{B.27}$$

such that no linear terms appear in our expansion (as expected for mechanical equilibrium). Only two independent, invariant scalars of second order can be formed from the strain tensor, namely e.g. the square of the trace, u_{ii}^2, and the sum[4] of all squared elements, u_{ik}^2. For small deformations, higher order terms can be neglected and we find

$$F = \frac{\lambda}{2}u_{ii}^2 + \mu u_{ik}^2\,. \tag{B.28}$$

It is to be noted that the strain tensor components u_{iz} vanish identically for monatomically thin plates,

$$u_{xz} = u_{yz} = u_{zz} = 0\,, \tag{B.29}$$

such that these components do not contribute to the elastic free energy. The energy scale is chosen in such a way that $F = 0$ for the undeformed body. It is common to express these

[3]The above calculations for the free energy per volume apply accordingly in two dimensions. Some care must be taken since $u_{iz} = 0$ in two dimensions.

[4]Note that $u_{ik}^2 = u_{ik}u_{ik} = u_{11}u_{11} + u_{12}u_{12} + \ldots$.

constants in terms of Young's modulus $\mathcal{E}$ and Poisson's ratio σ which are a measure for the stiffness of the material and its transverse contraction upon axial elongation, respectively:

$$\lambda = \frac{\mathcal{E}\sigma}{(1-\sigma^2)}\,, \quad \mu = \frac{\mathcal{E}}{2(1+\sigma)}\,. \tag{B.30}$$

With these expressions, (B.28) becomes

$$\begin{aligned} F &= \frac{\mathcal{E}\sigma}{2(1-\sigma^2)}u_{ii}^2 + \frac{\mathcal{E}}{2(1+\sigma)}u_{ik}^2 \\ &= \frac{\mathcal{E}}{2(1+\sigma)}\left(u_{ik}^2 + \frac{\sigma}{1-\sigma}u_{ii}^2\right)\,, \end{aligned} \tag{B.31}$$

where $i,k \neq z$ for monatomically thin plates. This form of the free energy will be used to derive differential equations for deformations. The stress tensor can be expressed in terms of the strain tensor,

$$\sigma_{ik} \overset{(B.26)}{=} \frac{\partial F}{\partial u_{ik}} = \frac{\mathcal{E}}{1+\sigma}\left(u_{ik} + \frac{\sigma}{1-\sigma}u_{ll}\delta_{ik}\right)\,, \tag{B.32}$$

with the explicit components

$$\begin{aligned} \sigma_{xx} &= \frac{\mathcal{E}}{1+\sigma}\left(u_{xx} + \frac{\sigma}{1-\sigma}(u_{xx}+u_{yy})\right) \\ &= \frac{\mathcal{E}}{(1+\sigma)(1-\sigma)}\left((1-\sigma)u_{xx} + \sigma(u_{xx}+u_{yy})\right) \\ &= \frac{\mathcal{E}}{(1+\sigma)(1-\sigma)}\left(u_{xx} + \sigma u_{yy}\right)\,, \\ \sigma_{yy} &= \frac{\mathcal{E}}{(1+\sigma)(1-\sigma)}\left(u_{yy} + \sigma u_{xx}\right) \\ \sigma_{xy} &= \frac{\mathcal{E}}{1+\sigma}u_{xy}\,. \end{aligned} \tag{B.33}$$

Monatomically thin plates

In a plate of monatomic thickness, all forces are constant with respect to the *effective elastic thickness* h. The deformation coordinates are

$$u_x\,, \quad u_y \quad \text{and} \quad u_z \approx \zeta(x,y)\,, \tag{B.34}$$

where ζ is the displacement of the "neutral" plane in the middle of the plate, as depicted in Fig. B.2. Due to its small thickness only very weak forces need to be applied to the plate surface in order to bend it. These external surface forces $\boldsymbol{P}$ can be neglected when compared to internal tensions such that $\sigma_{ik}n_k = 0$ (see Eq. (B.20)). For a small bending the surface normal vector $\boldsymbol{n}$ points along the z-axis, such that the stress tensor components σ_{iz} vanish. From Eqs. (B.12) and (B.29), we infer

$$u_{xz} = 0 \;\Rightarrow\; \frac{\partial u_x}{\partial z} = -\frac{\partial u_z}{\partial x}\,, \quad u_{yz} = 0 \;\Rightarrow\; \frac{\partial u_y}{\partial z} = -\frac{\partial u_z}{\partial y}\,. \tag{B.35}$$

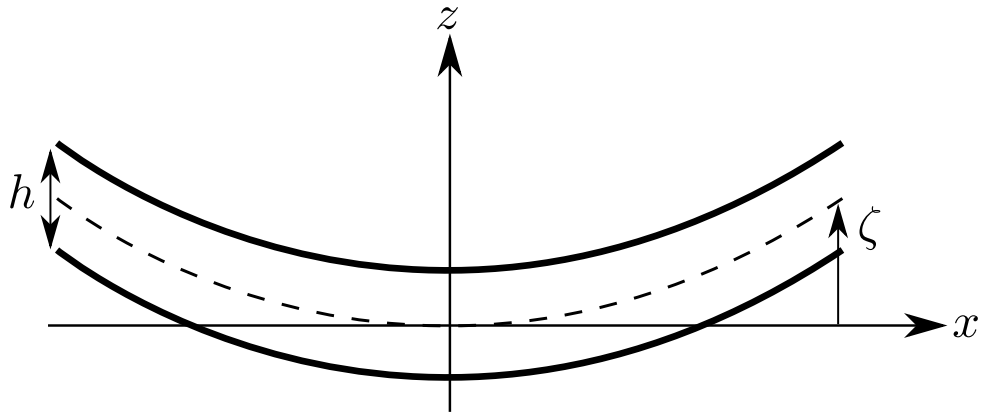

Figure B.2.: For monatomically thin plates with effective elastic thickness h, the out-of-plane displacement $u_z(x, y)$ can be described by the displacement of the neutral plane in the middle of the plate, $\zeta(x, y)$.

For a small bending, it is sufficiently exact to replace u_z by $\zeta(x, y)$. It follows that

$$\frac{\partial u_x}{\partial z} = -\frac{\partial \zeta}{\partial x}\,, \quad \frac{\partial u_y}{\partial z} = -\frac{\partial \zeta}{\partial y}\,, \tag{B.36}$$

and hence

$$u_x = -z\frac{\partial \zeta}{\partial x}\,, \quad u_y = -z\frac{\partial \zeta}{\partial y}\,, \tag{B.37}$$

where integration constants have been set to zero. The components of the strain tensor become

$$\begin{aligned} &u_{xx} = -z\frac{\partial^2 \zeta}{\partial x^2}\,, \quad u_{yy} = -z\frac{\partial^2 \zeta}{\partial y^2}\,, \quad u_{xy} = -z\frac{\partial^2 \zeta}{\partial x \partial y}\,, \\ &u_{xz} = u_{yz} = u_{zz} = 0\,. \end{aligned} \tag{B.38}$$

With this form of the strain tensor we write Eq. (B.31) as

$$\begin{aligned} F &= \frac{\mathcal{E}}{2(1+\sigma)}\left(u_{ik}^2 + \frac{\sigma}{1-\sigma}u_{ii}^2\right) \\ &= \frac{\mathcal{E}}{2(1+\sigma)}\left((u_{xx}^2 + u_{xy}^2 + u_{yx}^2 + u_{yy}^2) + \frac{\sigma}{1-\sigma}(u_{xx}^2 + u_{yy}^2 + 2u_{xx}u_{yy})\right) \\ &= \frac{\mathcal{E}z^2}{2(1+\sigma)}\left\{\left((\partial_x^2\zeta)^2 + (\partial_y^2\zeta)^2 + 2(\partial_x\partial_y\zeta)^2\right) + \frac{\sigma}{1-\sigma}\left((\partial_x^2\zeta)^2 + (\partial_y^2\zeta)^2 + 2\partial_x^2\zeta\partial_y^2\zeta\right)\right\} \\ &= \frac{\mathcal{E}z^2}{2(1+\sigma)}\left\{\left((\partial_x^2\zeta)^2 + (\partial_y^2\zeta)^2\right)\underbrace{\left(1 + \frac{\sigma}{1-\sigma}\right)}_{=\frac{1}{1-\sigma}} + 2(\partial_x\partial_y\zeta)^2 + \partial_x^2\zeta\partial_y^2\zeta\frac{2\sigma}{1-\sigma}\right\}\,. \end{aligned} \tag{B.39}$$

Then, the free energy per surface area turns out to be

$$\begin{aligned} F &= z^2 \frac{\mathcal{E}}{2(1+\sigma)} \left(\frac{1}{1-\sigma} \left((\partial_x^2 \zeta)^2 + (\partial_y^2 \zeta)^2 \right) + \frac{2\sigma}{1-\sigma} \partial_x^2 \zeta \partial_y^2 \zeta + 2 \left(\partial_x \partial_y \zeta \right)^2 \right) \\ &= z^2 \frac{\mathcal{E}}{2(1+\sigma)} \left(\frac{1}{1-\sigma} \left(\partial_x^2 \zeta + \partial_y^2 \zeta \right)^2 + 2 \left((\partial_x \partial_y \zeta)^2 - \partial_x^2 \zeta \partial_y^2 \zeta \right) \right) . \end{aligned} \tag{B.40}$$

To obtain the free energy of the whole plate with out-of-plane deformations, we must integrate the energy density F/h over the plate volume. In the z-direction, we integrate from $-h/2$ to $h/2$, where h is the effective elastic thickness of the monatomic plate. The other dimensions are integrated over the entire surface area of the plate,

$$\begin{aligned} F_{Pl} &= \int \frac{F}{h} \, \mathrm{d}V \\ &= \frac{2h^2}{3 \cdot 8} \frac{\mathcal{E}}{2(1+\sigma)} \frac{1}{1-\sigma} \iint \left(\left(\partial_x^2 \zeta + \partial_y^2 \zeta \right)^2 + 2(1-\sigma) \left((\partial_x \partial_y \zeta)^2 - \partial_x^2 \zeta \partial_y^2 \zeta \right) \right) \mathrm{d}x \mathrm{d}y \\ &= \frac{\mathcal{E} h^2}{24(1+\sigma)(1-\sigma)} \iint \left(\left(\partial_x^2 \zeta + \partial_y^2 \zeta \right)^2 + 2(1-\sigma) \left((\partial_x \partial_y \zeta)^2 - \partial_x^2 \zeta \partial_y^2 \zeta \right) \right) \mathrm{d}x \mathrm{d}y \, . \end{aligned} \tag{B.41}$$

Out-of-plane deformations

To find the equilibrium of the plate we have to minimize its total energy. Therefore, we first calculate the variation of the free energy given by Eq. (B.41). The integral consists of two terms, which we treat separately. With $\mathrm{d}f = \mathrm{d}x\mathrm{d}y$ and $\triangle = \partial_x^2 + \partial_y^2$, the former term becomes

$$\frac{1}{2} \delta \int (\triangle \zeta)^2 \, \mathrm{d}f = \int (\triangle \zeta) \, \delta (\triangle \zeta) \, \mathrm{d}f \, . \tag{B.42}$$

The correct prefactor will be restored later. With

$$\begin{aligned} \delta (\triangle \zeta) &= \sum_i \left(\partial_i (\triangle \zeta) \right) \delta_i = \sum_i \left(\triangle (\partial_i \zeta) \right) \delta_i = \sum_i \triangle \left((\partial_i \zeta) \, \delta_i \right) - \sum_i (\partial_i \zeta) \underbrace{(\triangle \delta_i)}_{=0} \\ &= \triangle \underbrace{\sum_i (\partial_i \zeta) \, \delta_i}_{= \delta \zeta} = \triangle (\delta \zeta) \, , \end{aligned} \tag{B.43}$$

we infer

$$\begin{aligned} \frac{1}{2} \delta \int (\triangle \zeta)^2 \, \mathrm{d}f &= \int (\triangle \zeta) \underbrace{(\boldsymbol{\nabla})^2}_{= \triangle} (\delta \zeta) \, \mathrm{d}f \\ &= \underbrace{\int \boldsymbol{\nabla} \cdot \left((\triangle \zeta) \boldsymbol{\nabla} (\delta \zeta) \right) \mathrm{d}f}_{=: S_1} - \underbrace{\int \left(\boldsymbol{\nabla} (\triangle \zeta) \right) \cdot \boldsymbol{\nabla} (\delta \zeta) \, \mathrm{d}f}_{=: S_2} . \end{aligned} \tag{B.44}$$

Using Gauss' Law, S_1 transforms to an integral over the plate boundaries,

$$S_1 = \oint (\triangle \zeta) \left(\boldsymbol{\nabla} (\delta \zeta) \right) \cdot \boldsymbol{n} \, \mathrm{d}l = \oint (\triangle \zeta) \left(\partial_n (\delta \zeta) \right) \mathrm{d}l \, , \tag{B.45}$$

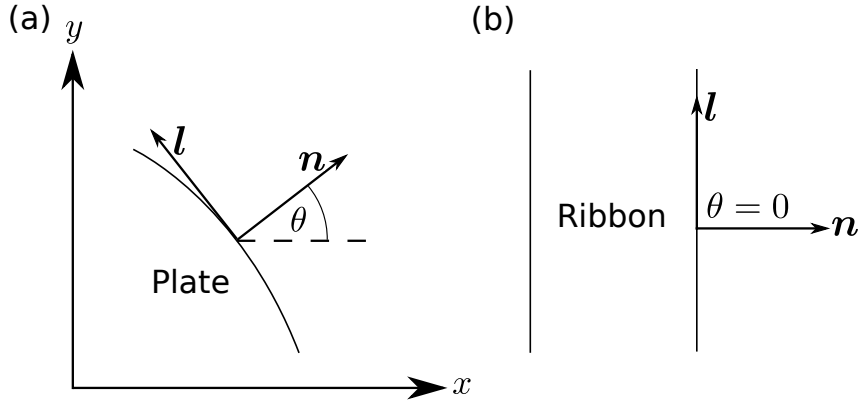

Figure B.3.: (a,b) The line element $\mathrm{d}l$ refers to the tangential vector $\boldsymbol{l}$ and the derivative $\partial_n = \boldsymbol{n} \cdot \boldsymbol{\nabla}$ to the normal vector $\boldsymbol{n}$. (b) For a rectangular ribbon with $\cos\theta = 1$ and $\sin\theta = 0$, Eqs. (B.61) and (B.62) become much simpler.

where $\boldsymbol{n}$ is the vector in the $x-y$-plane normal to the plate boundary and $\partial_n = \boldsymbol{n} \cdot \boldsymbol{\nabla}$ is the derivative along this direction, see Fig. B.3 (a).

With Gauss' Law once again, S_2 becomes

$$\begin{aligned} S_2 &= \int \boldsymbol{\nabla} \left(\delta\zeta \left(\boldsymbol{\nabla}(\triangle\zeta)\right)\right) \mathrm{d}f - \int \delta\zeta \boldsymbol{\nabla} \left(\boldsymbol{\nabla}(\triangle\zeta)\right) \mathrm{d}f \\ &= \oint \delta\zeta \left(\boldsymbol{\nabla}(\triangle\zeta)\right) \cdot \boldsymbol{n} \, \mathrm{d}l - \int \delta\zeta \triangle(\triangle\zeta) \, \mathrm{d}f \\ &= \oint \delta\zeta \partial_n(\triangle\zeta) \, \mathrm{d}l - \int \delta\zeta \left(\triangle^2\zeta\right) \mathrm{d}f \,. \end{aligned} \tag{B.46}$$

Now, the variation of the first term in Eq. (B.41) can be written as

$$\frac{1}{2}\delta \int (\triangle\zeta)^2 \, \mathrm{d}f = \int \delta\zeta \triangle^2\zeta \, \mathrm{d}f - \oint \delta\zeta \partial_n(\triangle\zeta) \, \mathrm{d}l + \oint \triangle\zeta \partial_n(\delta\zeta) \, \mathrm{d}l \tag{B.47}$$

Again omitting the prefactor, we vary the second term in Eq. (B.41):

$$\begin{aligned} &\delta \int \left((\partial_x\partial_y\zeta)^2 - \left(\partial_x^2\zeta\right)\left(\partial_y^2\zeta\right)\right) \mathrm{d}f \\ &\quad = \int \left(2(\partial_x\partial_y\zeta)(\partial_x\partial_y(\delta\zeta)) - \left(\partial_x^2(\delta\zeta)\right)\left(\partial_y^2\zeta\right) - \left(\partial_x^2\zeta\right)\left(\partial_y^2(\delta\zeta)\right)\right) \mathrm{d}f \,. \end{aligned} \tag{B.48}$$

For the integrand we use the equality

$$\begin{aligned} &\partial_x \underbrace{\left(\partial_y(\delta\zeta)\partial_x\partial_y\zeta - \partial_x(\delta\zeta)\partial_y^2\zeta\right)}_{=:\, v_x} + \partial_y \underbrace{\left(\partial_x(\delta\zeta)\partial_x\partial_y\zeta - \partial_y(\delta\zeta)\partial_x^2\zeta\right)}_{=:\, v_y} \\ &\quad = \partial_x\partial_y(\delta\zeta)\partial_x\partial_y\zeta + \partial_y(\delta\zeta)\partial_x^2\partial_y\zeta - \partial_x^2(\delta\zeta)\partial_y^2\zeta - \partial_x(\delta\zeta)\partial_x\partial_y^2\zeta \\ &\qquad + \partial_x\partial_y(\delta\zeta)\partial_x\partial_y\zeta + \partial_x(\delta\zeta)\partial_x\partial_y^2\zeta - \partial_y^2(\delta\zeta)\partial_x^2\zeta - \partial_y(\delta\zeta)\partial_x^2\partial_y\zeta \\ &\quad = 2\partial_x\partial_y\zeta\partial_x\partial_y(\delta\zeta) - \partial_x^2(\delta\zeta)\partial_y^2\zeta - \partial_y^2(\delta\zeta)\partial_x^2\zeta \,, \end{aligned} \tag{B.49}$$

where the left hand side is the divergence of a two-dimensional vector $\boldsymbol{v}$. Integrating this divergence, we find

$$\begin{aligned}\int (\partial_x v_x + \partial_y v_y)\,\mathrm{d}f &= \oint \boldsymbol{v}\cdot\boldsymbol{n}\,\mathrm{d}l \qquad\qquad (B.50)\\ &= \oint \Bigg(\underbrace{\cos\theta\left(\partial_y(\delta\zeta)\partial_x\partial_y\zeta - \partial_x(\delta\zeta)\partial_y^2\zeta\right)}_{=n_x v_x} + \underbrace{\sin\theta\left(\partial_x(\delta\zeta)\partial_x\partial_y\zeta - \partial_y(\delta\zeta)\partial_x^2\zeta\right)}_{=n_y v_y} \Bigg)\,\mathrm{d}l\,.\end{aligned}$$

On the plate boundaries, we can express the partial derivations by

$$\partial_x = \cos\theta\partial_n - \sin\theta\partial_l\,, \quad \partial_y = \sin\theta\partial_n + \cos\theta\partial_l\,, \qquad (B.51)$$

and find

$$\begin{aligned}&\oint \big\{\cos\theta\left(\sin\theta\partial_n(\delta\zeta)\partial_y\partial_y\zeta + \cos\theta\partial_l(\delta\zeta)\partial_x\partial_y\zeta - \cos\theta\partial_n(\delta\zeta)\partial_y^2\zeta + \sin\theta\partial_l(\delta\zeta)\partial_y^2\zeta\right)\\ &\qquad + \sin\theta\left(\cos\theta\partial_n(\delta\zeta)\partial_x\partial_y\zeta - \sin\theta\partial_l(\delta\zeta)\partial_x\partial_y\zeta - \sin\theta\partial_n(\delta\zeta)\partial_x^2\zeta - \cos\theta\partial_l(\delta\zeta)\partial_x^2\zeta\right)\big\}\,\mathrm{d}l\\ &= \oint \partial_n(\delta\zeta)\left(2\sin\theta\cos\theta\partial_x\partial_y\zeta - \cos^2\theta\partial_y^2\zeta - \sin^2\theta\partial_x^2\theta\right)\mathrm{d}l\\ &\qquad + \oint \partial_l(\delta\zeta)\left(\cos^2\theta\partial_x\partial_y\zeta + \sin\theta\cos\theta\partial_y^2\zeta - \sin^2\theta\partial_x\partial_y\zeta - \sin\theta\cos\theta\partial_x^2\zeta\right)\mathrm{d}l\\ &= \oint \partial_n(\delta\zeta)\left(2\sin\theta\cos\theta\partial_x\partial_y\zeta - \sin^2\theta\partial_x^2\zeta - \cos^2\theta\partial_y^2\zeta\right)\mathrm{d}l\\ &\qquad + \oint \partial_l(\delta\zeta)\left(\sin\theta\cos\theta\left(\partial_y^2\zeta - \partial_x^2\zeta\right) + \left(\cos^2\theta - \sin^2\theta\right)\partial_x\partial_y\zeta\right)\mathrm{d}l\,. \qquad (B.52)\end{aligned}$$

By partial integration the very last integral becomes

$$\begin{aligned}&\underbrace{\oint \partial_l\left((\delta\zeta)\left(\sin\theta\cos\theta\left(\partial_y^2\zeta - \partial_x^2\zeta\right) + \left(\cos^2\theta - \sin^2\theta\right)\partial_x\partial_y\zeta\right)\right)\mathrm{d}l}_{=0}\\ &\qquad - \oint (\delta\zeta)\partial_l\left(\sin\theta\cos\theta\left(\partial_y^2\zeta - \partial_x^2\zeta\right) + \left(\cos^2\theta - \sin^2\theta\right)\partial_x\partial_y\zeta\right)\mathrm{d}l\,, \qquad (B.53)\end{aligned}$$

such that

$$\begin{aligned}&\delta\int \left((\partial_x\partial_y\zeta)^2 - \left(\partial_x^2\zeta\right)\left(\partial_y^2\zeta\right)\right)\mathrm{d}f\\ &\qquad = \oint \partial_n(\delta\zeta)\left(2\sin\theta\cos\theta\partial_x\partial_y\zeta - \sin^2\theta\partial_x^2\zeta - \cos^2\theta\partial_y^2\zeta\right)\mathrm{d}l\\ &\qquad\quad - \oint (\delta\zeta)\partial_l\left(\sin\theta\cos\theta\left(\partial_y^2\zeta - \partial_x^2\zeta\right) + \left(\cos^2\theta - \sin^2\theta\right)\partial_x\partial_y\zeta\right)\mathrm{d}l. \qquad (B.54)\end{aligned}$$

Restoring all constants and with Eqs. (B.47) and (B.54), we get the variation of the free

energy,

$$\begin{aligned}\delta F_{Pl} &= \kappa \Bigg\{ \int \delta\zeta \triangle^2 \zeta \, \mathrm{d}f \\ &\quad - \oint \delta\zeta \, (\partial_n(\triangle\zeta) \\ &\qquad +(1-\sigma)\partial_l \left(\sin\theta\cos\theta \left(\partial_y^2\zeta - \partial_x^2\zeta\right) + \left(\cos^2\theta - \sin^2\theta\right)\partial_x\partial_y\zeta\right)\Big) \, \mathrm{d}l \\ &\quad + \oint \partial_n(\delta\zeta) \left(\triangle\zeta + (1-\sigma)\left(2\sin\theta\cos\theta\partial_x\partial_y\zeta - \sin^2\theta\partial_x^2\zeta - \cos^2\theta\partial_y^2\zeta\right)\right) \mathrm{d}l \Bigg\} \,, \end{aligned} \tag{B.55}$$

where we have introduced the *bending rigidity* for a monatomically thin plate,

$$\kappa = \frac{\mathcal{E}h^2}{12(1-\sigma^2)} \,. \tag{B.56}$$

In order to get the total energy minimum we have to add the potential energy. The potential energy is minus the work performed against external forces. Therefore, its variation δU is

$$\delta U = -\int P_z \delta\zeta \, \mathrm{d}f \,, \tag{B.57}$$

where P_z is an external force per surface area that acts perpendicular to the $x-y$-plane. Finally, the equilibrium condition is given by

$$\delta F_{Pl} - \delta U = 0 \,. \tag{B.58}$$

There are area and line integrals on the left hand side. The area integral

$$\int \left(\kappa\triangle^2\zeta - P_z\right)\delta\zeta \, \mathrm{d}f \tag{B.59}$$

only vanishes for arbitrary $\delta\zeta$ if

$$\kappa\triangle^2\zeta - P_z = 0 \,. \tag{B.60}$$

This equation describes equilibrium for out-of-plane deformations. The line integrals in Eq. (B.58) need to vanish as well, and this translates to boundary conditions. For free floating edges, $\delta\zeta$ and $\partial_n\delta\zeta$ may take any values at the boundaries such that the coefficients of the line integrals in Eqs. (B.55) and (B.58) have to vanish:

$$-\partial_n(\triangle\zeta) + (1-\sigma)\partial_l\left(\cos\theta\sin\theta\left(\frac{\partial^2\zeta}{\partial x^2} - \frac{\partial^2\zeta}{\partial y^2}\right) + \left(\sin^2\theta - \cos^2\theta\right)\frac{\partial^2\zeta}{\partial x\partial y}\right) = 0 \,, \tag{B.61}$$

$$\triangle\zeta + (1-\sigma)\left(2\sin\theta\cos\theta\frac{\partial^2\zeta}{\partial x\partial y} - \sin^2\theta\frac{\partial^2\zeta}{\partial x^2} - \cos^2\theta\frac{\partial^2\zeta}{\partial y^2}\right) = 0 \,. \tag{B.62}$$

In the special case of a rectangular plate aligned along the x- and y-axes (Fig. B.3 (b)) and with periodic boundaries along the y-axis, Eq. (B.61) becomes

$$\begin{aligned} 0 &= \mp\partial_x(\triangle\zeta) \pm (1-\sigma)\partial_y\left(-\frac{\partial^2\zeta}{\partial x\partial y}\right) \\ &= \pm\left(-\partial_x^3\zeta - \partial_x\partial_y^2\zeta - (1-\sigma)\partial_x\partial_y^2\zeta\right) \\ \Rightarrow\ 0 &= \partial_x^3\zeta + (2-\sigma)\partial_x\partial_y^2\zeta \,. \end{aligned} \tag{B.63}$$

Accordingly, Eq. (B.62) can be written as

$$\begin{aligned} 0 &= \partial_x^2\zeta + \partial_y^2\zeta + (1-\sigma)\left(-\frac{\partial^2\zeta}{\partial y^2}\right), \\ \Rightarrow\ 0 &= \partial_x^2\zeta + \sigma\partial_y^2\zeta\,. \end{aligned} \tag{B.64}$$

That is, a monatomically thin, rectangular plate with open boundaries along the x-axis and periodic boundaries along the y-axis needs to satisfy the boundary conditions given by Eqs. (B.63) and (B.64).

In-plane deformations

Another type of deformation is one that takes place within the plane of the plate with no bending involved. The deformations are homogeneous in z for a monatomically thick plate such that the strain tensor only depends on x and y. Usually, such deformations arise from forces acting on the plate edges or on the plate volume (like gravity) such that no forces act on the surface of the plate. A vanishing force per surface element means $\sigma_{ik}\eta_k = 0$, see Eq. (B.20). As there is no bending for in-plane deformations, we infer

$$u_{xz} = u_{yz} = u_{zz} = 0\,. \tag{B.65}$$

According to Eq. (B.33), the non-vanishing components of the strain tensor are

$$\sigma_{xx} = \frac{\mathcal{E}}{(1-\sigma^2)}(u_{xx} + \sigma u_{yy})\,, \quad \sigma_{yy} = \frac{\mathcal{E}}{(1-\sigma^2)}(u_{yy} + \sigma u_{xx})\,, \quad \sigma_{xy} = \frac{\mathcal{E}}{1+\sigma}u_{xy}\,. \tag{B.66}$$

For a free floating plate, no forces act on the plate edges,

$$\sigma_{ik}n_k = 0\,, \tag{B.67}$$

where $\boldsymbol{n}$ is the vector in the plate plane and normal to the plate boundary (n_i takes the role of $\mathrm{d}f_i$ in Fig. B.1). As above, we explicitly treat the special case of a rectangular plate as depicted in Fig. B.3 (b). Since $\boldsymbol{n} = (\pm 1, 0, 0)$, the σ_{xx} and σ_{yx} components of the stress tensor must vanish along the edges. That is, the deformations need to satisfy

$$\begin{aligned} & \sigma_{xx} = \frac{\mathcal{E}}{(1-\sigma^2)}(u_{xx} + \sigma u_{yy}) = 0\,, \\ \Rightarrow\quad & \partial_x u_x + \sigma\partial_y u_y = 0\,, \qquad \text{(B.68)} \\ & \sigma_{xy} = \frac{\mathcal{E}}{1+\sigma}u_{xy} = 0\,, \\ \Rightarrow\quad & \partial_x u_y + \partial_y u_x = 0\,, \qquad \text{(B.69)} \end{aligned}$$

at the plate boundaries.

Due to homogeneity along the z-direction, we can use $P_i = F_i$ in Eq. (B.17), such that the plate is in equilibrium if the equations

$$\begin{aligned} \left(\frac{\partial\sigma_{xx}}{\partial x} + \frac{\partial\sigma_{xy}}{\partial y}\right) + P_x &= 0\,, \\ \left(\frac{\partial\sigma_{xy}}{\partial x} + \frac{\partial\sigma_{yy}}{\partial y}\right) + P_y &= 0 \end{aligned} \tag{B.70}$$

are satisfied. Inserting Eq. (B.66) into these equations, we get

$$\begin{aligned}
\mathcal{E}\left(\frac{1}{(1-\sigma^2)}\frac{\partial^2 u_x}{\partial x^2}+\frac{1}{2(1+\sigma)}\frac{\partial^2 u_x}{\partial y^2}+\frac{1}{1+\sigma}\left(\frac{\sigma}{1-\sigma}+\frac{1}{2}\right)\frac{\partial^2 u_y}{\partial x\partial y}\right)+P_x &= 0\,,\\
\mathcal{E}\left(\frac{1}{(1-\sigma^2)}\frac{\partial^2 u_y}{\partial y^2}+\frac{1}{2(1+\sigma)}\frac{\partial^2 u_y}{\partial x^2}+\frac{1}{1+\sigma}\left(\frac{1}{2}+\frac{\sigma}{1-\sigma}\right)\frac{\partial^2 u_x}{\partial x\partial y}\right)+P_y &= 0\,. \qquad \text{(B.71)}
\end{aligned}$$

With

$$B := \mu+\lambda \overset{\text{(B.30)}}{=} \frac{\mathcal{E}}{2(1+\sigma)}+\frac{E\sigma}{(1-\sigma^2)}=\mathcal{E}\frac{(1-\sigma)+2\sigma}{2(1-\sigma^2)}=\frac{\mathcal{E}}{2(1-\sigma)}\,, \qquad \text{(B.72)}$$

$$B+\mu = 2\mu+\lambda \overset{\text{(B.30)}}{=} \frac{\mathcal{E}}{1+\sigma}+\frac{\mathcal{E}\sigma}{(1-\sigma^2)}=\mathcal{E}\frac{(1-\sigma)+\sigma}{(1-\sigma^2)}=\frac{\mathcal{E}}{1-\sigma^2}\,, \qquad \text{(B.73)}$$

we can express the bulk (B) and shear (μ) moduli of a three-dimensional body in terms of its Young's modulus and Poisson's ratio. The equations for in-plane equilibrium become

$$(B+\mu)\frac{\partial^2 u_x}{\partial x^2}+\mu\frac{\partial^2 u_x}{\partial y^2}+B\frac{\partial^2 u_y}{\partial x\partial_y}+P_x = 0\,, \qquad \text{(B.74)}$$

$$(B+\mu)\frac{\partial^2 u_y}{\partial y^2}+\mu\frac{\partial^2 u_y}{\partial x^2}+B\frac{\partial^2 u_x}{\partial x\partial_y}+P_y = 0\,. \qquad \text{(B.75)}$$

C. Symmetry and the piezoelectric tensor of hexagonal boron nitride

According to Neumann's principle, the symmetry of any physical property must be at least as high as the symmetry of the crystal [Nye]. Every (perfect) crystal can be attributed to one out of 32 crystal classes[1] (or point groups) [Ashcroft&Mermin]. These crystal classes can be further divided into seven crystal systems. All ideal crystals do exhibit symmetry and hence symmetry considerations can be a powerful and very elegant way to determine which elements of a tensor or operator may be nonzero. Here, we demonstrate that the point group $\bar{6}m2$ of hBN reduces the piezoelectric tensor of hBN to only one free parameter.

Tensors and their transformation

Tensors can be used to represent physical properties like conductivity. In a solid, the conductivity σ, which connects the current density $\boldsymbol{j}$ with the electric field $\boldsymbol{E}$ via[2] $j_k = \sigma_{kl}E_l$ is generally anisotropic, i.e. $\sigma_{kl} \neq \sigma_{\text{const.}}\delta_{kl}$. Conductivity is represented by a tensor of second rank. While every matrix is a second-rank tensor, not every second-rank tensor is a matrix. Both are square arrays of nine numbers (in $\mathbb{R}^3$), yet they mean different things. For example, the conductivity tensor σ_{ij} represents the physical property "conductivity" in the reference frame with coordinates x_i while an (improper) rotation matrix a_{ij} transforms from one (orthonormal) reference frame to another, $x'_i = a_{ij}x_j$, but does not represent a physical property. In short, tensors represent physical quantities w.r.t. a certain frame while (improper) rotation matrices are used to transform from one frame to another.

A physical property does not depend on the coordinates in which it is represented. That is, if its tensor components are known in the coordinates x_i, then they are implicitly also known in coordinates $x'_i = a_{ij}x_j$. Zeroth-rank tensors (scalars) like mass, charge, or length do not depend on the coordinate frame[3] such that the transformation is the identity operation, e.g., $m \mapsto m' = m$ for mass. First-rank tensors (vectors) like position, velocity, or angular momentum transform, obviously, like the coordinates, e.g., $v_i \mapsto v'_i = a_{ij}v_j$ for the velocity. Due to orthogonality, the back transformation is given by $v_i = a_{ji}v'_j$. The transformation for second-rank tensors can be deduced from the transformation for first-rank tensors. Going back to the example of conductivity, we find

$$j'_k = a_{kl}j_l = a_{kl}\sigma_{lm}E_m = \underbrace{a_{kl}\sigma_{lm}a_{nm}}_{=a_{kl}a_{nm}\sigma_{lm}}E'_n = \sigma'_{kn}E'_n\,, \quad \Rightarrow \quad \sigma'_{kn} = a_{kl}a_{nm}\sigma_{lm} \tag{C.1}$$

[1] For three dimensional crystals, that is. In two dimensions, there are only 10 point groups.

[2] We use Einstein's sum convention throughout, i.e., $\sigma_{kl}E_l = \sum_{l=1}^{3}\sigma_{kl}E_l$ and likewise.

[3] We restrict these consideration to orthonormal cartesian coordinates. The transformation matrices between such coordinate frames are orthogonal.

rank	$x \mapsto x'$	$x' \mapsto x$
0	$m' = m$	$m = m'$
1	$v'_i = a_{ij} v_j$	$v_i = a_{ji} v'_j$
2	$\sigma'_{ij} = a_{ik} a_{jl} \sigma_{kl}$	$\sigma_{ij} = a_{ki} a_{lj} \sigma'_{kl}$
3	$d'_{ijk} = a_{il} a_{jm} a_{kn} d_{lmn}$	$d_{ijk} = a_{li} a_{mj} a_{nk} d'_{lmn}$

Table C.1.: Transformation laws for tensors under the coordinate change $x_i \mapsto x'_i = a_{ij} x_j$.

and likewise $\sigma_{kn} = a_{lk} a_{mn} \sigma'_{lm}$. These transformations hold for all second-rank tensors. Iteratively, we can deduce the transformation for tensors of arbitrary rank, see Table C.1. In particular, an n-th rank tensor $t_{i\ldots k}$ transforms like a product of n coordinates,

$$\begin{aligned} t'_{i\ldots k} &= \underbrace{a_{ij} \ldots a_{kl}}_{n \text{ factors}} t_{j\ldots l} \,, \\ \underbrace{x'_i \ldots x'_k}_{n \text{ factors}} &= \underbrace{a_{ij} \ldots a_{kl}}_{n \text{ factors}} \underbrace{x_j \ldots x_l}_{n \text{ factors}} \,. \end{aligned} \tag{C.2}$$

The transformation $t_{i\ldots k} \mapsto t'_{j\ldots l}$ works accordingly,

$$\begin{aligned} t_{i\ldots k} &= a_{ji} \ldots a_{lk} t'_{j\ldots l} \,, \\ x_i \ldots x_k &= a_{ji} \ldots a_{lk} x'_j \ldots x'_l \,. \end{aligned} \tag{C.3}$$

Symmetry constraints on the piezoelectric tensor of hBN

The lattice of hBN belongs to the crystal class $\bar{6}m2$ (in Hermann-Mauguin notation; equivalent to D_{3h} in Schönflies notation) within the hexagonal crystal system. A stereographic projection of the point group $\bar{6}m2$ is shown in Fig. C.1. In particular, the crystal is invariant under the transformations

$$A_{m_1} : (x_1, x_2, x_3) \mapsto (-x_1, x_2, x_3) \,, \tag{C.4}$$

$$A_{m_3} : (x_1, x_2, x_3) \mapsto (x_1, x_2, -x_3) \,, \tag{C.5}$$

$$\begin{aligned} A_{\bar{6}} : \; & x_1 \mapsto -\left(\frac{1}{2} x_1 + \frac{\sqrt{3}}{2} x_2 \right) = -\frac{x_1}{2} - \frac{\sqrt{3}}{2} x_2 \\ & x_2 \mapsto -\left(-\frac{\sqrt{3}}{2} x_1 + \frac{1}{2} x_2 \right) = \frac{\sqrt{3}}{2} x_1 - \frac{1}{2} x_2 \\ & x_3 \mapsto -x_3 \,. \end{aligned} \tag{C.6}$$

The (third-rank) piezoelectric tensor is given by $d_{ijk} = \frac{\partial P_i}{\partial \sigma_{jk}}$ and is symmetric in the last two components because the stress tensor σ_{jk} is symmetric. The tensor components can be determined with some measurement apparatus that need not be further specified, here. Let us assume that in a certain position and orientation, our apparatus can measure d_{111}. Now, we act the map A_{m_1} on the position and orientation of our device while keeping the crystal unchanged. From the crystal / laboratory point of view, the apparatus

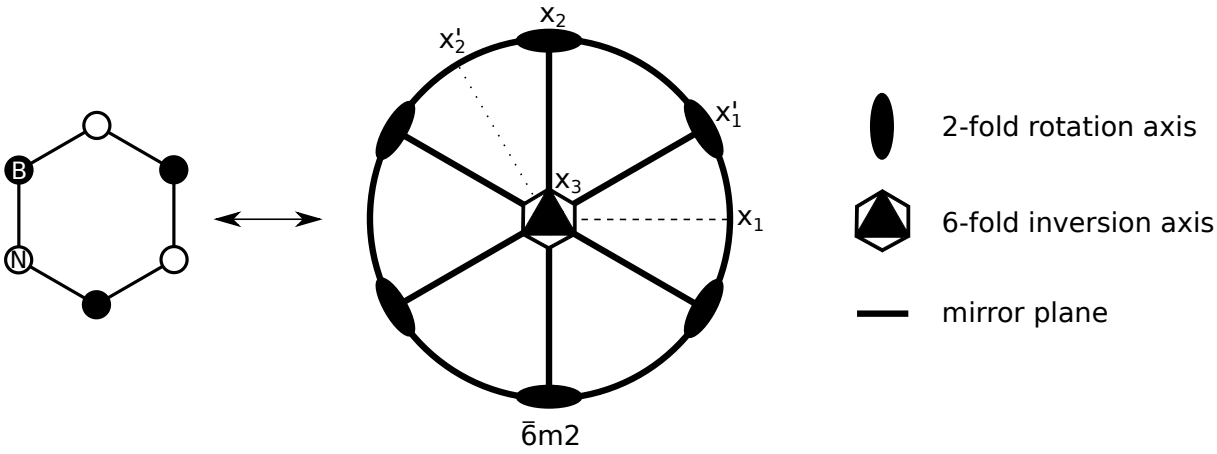

Figure C.1.: The lattice of hBN belongs to the point group $\bar{6}m2$ within the hexagonal crystal system. All symmetry elements are shown in the stereographic projection. The sixfold inversion axis is equivalent to a threefold rotation axis and a mirror plane perpendicular to it, see Eqs. (C.5) and (C.6). In addition to the standard orientation with a mirror plane perpendicular to the x_1-axis, $m \perp x_1$, we also show an orientation where a mirror plane is perpendicular to the x_2'-axis, $m \perp x_2'$. The orientation of the threefold rotation / sixfold inversion axis remains unchanged, $x_3' = x_3$.

now measures the tensor component $d'_{111} = -d_{111}$, where we have used Eq. (C.2) with $x'_1 x'_1 x'_1 = -x_1 x_1 x_1$. Yet from the measurement device point of view nothing has changed since the crystal is invariant under the map A_{m_1}. That is, the measurement must yield the same result as before, namely d_{111}. Of course, the measurement result is independent from the point of view, i.e. $d_{111} = d'_{111} = -d_{111} = 0$, because of symmetry. Due to Eqs. (C.2) and (C.4), all tensor components where the number of indices that equal 1 is odd vanishes, i.e. $d_{122} = d_{123} = d_{132} = d_{133} = d_{212} = d_{213} = d_{312} = d_{313} = d_{221} = d_{231} = d_{321} = d_{331} = 0$. Similar considerations hold for the map A_{m_3} such that $d_{113} = d_{131} = d_{223} = d_{232} = d_{311} = d_{322} = d_{333} = 0$. The only remaining elements are $d_{112} = d_{121}$, d_{211}, d_{222}, d_{233}, and $d_{323} = d_{332}$. Since d_{ijk} is symmetric in the last two components, the according coordinates in Eq. (C.2) can be commuted. By commuting only the last two coordinates but not the first, map $A_{\bar{6}}$ leads to

$$
\begin{aligned}
x_1(x_1x_2) \;&\mapsto\; \left(-\frac{1}{2}x_1 - \frac{\sqrt{3}}{2}x_2\right)\left(-\frac{\sqrt{3}}{4}x_1^2 + (\frac{1}{4} - \frac{3}{4})x_1x_2 + \frac{\sqrt{3}}{4}x_2^2\right) \\
&= \frac{\sqrt{3}}{8}x_1^3 + \frac{1}{4}x_1^2x_2 - \frac{\sqrt{3}}{8}x_1x_2^2 + \frac{3}{8}x_2x_1^2 + \frac{\sqrt{3}}{4}x_2x_1x_2 - \frac{3}{8}x_2^3\,, \\
\Rightarrow\; d_{112} \;&=\; \frac{\sqrt{3}}{8}d_{111} + \frac{1}{4}d_{112} - \frac{\sqrt{3}}{8}d_{122} + \frac{3}{8}d_{211} + \frac{\sqrt{3}}{4}d_{212} - \frac{3}{8}d_{222} \\
&=\; 0 + \frac{1}{4}d_{112} + \frac{3}{8}d_{211} - \frac{3}{8}d_{222}\,, \\
\Rightarrow\; d_{112} \;&=\; \frac{1}{2}(d_{211} - d_{222})\,,
\end{aligned}
\tag{C.7}
$$

where we have used that the tensor component d_{ijk} transforms like the coordinate product $x_i x_j x_k$, see Eq. (C.2) and Table C.1. In a similar fashion, we get $d_{211} = \frac{1}{3}(2d_{112} - d_{222})$, $d_{222} = -\frac{1}{3}(2d_{112}+d_{211})$, $d_{233} = 0$, and $d_{323} = 0$. We resolve that for hBN, crystal symmetry reduces the number of independent nonzero parameters of the piezoelectric tensor[4] from 18 to only one, namely $d_{112} = d_{211} = -d_{222}$.

We point out that for the hexagonal symmetry of the point group $\bar{6}m2$, two seemingly similar yet different lattice orientations need to be discerned. Here, we have chosen $m \perp x_1$, i.e., an orientation such that a mirror plane is perpendicular to the x_1-axis, see Figs. C.1 and 2.1. If the lattice is rotated by +30°, one mirror plane will be perpendicular to the x_2'-axis, i.e. $m \perp x_2'$, as shown in Fig. C.1. Due to the threefold rotation symmetry, this can be described most easily with a rotation[5] of -90°. With the map

$$A_\perp : \begin{pmatrix} x_1 \\ x_2 \\ x_3 \end{pmatrix} \mapsto \begin{pmatrix} 0 & 1 & 0 \\ -1 & 0 & 0 \\ 0 & 0 & 1 \end{pmatrix} \begin{pmatrix} x_1 \\ x_2 \\ x_3 \end{pmatrix} = \begin{pmatrix} x_2 \\ -x_1 \\ x_3 \end{pmatrix} = \begin{pmatrix} x_1' \\ x_2' \\ x_3' \end{pmatrix} , \tag{C.8}$$

and the reverse transformation according to Eq. (C.3), we find $d_{112} = a_{1i}a_{1j}a_{2k}d'_{ijk} = \delta_{i2}\delta_{j2}(-\delta_{k1})d'_{ijk}$, and thus $d_{112} = -d'_{221}$. Accordingly, we find $d'_{122} = -d_{211}$ and $d'_{111} = -d_{222}$. Consequently, the only free parameter in the rotated frame is $d'_{111} = -d'_{122} = -d'_{212}$, see also [Nye] and [Duerloo(2012)].

[4] As a third-rank tensor d_{ijk} has 27 elements. Yet d_{ijk} is symmetric in the last two components, $d_{ijk} = d_{ikj}$, which reduces the number of independent elements to 18, independent of crystal symmetry.

[5] The sign of the rotation matters, for the difference between +90° and -90° is a rotation of 180°. The crystal is not invariant under this rotation and our measurement device would return exactly the opposite value since strain is centrosymmetric and the polarization vector would point in the opposite direction.

D. Spin relaxation in bilayer graphene quantum dots

In order to confine charge carriers in graphene electrostatically, Klein's paradox demands a bandgap, see Subsec. 2.1.2 and [Katsnelson(2006)]. There are (at least) three situations that lead to a bandgap, namely (i) armchair graphene nanoribbons (depending on the ribbon width), (ii) monolayer graphene with a sublattice potential, and (iii) bilayer graphene with a layer-staggered potential. These situations allow for electrostatical confinement of electrons in quantum dots (QDs) and also break the valley degeneracy [Recher(2010)]. The benefits of carbon-based materials for spin coherence make such systems appealing for spintronics.

The spin relaxation times for systems based on situations (i) and (ii) have already been studied theoretically [Struck(2010), Droth(2013)]. However, neither of them is studied in experiment. For situation (i), the atomically precise construction of armchair graphene nanoribbons is a challenge in itself, even without additional electrostatic gating [Ruffieux(2012)]. A sublattice splitting (situation (ii)) can be realized within a graphene/hBN heterostructure (Subsec. 2.2.2) [Hunt(2013), Woods(2014)]. However, possible misalignment of the crystal axes of the two layers makes it difficult to reliably tailor a bandgap. In contrast, bilayer graphene with a perpendicular bias (situation (iii)) and electrostatic gating *is* studied in experiment [Goossens(2012), Varlet(2014), Varlet(2014-2)], but a theoretical work on the spin relaxation time in a bilayer graphene QD has, to our knowledge, not been performed, yet.

We envisage the calculation of the spin relaxation time T_1 via Fermi's golden rule in a similar way as in [Struck(2010)] and [Droth(2013)]. Such an analytic procedure relies on the form of the QD bound electronic states, the spin-orbit interaction, acoustic lattice dynamics, and the electron-phonon coupling to acoustic phonons in bilayer graphene. Below, we outline these fundamental building blocks.

Quantum dot bound electronic states

In the basis $(\psi_{AK}, \psi_{BK}, \psi_{AK'}, \psi_{BK'})$, the Hamiltonian of a single graphene layer, Eq. (2.17) with Δ=0, can be written as

$$\mathcal{H}_D = \begin{pmatrix} 0 & q_x - iq_y & 0 & 0 \\ q_x + iq_y & 0 & 0 & 0 \\ 0 & 0 & 0 & -q_x - iq_y \\ 0 & 0 & -q_x + iq_y & 0 \end{pmatrix} . \tag{D.1}$$

For a *valley-isotropic representation* [Beenakker(2008)], one may consider the unitary transformation

$$U = \begin{pmatrix} 1 & 0 & 0 & 0 \\ 0 & 1 & 0 & 0 \\ 0 & 0 & 0 & -1 \\ 0 & 0 & 1 & 0 \end{pmatrix} . \tag{D.2}$$

Under the transformation U, the basis becomes $(\psi_{AK}, \psi_{BK}, -\psi_{BK'}, \psi_{AK'})$ and the Hamiltonian takes the form

$$\mathcal{H}_D^{(U)} = U\mathcal{H}_D U^\dagger = \begin{pmatrix} 0 & q_x - iq_y & 0 & 0 \\ q_x + iq_y & 0 & 0 & 0 \\ 0 & 0 & 0 & q_x - iq_y \\ 0 & 0 & q_x + iq_y & 0 \end{pmatrix} , \tag{D.3}$$

which we may rewrite as

$$\tilde{\mathcal{H}}_D^{(U)} = \begin{pmatrix} 0 & q_x - iq_y \\ q_x + iq_y & 0 \end{pmatrix} , \tag{D.4}$$

if we bear in mind that the basis of this reduced form is (ψ_{AK}, ψ_{BK}) for the K-point (upper left block of Eq. (D.3)) and $(-\psi_{BK'}, \psi_{AK'})$ for the K'-point (lower right block of Eq. (D.3)). With this valley-isotropic representation of biased bilayer graphene (see also Eq. (2.35)) and an additional muffin tin confinement potential, Recher *et al.* have obtained the bound states of the resulting bilayer graphene QD [Recher(2009)].

Spin-orbit interaction and spin-phonon coupling

The full *spin-orbit interaction* $\mathcal{H}_{\text{biSOI}}$ of biased bilayer graphene can be derived from symmetry considerations [Guinea(2010), Konschuh(2012)]. With the Pauli matrices $\boldsymbol{\mu}$ (layer), $\boldsymbol{\sigma}$ (sublattice), $\boldsymbol{s}$ (electron spin), two-by-two unit matrices μ_0, σ_0 , s_0, and $\tau = \pm 1$ (valley), it can be denoted as

$$\mathcal{H}_{\text{biSOI}} = \mathcal{H}_{\text{I}} + \mathcal{H}_{\text{R}} + \mathcal{H}_{\text{inter}} + \mathcal{H}_{\text{el}}, \tag{D.5}$$

where the basis is similar to Eq. (2.32), $(\psi^{(A)}, \psi^{(B)}, \psi^{(A')}, \psi^{(B')}) \otimes (|\uparrow\rangle, |\downarrow\rangle)$, and

$$\begin{aligned} \mathcal{H}_{\text{I}} &= \frac{((\Delta_{\text{I}} - \Delta_{\text{I}}')\sigma_0 + (\lambda_{\text{I}} + \lambda_{\text{I}}')\sigma_z)\,\mu_0\tau s_z + ((\Delta_{\text{I}} + \Delta_{\text{I}}')\sigma_0 + (\lambda_{\text{I}} - \lambda_{\text{I}}')\sigma_z)\,\mu_z\tau s_z}{2} , \\ \mathcal{H}_{\text{R}} &= \frac{(\bar{\lambda}_0\mu_z + 2\lambda_{\text{R}}\mu_0)(\tau\sigma_x s_y - \sigma_y s_x)}{2} , \\ \mathcal{H}_{\text{inter}} &= -\frac{(\bar{\lambda}_4\sigma_z + \delta\lambda_4\sigma_0)(\tau\mu_x s_y + \mu_y s_x)}{2} , \\ \mathcal{H}_{\text{el}} &= \frac{\lambda_1}{2}\tau s_z(\mu_x\sigma_x - \mu_y\sigma_y) + \frac{\lambda_3}{4}\left(\mu_x(\tau\sigma_x s_y + \sigma_y s_x) + \mu_y(\tau\sigma_y s_y - \sigma_x s_x)\right) . \end{aligned} \tag{D.6}$$

Here, $\mathcal{H}_{\text{I}}$ and $\mathcal{H}_{\text{R}}$ are the intrinsic and Rashba-type Hamiltonians, respectively. The contribution $\mathcal{H}_{\text{inter}}$ comes from interlayer couplings and $\mathcal{H}_{\text{el}}$ from the layer bias. For

discussion of the coupling parameters Δ_I, Δ'_I, λ_I, λ'_I, $\bar{\lambda}_0$, λ_R, $\bar{\lambda}_4$, $\delta\lambda_4$, λ_1, and λ_3, we refer to [Konschuh(2012)].

For bilayer graphene, the spin-orbit interaction mediates the *spin-phonon coupling* in the same way as for monolayer graphene. As described in Sec. 3.3, $\mathcal{H}_\mathrm{biSOI}$ leads to an effective coupling of spin to in-plane phonons by admixing both spin-up and spin-down states in first order perturbation theory. Out-of-plane phonons lead to a local tilt of the lattice that can be considered in the spin-orbit interaction by correcting the electron spin ($\boldsymbol{s}$) orientation w.r.t. the sublattice spin ($\boldsymbol{\sigma}$) according to

$$s_x \mapsto s_x + (\partial_x u_z) s_z \,, \qquad s_y \mapsto s_y + (\partial_y u_z) s_z \,, \qquad s_y \mapsto s_z - (\partial_x u_z) s_x - (\partial_y u_z) s_y \,. \tag{D.7}$$

Applied to Eq. (D.5), these substitutions lead to an effective spin-phonon coupling to out-of-plane phonons.

Acoustic lattice dynamics

Upon spin relaxation, the Zeeman energy $g\mu_B B$, where g is the electron g-factor in graphene, μ_B is Bohr's magneton, and B is the magnetic field, is transferred to a lattice excitation with energy $\hbar\omega$. For typical laboratory magnetic fields $B{<}20\,\mathrm{T}$, the frequency ω corresponds to low-energy acoustic phonons at the center of the Brillouin zone. Phonons at the center of the Brillouin zone have a wavelength much longer than the atomic distance. This justifies a description with the continuum model.

Acoustic *in-plane deformations* (u_x, u_y) in bilayer graphene are described by a coupled set of differential equations,

$$\begin{aligned} \rho\ddot{u}_x &= (B+\mu)\partial_x^2 u_x + \mu\partial_y^2 u_x + B\partial_x\partial_y u_y \\ \rho\ddot{u}_y &= (B+\mu)\partial_y^2 u_y + \mu\partial_x^2 u_y + B\partial_x\partial_y u_x \,, \end{aligned} \tag{D.8}$$

where ρ is the surface mass density of bilayer graphene and B and μ are the bulk and the shear moduli, respectively. Note that we employ a quasi two-dimensional description where B, μ, and also Young's modulus $\mathcal{E}$ have the same dimension as in monolayer graphene. For bilayer graphene, it is not entirely clear if the relations of monatomically thin layers, given by Eq. (B.30), those of three-dimensional bulk material,

$$\lambda_\mathrm{3D} = \frac{\mathcal{E}_\mathrm{3D}\sigma}{(1-2\sigma)(1+\sigma)} \,, \qquad \mu_\mathrm{3D} = \frac{\mathcal{E}_\mathrm{3D}}{2(1+\sigma)} \,, \tag{D.9}$$

or none of them apply. Either way, the form of Eq. (D.8) remains unaffected and B and μ can be determined experimentally. Poisson's ratio σ is dimensionless and $\lambda{=}B{-}\mu$. With the ansatz $\boldsymbol{u} = \boldsymbol{u}^{(0)} e^{i(q_x x + q_y y - \omega t)}$, Eq. (D.8) becomes

$$\begin{aligned} -\rho\omega^2 u_x &= -(B+\mu)q_x^2 u_x - \mu q_y^2 u_x - B q_x q_y u_y \\ -\rho\omega^2 u_y &= -(B+\mu)q_y^2 u_y - \mu q_x^2 u_y - B q_x q_y u_x \,. \end{aligned} \tag{D.10}$$

With $q_x{=}0$, we resolve $-\rho\omega^2 u_x = -\mu q_y^2 u_x$ for the upper (transversal) component and $-\rho\omega^2 u_y = -(B+\mu)q_y^2 u_y$ for the lower (longitudinal) component. Analog relations hold for $q_y{=}0$, where the upper component corresponds to a longitudinal mode and the lower

component to a transversal one. The transversal ($\perp$) and longitudinal ($\parallel$) in-plane modes and sound velocities are thus given by

$$\begin{aligned} \boldsymbol{u}_\perp(\boldsymbol{q},t) &= \begin{pmatrix} u_x^{(\perp)} e^{i(q_y y-\omega_\perp t)} \\ u_y^{(\perp)} e^{i(q_x x-\omega_\perp t)} \end{pmatrix}, \qquad v_\perp = \frac{\omega_\perp}{q} = \sqrt{\frac{\mu}{\rho}}, \\ \boldsymbol{u}_\parallel(\boldsymbol{q},t) &= \begin{pmatrix} u_x^{(\parallel)} e^{i(q_x x-\omega_\parallel t)} \\ u_y^{(\parallel)} e^{i(q_y y-\omega_\parallel t)} \end{pmatrix}, \qquad v_\parallel = \frac{\omega_\parallel}{q} = \sqrt{\frac{(B+\mu)}{\rho}}. \end{aligned} \tag{D.11}$$

Out-of-plane deformations u_z are described by the differential equation

$$\rho \ddot{u}_z = -\kappa \left(\partial_x^2 + \partial_y^2\right)^2 u_z, \tag{D.12}$$

where the bending rigidity κ can be determined by experiment. Again, the form of this equation is identical to monolayer graphene and thin plates of three-dimensional bulk material. One easily verifies that the out-of-plane modes and their sound velocity are given by

$$u_z(\boldsymbol{q},t) = u_z e^{i(q_x x+q_y y-\omega_z t)}, \qquad v_z = \partial_q \omega_z = \partial_q \left(\sqrt{\frac{\kappa}{\rho}} q^2\right) = 2\sqrt{\frac{\kappa}{\rho}} q. \tag{D.13}$$

The two layers in bilayer graphene behave by and large independently because the van der Waals bond holding them together is much weaker than the in-plane σ bond. As a result, sound velocities can be approximated by the values for monolayer graphene, i.e. $v_\parallel \approx 19.5\,\mathrm{km/s}$, $v_\perp \approx 12.2\,\mathrm{km/s}$, and $v_z(q{=}0) = 0$ [Falkovsky(2008)]. The surface mass density is twice that of monolayer graphene and the same holds — in an approximation — for the elastic constants, because the contributions from the individual layers simply add up.

Electron-phonon coupling

As explained above, only acoustic phonons are relevant for spin relaxation processes where the lattice absorbs the Zeeman energy. Relative excitations of the individual layers in bilayer graphene w.r.t. each other correspond to optical lattice excitations and need not be considered for usual laboratory magnetic fields. As a result, the interlayer hopping t_{12} in Eq. (2.32) does not change in the process and the electron-phonon coupling is determined by the individual layers. The electron-phonon coupling in bilayer graphene is thus given by

$$\mathcal{H}_{\mathrm{biEPC}} = \mu_0(\mathcal{H}_{\mathrm{BLC}} + \mathcal{H}_{\mathrm{VEP}}) \tag{D.14}$$

where $\mathcal{H}_{\mathrm{BLC}}$ and $\mathcal{H}_{\mathrm{VEP}}$ are given by Eqs. (3.4) and (3.9), respectively. The minimal bilayer description given by Eq. (2.32) does not include a hopping between A' and B atoms, see Fig. 2.5. In bilayer graphene, this hopping is only slightly smaller than t_{12} and leads to a fictitious vector field $\bar{\boldsymbol{A}}$ similar to that of $\mathcal{H}_{\mathrm{BLC}}$ [Mariani(2012)]. This is because the hopping direction is not perpendicular to the graphene sheet but has an in-plane component that changes for acoustic in-plane modes.

Bibliography

[Anderson(1995)] M. H. Anderson, J. R. Ensher, M. R. Matthews, C. E. Wieman, and E. A. Cornell, *Observation of Bose-Einstein Condensation in a Dilute Atomic Vapor*, Science **269**, 198 (1995).

[Aharonov(1959)] Y. Aharonov and D. Bohm, *Significance of Electromagnetic Potentials in the Quantum Theory*, Physical Review **115**, 485 (1959).

[Ashcroft&Mermin] Neil W. Ashcroft and David D. Mermin, *Festkörperphysik*, 3rd edition, Oldenburg Wissenschaftsverlag (2007).

[Awschalom(2013)] David D. Awschalom, Lee C. Bassett, Andrew S. Dzurak, Evelyn L. Hu, and Jason R. Petta, *Quantum Spintronics: Engineering and Manipulating Atom-Like Spins in Semiconductors*, Science **339**, 1174 (2013).

[Bae(2010)] Sukang Bae, Hyeongkeun Kim, Youngbin Lee, Xiangfan Xu, Jae-Sung Park, Yi Zheng, Jayakumar Balakrishnan, Tian Lei, Hye Ri Kim, Young Il Song, Young-Jin Kim, Kwang S. Kim, Barbaros Özyilmaz, Jong-Hyun Ahn, Byung Hee Hong, and Sumio Iijima, *Roll-to-roll production of 30-inch graphene films for transparent electrodes*, Nature Nanotechnology **5**, 574 (2010).

[Bai] Chunli Bai, *Scanning Tunneling Microscopy and Its Application*, 2nd edition, Springer, Shanghai Scientific, and Technical Publishers (2000).

[Balakrishnan(2013)] Jayakumar Balakrishnan, Gavin Kok Wai Koon, Manu Jaiswall, A. H. Castro Neto, and Barbaros Özyilmaz, *Colossal enhancement of spin-orbit coupling in weakly hydrogenated graphene*, Nature Physics **9**, 284 (2013).

[Balandin(2008)] Alexander A. Balandin, Suchismita Ghosh, Wenzhong Bao, Irene Calizo, Desalegne Teweldebrhan, Feng Miao, and Chun Ning Lau, *Superior Thermal Conductivity of Single-Layer Graphene*, Nano Letters **8**, 902 (2008).

[Balasubramanian(2011)] Kannan Balasubramanian and Marko Burghard, *Chemie des Graphens*, Chemie in unsere Zeit **45**, 240 (2011).

[Barends(2014)] R. Barends, J. Kelly, A. Megrant, A. Veitia, D. Sank, E. Jeffrey, T. C. White, J. Mutus, A. G. Fowler, B. Campbell, Y. Chen, B. Chiaro, A. Dunsworth, C. Neill, P. O'Malley, P. Roushan, A. Vainsencher, J. Wenner, A. N. Korotkov, A. N. Cleland, and John M. Martinis, *Superconducting quantum circuits at the surface code threshold for fault tolerance*, Nature **508**, 500 (2014).

[Barkhofen(2013)] S. Barkhofen, M. Bellec, U. Kuhl, and F. Mortessagne, *Disordered graphene and boron nitride in a microwave tight-binding analog*, Physical Review B **87**,

035101 (2013).

[Beenakker(2008)] C. W. J. Beenakker, *Colloquium: Andreev reflection and Klein tunneling in graphene*, Reviews of Modern Physics **80**, 1337 (2008).

[Bernal(1924)] J. D. Bernal, *The Structure of Graphite*, Proceedings of the Royal Society of London – Series A **106**, 749 (1924).

[Berry(1984)] M. V. Berry, *Quantal Phase Factors Accompanying Adiabatic Changes*, Proceedings of the Royal Society A **392**, 45 (1984).

[Betti(2011)] A. Betti, G. Fiori, and G. Iannaccone, *Strong mobility degradation in ideal graphene nanoribbons due to phonon scattering*, Applied Physics Letters **98**, 212111 (2011).

[Bhowmick(2011)] Somnath Bhowmick, Abhishek K. Singh, and Boris I. Yakobsen, *Quantum Dots and Nanoroads of Graphene Embedded in Hexagonal Boron Nitride*, The Journal of Physical Chemistry C **115**, 9889 (2011).

[Binnig1982Pat] Gerd Binnig and Heinrich Rohrer, *Scanning tunneling microscope*, patent US 4343993 A, publication date: August 10$^{\text{th}}$, 1982.

[Boehm(1962)] H. P. Boehm, A. Clauss, G. Fischer, and U. Hofmann, *Surface Properties of Extremely Thin Graphite Lamellae*, Pergamon press reprint of the Proceedings of the Fifth Conference on Carbon, 73 (1962).

[Bohm] A. Bohm, A. Mostafazadeh, H. Koizumi, Q. Niu, and J. Zwanziger, *The Geometric Phase in Quantum Systems*, Springer (2003).

[Bol2012Pat] Ageeth A. Bol, Amal Kasry, Ahmed Maarouf, Glenn J. Martyna, Dennis M. Newns, Razvan A. Nistor, and George S. Tulevski, *Graphene Solar Cell*, patent US 20120000516 A1, publication date: January 5$^{\text{th}}$, 2012.

[Bolotin(2008)] K. I. Bolotin, K. J. Sikes, J. Hone, H. L. Stormer, and P. Kim, *Temperature-Dependent Transport in Suspended Graphene*, Physical Review Letters **101**, 096802 (2008).

[Braun(2011)] Matthias Braun, P. R. Struck, and Guido Burkard, *Spin exchange interaction with tunable range between graphene quantum dots*, Physical Review B **84** 115445 (2011).

[Brennen(1999)] Gavin K. Brennen, Carlton M. Caves, Poul S. Jessen, and Ivan H. Deutsch, *Quantum Logic Gates in Optical Lattices*, Physical Review Letters **82**, 1060 (1999).

[Brey(2006)] L. Brey and H. A. Fertig, *Electronic states of graphene nanoribbons studied with the Dirac equation*, Physical Review B **73**, 235411 (2006).

[Britnell(2012)] L. Britnell, R. V. Gorbachev, R. Jalil, B. D. Belle, F. Schedin, A. Mishchenko, T. Georgiou, M. I. Katsnelson, L. Eaves, S. V. Morozov, N. M. R. Peres, J. Leist, A. K. Geim, K. S. Novoselov, and L. A. Ponomarenko, *Field-Effect Tunneling Transistor Based on Vertical Graphene Heterostructures*, Science **335**, 947 (2012).

[Brodie(1859)] B. C. Brodie, *On the Atomic Weight of Graphite*, Philosophical Transactions of the Royal Society of London **149**, 249 (1859).

[Bulaev(2008)] Denis V. Bulaev, Björn Trauzettel, and Daniel Loss, *Spin-orbit interaction and anomalous spin relaxation in carbon nanotube quantum dots*, Physical Review B **77**, 235301 (2008).

[Bunch(2007)] J. Scott Bunch, Arend M. van der Zande, Scott S. Verbridge, Ian W. Frank, David M. Tanenbaum, Jeevak M. Parpia, Harold G. Craighead, and Paul L. McEuen, *Electromechanical Resonators from Graphene Sheets*, Science **315**, 490 (2007).

[Bunch(2008)] J. Scott Bunch, Scott S. Verbridge, Jonathan S. Alden, Arend M. van der Zande, Jeevak M. Parpia, Harold G. Craighead, and Paul L. McEuen, *Impermeable Atomic Membranes from Graphene Sheets*, Nano Letters **8**, 2458 (2008).

[Burkard(1999)] Guido Burkard, Daniel Loss, and David P. DiVincenzo, *Coupled quantum dots as quantum gates*, Physical Review B **59**, 2070 (1999).

[Burkard(2006)] Guido Burkard and Atac Imamoglu, *Ultra-long-distance interaction between spin qubits*, Physical Review B **74**, 041307(R), (2006).

[CastroNeto(2009)] A. H. Castro Neto, P. Guinea, N. M. R. Peres, K. S. Novoselov, and A. K. Geim, *The electronic properties of graphene*, Reviews of Modern Physics **81**, 109 (2009).

[CCBYSA3.0] The ideal crystalline structure of graphene is a hexagonal grid. © AlexanderAIUS, licensed under the Creative Commons Attribution-Share Alike 3.0 Unported license, http://tinyurl.com/mlvnuxr (retrieved on October 15$^{\text{th}}$, 2014).

[Chaikin&Lubensky] P. M. Chaikin and T. C. Lubensky, *Principles of condensed matter physics*, Cambridge University Press (1995).

[Chen(2008)] Jian-Hao Chen, Chuang Jang, Shudong Xiao, Masa Ishigami, and Michael S. Fuhrer, *Intrinsic and extrinsic performance limits of graphene devices on SiO_2*, Nature Nanotechnology **3**, 206 (2008).

[Chen(2008-2)] J.-H. Chen, C. Jang, S. Adam, M. S. Fuhrer, E. D. Williams, and M Ishigami, *Charged-impurity scattering in graphene*, Nature Physics **4**, 377 (2008).

[Childress(2006)] L. Childress, M. V. Gurudev Dutt, J. M. Taylor, A. S. Zibrov, F. Jelezko, J. Wrachtrup, P. R. Hemmer, and M. D. Lukin, *Coherent Dynamics of Coupled Electron and Nuclear Spin Qubits in Diamond*, Science **314**, 281 (2006).

[Chirolli(2008)] Luca Chirolli and Guido Burkard, *Decoherence in solid-state qubits*, Advances in Physics **57**, 225 (2008).

[Chuang(1998)] Isaac L. Chuang, Neil Gershenfeld, and Mark Kubinec, *Experimental Implementation of Fast Quantum Searching*, Physical Review Letters **80**, 3408 (1998).

[Cirac(1995)] J. I. Cirac and P. Zoller, *Quantum Computations with Cold Trapped Ions*, Physical Review Letters **74**, 4091 (1995).

[Dean(2010)] C. R. Dean, A. F. Young, I.Meric, C. Lee, L. Wang, S. Sorgenfrei, K. Watanabe, T. Taniguchi, P. Kim, K. L. Shepard, and J. Hone, *Boron nitride substrates for high-quality graphene electronics*, Nature Nanotechnology **5**, 722 (2010).

[Decker(2013)] Régis Decker, Jens Brede, Nicolae Atodiresei, Vasile Caciuc, Stefan Blügel, and Roland Wiesendanger, *Atomic-scale magnetism of cobalt-intercalated graphene*, Physical Review B **87**, 041403(R) (2013).

[Dedkov(2008)] Yu. S. Dedkov, M. Fonin, U. Rüdiger, and C. Laubschat, *Rashba Effect in the Graphene/Ni(111) System*, Physical Review Letters **100**, 107602 (2008).

[Deutsch(1985)] D. Deutsch, *Quantum theory, the Church-Turing principle and the universal quantum computer*, Proceedings of the Royal Society A **400**, 97 (1985).

[DiVincenzo(1984)] D. P. DiVincenzo and E. J. Mele, *Self-consistent effective-mass theory for intralayer screening in graphite intercalation compounds*, Physical Review B **29**, 1685 (1984).

[DiVincenzo(1998)] D. P. DiVincenzo and D. Loss, *Quantum information is physical*, Superlattices and Microstructures **23**, 419 (1998).

[DiVincenzo(1999)] D. P. DiVincenzo, G. Burkard, D. Loss and E. V. Sukhorukov, *Quantum computation and spin electronics*, NATO Advanced Study Institute, Series B: Physics **559**, Kluwer Academic (2000).

[Droth(2010)] Matthias Droth, *Spin coherence in graphene quantum dots*, Diploma Thesis, Universität Konstanz (2010).

[Droth(2011)] Matthias Droth and Guido Burkard, *Acoustic phonons and spin relaxation in graphene nanoribbons*, Physical Review B **84**, 155404 (2011).

[Droth(2013)] Matthias Droth and Guido Burkard, *Electron spin relaxation in graphene nanoribbon quantum dots*, Physical Review B **87**, 205432 (2013).

[Droth(2014)] Matthias Droth and Guido Burkard, *Magnetic-field tunable antiferromagnetism of vacancies in graphene nanoflakes*, arXiv:1405.5451 (2014).

[Duerloo(2012)] Karel-Alexander N. Duerloo, Mitchell T. Ong, and Evan J. Reed, *Intrinsic Piezoelectricity in Two-Dimensional Materials*, The Journal of Physical Chemistry Letters **3**, 2871 (2012).

[Eda(2008)] Goki Eda, Giovanni Fanchini, and Manish Chhowalla, *Large-area ultrathin films of reduced graphene oxide as a transparent and flexible electronic material*, Nature Nanotechnology **3**, 270 (2008).

[Ehrenberg(1949)] W. Ehrenberg and R. E. Siday, *The Refractive Index in Electron Optics and the Principles of Dynamics*, Proceedings of the Physical Society, Section B **62**, 9 (1949).

[Elias(2011)] D. C. Elias, R. V. Gorbachev, A. S. Mayorov, S. V. Morozov, A. A. Zhukov, P. Blake, L. A. Ponomarenko, I. V. Grigorieva, K. S. Novoselov, F. Guinea, and A. K. Geim, *Dirac cones reshaped by interaction effects in suspended graphene*, Nature

Physics **7**, 701 (2011).

[ElKady(2012)] Maher F. El-Kady, Veronica Strong, Sergey Dubin, and Richard B. Kaner, *Laser Scribing of High-Performance and Flexible Graphene-Based Electrochemical Capacitors*, Science **335**, 1326 (2012).

[Ezawa(2007)] Motohiko Ezawa, *Metallic graphene nanodisks: Electronic and magnetic properties*, Physical Review B **76**, 245415 (2007).

[Faccio(2009)] Ricardo Faccio, Pablo A. Denis, Helena Pardo, Cecilia Goyenola, and Álvaro W. Mombrú, *Mechanical properties of graphene nanoribbons*, Journal of Physics: Condensed Matter **21**, 285304 (2009).

[Falkovsky(2008)] L. A. Falkovsky, *Symmetry constraints on phonon dispersion in graphene*, Physics Letters A **372**, 5189 (2008).

[Farmer(2009)] Damon B. Farmer, Hsin-Ying Chiu, Yu-Ming Lin, Keith A. Jenkins, Fengian Xia, and Phaedon Avouris, *Utilization of a Buffered Dielectric to Achieve High Field-Effect Carrier Mobility in Graphene Transistors*, Nano Letters **9**, 4474 (2009).

[Fasolino(2007)] A. Fasolino, J. H. Los, and M. I. Katsnelson, *Intrinsic ripples in graphene*, Nature Materials **6**, 858 (2007).

[Fernández-Rossier(2007)] J. Fernández-Rossier and J. J. Palacios, *Magnetism in Graphene Nanoislands*, Physical Review Letters **99**, 177204 (2007).

[Feynman(1939)] R. P. Feynman, *Forces in Molecules*, Physical Review **56**, 340 (1937).

[Feynman(1960)] Richard P. Feynman, *There' Plenty of Room at the Bottom*, Engineering and Science **23**, 22 (1960).

[Feynman(1982)] Richard P. Feynman, *Simulating Physics with Computers*, International Journal of Theoretical Physics **21**, 467 (1982).

[Finkenstadt(2007)] Daniel Finkenstadt, G. Pennington, and M. J. Mehl, *From graphene to graphite: A general tight-binding approach for nanoribbon carrier transport*, Physical Review B **76**, 121405 (2007).

[Frank(2007)] I. W. Frank, D. M. Tanenbaum, A. M. van der Zande, and P. L. McEuen, *Mechanical properties of suspended graphene sheets*, Journal of Vacuum Science & Technology B **25**, 2558 (2007).

[Fujita(1996)] Mitsutaka Fujita, Katsunori Wakabayashi, Kyoko Nakada, and Koichi Kusakabe, *Peculiar Localized State at Zigzag Graphite Edge*, Journal of the Physical Society of Japan **65**, 1920 (1996).

[Gaebel(2006)] Torsten Gaebel, Michael Domhan, Iulian Popa, Christoffer Wittmann, Philipp Neumann, Fedor Jelezko, James R. Rabeau, Niklas Stavrias, Andrew D. Greentree, Steven Prawer, Jan Meijer, Jason Twamley, Philip R. Hemmer, and Jörg Wrachtrup, *Room-temperature coherent coupling of singe spins in diamond*, Nature Physics **2**, 408 (2006).

[GarciaSanchez(2008)] D. Garcia-Sanchez, A. M. van der Zande, A. San Paulo, B. Lassagne, P. L. McEuen, and A. Bachtold, *Imaging Mechanical Vibrations in Suspended Graphene Sheets*, Nano Letters **8**, 1399 (2008).

[Gazit(2009)] Doron Gazit, *Theory of the spontaneous buckling of doped graphene*, Physical Review B **79**, 113411 (2009).

[Geim(2007)] A. K. Geim and K. S. Novoselov, *The rise of graphene*, Nature Materials **6**, 183 (2007).

[Geim(2008)] Andre K. Geim and Philip Kim, *Carbon Wonderland*, Scientific American **298**, 90 (2008).

[Geim(2013)] A. K. Geim and I. V. Grigorieva, *Van der Waals heterostructures*, Nature **499**, 419 (2013).

[Giovannetti(2007)] Gianluca Giovannetti, Petr A. Khomyakov, Geert Brocks, Paul J. Kelly, and Jeroen van den Brink, *Substrate-induced band gap in graphene on hexagonal boron nitride: Ab initio density functional calculations*, Physical Review B **76**, 073103 (2007).

[Giraud(2012)] Paul Giraud, *Study of the Electronic Structure of Hexagonal Boron Nitride on Metal Substrates*, Master Thesis, Université des Sciences et Technologies Lille 1 (2012).

[Gisin(2002)] Nicolas Gisin, Grégoire Ribordy, Wolfgang Tittel, and Hugo Zbinden, *Quantum cryptography*, Reviews of Modern Physics **74**, 145 (2002).

[Gmitra(2009)] M. Gmitra, S. Konschuh, C. Ertler, C. Ambrosch-Draxl, and J. Fabian, *Band-structure topologies of graphene: Spin-orbit coupling effects from first principles*, Physical Review B **80**, 235431 (2009).

[Gmitra(2013)] Martin Gmitra, Denis Kochan, and Jaroslav Fabian, *Spin-Orbit Coupling in Hydrogenated Graphene*, Physical Review Letters **110**, 246602 (2013).

[Goossens(2012)] Augustinus (Stijn) M. Goossens, Stefanie C. M. Driessen, Tim A. Baart, Kenji Watanabe, Takashi Taniguchi, and Lieven M. K. Vanersypen, *Gate-Defined Confinement in Bilayer Graphene-Hexagonal Boron Nitride Hybrid Devices*, Nano Letters **12**, 4656 (2012).

[Grujić(2013)] M. Grujić, M. Tadić, and F. M. Peeters, *Antiferromagnetism in hexagonal graphene structures: Rings versus dots*, Physical Review B **87**, 085434 (2013).

[Güttinger(1932)] P. Güttinger, *Das Verhalten von Atomen im magnetischen Drehfeld*, Zeitschrift für Physik **73**, 169 (1932).

[Guinea(2009)] F. Guinea, M. I. Katsnelson, and A. K. Geim, *Energy gaps and a zero-field quantum Hall effect in graphene by strain engineering*, Nature Physics **6**, 30 (2010).

[Guinea(2010)] F. Guinea, *Spin-orbit coupling in a graphene bilayer and in graphite*, New Journal of Physics **12**, 083063 (2010).

[Hassel(1924)] O. Hassel and H. Mark, *Über die Kristallstruktur des Graphits*, Zeitschrift für Physik **25**, 317 (1924).

[Hämäläinen(2011)] Sampsa K. Hämäläinen, Zhixiang Sun, Mark P. Boneschanscher, Andreas Upptsu, Mari Ijäs, Ari Harju, Daniël Vanmaekelbergh, and Peter Liljeroth, *Quantum-Confined Electronic States in Atomically Well-Defined Graphene Nanostructures*, Physical Review Letters **107**, 236803 (2011).

[Han(2007)] Melinda Y. Han, Barbaros Özyilmaz, Yuanbo Zhang, and Philip Kim, *Energy Band-Gap Engineering of Graphene Nanoribbons*, Physical Review Letters **98**, 206805 (2007).

[Han(2008)] Wei-Qiang Han, Lijun Wu, Yimei Zhu, Kenji Watanabe, and Takashi Taniguchi, *Structure of chemically derived mono- and few-atomic-layer boron nitride sheets*, Applied Physics Letters **93**, 223103 (2008).

[Hanson(2007)] R. Hanson, L. P. Kouwenhoven, J. R. Petta, S. Tarucha, and L. M. K. Vandersypen, *Spins in few-electron quantum dots*, Reviews of Modern Physics **79**, 1217 (2007).

[Harrison] Walter A. Harrison, *Electronic Structure and the Properties of Solids*, W. H. Freeman and Company (1980).

[Harrison-2] Walter A. Harrison, *Elementary Electronic Structure*, World Scientific (1999).

[Hasegawa(2006)] Yasumasa Hasegawa, Rikio Konno, Hiroki Nakano, and Mahito Kohmoto, *Zero modes of tight-binding electrons on the honeycomb lattice*, Physical Review B **74**, 033413 (2006).

[Hellmann] H. Hellmann, *Einführung in die Quantenchemie*, Franz Deuticke (1937).

[Hirst(1997)] L. L. Hirst, *The microscopic magnetization: concept andapplication*, Reviews of Modern Physics **69**, 607 (1997).

[Hong(2013)] Jeongmin Hong, Elena Bekyarova, Walt A. de Heer, Robert C. Haddon, and Sakhrat Khizroev, *Chemically Engineered Graphene-Based 2D Organic Molecular Magnet*, ACS Nano **7**, 10011 (2013).

[Hu(2013)] Lung-Hao Hu, Feng-Yu Wu, Cheng-Te Lin, Andrei N. Khlobystov, and Lain-Jong Li, *Graphene-modified $LiFePO_4$ cathode for lithium ion battery beyond theoretical capacity*, Nature Communications **4**, 1687 (2013).

[Hunt(2013)] B. Hunt, J. D. Sanchez-Yamagishi, A. F. Young, M. Yankowitz, B. J. LeRoy, K. Watanabe, T. Taniguchi, P. Moon, M. Koshino, P. Jarillo-Herrero, and R. C. Ashoori, *Massive Dirac Fermions and Hofstadter Butterfly in a van der Waals Heterostructure*, Science **340**, 1427 (2013).

[Iijima(1991)] Sumio Iijima, *Helical microtubules of graphitic carbon*, Nature **354**, 56 (1991).

[Jaksch(1999)] D. Jaksch, H.-J. Briegel, J. I. Cirak, C. W. Gardiner, and P. Zoller, *En-*

tanglement of Atoms via Cold Controlled Collisions, Physical Review Letters **82**, 1975 (1999).

[Jiao(2009)] Liying Jiao, Li Zhang, Xinran Wang, Georgi Diankov, and Hongjie Dai, *Narrow graphene nanoribbons from carbon nanotubes*, Nature **458**, 877 (2009).

[Kane(1998)] B. E. Kane, *A silicon-based nuclear spin quantum computer*, Nature **393**, 133 (1998).

[Kane(2005)] C. L. Kane and E. J. Mele, *Quantum Spin Hall Effect in Graphene*, Physical Review Letters **95**, 226801 (2005).

[Katsnelson] Mikhail I. Katsnelson, *Graphene — Carbon in Two Dimensions*, Cambridge University Press (2012).

[Katsnelson(2006)] M. I. Katsnelson, K. S. Novoselov, and A. K. Geim, *Chiral tunnelling and the Klein paradox in graphene*, Nature Physics **2**, 620 (2006).

[Khaetskii(2001)] Alexander V. Khaetskii and Yuli V. Nazarov, *Spin-flip transitions between Zeeman sublevels in semiconductor quantum dots*, Physical Review B **64**, 125316 (2001).

[Kim(2009)] Keun Soo Kim, Yue Zhao, Houk Jang, Sang Yoon Lee, Jong Min Kim, Kwang S. Kim, Jong-Hyun Ahn, Philip Kim, Jae-Young Choi, and Byung Hee Hong, *Large-scale pattern growth of graphene films for stretchable transport electrodes*, Nature **457**, 706 (2009).

[Kim(2012)] Kyu Hun Kim, Youngseok Oh, and M. F. Islam, *Graphene coating makes carbon nanotube aerogels superelastic and resistant to fatigue*, Nature Nanotechnology **7**, 562 (2012).

[Kindermann(2012)] M. Kindermann, Bruno Uchoa, and D. L. Miller, *Zero-energy modes and gate-tunable gap in graphene on hexagonal boron nitride*, Physical Review B **86**, 115415 (2012).

[Kish(2002)] Laszlo B. Kish, *End of Moore's law: thermal (noise) death of integration in micro and nano electronics*, Physics Letters A **305**, 144 (2002).

[Klein(1929)] O. Klein, *Die Reflexion von Elektronen an einem Potentialsprung nach der relativistischen Dynamik von Dirac*, Zeitschrift für Physik **53**, 157 (1929).

[Konschuh(2010)] Sergej Konschuh, Martin Gmitra, and Jaroslav Fabian, *Tight-binding theory of the spin-orbit coupling in graphene*, Physical Review B **82**, 245412 (2010).

[Konschuh(2012)] S. Konschuh, M. Gmitra, D. Kochan, and J. Fabian, *Theory of spin-orbit coupling in bilayer graphene*, Physical Review B **85**, 115423 (2012).

[Kosynkin(2009)] Dmitry V. Kosynkin, Amanda L. Higginbotham, Alexander Sinitskii, Jay R. Lomeda, Ayrat Dimiev, B. Katherine Price, and James M. Tour, *Longitudinal unzipping of carbon nanotubes to form graphene nanoribbons*, Nature **458**, 872 (2009).

[Kotov(2012)] Valeri N. Kotov, Bruno Uchoa, Vitor M. Pereira, F. Guinea, and A. H. Cas-

tro Neto, *Electron-Electron Interactions in Graphene: Current Status and Perspectives*, Reviews of Modern Physics **84**, 1067 (2012).

[Krasheninnikov(2007)] A. V. Krasheninnikov and F. Banhart, *Engineering of nanostructured carbon materials with electron or ion beams*, Nature Materials **6** 723 (2007).

[Kroto(1985)] H. W. Kroto, J. R. Heath, S. C. O'Brien, R. F. Curl, and R. E. Smalley, *C_{60}: Buckminsterfullerene*, Nature **318**, 162 (1985).

[Kudin(2001)] Konstantin N. Kudin, Gustavo E. Scuseria, and Boris I. Yakobson, *C_2F, BN, and C nanoshell elasticity from ab initio computations*, Physical Review B **64**, 235406 (2001).

[Kuemmeth(2008)] F. Kuemmeth, S. Ilani, D. C. Ralph, and P. L. McEuen, *Coupling of spin and orbital motion of electrons in carbon nanotubes*, Nature **452**, 448 (2008).

[Kuzmenko(2008)] A. B. Kuzmenko, E. van Heumen, F. Carbone, and D. van der Marel, *Universal Optical Conductance of Graphite*, Physical Review Letters **100**, 117401 (2008).

[Landau&Lifschitz] L. D. Landau and E. M. Lifschitz, *Lehrbuch der theoretischen Physik, Band VII — Elastizitätstheorie*, 7^{th} edition, Akademie Verlag (1991).

[Lee(2008)] Changgu Lee, Xiaoding Wei, Jeffrey W. Kysar, and James Hone, *Measurement of the Elastic Properties and Intrinsic Strength of Monolayer Graphene*, Science **321**, 385 (2008).

[Lee(2014)] Jae-Hyun Lee, Eun Kyung Lee, Won-Jae Joo, Yamujin Jang, Byung-Sung Kim, Jae Young Lim, Soon-Hyung Choi, Sung Joon Ahn, Joung Real Ahn, Min-Ho Park, Cheol-Woong Yang, Byoung Lyong Choi, Sung-Woo Hwang, and Dongmok Whang, *Wafer-Scale Growth of Single-Crystal Monolayer Graphene on Reusable Hydrogen-Terminated Germanium*, Science **344**, 286 (2014).

[Leicht(2014)] Philipp Leicht, Lukas Zielke, Samuel Bouvron, Riko Moroni, Elena Voloshina, Lukas Hammerschmidt, Yuriy S. Dedkov, and Mikhail Fonin, *In Situ Fabrication Of Quasi-Free-Standing Epitaxial Graphene Nanoflakes On Gold*, ACS Nano **8**, 3735 (2014).

[Lemme(2007)] M. C. Lemme, T. J. Echtermeyer, M. Baus, and H. Kurz, *A Graphene Field Effect Device*, IEEE Electron Device Letters **28**, 282 (2007).

[Leturcq(2009)] Renaud Leturcq, Christoph Stampfer, Kevin Inderbitzin, Lukas Durrer, Christofer Hierold, Eros Mariani, Maximilian G. Schultz, Felix von Oppen, and Klaus Ensslin, *Franck-Condon blockade in suspended carbon nanotube quantum dots*, Nature Physics **5**, 327 (2009).

[Levitt] Malcoml H. Levitt, *Spin dynamics*, Wiley (2005).

[Levy(2010)] N. Levy, S. A. Burke, K. L. Meaker, M. Panlasigui, A. Zettl, F. Guinea, A. H. Castro Neto, and M. F. Crommie, *Strain-Induced Pseudo-Magnetic Fields Greater Than 300 Tesla in Graphene Nanobubbles*, Science **329**, 544 (2010).

[Li(2008)] Xiaolin Li, Xinran Wang, Li Zhang, Sangwon Lee, and Hongjie Dai, *Chemically Derived, Ultrasmooth Graphene Nanoribbon Semiconductors*, Science **319**, 1229 (2008).

[Lieb(1989)] Elliott H. Lieb, *Two Theorems on the Hubbard Model*, Physical Review Letters **62**, 1201 (1989).

[Lima(2010)] Matheus P. Lima, A. R. Rocha, Antônio J. R. da Silva, and A. Fazzio, *Mimicking nanoribbon behavior using a graphene layer on SiC*, Physical Review B **82**, 153402 (2010).

[Lin(2010)] Y.-M. Lin, C. Dimitrakopoulos, K. A. Jenkins, D. B. Farmer, H.-Y. Chiu, A. Grill, and Ph. Avouris, *100-GHz Transistors from Wafer-Scale Epitaxial Graphene*, Science **327**, 662 (2010).

[Lin(2011)] Yu-Ming Lin, Alberto Valdes-Garcia, Shu-Jen Han, Damon B. Farmer, Inanc Meric, Yanning Sun, Yanqing Wu, Christos Dimitrakopoulos, Alfred Grill, Phaedon Avouris, and Keith A. Jenkins, *Wafer-Scale Graphene Integrated Circuit*, Science **332**, 1294 (2011).

[Liu(2009)] P. Liu and Y. W. Zhang, *Temperature-dependent bending rigidity of graphene*, Applied Physics Letters **94**, 231912 (2009).

[Lloyd(2000)] Seth Lloyd, *Ultimate physics limits to computation*, Nature **406**, 1047 (2000).

[Loss(1998)] Daniel Loss and David P. DiVincenzo, *Quantum computation with quantum dots*, Physical Review A **57**, 120 (1998).

[Luo(2011)] Zhengtang Luo, Seungchul Kim, Nicole Kawamoto, Andrew M. Rappe, and A. T. Charlie Johnson, *Growth Mechanism of Hexagonal-Shape Graphene Flakes with Zigzag Edges*, ACS Nano **5**, 9154 (2011).

[Manin(1980)] Yu. I. Manin, *The computable and incomputable*, Sovetskoe Radio [in Russian], (1980).

[Marder] Michael P. Marder, *Condensed Matter Physics*, Wiley-Interscience (2010).

[Mariani(2008)] Eros Mariani and Felix von Oppen, *Flexural Phonons in Free-Standing Graphene*, Physical Review Letters **100**, 076801 (2008).

[Mariani(2009)] Eros Mariani and Felix von Oppen, *Electron-vibron coupling in suspended carbon nanotube quantum dots*, Physical Review B **80**, 155411 (2009).

[Mariani(2012)] Eros Mariani, Alexander J. Pearce, and Felix von Oppen, *Fictitious gauge fields in bilayer graphene*, Physical Review B **86**, 165448 (2012).

[McCann(2006)] Edward McCann and Vladimir I. Fal'ko, *Landau-level degeneracy and quantum Hall effect in a graphite bilayer*, Physical Review Letters **96**, 086805 (2006).

[McCann(2006-2)] Edward McCann, *Asymmetry gap in the electronic band structure of bilayer graphene*, Physical Review B **74**, 161403(R) (2006).

[Mele(2002)] E. J. Mele and Petr Král, *Electric Polarization of Heteropolar Nanotubes as*

a geometric Phase, Physical Review Letters **88**, 056803 (2002).

[Mermin(1966)] N. D. Mermin and H. Wagner, *Absence of Ferromagnetism or Antiferromagnetism in One- or Two-Dimensional Isotropic Heisenberg Models*, Physical Review Letters **17**, 1133 (1966).

[Mermin(1968)] N. D. Mermin, *Crystalline Order in Two Dimensions*, Physical Review **176**, 250 (1968).

[Messiah] Albert Messiah, *Quantenmechanik 2*, 3rd edition, Walter de Gruyter (1990).

[Meyer(2007)] Jannik C.Meyer, A. K. Geim, M. I. Katsnelson, K. S. Novoselov, T. J. Booth, and S. Roth, *The structure of suspended graphene sheets*, Nature **446**, 60 (2007).

[Min(2006)] Hongki Min, J. E. Hill, N. A. Sinitsyn, B. R. Sahu, Leonard Kleinman, and A. H. MacDonald, *Intrinsic and Rashba spin-orbit interactions in graphene sheets*, Physical Review B **74**, 165310 (2006).

[Min(2007)] Hongki Min, Bhagawan Sahu, Sanjay K. Banerjee, and A. H. MacDonald, *Ab initio theory of gate induced gaps in graphene bilayers*, Physical Review B **75**, 155115 (2007).

[Min(2011)] Seung Kyu Min, Woo Youn Kim, Yeonchoo Cho, and Kwan S. Kim, *Fast DNA sequencing with a graphene-based nanochannel device*, Nature Nanotechnology **6**, 162 (2011).

[Mohr(2007)] M. Mohr, J. Maultzsch, E. Dobardžić, S. Reich, I. Milošević, M. Damnjanović, A. Bosak, M. Krisch, and C. Thomsen, *Phonon dispersion of graphite by inelastic x-ray scattering*, Physical Review B **76**, 035439 (2007).

[Moore(1965)] Gordon E. Moore, *Cramming More Components onto Integrated Circuits*, Electronics 114 (1965).

[Nair(2008)] R. R. Nair, P. Blake, A. N. Grigorenko, K. S. Novoselov, T. J. Booth, T. Stauber, N. M. R. Peres, and A. K. Geim, *Fine Structure Constant Defines Visual Transparency of Graphene*, Science **320**, 1308 (2008).

[Nair(2012)] R. R. Nair, M. Sepioni, I-Ling Tsai, O. Lehtinen, J. Keinonen, A. V. Krasheninnikov, T. Thomson, A. K. Geim, and I. V. Grigorieva, *Spin-half paramagnetism in graphene induced by point defects*, Nature Physics **8**, 199 (2012).

[Nielsen&Chuang] Michael A. Nielsen and Isaac L. Chuang, *Quantum Computation and Quantum Information*, Cambridge University Press (2004).

[Nika(2009)] D. L. Nika, E. P. Pokatilov, A. S. Askerov, and A. A. Balandin, *Phonon thermal conduction in graphene: Role of Umklapp and edge roughness scattering*, Physical Review B **79**, 155413 (2009).

[Nolting7] Wolfgang Nolting, *Grundkurs Theoretische Physik 7 — Viel-Teilchen-Theorie*, 7th edition, Springer (2009).

[Nomura(2006)] Kentaro Nomura and Allan H. MacDonald, *Quantum Hall Ferromag-*

netism in Graphene, Physical Review Letters **96**, 256602 (2006).

[Novoselov(2004)] K. S. Novoselov, A. K. Geim, S. V. Morozov, D. Jiang, Y. Zhang, S. V. Dubonos, I. V. Grigorieva, and A. A. Firsov, *Electric Field Effect in Atomically Thin Carbon Films*, Science **306**, 666 (2004).

[Novoselov(2005)] K. S. Novoselov, A. K. Geim, S. V. Morozov, D. Jiang, M. I. Katsnelson, I. V. Grigorieva, S. V. Dubonos, and A. A. Firsov, *Two-dimensional gas of massless Dirac fermions in graphene*, Nature **438**, 197 (2005).

[Novoselov(2005-2)] K. S. Novoselov, D. Jiang, F. Schedin, T. J. Booth, V. V. Khotkevich, S. V. Morozov, and A. K. Geim, *Two-dimensional atomic crystals*, Proceedings of the National Academy of Sciences of the United States of America **102**, 10451 (2005).

[Novoselov(2012)] K. S. Novoselov, V. I. Fal'ko, L. Colombo, P. R. Gellert, M. G. Schwab, and K. Kim, *A roadmap for graphene*, Nature **490**, 192 (2012).

[Nye] J. F. Nye, *Physical Properties of Crystals — Their Representation by Tensors and Matrices*, Oxford University Press (2009).

[O'Connell(2010)] A. D. O'Connell, M. Hofheinz, M. Ansmann, Radoslaw C. Bialczak, M. Lenander, Erik Lucero, M. Neeley, D. Sank, H. Wang, M. Weides, J. Wenner, John M. Martinis, and A. N. Cleland, *Quantum ground state and single-photon control of mechanical resonator*, Nature **464**, 697 (2010).

[Ohta(2006)] Taisuke Ohta, Aaron Bostwick, Thomas Seyller, Karsten Horn, and Eli Rotenberg, *Controlling the electronic structure of bilayer graphene*, Science **313** 951 (2006).

[Oshima(1988)] C. Oshima, T. Aizawa, R. Souda, and Y. Ishiziwa, *Surface phonon dispersion of graphite (0001) over the entire energy region*, Solid State Communications **65**, 1601 (1988).

[Oshima(1997)] Chuhei Oshima and Ayato Nagashima, *Ultra-thin epitaxial films of graphite and hexaongal boron nitride on solid surfaces*, Journal of Physics: Condensed Matter **9**, 1 (1997).

[Ouyang(2008)] Yijian Ouyang, Xinran Wang, Hongjie Dai, and Jing Guo, *Carrier scattering in graphene nanoribbon field-effect transistors*, Applied Physics Letters **92**, 243124 (2008).

[Palacios(2008)] J. J. Palacios, J. Fernández-Rossier, and L. Brey, *Vacancy-induced magnetism in graphene and graphene ribbons*, Physical Review B **77**, 195428 (2008).

[Pályi(2012)] András Pályi, P. R. Struck, Mark Rudner, Karsten Flensberg, and Guido Burkard, *Spin-Orbit-Induced Strong Coupling of a Single Spin to a Nanomechanical Resonator*, Physical Review Letters **108**, 206811 (2012).

[Pancharatnam(1956)] S. Pancharatnam, *Generalized Theory of Interference, and its Applications. Part I. Coherent Pencils*, Proceedings of the Indian Academy of Sciences, Section A **44**, 247 (1956).

[Paszkowicz(2002)] W. Paszkowicz, J. B. Pelka, M. Knapp, T. Szyszko, and S. Podsiadlo, *Lattice parameters and anisotropic thermal expansion of hexagonal boron nitride in the 10-297.5 K temperature range*, Applied Physics A **75**, 431 (2002).

[Peierls(1933)] R. Peierls, *Zur Theorie des Diamagnetismus von Leitungselektronen*, Zeitschrift für Physik **80**, 763 (1933).

[Peng(2012)] Qing Peng, Wei Ji, and Suvranu De, *Mechanical properties of the hexagonal boron nitride monolayer: Ab initio study*, Computational Materials Science **56**, 11 (2012).

[Pereira(2006)] Vitor M. Pereira, F. Guinea, J. M. B. Lopes dos Santos, N. M. R. Peres, and A. H. Castro Neto, *Disorder Induced Localized States in Graphene*, Physical Review Letters **96**, 036801 (2006).

[Pereira(2009)] Vitor M. Pereira, A. H. Castro Neto, and N. M. R. Peres, *Tight-binding approach to uniaxial strain in graphene*, Physical Review B **80**, 045401 (2009).

[Pesin(2012)] Dmytro Pesin and Allan H. MacDonald, *Spintronics and pseudospintronics in graphene and topological insulators*, Nature Material **11**, 409 (2012).

[Petta(2005)] J. R. Petta, A. C. Johnson, J. M. Taylor, E. A. Laird, A. Yacoby, M. D. Lukin, C. M. Marcus, M. P. Hanson, and A. C. Gossard, *Coherent Manipulation of Coupled Electron Spins in Semiconductor Quantum Dots*, Science **309**, 2180 (2005).

[Phark(2011)] Soo-hyon Phark, Jérôme Borme, Augusto León Vanegas, Marco Corbetta, Dirk Sander, and Jürgen Kirschner, *Direct Observation of Electron Confinement in Epitaxial Graphene Nanoislands*, ACS Nano **5**, 8162 (2011).

[Qi(2012)] Zenan Qi and Harold S. Park, *Intrinsic energy dissipation in CVD-grown graphene nanoresonators*, Nanoscale **4**, 3460 (2012).

[Radisavljevic(2011)] B. Radisavljevic, A. Radenovic, J. Brivio, V. Giacometti, and A. Kis, *Single-layer MoS_2 transistors*, Nature Nanotechnology **6**, 147 (2011).

[Rakhmanov(2012)] A. L. Rakhmanov, A.V. Rozhkov, A. O. Sboychakov, and Franco Nori, *Instabilities of the AA-stacked graphene bilayer*, Physical Review Letters **109**, 206801 (2012).

[Recher(2009)] Patrik Recher, Johan Nilsson, Guido Burkard, and Björn Trauzettel, *Bound states and magnetic field induced valley splitting in gate-tunable graphene quantum dots*, Physical Review B **79**, 085407 (2009).

[Recher(2010)] Patrik Recher and Björn Trauzettel, *Quantum dots and spin qubits in graphene*, Nanotechnology **21**, 302001 (2010).

[Reddy(2006)] C. D. Reddy, S. Rajendran, and K. M. Liew, *Equilibrium configuration and continuum elastic properties of finite sized graphene*, Nanotechnology **17**, 864 (2006).

[Ribeiro(2009)] R. M. Ribeiro, Vitor M. Pereira, N. M. R. Peres, P. R. Briddon, and A. H. Castro Neto, *Strained graphene: tight-binding and density functional calculations*, New Journal of Physics **11**, 115002 (2009).

[Ribeiro(2011)] R. M. Ribeiro and N. M. R. Peres, *Stability of boron nitride bilayers: Ground-state energies, interlayer distances, and tight-binding description*, Physical Review B **83**, 235312 (2011).

[Robertson(1984)] John Robertson, *Electronic structure and core exciton of hexagonal boron nitride*, Physical Review B **29**, 2131 (1984).

[Robertson(2013)] Alex W. Robertson, Barbara Montanari, Kuang He, Christopher S. Allen, Yimin A. Wu, Nicholas M. Harrison, Angus I. Kirkland, and Jamie H. Warner, *Structural Reconstruction of the Graphene Monovacancy*, ACS Nano **7**, 4495 (2013).

[Rohling(2012)] Niklas Rohling and Guido Burkard, *Universal quantum computing with spin and valley states*, New Journal of Physics **14**, 083008 (2012).

[Rudner(2010)] Mark S. Rudner and Emmanuel I. Rashba, *Spin relaxation due to deflection coupling in nanotube quantum dots*, Physical Review B **81**, 125426 (2010).

[Ruess(1948)] G. Ruess and F. Vogt, *Höchstlamellarer Kohlenstoff aus Graphitoxyhydroxyd*, Monatshefte für Chemie und verwandte Teile anderer Wissenschaften **78**, 222 (1948).

[Ruffieux(2012)] Pascal Ruffieux, Jinming Cai, Nicholas C. Plumb, Luc Patthey, Deborah Prezzi, Andrea Ferretti, Elisa Molinari, Xinling Feng, Klaus Müllen, Carlo A. Pignedoli, and Roman Fasel, *Electronic Structure of Atomically Precise Graphene Nanoribbons*, ACS Nano **6**, 6930 (2012).

[Rycerz(2007)] A. Rycerz, J. Tworzydło, and C. W. Beenakker, *Valley filter and valley valve in graphene*, Nature Physics **3**, 172 (2007).

[Sai(2003)] Na Sai and E. J. Mele, *Microscopic theory for nanotube piezoelectricity*, Physical Review B **68**, 241405(R) (2003).

[Saini(2014)] Angela Saini, *EU Graphene Flagship aims for technological breakthroughs*, MRS Bulletin **39**, 393 (2014).

[Samsung2014SR] Samsung Electronics, *Sustainability Report 2014*, http://tinyurl.com/o45ln76 (retrieved on October 16$^{\text{th}}$, 2014).

[Savage(2012)] Neil Savage, *Super carbon*, Nature **483**, S31 (2012).

[Scholar] Google Scholar, http://scholar.google.com/ (retrieved on October 15$^{\text{th}}$, 2014).

[Schrieffer(1966)] J. R. Schrieffer and P. A. Wolff, *Relation between the Anderson and Kondo Hamiltonians*, Physical Review **149**, 491 (1966).

[Semenoff(1984)] Gordon W. Semenoff, *Condensed-Matter Simulation of a Three-Dimensional Anomaly*, Physical Review Letters **53**, 2449 (1984).

[Shapira] Philip Shapira, Jan Youtie, and Sanjay Arora, *Early Patterns of Commercialization in Graphene*, in *Science, Technology and Innovation Policy for the Future*, Springer (2013).

[Shivaraman(2009)] Shriram Shivaraman, Robert A. Barton, Xun Yu, Jonathan Alden,

Lihong Herman, MVS Chandrasekhar, Jiwoong Park, Paul L. McEuen, Jeevak M. Parpia, Harold G. Craighead, and Michael G. Spencer, *Free-Standing Epitaxial Graphene*, Nano Letters **9**, 3100 (2009).

[Shor(1994)] Peter W. Shor, *Algorithms for Quantum Computation: Discrete Logrithms and Factoring*, Proceedings of the 35$^{\text{th}}$ Symposium on Foundations of Computer Science, 124 (1994).

[Shor (1997)] Peter W. Shor, *Polynomial-Time Algorithms for Prime Factorization on a Quantum Computer*, SIAM Journal on Computing **26**, 1484 (1997).

[Sławińska(2010)] J. Sławińska, I. Zasada, and Z. Klusek, *Energy gap tuning in graphene on hexagonal boron nitride bilayer system*, Physical Review B **81**, 155433 (2010).

[Soclof1983Pat] Sidney I. Soclof, *Method of making sub-micron dimensioned NPN lateral transistor*, patent US 4415371 A, publication date: November 15$^{\text{th}}$, 1983.

[Steele(2009)] G. A. Steele, A. K. Hüttel, B. Witkamp, M. Poot, H. B. Meerwaldt, L. P. Kouwenhoven, and H. S. J. van der Zant, *Strong Coupling Between Single-Electron Tunneling and Nanomechanical Motion*, Science **325**, 1103 (2009).

[Struck(2010)] P. R. Struck and Guido Burkard, *Effective time-reversal symmetry breaking in the spin relaxation in a graphene quantum dot*, Physical Review B **82**, 125401 (2010).

[Subramaniam(2012)] D. Subramaniam, F. Libisch, Y. Li, C. Pauly, V. Geringer, R. Reiter, T. Mashoff, M. Liebmann, J. Burgdörfer, C. Busse, T. Michely, R. Mazzarello, M. Pratzer, and M. Morgenstern, *Wave-Function Mapping of Graphene Quantum Dots with Soft Confinement*, Physical Review Letters **108**, 046801 (2012).

[Sun(2008)] Xiaoming Sun, Zhuang Liu, Kevin Welsher, Joshua Tucker Robinson, Andrew Goodwin, Sasa Zaric, and Honjie Dai, *Nano-graphene oxide for cellular imaging and drug delivery*, Nano Research **1**, 203 (2008).

[Suzuura(2002)] Hidekatsu Suzuura and Tsuneya Ando, *Phonons and electron-phonon scattering in carbon nanotubes*, Physical Review B **65**, 235412 (2002).

[Svore(2005)] Krysta M. Svore, Barbara M. Terhal, and David P. DiVincenzo, *Local fault-tolerant quantum computation*, Physical Review A **72**, 022317 (2005).

[Takakura(2014)] T. Takakura, A. Noiri, T. Obata, T. Otsuka, J. Yoneda, K. Yoshida, and S. Tarucha, *Single to quadruple quantum dots with tunable tunnel couplings*, Applied Physics Letters **104**, 113109 (2014).

[Tao(2011)] Chenggang Tao, Liying Jiao, Oleg V. Yazyev, Yen-Chia Chen, Juanjuan Feng, Xiaowei Zhang, Rodrigo B. Capaz, James M. Tour, Alex Zettl, Steven G. Louie, Hongjie Dai, and Michael F. Crommie, *Spatially resolving edge states of chiral graphene nanoribbons*, Nature Phyiscs **7**, 616 (2011).

[Thompson(2006)] Scott E. Thompson and Srivatsan Parthasarathy, *Moore's law: the future of Si microelectronics*, Materials Today **9**, 20 (2006).

[Tombros(2007)] Nikolaos Tombros, Csaba Jozsa, Mihaita Popinciuc, Harry T. Jonkman,

and Bart J. van Wees, *Electronic spin transport and spin precession in single graphene layers at room temperature*, Nature **448**, 571 (2007).

[Tombros(2008)] N. Tombros, S. Tanabe, A. Veligura, C. Jozsa, M. Popinciuc, H. T. Jonkman, and B. J. van Wees, *Anisotropic Spin Relaxation in Graphene*, Physical Review Letters **101**, 046601 (2008).

[Topsakal(2009)] M. Topsakal, E. Aktürk, and S. Ciraci, *First-principles study of two- and one-dimensional honeycomb structures of boron nitride*, Physical Review B **79**, 115442 (2009).

[Trauzettel(2007)] Björn Trauzettel, Denis V. Bulaev, David Loss, and Guido Burkard, *Spin qubits in graphene quantum dots*, Nature Physics **3**, 192 (2007).

[Uchoa(2008)] Bruno Uchoa, Valeri N. Kotov, N. M. R. Peres, and A. H. Castro Neto, *Localized Magnetic States in Graphene*, Physical Review Letters **101**, 026805 (2008).

[Vanderbilt(1990)] David Vanderbilt, *Soft self-consistent pseudopotentials in a generalized eigenvalue formalism*, Physical Review B **41**, 7892 (1990).

[Vandersypen(2001)] Lieven M. K. Vandersypen, Matthias Steffen, Gregory Breyta, Costantino S. Yannoni, Mark H. Sherwood and Isaac L. Chuang, *Experimental realization of Shor's quantum factoring algorithm using nuclear magnetic resonance*, Nature **414**, 883 (2001).

[VanVleck(1940)] J. H. Van Vleck, *Paramagnetic Relaxation Times for Titanium and Chrome Alum*, Physical Review **57**, 426 (1940).

[Varlet(2014)] Anastasia Varlet, Ming-Hao Liu, Viktor Krueckl, Dominik Bischoff, Pauline Simonet, Kenji Watanabe, Takashi Taniguchi, Klaus Richter, Klaus Ensslin, and Thomas Ihn, *Fabry-Pérot Interference in Gapped Bilayer Graphene with Broken Anti-Klein Tunneling*, Physical Review Letters **113**, 116601 (2014).

[Varlet(2014-2)] Anastasia Varlet, Dominik Bischoff, Pauline Simonet, Kenji Watanabe, Takashi Taniguchi, Thomas Ihn, Klaus Ensslin, Marcin Mucha-Kruczyński, and Vladimir I. Fal'ko, *Anomalous Sequence of Quantum Hall Liquids Revealing a Tunable Lifshitz Transition in Bilayer Graphene*, Physical Review Letters **113**, 116602 (2014).

[Veendrick] Harry Veendrick, *Deep-Submicron CMOS ICs*, 2nd edition, Springer (2000).

[Wallace(1947)] P. R. Wallace, *The Band Theory of Graphite*, Physical Review **71**, 622 (1947).

[Wallraff(2004)] A. Wallraff, D. I. Schuster, A. Blais, L. Frunzio, R.-S. Huang, J. Majer, S. Kumar, S. M. Girvin, and R. J. Schoelkopf, *Strong coupling of a single photon to a superconducting qubit using circuit quantum electrodynamics*, Nature **431**, 162 (2004).

[Wang(2008)] Xuan Wang, Linjie Zhi, and Klaus Müllen, *Transparent, Conductive Graphene Electrodes for Dye-Sensitized Solar Cells*, Nano Letters **8**, 323 (2008).

[Wang(2011)] Xinran Wang, Yijian Ouyang, Liying Jiao, Hailiang Wang, Liming Xie, Justin Wu, Jing Guo, and Hongjie Dai, *Graphene nanoribbons with smooth edges behave*

as quantum wires, Nature Nanotechnology **6**, 563 (2011).

[Wang(2012)] Qing Hua Wang, Kouroush Kalantar-Zadeh, Andras Kis, Jonathan N. Coleman, and Michael S. Strano, *Electronics and optoelectronics of two-dimensional transition metal dichalcogenides*, Nature Nanotechnology **7**, 699 (2012).

[Watanabe(2004)] Kenji Watanabe, Takashi Taniguchi, and Hisao Kanda, *Direct-bandgap properties and evidence for ultraviolet lasing of hexagonal boron nitride single crystal*, Nature Materials **3**, 404 (2004).

[Wiesendanger(2009)] Roland Wiesendanger, *Spin mapping at the nanoscale and atomic scale*, Reviews of Modern Physics **81**, 1495 (2009).

[Woods(2014)] C. R.Woods, L. Britnell, A. Eckmann, R. S. Ma, J. C. Lu, H. M. Guo, X. Lin, G. L. Yu, Y. Cao, R. V. Gorbachev, A. V. Kretinin, J. Park, L. A. Ponomarenko, M. I. Katsnelson, Yu. N. Gornostyrev, K. Watanabe, T. Taniguchi, C. Casiraghi, H-J. Gao, A. K. Geim, and K. S. Novoselov, *Commensurate–incommensurate transition in graphene on hexagonal boron nitride*, Nature Physics **10**, 451 (2014).

[Worsley(2010)] Marcus A. Worsley, Peter J. Pauzauskie, Tammy Y. Olson, Juergen Biener, Joe H. Satcher, Jr., and Theodore F. Baumann, *Synthesis of Graphene Aerogel with High Electrical Conductivity*, Journal of the American Chemical Society **132**, 14067 (2010).

[Wunsch(2008)] B. Wunsch, F. Guinea, and F. Sols, *Dirac-point engineering and topological phase transitions in honeycomb optical lattices*, New Journal of Physics **10**, 103027 (2008).

[Xiao(2010)] Di Xiao, Ming-Che Chang, and Qian Niu, *Berry phase effects on electronic properties*, Reviews of Modern Physics **82**, 1959 (2010).

[Xiong(2007)] Shi-Jie Xiong and Ye Xiong, *Anderson localization of electron states in graphene in different types of disorder*, Physical Review B **76**, 214204 (2007).

[Yazyev(2007)] Oleg V. Yazyev and Lothar Helm, *Defect-induced magnetism in graphene*, Physical Review B **75**, 125408 (2007).

[Yazyev(2008)] Oleg V. Yazyev, *Magnetic Correlations at Graphene Edges: Basis for Novel Spintronics Devices*, Physical Review Letters **100**, 047209 (2009).

[Yazyev(2010)] Oleg V. Yazyev, *Emergence of magnetism in graphene materials and nanostructures*, Reports on Progress in Physics **73**, 056501 (2010).

[Yazyev(2011)] Oleg V. Yazyev, Rodrigo B. Capaz, and Steven G. Louie, *Theory of magnetic edge states in chiral graphene nanoribbons*, Physical Review B **84**, 115406 (2011).

[Yoon(2011)] Youngki Yoon, Dmitri E. Nikonov, and Sayeef Salahuddin, *Role of phonon scattering in graphene nanoribbon transistors: Nonequilibrium Green's function method with real space approach*, Applied Physics Letters **98**, 203503 (2011).

[Zakharchenko(2011)] K. V. Zakharchenko, M. I. Katsnelson, and A. Fasolino, *Finite Temperature Lattice Properties of Graphene beyond the Quasiharmonic Approximation*,

Physical Review Letters **102**, 046808 (2009).

[Zhang(2005)] Yuanbo Zhang, Yan-Wen Tan, Horst L. Stormer, and Philip Kim, *Experimental observation of the quantum Hall effect and Berry's phase in graphene*, Nature **438**, 201 (2005).

[Zhang(2009)] Yuanbo Zhang, Victor W. Brar, Caglar Girit, Alex Zettl, and Michael F. Crommie, *Origin of spatial charge inhomogeneity in graphene*, Nature Physics **5**, 722 (2009).

[Zhang(2013)] Xiaowei Zhang, Oleg V. Yazyev, Juanjuan Feng, Liming Xie, Chenggang Tao, Yen-Chia Chen, Liying Jiao, Zahra Pedramrazi, Alex Zettl, Steven G. Louie, Hongjie Dai, and Michael F. Crommie, *Experimentally Engineering the Edge Termination of Graphene Nanoribbons*, ACS Nano **7**, 198 (2013).

[Zurek(2003)] Wojciech Hubert Zurek, *Decoherence, einselection, and the quantum origins of the classical*, Reviews of Modern Physics **75**, 715 (2003).